Electrostatic Properties of Particles for Inhalation

Rowland, Martin

Award date:
2014

Awarding institution:
University of Bath

Electrostatic Properties of Particles for Inhalation

Martin Gregory Rowland

A Thesis Submitted for the Degree of Doctor of Philosophy

University of Bath

Department of Pharmacy and Pharmacology

October 2014

Table of Contents

Abstract

Dry powder inhalers (DPIs) and pressurised metered dose inhalers (pMDIs) are devices used to deliver therapeutic agents to the lungs. Typically, inhaled active pharmaceutical ingredients (APIs) are electrically resistive materials and are prone to accumulating electrostatic charge. The build-up of charge on inhaled therapeutics has traditionally been viewed as a nuisance as it may result in problems such as weighing errors, agglomeration, adhesion to surfaces and poor flow. Energetic processing steps such as micronisation, blending, blister/capsule filling as well as fluidisation of the dose will result in a large number of particulate collisions which can result in charge transfer. Charge present on aerosol particles may also affect the *in vivo* performance by altering the inhaler delivery efficiency and promoting electrostatic precipitation within the lung.

This study aimed to develop and assess repeatable and reliable methods of performing electrostatic measurements of particles for inhalation and to understand the relationship of charge with environmental relative humidity.

A powder ladle was constructed to perform net charge measurements of inhalation grades of lactose and used to assess the extent of triboelectrification during low shear turbula blending. Results demonstrated the importance of the method of addition used to transfer a sample to a net charge measurement device.

The electrical properties of DPI formulations were investigated using a Charge Decay Time Analyser. It was determined that both API concentration and relative humidity play an essential role in governing the extent to which a DPI formulation can become electrostatically charged and the subsequent rate of charge decay.

Finally, the bipolar Next Generation Impactor (bp-NGI) was developed and assessed as a tool to measure the bipolar charge to mass ratios of therapeutic aerosol particles in order to address the unmet need of combining a bipolar charge measurement system with an industry standard aerosol particle size classifier.

List of Figures

List of Tables

Acknowledgements

I would like to thank my academic supervisor, Professor Robert Price, for accepting me as a candidate for this PhD project, for teaching me about the fundamental principles of aerosol pharmaceutical technology and electrostatic measurements, for the motivational talks and for the advice and support. I would also like to thank Dr Jagdeep Shur for help with practical aspects of the project and many useful insights which were of enormous help. The help of Paul Frith and Dr Janusz Kulon for aid with design and construction of the bp-NGI is also enormously appreciated.

My industrial supervisors Alessandro Cavecchi, Frank Thielmann and Nuno Silva are thanked for guidance during the project, interesting discussions and feedback during teleconferences and for providing me with opportunity to present data to colleagues in Basel. I am grateful to Novartis Pharma AG for funding and hope that findings presented in this thesis will be a catalyst for further research into aerosol electrostatics and the effect on drug product performance.

Past and present members of the Pharmaceutical Surface Science Research Group at the University of Bath including Dr Hanne Kinnunen, Charlotte McDonnell, Dr Michelle Smith, Christopher Vernall and last but certainly not least, Dr Roberto Depasquale are thanked for being a constant source of advice as well as good friends.

Moving to Bath and not knowing anyone upon arrival I was fortunate to meet some great people including James Canton, Dave Peacock, Mizuho Ozaki, Dr Ettore Barbieri, Dr Joe Kinrade, Gina Shaw, Berenice Scandone, Auxilia Anne George, Chen Ying, Lee Collins, Kyle Selman, Rupinder Hunjan, Thomas Anderson and Robert Stringer. Thanks for your friendship and for the fun times that I had in Bath with you all.

Finally I would like to thank Mum, Dad, Geoff, Katie and Dexter for putting up with me and being a constant source of love and support. I couldn't have made it this far without you.

List of Symbols and Abbreviations

A	Amps
AE	Aeration energy
A_H	Hamaker constant
API	Active pharmaceutical ingredient
atm	atmosphere
β	liquid-vacuum permittivity ratio
BCMS	Bipolar charge measurement system
BDS	base deactivated silanol
BNC	Bayonet Neill-Concelman
bp-NGI	bipolar Next Generation Impactor
C	Coulomb
CBD	conditioned bulk density
Cc	slip correction factor
CDTA	charge decay time analyser
cm	centimetres
cm^3	centimetres cubed
CV	acceptance value
°C	degrees Celsius
Δ	change in
d	diameter
DC	direct current
DFI	dynamic flow index
Dif	diffusion coefficient
DPI	dry powder inhaler
DUSA	dose uniformity sampling apparatus
DVS	dynamic vapour sorption
d_{50}	particle cut off diameter
ε_0	relative permittivity of free space
ε_r	relative permittivity of the environment
e	Euler's number
E	Electric field strength
ELPI	electrical low pressure impactor
ELS	evaporative light scattering
eNGI	electrical Next Generation Impactor

η	viscosity
ϕ	work function
F	Farad
F_c	capillary force
FE	fluidisation energy
FP	fluticasone propionate
F_{vw}	van der Waals force
g	gravitational acceleration constant
γ	surface tension
HPLC	high performance liquid chromatography
I	current
J	Joule
k	Boltzmann constant
K_e	Coulomb's constant
Kn	Knudsen's number
K_{precip}	precipitation efficiency
kV	kiloVolt
l	length
L	litres
$Lmin^{-1}$	litres per minute
µC	microCoulomb
µL	microLitre
µm	micrometre
µg	microgram
m	mass
mg	milligrams
min	minute
mL	millilitre
n	number
nA	nanoAmp
nC	nanoCoulomb
NGI	Next Generation Impactor
ODS	octadecyl silane
Ψ	flow rate
p	pressure
pC	picoCoulomb

Ph. Eur.	European Pharmacopoeia
pMDI	pressurised metered dose inhaler
Q	charge
ρ_a	air density
ρ_e	electrical resistivity
ρ_p	particle density
r	radius
R	resistance
Re	Reynold's number
RH	relative humidity
RP-HPLC	reverse phase high performance liquid chromatography
RPM	revolutions per minute
RSD	relative standard deviation
σ	conductivity
s	second
S	separation distance
S.D.	standard deviation
SEM	scanning electron microscopy
Stk	Stokes number
SX	salmeterol xinafoate
τ	time constant
t	time
T	temperature
™	trademark
$T_{10\%}$	Time taken for a value to fall to 10% of its initial value
$T_{1/e}$	Time taken for a value to fall to 1/e of its initial value
USP	United States Pharmacopoeia
UV	ultraviolet
V	Volts
V_c	contact potential difference
V_s	initial surface potential
v/v	volume in volume
v_0	velocity
v_{ts}	terminal settling velocity
W	jet diameter
w/w	weight in weight

Chapter 1 Introduction

1.1 Respiratory drug delivery

1.1.1 Respiratory tract physiology

The respiratory system is the means by which aerobic respiration is performed by all mammals. In human physiology it begins with the pharynx and larynx, which lead to the oropharynx, followed by the trachea and finally the lungs. The purpose of the lung is to absorb gaseous oxygen into the circulatory system and release carbon dioxide back out into the external environment (Griffith *et al.* 2009). A schematic representation of human lung physiology is shown in Figure 1.1 (Griesenbach *et al.* 2004). The trachea bifurcates into the left and right main bronchi of each lung. The bronchi in turn bifurcate into shorter and smaller diameter bronchi and with successive narrowing and shortening of the passages the bronchioles are reached.

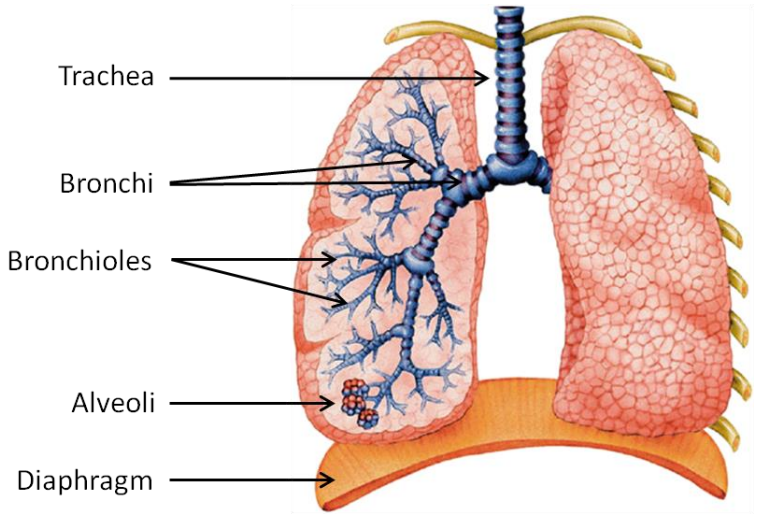

Figure 1.1 Diagram of human respiratory tract (adapted from Griesenbach *et al.*, 2004)

The bronchioles in turn bifurcate many times leading to alveolar sacs consisting of many alveoli at the periphery of the lung. In all there are approximately 23 bifurcations from the trachea to the alveoli (Prokopovich 2013). The alveoli are supplied with an abundant blood supply which facilitates efficient gaseous transfer. The respiratory volume of a pair of typical adult lungs is approximately 4 litres, however, the successive bifurcation of the airways and spherical shape of the alveoli result in an extremely large

internal surface area of the lungs in the order of 50 m^2 (Hasleton 1972). The internal surfaces of the entire respiratory tract are covered in epithelial cells which can perform a number of functions including the removal of airborne particles via mucociliary clearance where the cells produce a layer of mucus which works together with upward beating cilia hairs to expel foreign particulates (Knowles and Boucher 2002).

1.1.2 Common respiratory diseases and their treatments

1.1.2.1 Asthma

Asthma is the most prevalent respiratory illness with an estimated 235 million sufferers worldwide (WHO 2011). When an asthma sufferer is exposed to a substance which irritates the airways, known as an asthma trigger, an inflammatory response is produced which causes constriction of the airway smooth muscles, inflammation as well as mucus secretion (Knox *et al.* 2000). A prolonged reaction can lead to an asthma attack where the sufferer has greatly restricted breathing capacity which may result in hospitalisation and in severe cases, death (Sidebotham and Roche 2003). The root causes have yet to be definitively proven, however, genetic predisposition, diet, hygiene, pollution, chemicals and smoking have all been suggested as possibilities (Gern *et al.* 1999). Worryingly, the prevalence of asthma worldwide is increasing, not just in western cultures, but also in developing countries (Beasley *et al.* 2000) and so treatments for asthma remain an important area of pharmaceutical research.

Therapeutic agents for asthma include corticosteroids such as budesonide and fluticasone propionate which reduce and control inflammation (Kimura *et al.* 2009) and beta-adrenoceptor agonists (beta agonists) which are bronchodilators used to open the airways (Matera *et al.* 2008). Beta agonists may be short acting but provide a rapid onset of action such as in the case of salbutamol sulphate and are useful to alleviate asthma attacks (Cullum *et al.* 1969). Other beta agonists are long acting including formoterol fumarate, salmeterol xinafoate and ultra-long acting such as indacaterol maleate, which are used as maintenance therapies and may be taken once or twice daily as a preventative treatment (Brookman *et al.* 2007, Dahl *et al.* 2010). It is common for corticosteroids and beta agonists to be provided to asthma patients in a combined dose and many combinations are currently available on the market (Chung and Adcock 2004).

1.1.2.2 Chronic obstructive pulmonary disease

Chronic obstructive pulmonary disease (COPD) is currently the fourth leading cause of chronic morbidity and mortality in the United States and by 2020 is projected to reach the top five on the list in terms of burden of worldwide diseases (Rabe *et al.* 2007). COPD is primarily caused by smoking and pollution resulting in chronic inflammation that leads to alveolar wall destruction known as emphysema. This results in increased numbers of alveolar macrophages, neutrophils and cytotoxic T-lymphocytes, and the release of multiple inflammatory mediators including lipids, chemokines, cytokines and growth factors (Barnes *et al.* 2003). Other symptoms include tightening and constriction of the lung air passages, mucus secretion, wheezing and cough (Abbas *et al.* 2014).

The most effect treatment for COPD is smoking cessation, however, as in the case of asthma, combination treatments of corticosteroids and long acting beta agonists are commonly used to alleviate the symptoms (Miller-Larsson and Selroos 2006). Anticholinergics, also known as muscarinic antagonists, such as ipratropium and tiotropium, which act as bronchodilators by reducing smooth muscle contraction, may also be prescribed (Disse 2001).

1.1.3 Drug particle deposition within the lung

1.1.3.1 Inertial impaction

Inertial impaction is one of the dominant mechanisms of particle deposition in the lung and occurs mainly in the bronchi and bronchioles (Sbirlea-Apiou *et al.* 2007). As the patient inhales therapeutic aerosol particles, the airstream changes direction multiple times as it passes through the repeating bifurcations of the internal lung structure. At each bifurcation particles above a certain mass will possess too much momentum to be able to change direction with the airflow and so will impact on the respiratory surface. The probability that a particle impact will occur is calculated by the Stokes number (Stk), which is a dimensionless parameter given by Equation 1.1.

$$Stk = \frac{\rho_p d^2 V}{18\eta r} \qquad \text{Equation 1.1}$$

Where ρ_p is the density of the particle, d is the diameter of the particle, V is the velocity of the air, η is the viscosity of the air and r is the radius of the airway. The greater the

value of the Stokes number, the greater the chance that the particle will impact onto the airway surface (Kiao *et al.* 2010). For Stokes' law to be valid, the airflow through the lung must be laminar. Therefore the value for the Reynold's number, given by Equation 1.2 needs to be between 300-3000.

$$Re = \frac{\rho_a V d}{\eta} \qquad \text{Equation 1.2}$$

If the Reynold's number falls outside this range, particle deposition will occur not only as a result of inertial impaction, but also as a result of turbulence. However, given average geometries and inspiratory flow rates, laminar flow is typical within the human lung with the possible exception of the trachea (Carvalho *et al.* 2011).

1.1.3.2 Sedimentation

Sedimentation is the process by which particles are suspended in the respiratory tract due to the effect of gravity as a function of time. If the breath hold time is increased more time is allowed for particles to sediment which can increase lung deposition (Zeng *et al.* 2001). Assuming that the relative velocity of the surface of the particle and the airstream is zero, Stokes' Law can be used to predict the terminal settling velocity (v_{ts}) during sedimentation for spherical particles with diameters in the range 1-40 μm according to Equation 1.3.

$$v_{ts} = \frac{(\rho_p - \rho_a) d^2 g}{18\eta} \qquad \text{Equation 1.3}$$

Where ρ_a is the density of air and g is the gravitational acceleration (Gonda 2004). For particles smaller than 10 μm a slip correction factor (C_c) should be applied to Stokes' law as shown in Equation 1.4.

$$C_c = 1 + Kn \left[A_1 + A_2\, exp - \left(\frac{A_3}{Kn}\right)\right] \qquad \text{Equation 1.4}$$

Where Kn is the Knudsen number and A_1, A_2 and A_3 are experimentally determined constants. The size dependence is related to the downward gravitational force of the particle and the resistive force for which Stokes' law is valid.

1.1.3.3 Diffusion

Diffusion occurs when particles are small enough to be able to be displaced by molecular gas bombardment which is described by Brownian motion (Yu and Hu 1983). The ability of a particle to be displaced is determined by its diffusion coefficient, Dif, given by the Stokes-Einstein Equation as shown in Equation 1.5 (Gonda 2004).

$$Dif = \frac{kT}{3\pi\eta d} \qquad \text{Equation 1.5}$$

Where k is the Boltzman constant and T is the absolute temperature. In reality only sub-micron diameter particles are expected to be influenced by Brownian motion during respiratory drug delivery within the alveolar regions of the lung.

1.1.3.4 Interception

Interception may occur for non-spherical, irregularly shaped aerosol particles which do not possess a central centre of mass. In this case the distal end of the particle may encounter the airway surface earlier than would be predicted using the inertial impaction, sedimentation or diffusion theories (Zhang *et al.* 1996). This can lead to the particle being deposited higher in the respiratory tract than may be predicted. In reality, as the airway diameter is much larger than the typical API aerodynamic diameter, interception is not thought to be an important factor in regional lung deposition.

1.1.3.5 Electrostatic Precipitation

Electrostatic precipitation may cause particle deposition by three main methods. Firstly, as an aerosol cloud of particles charged with the same polarity is generated, the like charges will repel which will cause the particles to move apart from one another. In a confined space such as the bronchi this will lead to an increase in the deposition (Mayya and Sapra 2002). Secondly, as a charged particle approaches an uncharged surface within the respiratory system, an “image charge” of opposite polarity may be induced onto said surface which will enhance the attraction between the two, and hence increase the probability of deposition by electrostatic precipitation (Soltani and Ahmadi 1999). Finally, negative charges occur naturally on the surfaces of cell membranes and so if a positively charged aerosol particle approaches, the electrostatic attraction will thus increase the amount of deposition (Patton *et al.* 2004). A summary

of previously published literature discussing the clinical relevance of aerosol charge can be found in section 1.3.5.

1.1.4 Pharmaceutical devices for delivering aerosols to the lung

1.1.4.1 Nebulisers

Nebulisers use compressed gas or ultrasound to convert aqueous solutions or suspensions of respiratory drug products into a fine aerosol mist which is inhaled by the patient, either directly from the mouthpiece of the device or using a facemask (Lass *et al.* 2006). The operation of a nebuliser is neither patient driven nor requires coordinated breathing which can help to increase patient adherence (Latchford *et al.* 2009). In addition nebulisers may be used for prolonged periods of time compared with pMDIs and DPIs which can increase the maximum dose delivered (Everard *et al.* 1992). Due to limitations such as cost, noise, a lack of portability and the need for hygienic conditions, nebulisers are often restricted to hospital environments (Demir and Saryal 2003). However, recent developments such as personalised miniature nebulisers may start to overcome these limitations (Knoch and Keller 2005).

1.1.4.2 Electrosprays

Electrosprays are created with the use of a cone-jet which operates by passing a liquid slowly through an electrified capillary needle, creating charged droplets which is known as spray atomization. The droplets possess a narrow particle size distribution and tight control is achievable making electrosprays suitable for inhaled therapeutics (Gomez 2002). The scaling law of the spray current, I, emitted from an electrified liquid meniscus of a highly conducting liquid is described by Equation 1.6.

$$I = f(\beta)\left\{\frac{\psi\sigma\gamma}{\beta}\right\}^{1/2} \qquad \text{Equation 1.6}$$

Where ψ is the flow rate, γ is the surface tension, σ is the electrical conductivity and β is the liquid-vacuum permittivity ratio. f is a dimensionless function dependent on the liquid used which may be experimentally determined (Gañán-Calvo *et al.* 1997). In order to prevent image forces from causing deposition in the upper regions of the respiratory tract Noakes *et al.* devised an electrospray system which incorporates a

corona discharge of opposite polarity to neutralise the charge present on the droplets (Noakes *et al.* 1990). Studies have indicated that the efficiency of electrosprays at delivering drug particles to the lung may be significantly improved with respect to current approaches and research has been conducted to commercialise the technology as a portable liquid dose inhaler (Placke and Zimlich 2002).

1.1.4.3 Pressurised metered dose inhalers (pMDIs)

The first pMDI was developed by Riker laboratories in 1956 for use with epinephrine and isoproterenol, the idea coming from comparing a can of hairspray to a nebuliser (Anderson 2005). The design consists of a pressurised canister containing a propellant, surfactant and a suspension or solution of the therapeutic agent (Rubin and Fink 2005). Originally chlorofluorocarbons (CFCs) were used as the propellant, but due to the harmful effect they have been shown to have on the environment, modern pMDIs use hydrofluorocarbons such as hydrofluoroalkane (HFA) 134a instead (Noakes 2002). A known volume of the pMDI suspension fills a metering chamber which is surrounded by a plastic actuator and mouthpiece. In order to release the dose, the pMDI is depressed or actuated which produces a fine atomised spray over approximately 100-200 milliseconds (Dunbar 1998). The greatest limitations of pMDIs are that often inconsistent dosing occurs as a result of poor patient breath coordination, excessive inspiratory flow velocity and the cold Freon effect which can result in inefficient delivery of the API and poor patient compliance (Grossman 1994).

1.1.4.4 Dry Powder Inhalers (DPIs)

Over the past forty years, DPIs have become increasingly used due to the limitations of pMDIs (Grossman 1994). DPIs are routinely employed to deliver bronchodilators and corticosteroids used in the maintenance of asthma and chronic obstructive pulmonary disease (COPD) (Newman 2004). A dry powder inhaler formulation usually consists of micronised drug particles blended with larger coarse lactose carrier particles that promote flow properties, reduce aggregation and help in dispersion (Alagusundaram *et al.* 2010). They have the added advantage of being actuated by the patient's own inspiratory flow improving the delivery efficiency as compared with pMDIs, where ensuring correct patient inhaler technique is a constant challenge.

Many different designs of DPI inhalers have been produced such as capsule, blister and powder reservoir devices. In a capsule based device such as the Aerolizer® device (Novartis, Switzerland), a capsule, usually manufactured from HPMC or gelatin containing the DPI formulation, is pierced by the user within the device. Blister devices such as the Diskus™ device (Glaxo Smithkline, UK) operate by a similar principle except that the doses are contained within a blister strip located inside the inhaler. Powder reservoir devices such as the NEXThaler™ (Chiesi, Italy) contain a bulk reservoir of the DPI formulation which is metered by a dosing mechanism inside the device. Blister and reservoir devices, although more expensive to manufacture, provide the benefit of complete containment of the DPI formulation as well as the capability of including a dose counter.

1.1.5 Characteristics of particle interactions

1.1.5.1 Van der Waals forces

Van der Waals forces are experienced by atoms, molecules and surfaces and can be attractive or repulsive in air. They are relatively weak compared to covalent bonds and ionic interactions but fundamentally contribute to the forces of cohesion and adhesion between macroscopic objects. They are anisotropic in nature meaning they are dependent on the particular orientation with which the two bodies approach each other. The van der Waals forces are classified into dipole-dipole, dipole-induced dipole and induced dipole-induced dipole, with dipole-dipole interactions being the strongest in nature. The van der Waals force (F_{vw}) between two spherical objects of radii r_1 and r_2 is described by Equation 1.7.

$$F_{vw} = \frac{A_H r_1 r_2}{(r_1 + r_2) 6 d^2} \qquad \text{Equation 1.7}$$

Where A_H is the Hamaker constant (~10^{-19} – 10^{-20} J) and d is the distance between the two objects (Overbeek and Sparnaay 1954). The van der Waals force between two species is proportional to the inverse of the square of the distance between them. As such they will be much more significant in bulk powders where there is intimate contact between particle surfaces as compared with gases where the constituent species are relatively far apart. In reality, particulate systems rarely consist of perfect spheres and the van der Waals forces will be more considerable as the surface contact area

between particles will be greater and the distance between the species reduced (Visser 1989).

1.1.5.2 Capillary forces

Capillary forces between particles caused by the condensation of water from a humid atmosphere may lead to a significant increase in the cohesive strength of a bulk powder which may in turn affect its flowability and deagglomeration characteristics (Stevens *et al.* 2009). The presence of condensed water in between two particles may lead to the formation of a pendular bridge which will act to hold the particles together via a meniscus or capillary force. The shape of the particles and the type of interparticle contact will affect the strength of the bridge and hence the magnitude of the force (Tselishchev and Val'tsifer 2003). The capillary force, F_c, between two identical spherical objects of radius, r_1, is given by Equation 1.8.

$$F_c = 2\pi r_1 \gamma \qquad \text{Equation 1.8}$$

Where γ is the surface tension of the aqueous bridge. Studies have shown that non surface specific capillary forces play a significant role in the adhesion between drug particle and carrier particle in DPI formulations. The behaviour is heavily dependent on the ambient relative humidity as this will determine the amount of water adhered to the particle surface (Price et al. 2002, Young et al. 2004).

1.1.5.3 Electrostatic interactions

Electrostatic interactions are considered as the third main force which governs particle interactions. A comprehensive summary can be found in the following section 1.2.

1.2 Fundamental Theory of Electrostatic Charge

1.2.1 Definition and fundamental principles

According to Aristotle, the first person attributed with recording the phenomenon of electrostatic charge was the Greek scientist Thales of Miletus (c. 600 B.C.), who observed the ability of the material amber to attract light materials such as paper or feathers (Sheean 1930). Charge is a fundamental property of two atomic particles – the proton and the electron. Protons in the nucleus of an atom are positively charged and the orbiting electrons are negatively charged. Like charges repel and opposite charges attract and this electrostatic attraction holds electrons in their orbits around the nuclei of atoms.

1.2.1.1 Coulombic forces

The force of attraction or repulsion experienced by two charged bodies is described by Coulomb's law, given by Equation 1.9.

$$F = k_e \frac{Q_1 Q_2}{r^2} \qquad \text{Equation 1.9}$$

Where F is the force of attraction or repulsion between the two charged bodies, Q_1 is the magnitude of charge on body 1, Q_2 is the charge on body 2 and r is the distance between them. k_e is Coulomb's constant as described by Equation 1.10.

$$k_e = \frac{1}{4\pi\varepsilon_0\varepsilon_r} \qquad \text{Equation 1.10}$$

Where ε_0 is the relative permittivity of free space and ε_r is the relative permittivity of the environment in which the two charges are contained.

Charge is measured in Coulombs, C, where one Coulomb is one ampere.second (A.s). The charge of an electron (e = -1.602 x 10^{-19} C), was first measured by Millikan and Fletcher in 1909 in what became famously known as Millikan's oil drop experiment, which used an electric field to counter gravitational and drag effects and suspend small ionised droplets of oil in mid-air (Millikan 1911).

1.2.1.2 Field Strength and Voltage

All charged bodies will possess an electric field associated with the charge present. The electric field strength, E, at a distance from a body, r, with charge, Q, is described by Equation 1.11.

$$E = \frac{Q}{4\pi\varepsilon_0\varepsilon_r r^2} \qquad \text{Equation 1.11}$$

The electric field generated by a charged spherical object may be visualised by imagining field lines emanating from the body as shown in Figure 1.2.

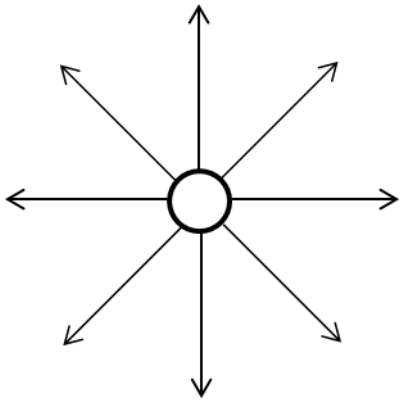

Figure 1.2 Electric field lines emanating from a charged sphere

Voltage, also described as potential difference, is measured in Joules per Coulomb ($J.C^{-1}$) and is defined as the integral of the field strength between two points in an electric field as described by Equation 1.12.

$$V(A) - V(B) = \int_A^B Eda \qquad \text{Equation 1.12}$$

Where $V(A) - V(B)$ is the voltage, or potential difference between two points A and B in an electric field at a distance of a apart. Voltage may also be described as the difference in electrical potential energy of a unit charge transported between two points.

1.2.1.3 Capacitance

The potential difference, V, of a body with charge, q, with respect to ground is proportional to the charge on the body as determined by its capacitance, Ca, as described by Equation 1.13.

$$Ca = {}^{q}/_{V} \qquad \text{Equation 1.13}$$

Capacitance is measured in Farads, F, and a Farad capacitor with a charge of 1 Coulomb has a potential difference of 1 Volt between the charged body and ground. Capacitors are utilised to store electric charge and electrometers used for the measurement of charge contain capacitors in to which the charge will flow.

1.2.1.4 Current

Current, I, measured in Amperes or Amps, is defined as the flow of electric charge as function of time, t, as described by Equation 1.14.

$$I = {}^{q}/_{t} \qquad \text{Equation 1.14}$$

One Amp is equal to one Coulomb of charge per second. In electronics currents normally consist of a flow of electrons moving through a conductive metallic wire and are also used to transfer electrical signals and energy.

1.2.1.5 Resistance and conductance

Resistance, R, measured in Ohms, is defined by Ohm's law as described by Equation 1.15 and is a measure of the degree to which a material will resist a current flowing through it or across its surface.

$$R = {}^{V}/_{I} \qquad \text{Equation 1.15}$$

Electrical resistivity, ρ_e, described by Equation 1.16 is governed by the relationship of a material's length, l, and cross sectional area, A and provides a way of predicting the charge decay rate of a charged body.

$$\rho_e = R\frac{A}{l}$$ Equation 1.16

If the electrical resistivity is low then electrons may freely flow through the body to earth or to other materials and the charge decay time will be rapid. If the body is more electrically resistive, also known as insulating, then charge decay times will be much longer as electrons may not easily flow through the body's structure. Materials such as metals will have low electrical resistivity as electrons are easily able to move through the structure. Conductivity, σ, is simply the inverse of resistivity and describes the ease with which a current may pass through a material.

1.2.2 Electron transfer via triboelectrification

When two different materials with differing electrostatic properties come into physical contact with each other and subsequently separated, an exchange of charged species, normally electrons may occur. After the exchange each material will be left with an unequal net charge of opposite sign, an example of the contact between to insulators resulting in electron transfer is shown in Figure 1.3.

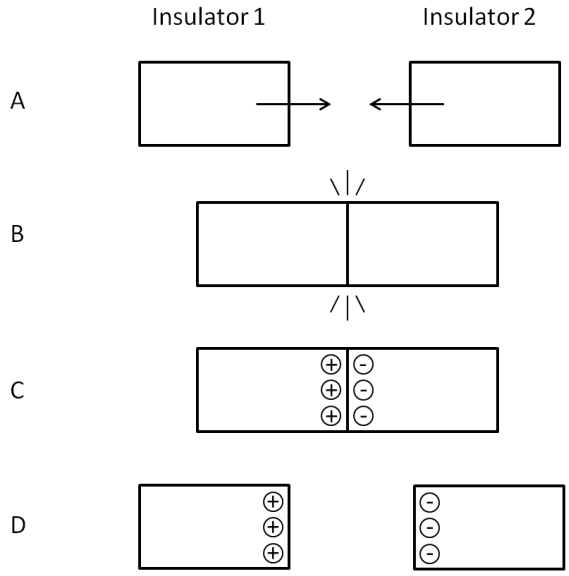

Figure 1.3 Two insulators becoming electrostatically charged via triboelectrification

In Figure 1.3 A two different, uncharged insulators move towards each other, in Figure 1.3 B the insulators come into surface contact with each other, in Figure 1.3 C, a transfer of electrons occurs from Insulator 1 to Insulator 2, resulting in Insulator 1

becoming positively charged and Insulator 2 becoming negatively charged. In Figure 1.3 D, after the insulators have become charged they become separated.

This phenomenon is known as contact-electrification or triboelectrification, and the process of rubbing or colliding two materials together to deliberately cause this phenomenon is known as tribocharging or triboelectric charging (Kwetkus 1998). Many common materials are susceptible to this phenomenon and may be placed on a triboelectric series an example of which is shown in Figure 1.4.

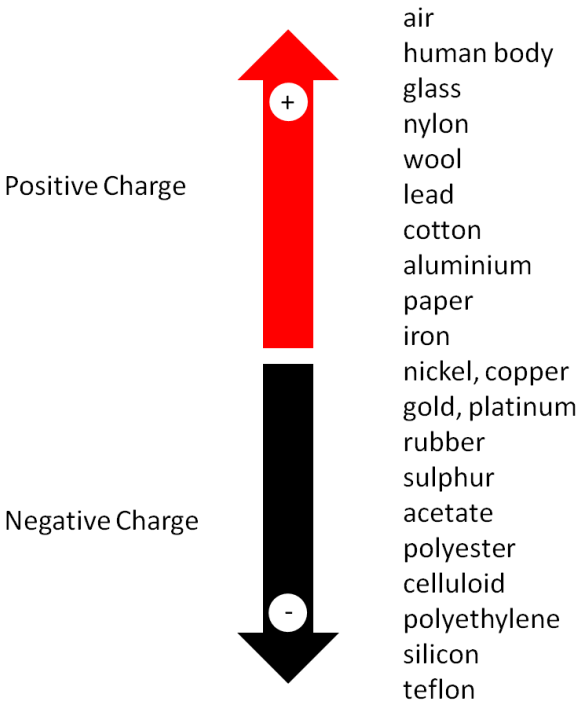

Figure 1.4 Triboelectric series of a selection of common materials

Each material is placed on the scale according to its charging propensity when rubbed against another material on the scale. For example, if a piece of polyester is rubbed with wool, the polyester will become negatively charged, and the wool positively charged. Powders, which have small particle sizes and large surface area to mass ratios are susceptible to extensive tribocharging during energetic processes such as in the case of volcanic eruptions and the movement of dust and sand by the wind (Kok and Lacks 2009). In extreme cases, a large build-up of electrostatic charge has even been responsible for dust explosions where either a corona, brush or spark discharge is of an energy greater than the Minimum Ignition Energy (MIE) of the dust cloud (Manjunath 2011). Applications have been developed to exploit this phenomena where the motion of charged particles is controlled such as in electrostatic precipitation for

example in photocopiers, printing, electrophotography (Hoshino *et al.* 2010) and the manufacture of sandpaper (Schlacht 1941).

1.2.2.1 Work function

The amount of charge transferred during triboelectrification of two conductive materials will depend on the work functions of the each material, which is a measure of how much energy is required to remove an electron from the Fermi level of the material to its vacuum energy level. Charge transfer ceases when the Fermi levels of the two materials become equal, minimising the difference in energy (Matsusaka *et al.* 2010). Figure 1.5, shows an approximation of the change in energy of two dissimilar conductive materials (e.g. metals) pre and post a triboelectrification event where a single electron is transferred from one conductor to the other.

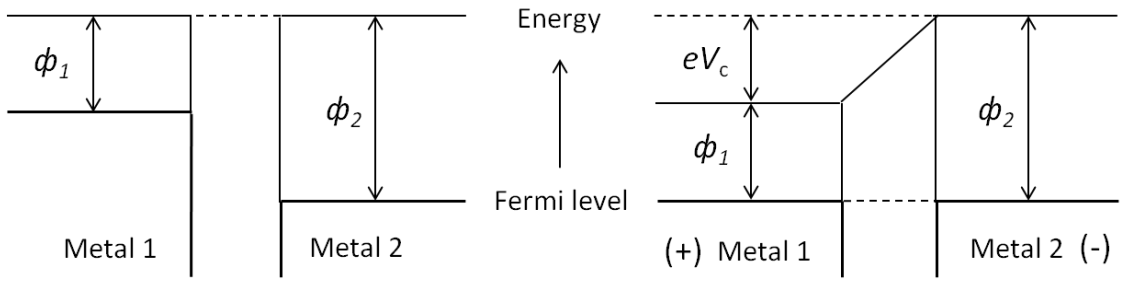

Figure 1.5 Electron transfer between two metals upon triboelectrification (adapted from Matsusaka et al. 2010)

Assuming the contact between the materials results in thermodynamic equilibrium, the contact potential difference, Vc, between the materials is described by Equation 1.17 (Harper 1967).

$$V_C = -\frac{\phi_1 - \phi_2}{e} \qquad \text{Equation 1.17}$$

Where ϕ_1 is the work function of material 1, ϕ_2 is the work function of material 2 and e is the elementary charge. The amount of charge transferred between the two materials ΔQ, is given by Equation 1.18.

$$\Delta Q = Ca_0 V_C$$ Equation 1.18

Where Ca_0 is the capacitance between the bodies at a separation distance where charge is no longer transferred between them. The theory agrees fairly well with experimental data generated (Harper 1967), and any discrepancies may be due to, for example, surface contaminants, environmental effects and surface roughness of the materials tested.

1.2.2.2 Effective work function

For insulator - conductor contacts, as there is an absence of labile electrons in the insulator, the idea of an effective work function for the insulator may be used to estimate the amount of charge transferred (Davies 1969). The contact potential difference for an insulator-metal contact may thus be approximated using Equation 1.19.

$$V_C = -\frac{\Phi_{ins} - \Phi_{con}}{e}$$ Equation 1.19

Where ϕ_{ins} is the effective work function of the insulative material and ϕ_{con} is the work function of the conductive material. After the charge is transferred the energy levels of the two materials are assumed to be equalised. Some agreement is found with experimental data (Davies 1969) however, the theory does not always hold for insulator-insulator contacts.

1.2.2.3 Surface state model

The work function and effective work function theories generally hold experimentally when one of the components is a conductive material. However, for insulator-insulator contacts the theory may not always apply due to the lack of the presence of labile electrons which are easily transferred from one material to the other. The surface state model assumes that the movement of electrons is more restricted and the available energy level is referred to as the surface state (Lowell and Rose-Innes 1980). When two materials come into contact, the electrons from the filled surface state of one material transfer to the empty surface state of the other in order to equalise the energy difference as shown in Figure 1.6.

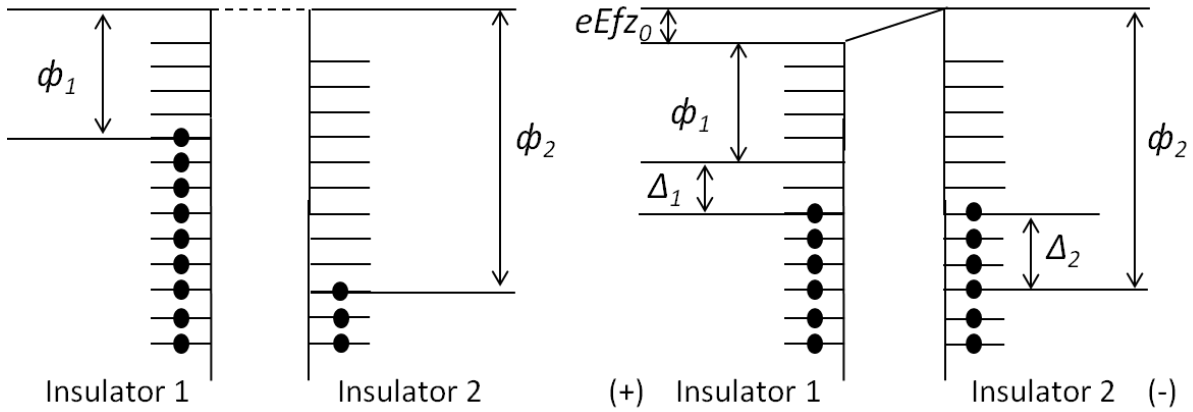

Figure 1.6 Surface state model for an insulator-insulator contact (adapted from Matsusaka et al. 2010).

After insulators come into contact the charge transfer causes the Fermi level of insulator 1 to change by Δ_1 and the Fermi level of insulator 2 to change by Δ_2. The difference between the charge of the two materials also produces a potential difference, $eEfz_0$. Therefore the expression for the energy level is given by Equation 1.20 (Lowell and Truscott 1986a).

$$\Phi_1 + \Delta_1 + eEfz_0 = \Phi_2 - \Delta_2 \qquad \text{Equation 1.20}$$

This theory has been shown to be accurate for the charging of toner particles during electrophotography (Cotler *et al.* 1995).

1.2.2.4 Electron Affinity

Electron affinity, measured in kJ/mol, is defined as the amount of energy released when an electron is added to a neutral atom or molecule in the gaseous state to form a negatively charged ion. If the process is energetically favourable, the enthalpy will be negative and energy will be released. If a material has a high electron affinity an atom or molecule in its surface will easily pick up electrons and if the material has a low electron affinity the reverse will be the case. Electron affinity tends to follow the eight electron rule whereby atoms will seek to either lose or gain electrons so that a full outer shell of eight electrons is achieved. For example, a sodium atom loses an electron to become an Na^+ ion or a chlorine atom gains an electron to become a Cl^- ion.

1.2.2.5 Ion transfer

Surface impurities which may be ionic in nature have been suggested to play a role in the tribocharging of insulators. Ion transfer during the contact between two dissimilar materials has been described previously (Robins *et al.* 1975, Mizes *et al.* 1990, Williams 2011) and ions may exist on the surface of both conductors and insulators, held in place either by weak van der Waals forces or solvated in a thin layer of surface moisture. However, the presence of water on the surface of a material will increase its conductivity and lower the electrical breakdown strength of air, resulting in a decrease in the charge present by increasing the charge decay rate (Lee 1994). Without determining precisely which ions are present on the surface of materials pre and post triboelectrification events, and the extent of adsorbed moisture present it cannot be concluded for certain whether ion transfer plays a dominant role in the transfer of charge from one species to another. However, artificially doping surfaces with ions has been exploited, for example with the use of charge control agents in the electrophotographic industry (Anderson 1996).

1.2.2.6 Material Transfer

When two materials come into contact it is possible that rather than electrons or ions being transferred, material such as solid particles may be transferred from the surface of one material to the other. If the material which is transferred carries electrostatic charge, charge will be transferred from one material to the other (Lowell and Rose-Innes 1980). Charge transfer during insulator-insulator or metal-insulator contact may not be influenced by previous identical contacts. It has been demonstrated that material transfer occurs to a large extent on the first contact and to a much smaller extent on subsequent contacts and therefore it may be concluded that material transfer is not the primary mechanism of contact electrification (Lowell 1977b). However, common manufacturing techniques for DPI formulations include coating coarse lactose carrier particles with micronized API particles. If the API particles carry charge then the resultant API-lactose agglomerates will also be charged.

1.2.3 Bipolar charge

Many of the theoretical models developed to describe charge transfer and triboelectrification assume that charged species are only transferred from one material to another resulting in a unipolar charge distribution for each material present during the contact (Saini *et al.* 2007). During the manufacture of respiratory drug products, respiratory particles will undergo collisions with many different types of materials such as stainless steel, used to construct equipment for micronizing and blending, gelatin or hydroxypropylmethyl cellulose (HPMC) used for capsules and the plastic and metal components of the inhaler. Excipient-excipient, excipient-API and API-API collisions will also lead to charge transfer (Castle and Schein 1995). In this case the overall net charge of the powder will remain constant but due to the different types of collisions involved some particles will become positively charged and some will become negatively charged, resulting in a bipolar charge distribution within the powder where the particles will be both positively and negatively charged at the same time. This may be difficult to assess accurately using conventional methods of measuring net charge as net charge only provides a sum of the positive and negative charges present (Lowell and Truscott 1986b). A graphical representation explaining this phenomenon is shown in Figure 1.7.

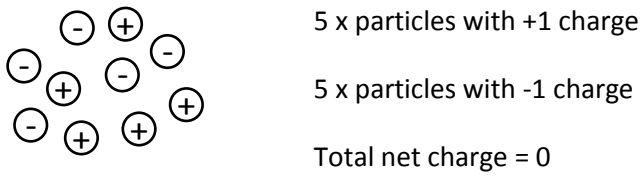

Figure 1.7 Representation of a group of bipolarly charged particles.

In this example it is assumed that each positively charged particle has lost one unit of elementary charge causing the total overall positive charge in the system to be +5. Each negatively charged particle has gained one unit of elementary charge and the overall negative charge in the system is -5. If the particles are collected together then the overall net charge recorded for the system will be zero as the positive and negative charges will cancel each other out.

1.2.4 Static charge decay

Once a material becomes electrostatically charged, the charge will decay over time and the material will return to its original, neutral state. For conductive materials this may be due to a flow of electrons to or from the conductor to another material, or to earth. Electrons will flow relatively quickly through conductors and this will result in short charge decay times in the order of seconds to minutes. For insulators, where the movement of electrons is much slower, the static charge decay rates can be much slower, taking many minutes, hours or even days. In this situation, oppositely charged carriers, electrons or ions will be attracted by the electric field created by the charged body. As they come into proximity of the body their electric field superimposes the electric field of the charged body making the total field decrease (Jonassen 2002). Charge decay may occur in three different ways:

- Charge decay of a capacitive system: an insulated conductor characterised by its capacitance, Ca and resistance to ground, R.
- Charge decay of a non-conducting system: the charge is located on a semiconducting material with a given resistivity, ρ, and permittivity, ε, where charge decay occurs through the material or along its surface.
- Charge decay through the air, facilitated by the presence of moisture as the water layer acts as a conductor

The general relationship which provides the rate of charge decay of a charged material is given by Equation 1.21

$$Q = Q_0 \, e^{\frac{-1}{\tau}} \qquad \text{Equation 1.21}$$

Where Q is the charge at a given time, Q_0 is the initial charge and τ is the time constant, given by Equation 1.22, which indicates the time taken for the charge to decay to 1/e of its initial value = 36.8%.

$$\tau = RCa \qquad \text{Equation 1.22}$$

Where R is the material's resistance and Ca is its capacitance. For an electrically insulating material, it is assumed that the charge is not uniformly distributed throughout the material, but instead resides at the surface where a charging event, such as triboelectrification has occurred. In this case the concept of surface charge density may

instead be used to calculate the charge decay rate which is governed by the same mathematical relationship. As suggested by Coelho et al. charge decay of resistive materials follows an exponential route (Coelho et al. 1989) and this has been demonstrated for both polymers and active pharmaceutical ingredients (Carter *et al.* 1998).

1.2.5 Effect of relative humidity

Variations in particle morphology will affect the surface area and roughness and hence the degree of surface water condensation (Young *et al.* 2007). In addition the chemical structure of the functional groups at the surface will determine the extent of surface water coverage - polar functional groups will attract polar water molecules through van der Waals forces, whereas non-polar functional groups will not bind water as strongly. As mentioned in section 1.2.4, relative humidity can increase the static charge decay rate of charged materials. The presence of water will act to reduce the surface resistivity by increasing the dielectric permittivity (Lutz and Kindersberger 2009) and at high humidity absorbed moisture may increase the material's overall conductivity (Kwok and Chan 2008a) and even change the surface chemistry (Young *et al.* 2007).

The amount of bound surface water increases with increasing humidity until a sorption-desorption equilibrium is reached (Lutz and Kindersberger 2009). It is essential that during electrostatic measurements the sample being tested is equilibrated for sufficient time at the specified humidity in order to allow the equilibrium to be established and that the humidity is kept constant throughout the course of the experiment.

1.3 Processes resulting in electrostatic charge build up on DPI particles

1.3.1 Formulation and processing

Electrostatic charge build-up on DPI formulation particles will mainly occur during formulation preparation, where the active pharmaceutical ingredient is blended with course carrier lactose, and processing, where the formulation is placed in storage, dispensed into capsules or blister strips or transferred to a powder reservoir device. During these processes as particles are disturbed and agitated they undergo collisions

with themselves and the surfaces with which they come in contact with. During such collisions particles will become charged via the mechanism of triboelectrification which may result in a bipolar charge distribution. This may affect the physical structure of the blend and result in processing problems such as weighing errors, agglomeration, poor flow, adhesion to container surfaces, reduced API recovery, loss of content uniformity and manual handling difficulties. The presence of charge on a DPI formulation, which does not decay quickly with time, may result in variable formulation performance.

1.3.1.1 Micronisation

Although electrostatic charge build up on an API during micronisation is not commonly reported in the literature, it is a well-known issue observed in industrial manufacturing sites. Micronisation is a highly energetic process where course API crystals are entrained in an airflow and jet milled so that they are impacted into the metallic surfaces of the mill at very high velocities. This results in the crystals breaking apart into smaller fragments and the goal is to achieve a particle size diameter of less than 5µm so that the particles will be therapeutically available when aerosolised as part of a DPI formulation. The impact of the API crystals with the mill and subsequent transfer to a storage container results in a high level of static charge build up on the API particles, making them difficult to handle and process. Recent developments in the field of supercritical fluids have produced processes where particles of suitably small diameter for inhaled drug delivery may be prepared (Chen *et al.* 2002). Shekunov *et al.* utilised supercritical CO_2 to produce salmeterol xinafoate particles of suitable particle diameter for respiratory drug delivery. Post processing, the particles were characterised for a range of physico-chemical properties including surface energy using inverse gas chromatography and electrostatic charge using a Faraday pail. The supercritical salmeterol particles were compared with salmeterol particles which had been prepared using a conventional micronisation process. Results demonstrated that both the surface energies and electrostatic charge values were lower for the supercritical particles indicating that supercritical fluid technology may be preferential to micronisation as the amount of charge build up on the particles is reduced (Shekunov *et al.* 2002).

1.3.1.2 Blending

Blending of DPI formulations may be low shear or high in nature and involves agitating a mixture of the API and the course carrier lactose in order to produce a homogeneous blend with suitable content uniformity. As particles experience movement within the vessel, they experience collisions with each other and with the walls of the vessel resulting in triboelectrification of the particle surfaces. The quantity of charge build up will depend on a number of factors including the blending vessel material (Elajnaf *et al.* 2006), the humidity of the environment and electrostatic properties of the particle surfaces (Nemeth *et al.* 2003), the presence of contamination (Eilbeck *et al.* 2000), the extent of amorphous content (Murtomaa *et al.* 2002) and the speed and length of time that the formulation is blended for (Pingali *et al.* 2009). Local temperature fluctuations during turbulent flow may also affect the extent of triboelectrification (Grant *et al.* 1968). Once the blending process has been completed, residual charge may remain on the formulation and this may adversely affect the flow, handling characteristics and ability to dispense the formulation into capsules or blisters. Charge measurements of DPI formulations post blending typically rely on pouring the sample out of the blending vessel and into a Faraday pail. This may result in additional triboelectrification of the powder as it slides over the surface of the vessel walls which may create variability in the results generated.

1.3.1.3 Further processing

In addition to micronisation and blending further processing steps may result in the triboelectrification of powders. The British Standards Institute lists typical charge values for a medium resistivity powder as shown in Table 1.1 (BSI 1991).

Operation	Charge to mass ratio (nC/g)
Sieving	10^{-3} - 10^{-6}
Pouring	10^{-1} - 10^{-3}
Feed transfer	1 - 10^{-2}
Micronizing	10^{2} - 10^{-1}
Pneumatic Conveying	10^{3} - 10^{-1}

Table 1.1 Typical charge to mass ratios experienced by a medium resistivity powder during powder handling processes

If these processes are not tightly controlled, charge build up may be variable which may lead to difficulty in processing DPI blends and lead to the problems described previously. As such, many companies seek to mitigate charge build up using methods such as active static eliminators (Revel *et al.* 2003).

1.3.2 Dynamic charge generation upon inspiratory flow

Not only will DPI formulations experience charge build up during manufacturing and processing but they will also undergo triboelectrification upon aerosolisation within an inhaler. The process of aerosolisation requires the patient to inspire through the device, drawing air through it at high velocity. This will cause the particles to deagglomerate from each other, fluidise and enter the air stream. Typically the particles do not exit the inhaler immediately, but circulate within the internal cavity of the inhaler for some time where they may undergo numerous interparticulate collisions and collisions with the device material. Shur *et al.* demonstrated using computational fluid dynamics that the velocity of the air travelling through a modified cyclohaler will influence the particle impact velocities and frequency (Shur *et al.* 2012) and these impacts will govern the extent of triboelectrification. The extent of charge build up will also depend on a number of other factors including the deaggregation mechanism of the device, the device material, the physico-chemical and electrical properties of the particles (Wong *et al.* 2014), the flow rate and humidity of the air (Rowley and Mackin 2003), and the capsule material in the case of capsule based devices. Due to the multicomponent nature of the formulation and the different materials used to construct the device the particles will experience many different types of collisions which can lead to the generation of a bipolar charge distribution. The resultant Coulombic interactions

between the particles may affect the extent of deaggregation of the API from the lactose carrier which in turn will affect the formulation performance. In addition the presence of electrostatic charge may affect the *in vivo* deposition of the aerosol particles as described in section 1.3.3.

1.3.3 Clinical relevance of aerosol particle charge

As described in sections 1.3.1 and 1.3.2, numerous processes may result in the generation of electrostatic charge on respiratory aerosol particles. After manufacturing is complete and the dosage form is packaged and labelled, a delay ranging from weeks to months may occur before the medication may reach the patient. It is assumed that during this time that any electrostatic charge present will have dissipated. However, the API and carrier particles may become electrostatically charged upon the highly energetic process of aerosolisation, which occurs as the patient takes the medication and so a large proportion of the inspired dose will be statically charged. A bipolar charge distribution may result, with charged particles of opposite signs attracting each other and charged particles of the same sign repelling each other. Regardless of the polarity, as a charged particle approaches the wall of an airway it can induce an image charge on its surface which will enhance its attraction and subsequent deposition (Bailey 1997).

Several studies have been performed to determine the effect of particle charge on the extent of *in vivo* deposition. Fraser measured the *in vivo* deposition of dust particles in a rabbit model and found that deposition increased with increasing charge magnitude (Fraser 1966). Ali *et al*. observed an increase in deposition with increasing particle charge and mass in a replica cast of a human oral pharyngeal laryngeal airway (Ali *et al*. 2009b). Chan and Yu observed a significant increase in deposition in the bronchial airways of a hollow human lung cast for particles of 2-5μm with 360-1100 electrons of charge per particle (Chan and Yu 1982). Melandri *et al*. measured the deposition of inhaled charged carnauba wax particles with particle diameters of 0.3, 0.6 and 1.1μm in human volunteers at a range of inspiratory flow rates and showed increasing particle deposition with increasing particle charge (Melandri *et al.* 1983). Bailey *et al*. developed a mathematical model of the lung using computational tools and modelled the deposition of 0.5 and 5μm diameter particles at 0, 50 and 200 electrons of charge per particle. Results demonstrated that charged particles deposited more efficiently in the bronchioles and alveolar regions due to their confined space and that deposition was

enhanced with increasing particle charge and duration of patient breathing pause (Bailey *et al.* 1998). Newhouse *et al*. conducted a study of inhaled tobramycin in healthy volunteers where the API was absorbed over several hours, this has been attributed to positive charge on the API molecule binding to the naturally occurring negative charges on the surfaces of cell membranes (Newhouse *et al*. 2003, Patton *et al*. 2004). Thus from previously published work it may be concluded that the presence of electrostatic charge on respirable aerosol particles is an important factor in determining the extent of *in vivo* deposition and hence the efficacy of the therapy.

1.4 Techniques for the measurement of bulk powder and aerosol particle charge

1.4.1 Static measurements

1.4.1.1 Faraday pail

The first commonly used piece of equipment employed to measure the net electrostatic charge of materials was the Faraday pail. It is based on an experiment conducted by Michael Faraday in 1843, who demonstrated the effect of placing a statically charged object within a conductive chamber. In Faraday's experiment a metal ice pail was connected to a gold leaf electroscope. As he lowered a charged metal sphere into the pail, without touching it, the charge of the sphere induced an equal and opposite charge on the inner surface of the pail. This in turn, caused an electrical current to flow to the electroscope which indicated the presence of the charge by the gold leaf moving position. As the sphere was then removed from the pail, the electroscope reading then returned to zero, indicating that the charge on the pail was induced by the sphere. If the sphere was placed in the pail and then touched the internal surface, the electroscope would record the same value for the charge, but then as the sphere was removed, the electroscope reading would remain constant. This indicated that the charge on the sphere had been transferred to the pail through surface contact. By charging the sphere in a repeatable way Faraday proved that the measurement of the induced charge is the same as the measurement of the charge through physical contact (Faraday 1844). Modern Faraday pails use an electrometer rather than a gold leaf oscilloscope to measure the charge of objects placed within them. Rather than moving a gold leaf, the flow of charge is stored within a capacitor in the electrometer from

which the charge value is recorded (Gross 1950). A diagram of a typical Faraday pail is shown in Figure 1.8 and shows the inner well where samples are placed, and the connection to the electrometer. The diagram also shows an electrically grounded outer well which surrounds and is electrically isolated from the inner well by PTFE insulation. The purpose of the outer well is to shield the inner well from external electric fields and thus ensure the accuracy of the measurement.

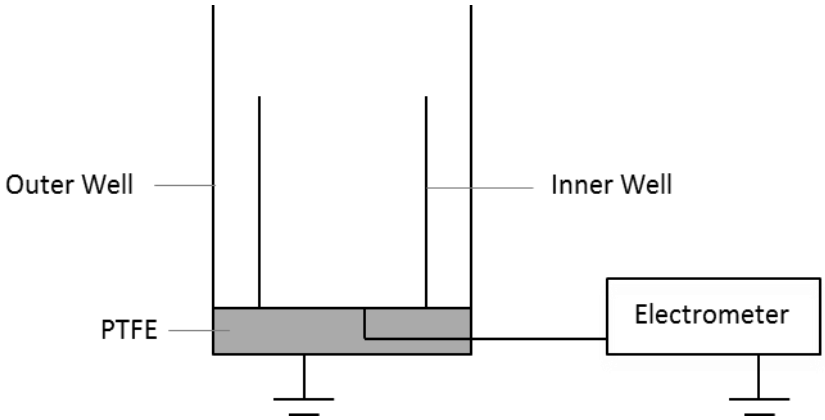

Figure 1.8 Diagram of Faraday pail and electrometer

The Faraday pail has been used extensively for performing measurements of the net charge of pharmaceutical grade powders. Murtomaa *et al.* measured the effect of the triboelectric charging of various lactose grades by sliding powder samples through a polypropylene tube and found that the extent of triboelectrification increased with increasing amorphous content (Murtomaa *et al.* 2002). Rowley used a Faraday pail to determine the extent of triboelectrification of salbutamol sulphate DPI formulations during cyclone charging and found an increase in the air flow velocity correlated with an increase charge build up (Rowley 2001). Supuk *et al*. constructed an oscillating shaker to tribocharge powder samples in a repeatable way and measured the net charge build-up of a variety of pharmaceutical excipients and APIs by pouring samples directly from the shaker and into the Faraday pail (Supuk *et al.* 2009).

Measurements recorded by the Faraday pail return values in multiples of the elementary unit of charge, Coulombs, and measurements are normalised by dividing the charge of the sample by its mass in order to provide a measurement of charge density. They are limited by the fact that they are unable to record the bipolar charge distributions of powder samples and are only capable of recording the total net charge present.

1.4.1.2 Multiple Faraday pail system

A system developed by Sharmene Ali *et al.* comprises of nine Faraday pails laid out in a cross formation as shown in Figure 1.9. The system was used to characterise the electrostatic charge of three different polymer powders used for electrostatic powder coating (Sharmene Ali *et al.* 1998).

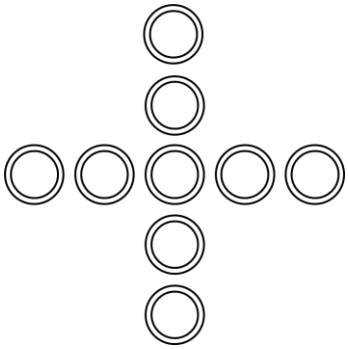

Figure 1.9 Nine Faraday pails arranged in a cross formation (adapted from Sharmene *et al.*, 1998)

The authors imparted electrostatic charge to the polymer powders by means of a fluid bed drier with PVC walls and then dropped the powder into the Faraday pails using a powder scoop from a predetermined height. The results demonstrated that each of the powders exhibited a bipolar charge distribution with different polarity charges being recorded as a function of the radial distance from the central pail. In addition the authors developed a mathematical model to describe the trajectories of the bipolarly charged particles taking into account the range of electrical, gravitational and drag forces on each particle (Sharmene Ali *et al.* 1998). Although this application allows bipolar charge of particles to be measured using Faraday pails, the charge measurements generated by each pail cannot be proven to be real bipolar charge as there is no way to discern whether complete charge separation of the particles had occurred during their time of flights. The system is also unsuitable for correlating bipolar charge with pharmaceutical aerosol particle performance.

1.4.1.3 Atomic Force Microscopy (AFM)

Atomic force microscopy (AFM) has become a commonly used technique to measure adhesive and cohesive forces during particle interactions of DPIs (Begat *et al.* 2004). AFM studies have also been used to characterise the electrostatic charge present on model spheres (Gady *et al.* 1996) and electrophotographic materials (Zhou *et al.* 2003).

Bunker *et al*. mounted single lactose particles onto AFM cantilever tips at a relative humidity of 0.1%. The long range electrostatic forces of the charged lactose particles were subsequently characterised by generating force-distance curves. Single contact electrification and tribocharging were simulated by varying the lactose-glass contact time. Results demonstrated that increasing lactose-glass contact time increased the electrostatic charge present. Also by increasing the humidity from 0.1% to 5% resulted in the dissipation of the charge generated on the lactose particle.

1.4.2 Dynamic measurements

1.4.2.1 Electrical Single Particle Aerodynamic Relaxation Time Analyser (ESPART)

The electrical single particle aerodynamic relaxation time (ESPART) particle analyser uses laser-Doppler velocimetry to simultaneously determine aerodynamic diameter and electrostatic charge of single particles with diameters of less than 70µm (Mazumder *et al.* 1983). Particles are introduced to the system and fall vertically in between two laser beams where they are either simultaneously subjected a DC electric field and an oscillating acoustic field or to an AC electric field on its own. In the DC application, the acoustic field causes the particles to oscillate and their motions are tracked by the lasers. Due to the particle's mass, a phase lag will be discerned and this is proportional to the particle's aerodynamic diameter. The DC electric field will bend the particle's trajectory and the amount of bend will be dependent on the polarity of the charge carried and the charge to mass ratio. Thus by performing both measurements simultaneously the quantity and polarity of the charge may be calculated. In AC mode, the polarity of the electric field switches from positive to negative at a frequency of 50 Hz and this causes the particle to oscillate backwards and forwards in direction creating a phase lag detected by the lasers. The magnitude of the phase lag allows the particle diameter (proportional to the mass) to be calculated and the amplitude of the particle oscillations (equivalent to the distance moved by the particle) allowing the quantity of charge to be calculated. Software developed for use with the ESPART counts the particles detected by the laser and assigns each particle into a diameter range (Mazumder *et al.* 1983).

Although the ESPART can perform highly accurate measurements it is limited by the speed at which the lasers can track particles falling through the detectors. Also it is only capable of measuring a single particle at a time and thus cannot measure all of the

particles entrained in the air flow and is not suitable for determining the performance of inhalation formulations.

1.4.2.2 Aerosol electrometer apparatus

The aerosol electrometer apparatus as shown in Figure 1.10 is a dynamic charge measurement technique suitable for the measurement of the net charge of the fine particle fraction of pharmaceutical aerosols (Byron *et al.* 1997). An inhaler is attached to a metal throat which in turn is connected to an impaction stage identical to the Marple Miller Cascade Impactor 5µm cut off stage which removes course carrier particles if a DPI formulation is analysed. The entire fine particle fraction of the emitted dose is collected in an aerosol filter, housed in a Faraday pail which shields the filter from external electric fields and stray charges. As charged particles impact onto the filter the current generated is recorded by an electrometer as a function of time. Equation 1.23 describes the relationship between charge, Q, current, I and time, t.

$$Q = It \qquad \text{Equation 1.23}$$

Integration of Equation 1.23 with respect to time yields Equation 1.24.

$$Q = \int_{t_i}^{t_f} I \, dt \qquad \text{Equation 1.24}$$

Where t_i is the initial time that the current is recorded and t_f is the time at which the current returns to the baseline. Therefore by plotting the current vs time profiles generated and calculating the area under the curve, the total net charge of particles deposited onto the impaction stage may be determined.

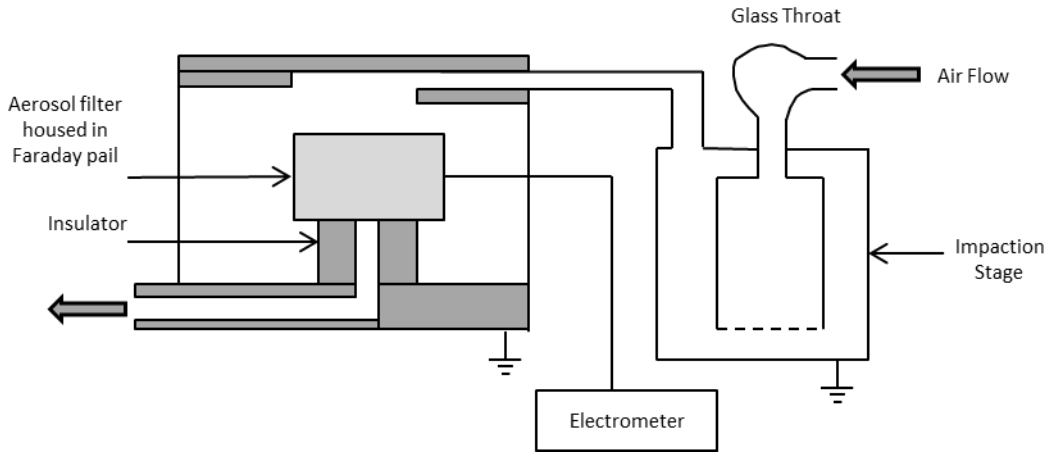

Figure 1.10 Aerosol electrometer apparatus (adapted from Byron *et al.,* 1997).

The apparatus was used to characterise the net charge of the fine particle fractions of DPI formulations emitted from the Turbuhaler® and Dryhaler® devices with a range of different active pharmaceutical ingredients. Results demonstrated that the net charge values were influenced by the device design and therefore aerosol deaggregation mechanism, shot number through the device and the particle physico-chemical properties.

1.4.2.3 Electrical Low Pressure Impactor (ELPI)

The ELPI, as shown in Figure 1.11, was originally designed to perform particle size distribution measurements of charged airborne particles (Keskinen *et al.* 1992). The instrument consists of a diode type corona charger coupled to a 13 stage Berner type multijet low pressure impactor which can be used to classify aerosol particles in the size range of 0.3-10µm. Initially the corona voltage was set to ±5 kV with the aim of producing an electric field which would induce a known, particle size dependent quantity of charge to particles entering the impactor stages. As particles impact onto the stages of the ELPI, the currents induced by the charges present on the particles are recorded using the electrometers. As for the aerosol electrometer apparatus, by integrating the current with respect to time, the net charge of the particles deposited may be calculated.

Originally the ELPI was used for industrial applications such as the measurement of particles emitted by combustion engines (Ahlvik *et al.* 1998) but it has also been used for measuring pMDI (Crampton *et al.* 2004) and DPI particles (Kwok and Chan 2008a). This was achieved by modifying the ELPI such that a USP throat was connected to the

inlet and the corona charger was switched off to ensure that charge readings recorded were an inherent property of the formulation aerosolisation process and not artificially created. Glover & Chan found no significant difference in the charge of pMDI particles with the corona switched off compared to when it was switched on (Glover and Chan 2004b). Although the ELPI is not a pharmacopeia impactor it is a useful tool for recording the net charge of aerosols deposited, however, it is unable to accurately record bipolar charge. The ELPI stages may be washed down and the diluent analysed via HPLC to determine the mass of the particles present on each stage allowing for the net charge to mass ratios of the particles to be determined.

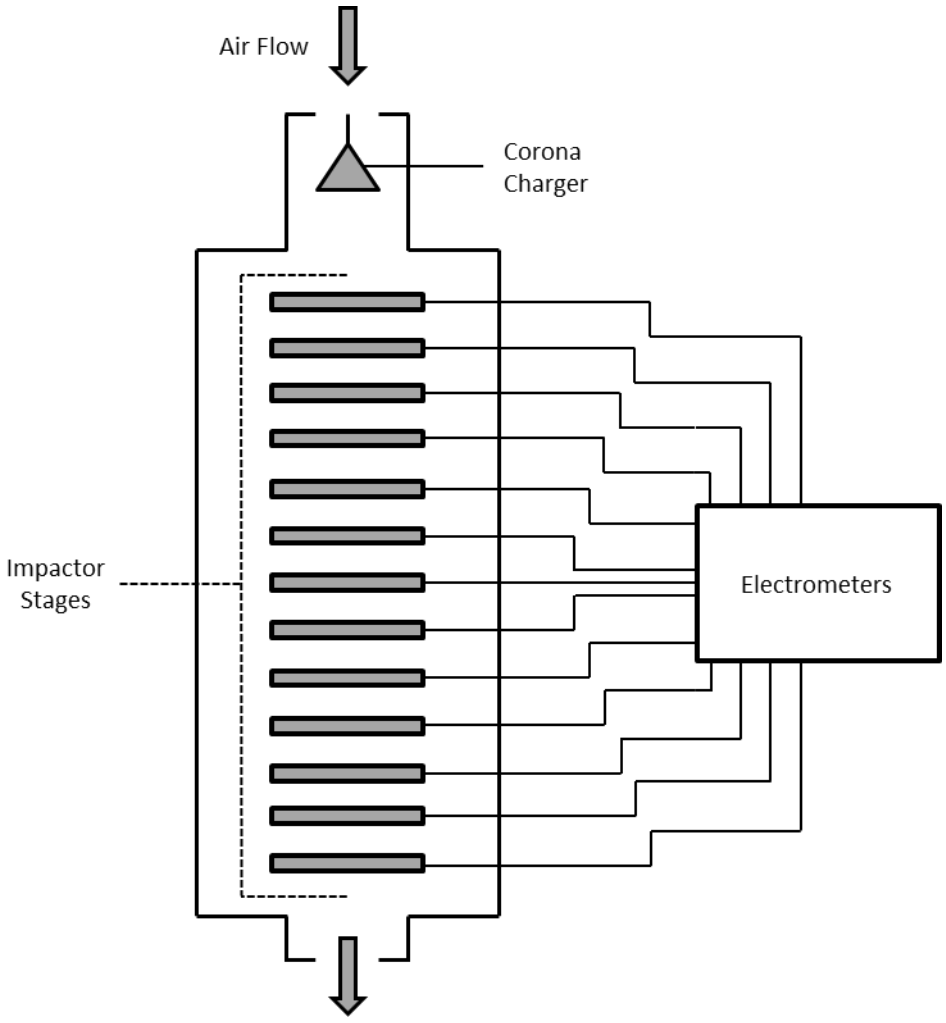

Figure 1.11 Schematic of the Electrical Low Pressure Impactor (adapted from Keskinen *et al.*, 1992)

1.4.2.4 Electrostatic twin stage impinger

A device developed by Zhu *et al*. incorporated electrostatic measurements with a modified pharmacopoeia twin stage impinger with the aim of classifying the net charge of the entire aerosol dose, rather than just particles in the range of 0.3-10µm as may be achieved with the ELPI (Zhu *et al.* 2008). The apparatus allows for measurements of the currents generated as charged aerosol particles are collected in the upper and lower impinger stages. As for the aerosol electrometer apparatus and ELPI, by integrating the current with respect to time, the net charge of the particles deposited may be calculated. A formulation containing Inhalac 230®, with an median particle diameter of 80.2µm and micronised salbutamol sulphate, with an median diameter of 4.3µm was aerosolised with a Rotahaler® and analysed using the apparatus. It was found that the Inhalac 230®, collected in the upper stage was found to carry a net positive charge and that salbutamol sulphate, collected in the lower stage was found to carry a net negative charge which was in line with measurements recorded using a conventional Faraday pail (Zhu *et al.* 2008). However, charge balance between the two formulation components was not observed. Although the electrostatic twin stage impinger is useful for determining the net charge of the coarse carrier lactose in DPI formulations, the mass of the lactose was not recorded. In addition a detailed aerodynamic particle size and charge classification of the fine particles is not able to be calculated and the equipment would not be able to provide accurate charge to mass ratio measurements of a DPI formulation containing a milled grade of lactose containing fine particles.

1.4.2.5 Electrostatic Next Generation Impactor (eNGI)

The Next Generation Impactor, is a pharmacopoeia tool used to classify the aerodynamic particle size distributions (APSDs) of pharmaceutical inhalation products and a detailed description of the operation may be found in Chapter 2, section 2.3. The electrical Next Generation Impactor (eNGI) as shown in Figure 1.12 was first developed by Hoe *at al.* at the University of Sydney in 2009. The authors took the idea of the ELPI and combined it with the NGI in order to perform net charge measurements of aerosol particles deposited onto each impactor stage (Hoe *et al.* 2009c).

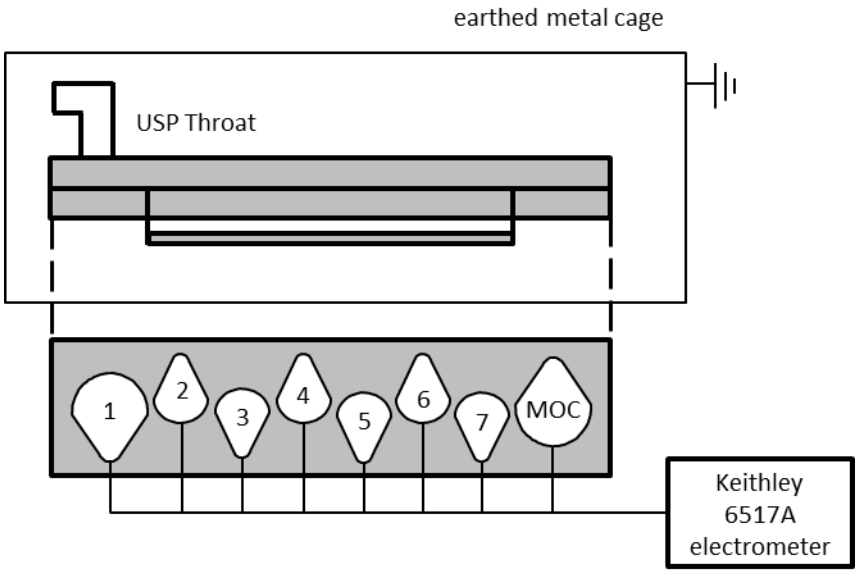

Figure 1.12 The electrical Next Generation Impactor (adapted from Hoe *et al.,* 2009)

The collection cups of the NGI are covered with an acrylic latex coating, which electrically isolates the cup from the impactor body which has the effect of turning each cup into a Faraday pail. Each cup is connected via a BNC connector and coaxial cable to a scanner card and electrometer which measures the current transferred from the aerosol particles deposited. As for the aerosol electrometer apparatus, by integrating the current with respect to time, the net charge of the particles deposited may be calculated. After the net charge measurements are recorded the NGI cups are washed and the API deposited is quantified using HPLC allowing for the net charge to mass ratios to be determined. The NGI as a whole is contained within an earthed metal cage in order to shield the cups from external electric fields and stray charges. The authors used the equipment to characterise Flixotide® pMDI and demonstrated equivalence with net charge measurements determined by the ELPI and that the eNGI generated identical measurements to the NGI in terms of aerodynamic particle size classification (Hoe *et al.* 2009c). A further study looked at the effect of flow rate on the net charge to mass ratios of the pMDIs Flixotide™, Seretide™ and Serevent™. They found that as the flow rate increased, the fine particle fraction increased, as did the net charge to mass ratio values (Hoe *et al.* 2009a). The authors also used the eNGI to perform net charge measurements of Pulmicort® and Bricanyl® DPIs and found comparable readings to those generated with the ELPI. In the same study the authors found that the net charge to mass ratio values generated increased as a function of flow rate with a concomitant increase in fine particle fraction (Hoe *et al.* 2009b).

Whilst the eNGI is undoubtedly a useful tool for characterising both the aerodynamic particle size distributions and net charge to mass ratios and makes use of an accepted pharmacopoeia impactor, like the ELPI it does not allow for the bipolar charge to mass ratios of aerosol particles to be calculated.

1.4.2.6 Bipolar Charge Measurement System (BCMS)

In order to address the unmet need for measuring the bipolar charge present on pharmaceutical aerosol particles Balachandran's group at the University of Brunel devised a bipolar charge measurement system (BCMS) as shown in Figure 1.13 (Kulon *et al.* 2001). The system consists of a metal tube, 39mm in diameter, 300mm in length split in half via a central block into two D shape passages. Three wires, 1mm in diameter, run along the length of each passage, with one set of wires having a positive voltage of 5kV applied and the other with a negative voltage of 5kV applied. Using a vacuum pump, suction is created to cause air to flow the tube at a known flow rate, with half of the air flow entering each section. In the positive section, the electric field generated by the high voltage on the wires repels the positively charged particles onto electrically isolated sections of the outer tube and the charge of the particles on each section is recorded using an electrometer. The same occurs for the negative section with the charge of the negative particles recorded. Whilst particles with the same polarity of charge are repelled onto the surface of the tube, oppositely charged particles are attracted to the wires. Thus this system allows for the simultaneous measurement of both the negative and positive charges present on the aerosol particles entering it. Knowing the flow rate of the air, the electrical mobilities of the particles, that is, the ability of a charged particle to move within an electric, field may also be calculated. However, the quantities of aerosol particles deposited on each section were not recorded and the system is not compatible with any pharmacopoeia impactors.

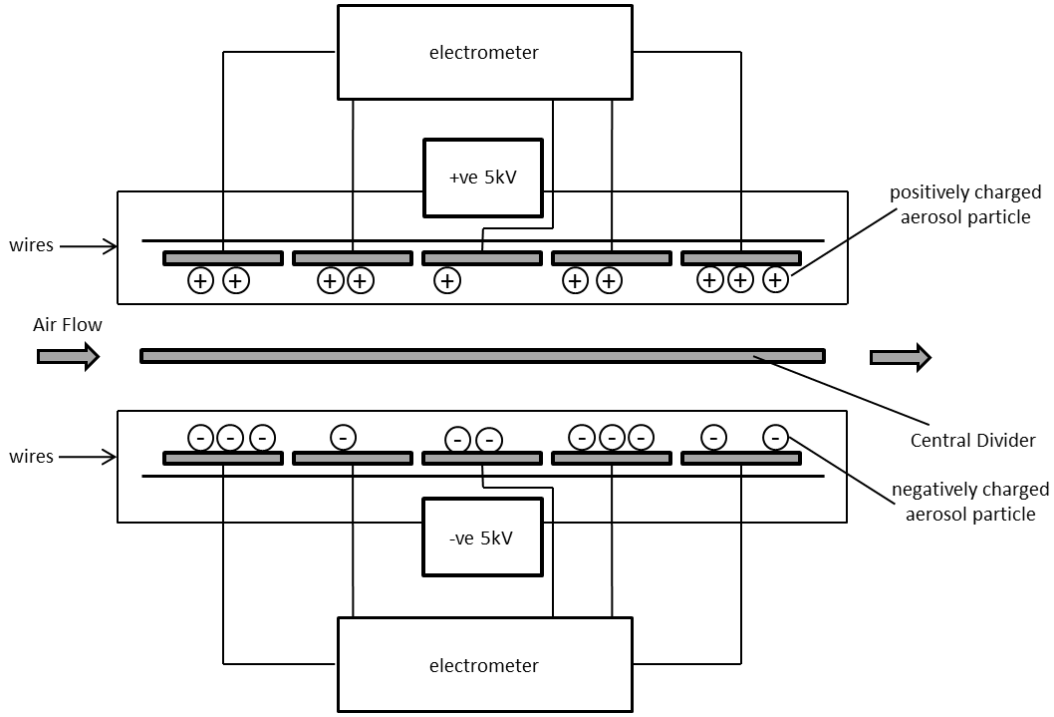

Figure 1.13 Schematic of the bipolar charge mobility analyser, charged particles deposited on HV wires not shown for clarity (adapted from Kulon *et al.,* 2001).

1.4.2.7 The Dekati Ltd. BOLAR™

The BOLAR™ is a bipolar charge measurement system which has recently been developed by Dekati Ltd. in collaboration with GlaxoSmithKline, Tampere University and the Finnish Meteorological institute (Yli-Ojanpera *et al.* 2014). Working under the same theoretical principals as the BCMS, the system is able to separate bipolarly charged aerosol particles into their respective positively and negatively charged components using electrostatic precipitation. The charge measurement system is incorporated with an aerosol impactor and the instrument is controlled by Bipolar Electrical Collection Units (BECUs). A schematic of the experimental set up operating at a flow rate of 60 $Lmin^{-1}$ is shown in Figure 1.14.

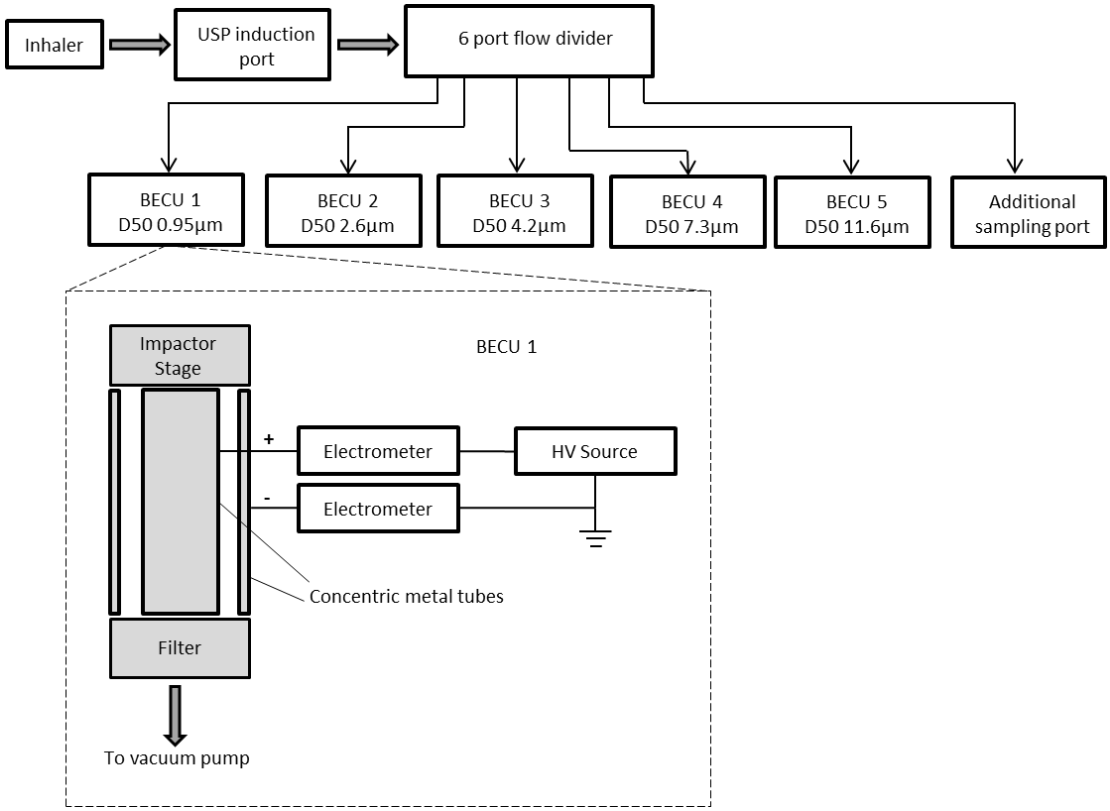

Figure 1.14 Schematic of the Dekati Ltd. Bolar™ (adapted from Yli-Ojanpera *et al.* 2014)

An inhaler is connected to the equipment via a USP induction port which in turn is connected to a six port flow divider. Five BECUs are connected to ports on the flow divider as well as an additional sampling port. Each BECU consists of an impactor stage and an electrostatic precipitator which is composed of two concentric metal tubes, the inner connected to a +1 kV high voltage source and the outer connected to a -1 kV high voltage source. This facilitates the precipitation of charged particles with sufficient electrical mobility to be deflected by the electric fields and onto the tube walls. Once the particles are precipitated their charge is recorded using the same methodology as for the ELPI and the eNGI. Each BECU has a specific particle cut off diameter e.g. for BECU 4, only particles of 4.2 µm and below are permitted to enter the electrostatic precipitator. The sequence of events involves selection of the aerosol particle diameter size range using the appropriate impactor, separation of the positive, negative and neutral particles, charge measurement of each class of particles, mass measurements of each class of particles and finally calculation of the charge to mass ratios. By subtracting the charge and mass values generated from one BECU by another the bipolar charge to mass ratios of a specific particle diameter range may be determined. For example by subtracting the values generated by BECU 4 from the

values generated by BECU the bipolar charge to mass ratios of a particle diameter range of 7.3 µm to 11.6 µm may be calculated (Yli-Ojanpera *et al.* 2014).

Although the BOLAR™ is undoubtedly a big step forward in accurately quantifying the bipolar charge to mass ratios of aerosol particles it is not capable to incorporate the equipment with an approved pharmacopoeia impactor.

1.5 Aims of the study, hypotheses and thesis structure

Despite a large amount of research that has been conducted in recent years in the area of aerosol electrostatics, the precise mechanisms governing the electrostatic properties of particles for inhalation remain under contention, without a clear answer as to which theories explaining the mechanisms of charge transfer are truly accurate and which play a dominant role in determining the extent of triboelectrification during pharmaceutical processing and respiratory drug delivery. The generation of electrostatic charge during manufacturing and processing on the microstructure of a DPI blend and its relationship with fine particle performance is still relatively poorly understood. The i*n vitro* and *in vivo* performance of a DPI is directly related to the physical properties of the blend and the presence of electrostatic charge is suspected as a cause of increased powder cohesion, reduction in deaggregation and therefore reduction in performance.

Moreover, although methods for measuring charge build up on pharmaceutical powders are available, they are prone to operator error and are notoriously difficult to repeat. Static measurement systems such as the Faraday pail are commonly applied, however, they are only capable of measuring the net charge of samples and do not take into account the bipolar charge distribution which may be present in a powder sample. Dynamic systems for measuring the net charge of aerosol particles upon aerosolisation have been developed, however they suffer from the same insensitivity. Bipolar charge measurement systems have been developed, however these are not compatible with standard pharmacopeia testing equipment.

This project aims to achieve the following goals:

- Validate novel methodologies for determining electrostatic charge build up on DPI formulations during processing.
- Determine the effect of API concentration on the susceptibility of DPI blends to become electrostatically charged.

- Determine the influence of environmental relative humidity on the static charge build-up of DPI formulations and subsequent charge decay rate.
- Develop a novel aerosol impactor for the measurement of bipolar charge to mass ratios of aerosol particles compatible with an approved pharmacopoeia aerosol impaction method.
- Perform dynamic charge measurements of capsules and devices during DPI formulation aerosolisation and simultaneously measure the aerosol particle charge.

This project aims to investigate the following hypotheses:

- DPI formulations will become negatively charged when the particles come into contact with stainless steel surfaces during processes such as pouring, sieving and blending.
- The contribution to the electrostatic properties of a DPI formulation will be far greater from the API, which is normally electrically resistive, than the lactose carrier, which is electrically conductive.
- Relative humidity will reduce the ability of a DPI formulation to become electrostatically charged and will increase the subsequent rate of charge decay.
- Aerosolised pMDI and DPI formulations will possess a bipolar charge distribution, the magnitude of which will be dependent on the electrostatic and physico-chemical properties of the formulation and the inhaler, the aerosolisation mechanism and the environmental conditions.

In order to achieve these goals, the structure of this thesis is set out as follows:

Chapter 1 – Introduction
Chapter 2 – General methods
Chapter 3 – Net charge measurements of inhalation grade lactose
Chapter 4 – The effect of relative humidity on the static charge decay rate of DPI formulations
Chapter 5 – Measuring the bipolar charge distributions of commercial pMDI suspensions using the bipolar Next Generation Impactor
Chapter 6 – The effect of relative humidity on the electrostatic properties of a budesonide DPI formulation
Chapter 7 – General conclusions and further work

Chapter 2 General Methods

2.1 General physico-chemical characterisation

2.1.1 Scanning electron microscopy

2.1.1.1 Theory

Scanning electron microscopy (SEM) is commonly used to provide qualitative visual representations of the morphology and particle size of APIs and lactose carrier particles for inhalation. In addition, information can be gained on the structure of a DPI blend including the extent of agglomeration of the API and the extent of lactose carrier particle surface coverage. Typically, a conductive sample is irradiated with a highly focussed electron beam which results in both penetration backscattering and secondary electron scattering from the surface of the sample. Backscattering occurs as the result of electrons from the beam interacting with the surface of the sample and secondary electron scattering occurs from low energy electrons from the sample itself (Wells 1974). Typically the images created achieve very high resolution in the order of nanometers and high quality 3D images are produced of sample surfaces.

A simplified schematic of a scanning electron microscope is shown in Figure 2.1. An electron beam in the order of 40 keV is passed through condenser lenses in order to narrow the beam produce a beam of suitable diameter, known as the spot size. The deflectors, which consist of two pairs of electromagnetic coils, are used to move and split the beam and allow for the magnification of the sample surface to be controlled. The beam is passed through the objective lens which allows for stigmatism reduction and the image to be focussed. The back scattering electron detectors and secondary electron detector collect electrons emitted from the sample surface of the sample. The collected electrons are then accelerated, the signal amplified and then sent to the display which generates a visual representation of the sample surface. The system is kept under constant high vacuum which prevents air molecules from interfering with the electron beam and the sample surface which would lead to distortions in the image generated.

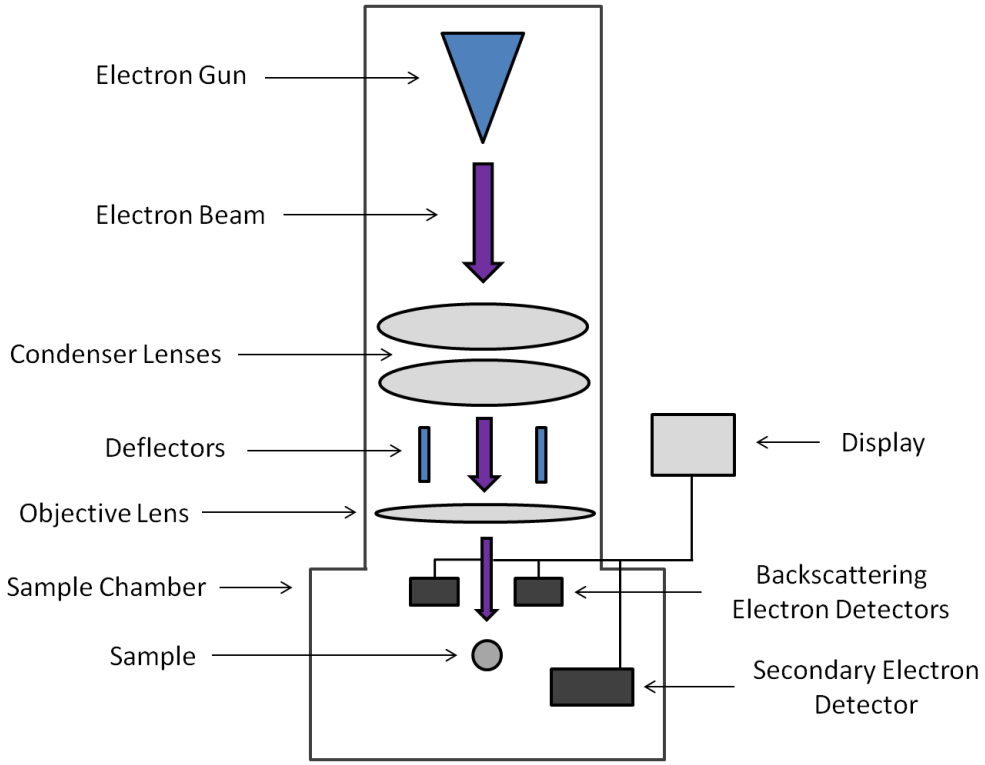

Figure 2.1 Simplified schematic of a scanning electron microscope

2.1.1.2 Measurement methodology

Scanning electron microscopy (SEM) images of the lactose samples was performed on a JEOL JSM-6480LV (JEOL, Tokyo, Japan). SEM imaging of non-conductive materials is not possible due to an absence of low energy electrons in the sample surface and so samples were mounted on sticky carbon tabs and coated with a thin layer of gold using an Edwards sputter coater S150B (Edwards, Israel) for 5 minutes prior to analysis. An acceleration voltage of 10 kilovolts was used for the imaging.

2.1.2 Particle size

2.1.2.1 Theory

The particle size of aerosol particles for inhalation is a significant factor which affects the performance of the formulation. In order to reach the deep lung and be therapeutically effective at typical values of human inspiratory flow rate, API particles must normally have a diameter of less than 5 μm to pass through the mouth, throat and upper airways of the patient. In addition, the diameter of the coarse carrier particles of

the formulation will also affect its performance (Shur *et al.* 2008). In addition, particle size measurements are routinely performed during DPI formulation development and the data generated is included in regulatory submissions as part of the specification of the drug product.

The most commonly used technique employed to measure the particle size distributions of particles for inhalation is laser diffraction. When a beam of monochromatic light is focussed through a dispersion of particles which have a dielectric constant different from unity, the light will be either absorbed or diffracted (Xu 2002). Diffraction results in a scattering of the light and typically interactions with smaller particles result in larger scattering angles as well as lower intensities (Newton 1982). The scattering pattern generated is integrated and used to calculate a weighted distribution of the volume equivalent diameters of the particles by applying a suitable mathematical model (Shekunov *et al.* 2007).

Two different mathematical models are commonly employed for interpolating data from laser diffraction measurements which are Mie and Fraunhofer theories (Schwarz *et al.* 2001). Mie theory is generally considered to be more accurate and makes the assumption that the particles are smooth and spherical and that scattering is caused by the difference between the refractive index of the particles and their surrounding medium (Mie 1908). However, Mie theory is difficult to employ as it requires a large amount of computing power and the particles are not spherical, have rough surfaces and are of unknown refractive index. Fraunhofer theory is more suitable to employ as it assumes that the particles are much larger than the wavelength of the light and that no other interactions other than scattering take place between the light and the particle (Xu 1997).

2.1.2.2 Measurement Methodology

Lactose samples were dispersed dry at a pressure of 2 bars using a RodosT4 disperser and a Vibri feeder (Sympatec GmbH, Germany). API samples were measured in a wet cell with a small quantity of the particles being redispersed in a solution of 0.1% w/v of lecithin (BDH Ltd., Poole, UK) in cyclohexane by sonicating for 5 minutes. The resultant suspension was then diluted down to 50 ml in the cuvette to produce an optical concentration of not more than 15%. Particle size measurements

were performed using a HELOS laser diffraction sensor with an R4 lens and analysis was performed using WINDOX 4.0 software (Sympatec GmbH, Germany). Five repeat measurements were taken for each sample and the values recorded for the d_{10}, d_{50} and d_{90} were averaged as well as the percentage of particles less than 5 µm.

2.1.3 API and lactose assay by HPLC

2.1.3.1 Theory

High performance liquid chromatography (HPLC) is commonly used in the pharmaceutical industry to assess the assay, content uniformity and *in vitro* performance of DPIs (Erni 1990). The technique involves dissolving the sample to be measured in a solvent of a known volume. A small quantity of this solution is then placed into a vial and a known volume is then injected into a flow of a solvent mobile phase which is pumped through an HPLC system. The mobile phase passes through a stationary phase which is normally attached to the surface of small silica particles, with preselected diameters, which are tightly packed within a stainless steel column (Unger *et al.* 2008). As the mobile phase passes through the column, the analyte interacts with the functional groups of the stationary phase and thus travels more slowly through the column than the mobile phase. Various analytes may be separated due to differences in their distribution coefficients (D). The distribution coefficient is defined as the ratio of the affinity of the analyte to the stationary phase to the affinity of the analyte to the mobile phase. If multiple analytes are to be analysed, for example an API together with various degradation products, or two different APIs as part of a combination drug product, differences in the polarity, functional groups or chiral centres of the molecules will result in differing distribution coefficients and therefore retention times (Rt) as long as suitable chromatographic conditions are employed (Perera and Lough 2011). Once the analytes exit the column, a detector such as a UV photospectrometer, evaporative light scattering detector or mass spectrometer may be used to determine the concentration of the analyte which entered the column. By comparing with a calibration curve created from samples of known concentrations, the amount of material originally dissolved into the solution may be determined. Factors which influence the retention time include the chemical structure of the analytes, the flow rate, pressure and composition of the mobile phase, the type of column stationary phase, the column length and temperature and the overall volume of the system (Stankovich *et al.* 2014).

2.1.3.2 Measurement methodology

2.1.3.2.1 Active Pharmaceutical Ingredients

The HPLC system consisted of a pump (Jasco PU-980, Jasco Corp., Japan) coupled to an autosampler (Jasco AS-950) and UV detector (Jasco UV-975) set at the required wavelength for the determination of the API. Separation was performed using a suitable column (either ODS or BDS stationary phase) maintained at the required temperature using a column oven (Jasco CO-965). The mobile phase selected was filtered through a 0.45µm nylon membrane (Whatman International Ltd., Maidstone, UK) and degassed. The retention time for the API was recorded, quantification was carried out by an external standard method and linearity was checked between 0.5 and 50 µg/mL. Precise chromatographic conditions employed for each API are summarised in the methods sections in subsequent chapters.

2.1.3.2.2 Lactose

The same HPLC system was used to characterise lactose as for the APIs. An amine-bonded silica gel column (APS-2 Hypersil, 100x3mm, Thermo Scientific, Waltham, MA, USA) was used for chromatographic separation of lactose as the amine groups on the stationary phase interact with the reducing groups of carbohydrates allowing for efficient separation (Wei and Ding 2000). As lactose does not possess a UV active chromophore an evaporative light scattering detector (ELS 1000, Polymer Labs, Church Stretton, Shropshire, UK) was employed using previously developed methodology (Beilmann *et al.* 2006). The detector works by nebulising the eluent using a flow of pressurised nitrogen gas and then heating the resultant aerosol to drive off the solvent as shown in Figure 2.2. The resultant solid lactose particles then pass through a light detector which measures their optical concentration, producing a peak with the intensity corresponding to the concentration of lactose contained in the mobile phase. The mobile phase consisted of 75 : 25 acetonitrile to deionised water and the injection volume was 100 µl. The column was maintained at 30ºC and the retention time for lactose was 1.37 minutes.

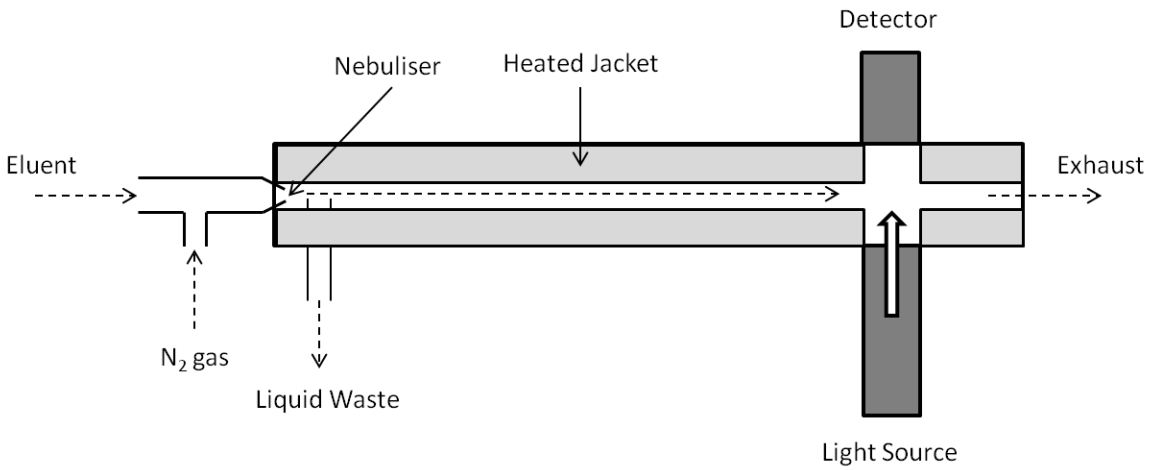

Figure 2.2 Schematic of an evaporative light scattering detector

The nebuliser temperature of the ELS detector was set to 60ºC and the evaporation temperature to 110ºC. The flow rate was 1.0 mL/min and the gas flow rate was set to 1.5. The retention time for lactose was recorded, quantification was carried out by an external standard method and linearity was checked between 0.5 and 50 µg/mL. The plot of peak area against concentration was found to follow a quadratic function as has been observed previously with similar evaporative light scattering experiments (Hewitt *et al.* 2008).

2.2 Manufacture of DPI formulations

2.2.1 Theory

Doses of therapeutically active compounds to the lung are often relatively small, typically in the range 25-500 µg, which equates to a very low volume of solid powder. In order to reach the deep lung, API particles are usually micronised to produce particles which possess an aerodynamic diameter of less than five microns. This results in a powder with a large mass to surface area ratio with a high level of inter-particle cohesive forces, which cause poor deagglomeration and fluidisation characteristics. In the case of pMDIs the API particles are suspended in a liquid propellant which is aerosolised through a valve. However, in order to inhale the therapeutic dose, the patient must coordinate their breathing when the canister is depressed which can lead to compliance problems as a result of poor technique.

To overcome the limitations of pMDIs, DPI formulations were developed in which APIs are mixed with inert carrier particles such as mannitol or, more commonly, lactose

monohydrate in order to provide formulations with suitable flow and handling properties, which allows for easier metering of doses into capsules or blisters (Prime *et al.* 1997). Homogeneous mixtures of API and carrier particles must be produced in order to ensure uniformity of the delivered dose which is typically achieved by blending using either low or high shear systems. The carrier particles are usually larger in diameter, in the order of hundreds of microns, than the API, which is normally micronised to produce particles in a sub five micron range. In order to produce robust, homogeneous DPI formulations, the API and lactose raw materials are sieved prior to blending in order to break up any large agglomerates. After sieving, the API and lactose are blended using optimised conditions to produce a homogenous mixture prior to encapsulation into gelatin or HPMC capsules or packaging into blisters. API and lactose particles are highly susceptible to triboelectrification during processing and handling, making manufacturing of drug only DPI formulations technically challenging due to the resultant poor flow characteristics (Pingali *et al.* 2009).

2.2.2 Sieving and blending

Unless otherwise stated, DPI formulations containing lactose and an API were prepared using a small scale laboratory process. 10% of the lactose required was passed through an 850µm mesh sieve, followed by the total amount of the API, followed by a further 10% of the total lactose required in order to make a lactose-API sandwich. This sandwich was then blended in a stainless steel vessel at 22 RPM for 10 minutes using a type T2F Turbula blender (WAB, Nidderau-Heldenbergen, Germany) to create a preblend. Half of the remaining lactose was then passed through the sieve, followed by the preblend, followed by the remaining lactose, in order to make a second sandwich. This sandwich was then blended for a further 20 minutes at 22 RPM. Stainless steel vessels were selected so that approximately one half to two thirds of the blending vessel volume was empty to facilitate thorough mixing. Once the final blending step was completed, the blend was transferred to a polythene bag and was stored in a relative humidity chamber with a saturated salt solution of potassium carbonate at 43% RH (Fisher Bioreagents, NJ, USA) in an air conditioned room maintained at 20 ± 2 ^{0}C, unless otherwise stated.

2.2.3 Assay and content uniformity

Assay of the API and content uniformity measurements were performed using a suitable HPLC method for the API according to USP monograph <905> Uniformity of Dosage Units (USP 2011). 10 x 25mg samples were removed from the blend from random locations and dissolved with sonication in 100 mL of the appropriate mobile phase. The batch was passed if the mean assay was within 95-110% and the acceptance value, L1, was less than 15.0.

2.2.4 Capsule Filling

Size three HPMC capsules (Qualicaps, Madrid, Spain) were selected for the studies. Capsules were filled by hand using a five place analytical balance (Sartorius BP911D, Surrey, UK) to 25.0 ± 0.05 mg. Once filled, capsules were stored in a relative humidity chamber with a saturated salt solution of potassium carbonate at 43% RH (Fisher Bioreagents, NJ, USA) in an air conditioned room maintained at 20 ± 2 ^{0}C unless otherwise stated.

2.3 Conventional in vitro performance analysis with the Next Generation Impactor (NGI)

2.3.1 Background

In vitro experiments are crucial for determination of the performance of an inhaled drug product formulation. The most common techniques, as listed in the European and United States pharmacopoeias (PhEur 2008, USP 2011), are performed using impingers or cascade impactors which are collectively known as aerodynamic particle size classifiers. These instruments allow for determination of an API specific, aerodynamic particle size distribution classification. Early impactors were adapted from instruments developed for measurements of environmental aerosol particles (Mitchell and Pilcher 1959) and deposition of particles onto agar plates for cell cultures (Andersen 1958) and were not optimised for inhaler formulations. In order to standardise testing, a consortium of pharmaceutical companies compiled a list of key attributes required of an impactor which included: complete recovery of the dose

delivered, ease of use for the operator, the ability to operate over a range of flow rates and being automatable. This resulted in the development of the Next Generation Impactor (NGI), the design and calibration of which is summarised by Marple *et al*. (Marple *et al*. 2003a, Marple *et al*. 2003b).

2.3.2 Theory

The NGI operates by aerosolising the dose from an inhaler and drawing the resultant aerosol particles through a cascade impactor with a flow of laminar air. The impactor consists of seven impaction stages and a micro orifice collector (MOC). Each impaction stage consists of a number of jets which are directed towards a collection cup where aerosols of a specific aerodynamic diameter range are impacted. Stage 1 has the largest jet diameter followed by stage 2 and so on, until the air stream reaches the MOC which has the smallest jet diameter. A diagram of an impaction stage is shown in figure 2.3.

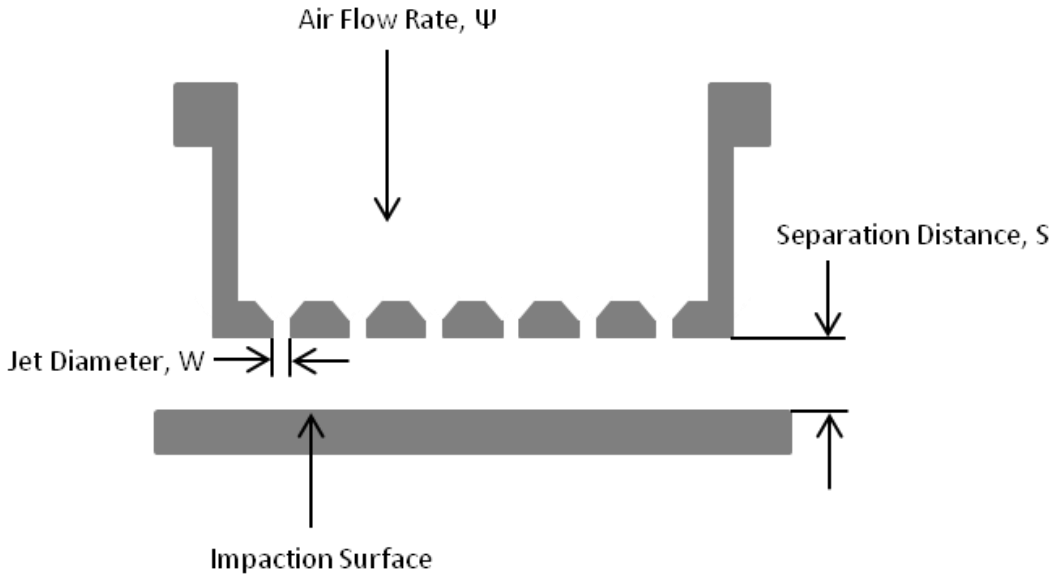

Figure 2.3 Diagram of an impaction stage, adapted from Marple *et al*. 2003b

As air passes through the jets, entrained aerosol particles either collect on the impaction surface or are carried through to the next stage. The jets are designed so that at the flow rate range of the NGI, 15-100 $Lmin^{-1}$, the air will travel in a laminar fashion, with a Reynold's number, Re, in the range $500 < Re < 3000$. The Reynold's number for a given jet with diameter, *W*, is given by Equation 2.1 (Marple *et al.* 2003b).

$$Re = \rho W V_0 / \eta$$ Equation 2.1

Where ρ is the density, V_0 is the velocity and μ is the viscosity of the air. The aerodynamic cut off diameter, d_{50}, for a given stage is calculated by using Stokes Law as described in Equation 2.2.

$$d_{50} = \sqrt{\frac{9\pi\eta n W^3}{4_{\rho_{ae}}\Psi}}\sqrt{St_{50}}$$ Equation 2.2

Where η is the viscosity of air at 25°C, n is the number of jets of the given impaction stage, ρ_{ae} is the unit density of the particle, Ψ is the total volumetric flow rate through the impactor stage and St_{50} is the Stokes number at 50% collection efficiency (Marple *et al.* 2003b). The Stokes number is determined from the ratio of the separation distance, S to the jet diameter, W. For round nozzles and in most impactors, $\sqrt{St_{50}}$ = 0.495. As the impaction stages decrease from Stage 1 to the MOC, the number of jets increases and the jet diameters and separation distances both decrease. This leads to the overall aerodynamic particle cut off diameter decreasing with each successive stage.

The cut off diameter of particles, $d_{50,}$ for each NGI stage are given by Marple *et al*. for flow rates of 30 and 60 and 100 L/min (Marple *et al.* 2003a). Using Equation 2.3 as given in the United States Pharmacopoeia (USP) unknown particle cut off diameters, D_{50}, at a flow rate, Ψ, may be determined from the known particle cut off diameters $D_{50,Qn}$, from a known flow rate, Ψn (USP 2011).

$$D_{50,Q} = D_{50,Qn}\,(\Psi n/\Psi)^{1/2}$$ Equation 2.3

Substituting particle cut off diameter values from Marple *et al.* for a flow rate 60 L/min into Equation 2.3 produces values for particle cut off diameters at 90 L/min. The particle cut off diameters for the NGI for flow rates of 30, 60 and 90 L/min for each NGI stage are given in Table 2.1.

NGI Stage	Particle Cut off Diameter (D_{50}) µm		
	30 L/min	60 L/min	90 L/min
1	11.7	8.06	6.48
2	6.40	4.46	3.61
3	3.99	2.82	2.30
4	2.30	1.66	1.37
5	1.36	0.94	0.76
6	0.83	0.55	0.43
7	0.54	0.34	0.26
MOC	0.36	0.14	0.13

Table 2.1 Calculated values for the particle cut off diameter for the NGI at 30, 60 and 90 L/min

2.3.3 Experimental Setup

The NGI complete with preseparator and throat are displayed in Figure 2.4.

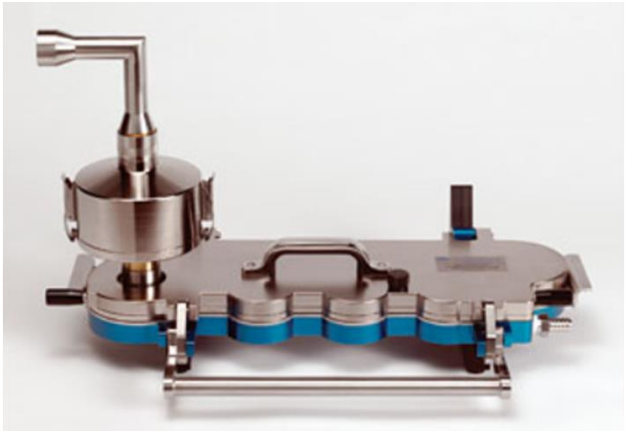

Figure 2.4 The Next Generation Impactor complete with USP induction port and preseparator (reproduced with permission from Copley Scientific)

The device is connected using a rubber mouthpiece to the USP throat which is used to mimic the throat and upper airway. Although crude in its design, the throat collects a large quantity of coarse carrier lactose particles due to it possessing a sharp 90° bend. However, research is currently underway in order to optimise the geometry of the USP throat to provide a more representative model of human physiology (Zhang *et al*. 2006, Mitchell *et al*. 2012). The throat is then connected to a preseparator which is also used to remove additional coarse carrier lactose particles. Owing to the large particle size of the carrier lactose, deposition within the preseparator is governed primarily by gravitational forces rather than impaction (Marple *et al.* 2003b). The preseparator is connected to the impactor body where the airflow passes through Stages 1-7 and the MOC. Each stage has a collection cup below it where aerosol particles of a given particle diameter range for the flow rate employed are impacted.

2.3.4 Measurement Methodology

The collection cups of the NGI were coated with a solution of 1% w/w silicone oil in hexane in order to prevent particle bounce. The solution was allowed to dry so that the hexane evaporated leaving a thin film of silicone oil in order to eliminate particle bounce.

The preseparator was filled with 15mL of mobile phase, The NGI was then assembled and the lid closed. The flow rate of air through the NGI was produced using a vacuum pump connected to a TPK critical flow controller (Copley Scientific, Nottingham, UK). The flow rate was measured using a DFM2000 flow meter (Copley Scientific, Nottingham, UK) and adjusted using the TPK to a flow rate so that a 4 kPa pressure drop across the device was achieved for DPIs. As described by Mohammed *et al*, the ratio of the pressure downstream, P2, to upstream, P3, of the TPK valve was maintained at ≤ 0.5 to ensure critical flow through the DPI and laminar flow through the NGI (Mohammed *et al.* 2012).

A capsule of the DPI formulation was then placed within the Aerolizer device, the capsule was pierced and then the closed device was placed within the rubber mouthpiece connected to the USP throat so that an air tight seal was formed. The timing of the TPK was adjusted so that a total of 4 litres of air was drawn through the system, for example at a flow rate of 90 L/min air was drawn through the system for 2.7

seconds. 4 litres was selected as a typical volume representative of patient lung capacity.

Five shots were actuated through the system and once this was completed the individual components including the capsules, device, mouthpiece and throat, were washed using mobile phase into separate volumetric flasks to recover the API. 85mL of mobile phase was added to the preseparator, the cups for stages 1-5 of the NGI were washed with 20mL of mobile phase, cups for stages 6-7 were filled with 5mL of mobile phase and the cup for the MOC was filled with 10mL of mobile phase to recover the API. Samples from the washed components along with samples from the NGI collection cups were analysed using HPLC to calculate the API mass deposition profile.

2.3.5 *In vitro* performance indicators

The total amount of drug recovered for each NGI experiment was calculated from the HPLC results as a percentage of the theoretical delivered dose from the formulation. The mean mass aerodynamic diameter (MMAD), geometric standard deviation (GSD) and fine particle mass (FPM) of the API particles were calculated using the cumulative impactor stage by stage API deposition data according to standard regulatory guidance (EMEA 2006). The FPM indicates the mass of aerosol particles less than 5µm which are believed to be small enough to be therapeutically active. The MMAD is calculated from the plot of the cumulative percentage of mass less than the stated cut-off diameter versus the cut-off diameter by determination of the diameter at 50% and indicates the mean aerodynamic diameter of these respirable aerosol particles (EMEA 2006). The fine particle fraction of the emitted dose (FPF_{ED}) may also be quoted which is the FPM divided the total dose theoretically available.

2.4 Electrostatic measurements of net charge

2.4.1 Faraday Pail for net charge measurements

2.4.1.1 Theory

The fundamental theory describing the Faraday Pail is described in Chapter 1, Section 1.4.1.

2.4.1.2 Measurement Methodology

The electrometer used in conjunction with the Faraday pail was a Keithley Instruments 6517B electrometer (Keithley Instruments, Cleveland, USA), which was connected to the Faraday pail via a coaxial cable with Bayonet Neill Concelman (BNC) connector. The electrometer was set to measure in charge mode (Q) with the appropriate range in Coulombs (C). Prior to introducing a sample to the pail, the electrometer capacitor was discharged using the ZCHK button and then the electrometer reading was zeroed using the REL button. During all measurements the operator wore a conductive wristband connected to earth to prevent additional charging of the measured sample. Once the charge of the sample was measured, the sample was transferred to a weighing boat and the mass measured using a five place analytical balance (Sartorius BP211D, Surrey, UK). Values were reported in terms of charge density (nC/g) by dividing the charge measured on the sample by its mass. Values of the net charge density were determined in triplicate unless otherwise stated. The temperature and humidity of the environment during each net charge measurement was also recorded for reference using a hygrometer (Rotronic Hygropalm, West Sussex, UK). For powder samples the inner cup of the Faraday pail was washed in between each set of sample measurements with water and methanol twice, dried in a Gallenkamp OV-440 oven at 60ºC (Gallenkamp, Loughborough, UK) and allowed to cool to room temperature.

2.4.2 Flow Through Faraday Pail for dynamic charge measurements

2.4.2.1 Theory

A flow through Faraday Pail (FTF) was designed in order to record dynamic net charge measurements of a DPI inhaler upon aerosolisation of a formulation. The FTF was

cylindrical in shape and may be thought of as a bottomless conventional Faraday Pail as shown in Figure 2.5.

Figure 2.5 Flow through Faraday pail

The design was based on equipment developed by Chow *et al.* who used a similar system to measure the dynamic charge generated upon aerosolisation of Inhalac® 230 from a Rotahaler® device (GlaxoSmithkline, Ware, UK) at varying flow rate and humidity (Chow *et al.* 2008). This system was based on the air stream Faraday cages developed by Kulvanich and Stewart who measured net charge to mass ratios of a range of API-excipient aerosol particles (Kulvanich and Stewart 1987) and Peart *et al.* who measured the net charge generated during deagglomeration of lactose-salbutamol sulphate blends (Peart *et al*. 1996). The system works by measuring the charge build up on materials based on induction, as opposed to contact.

2.4.2.2 Measurement Methodology

The FTF was clamped horizontally and attached to a stand at the correct height to measure an inhaler based on the experimental set up required. Figure 2.6 shows the experimental setup utilising a dose uniformity sampling apparatus (DUSA, Copley Scientific, Nottingham, UK) but the FTF may also be used with an impactor or other similar test apparatus.

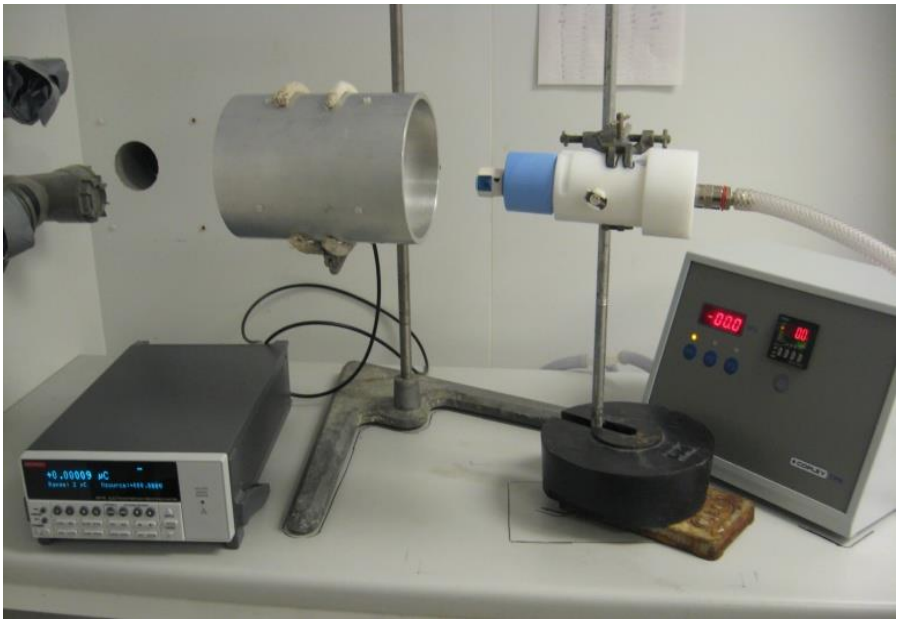

Figure 2.6 Experimental set up with electrometer, FTF, Aerolizer® device, DUSA and TPK

Prior to all experiments, capsules and devices used were allowed to equilibrate for a minimum of 24 hours in order to allow any charge present to dissipate. In order to perform a dynamic charge measurement, a capsule was pierced and placed within the device. The device was then placed inside the rubber mouthpiece at the same depth each time. The stand holding the DUSA (or other test equipment) was retained in the same position throughout the experiments. The stand holding the FTF was adjusted to the correct height, so that the FTF could be moved horizontally across ensuring that the device was positioned exactly the centre of the FTF at the same depth each time. The simple act of the operator opening and closing the device was expected to tribocharge the exterior surfaces of the device in an unrepeatable way and so once the FTF had been positioned over the device, the electrometer capacitor was discharged using the ZCHK button and then the electrometer reading was zeroed using the REL button. Once the display was zeroed, readings were taken of the charge value at intervals of 0.12 seconds and stored in the electrometer data buffer. Then a capsule was aerosolised within the inhaler, resulting in the dynamic charge of the inhaler, capsule and formulation during the aerosolisation process being recorded. A typical plot of the dynamic charge measurement plotted as a function of time for a placebo of 12.5mg Respitose™ ML001 in an HPMC capsule at 90 L/min is shown in Figure 2.7.

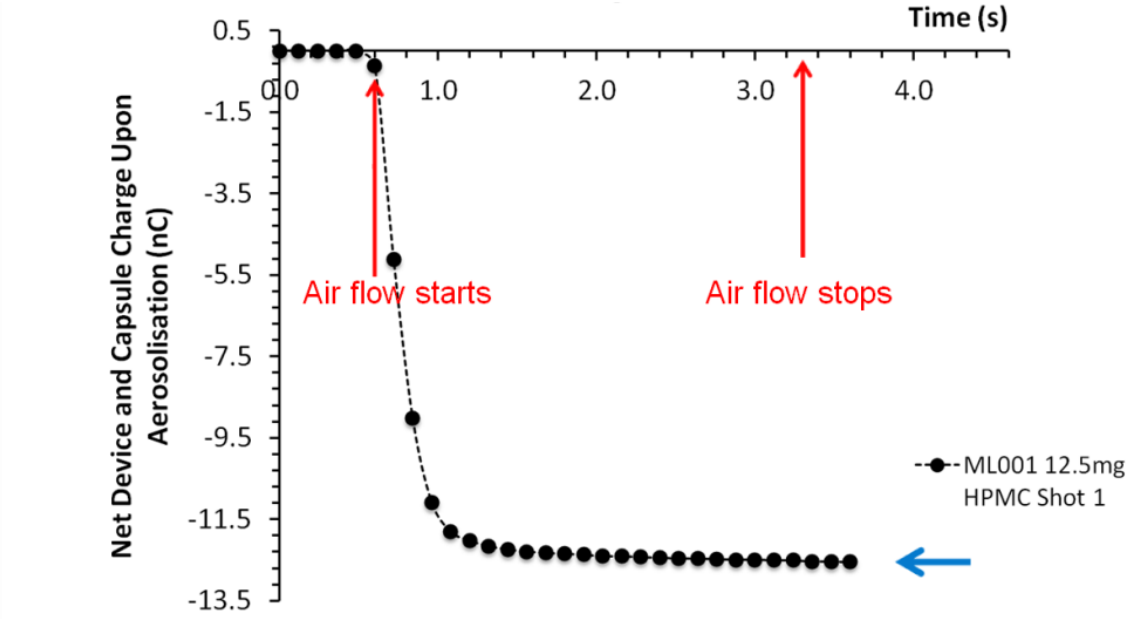

Figure 2.7 Typical dynamic charge vs time plot generated with the flow through Faraday pail

The first five values of net dynamic charge prior to the commencement of air flow were recorded to ensure that no drift in the dynamic charge values were observed and values were recorded for the duration which the airflow travelled through the device. Once the airflow started, a rapid increase in the net negative dynamic charge was observed up until an equilibration point indicated by the horizontal arrow in Figure 2.7 Values of the net charge density were determined in triplicate unless otherwise stated.

2.5 Design of the bipolar Next Generation Impactor (bp-NGI) for measurement of bipolar charge to mass ratios and in vitro performance of pharmaceutical aerosol particles

2.5.1 Introduction

Upon aerosolisation of either a pMDI or a DPI, both carrier and drug particles present in the formulation enter a high kinetic energetic state. This results in particles experiencing numerous collisions with each other and with the inhaler during which electron transfer may occur via the process of triboelectrification, causing the creation of highly charged species. The presence of static charge on therapeutic aerosol

particles may affect the *in vivo* performance of the formulation due to increased API deposition within the inhaler or capsule, increased adhesion between the API particle and carrier particle surfaces and increased deposition of aerosol particles within the throat and upper airway (Chan and Yu 1982). Electrostatic charges on aerosol particles are thought to enhance deposition by increasing attractive forces to airway surfaces. According to Coulomb's law as described in Equation 2.4, the strength of the electrostatic field a charged particle will possess relative to an object is inversely proportional to the square of the distance of the object to the centre of the particle. Therefore electrostatic attraction is particularly relevant in the small airways and alveoli due to their confined internal spaces (Kwok and Chan 2009).

$$|E| = \frac{1}{4\pi\varepsilon_0\varepsilon_r r^2}|Q| \qquad \text{Equation 2.4}$$

Where $|E|$ is the magnitude of the electric field in Volts per metre, ε_0 is the permittivity of free space, ε_r is the permittivity of the medium the electric field is contained in, r is the distance of the charged particle from the object and $|Q|$ is the magnitude of the charge on the particle.

Electrostatic precipitation utilises the concept of electrical mobility which is the ability of a charged particle to move within an electric field. It is routinely employed in a wide range of applications such as the electrophotographic industry, where charged particles adhere to paper during photocopying (Adachi *et al*. 2005, Schein 2008, Hoshino *et al*. 2010), the cleaning of exhaust gases released during combustion (Jaworek *et al.* 2006), and electrostatic spraying for painting conductive materials (Schmitt and Lebienvenu 2003). Separation of bipolarly charged aerosol particles into their separate negative and positive population distributions may be achieved by employing negative or positive electric fields, in order to repel or attract the particles away from each other. Systems such as those developed by Kulon *et al.* and O'Leary *et al.* allow the ratio of negatively to positively charged particles - the bipolar charge ratio as well as the quantity of charge present on the particles to be measured, but were not suited for determinations of the mass of the particles precipitated (Kulon and Balachandran 2001, O'Leary *et al*. 2008). More recently, the Bolar™ (Dekati Ltd., Finland) was designed as a bespoke piece of equipment for measuring bipolar charge distributions of aerosol particles (Yli-Ojanpera *et al.* 2014). As such a novel apparatus for performing bipolar

charge measurements and quantifications of aerosol particles – the Bipolar Next Generation Impactor (bp-NGI) is presented.

2.5.2 Design

A schematic representation of the bp-NGI for operation with a DPI device is shown in Figure 2.8. The apparatus employs two electrostatic precipitators which efficiently collect both negatively and positively charged aerosol particles. Aerosol particles travel through the particular NGI stage and the flow is bifurcated into the two precipitators with one electrode being held at a high negative voltage and the other at the same but opposite polarity voltage with high voltage sources (Spellman, CZE1000R, West Sussex, UK).

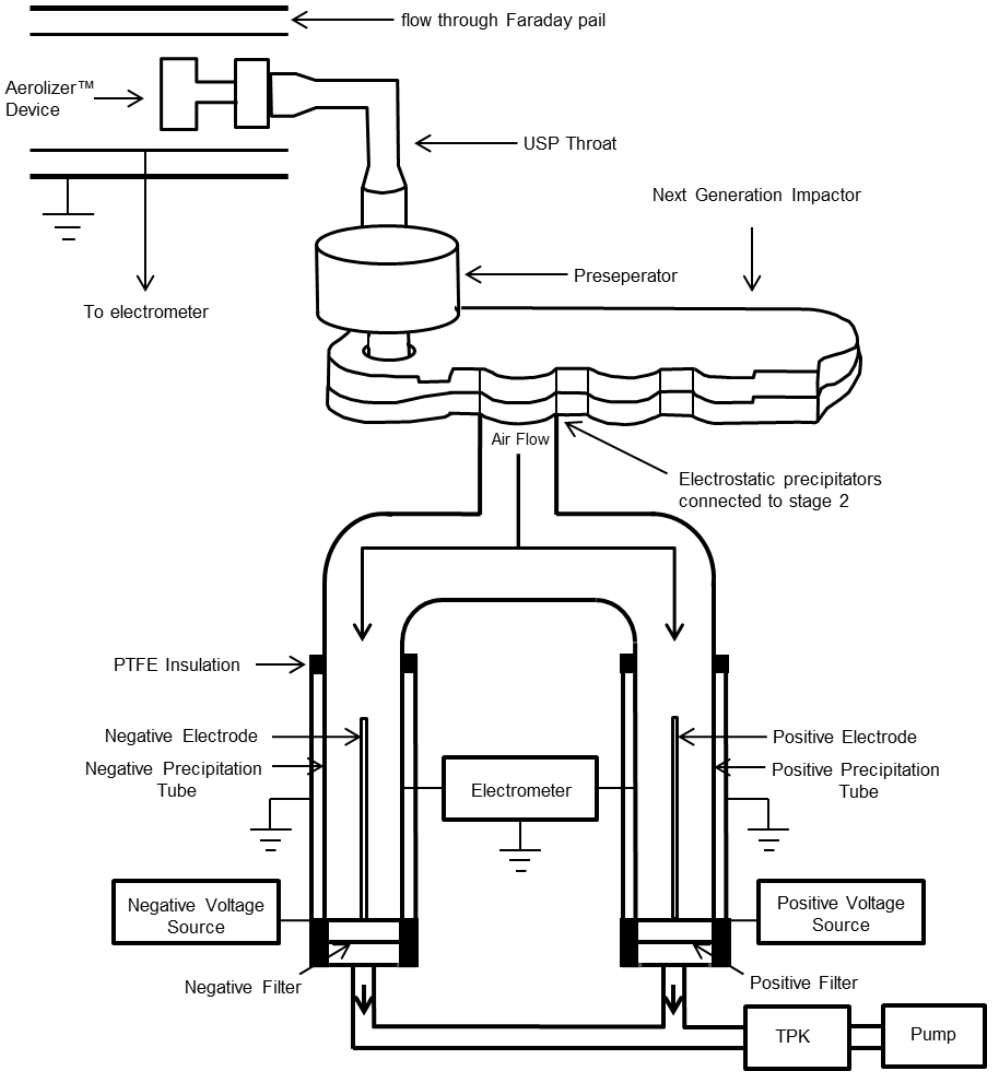

Figure 2.8 Diagram of bp-NGI experimental set up

A summary of the deposition profile of bipolar charged particles is shown in Table 2.2. Negatively charged particles are repelled by the negative electrode and are deposited onto the negative precipitation tube and positive electrode. Positively charge particles are similarly deposited onto the negative electrode and are repelled by the positive electrode onto the positive precipitation tube. Aerosol particles with a very low electrical mobility, which are not precipitated onto either the electrodes or the precipitation tubes, are collected on 0.45μm filters (Whatman, Fisher Scientific, UK) housed at the base of each precipitation tube.

Negatively Charged Particles	Positively Charged Particles	Low Electrical Mobility Particles
Negative Precipitation Tube	Positive Precipitation Tube	Negative Filter
Positive Electrode	Negative Electrode	Positive Filter

Table 2.2 Deposition profile of bipolar charged particles within the bp-NGI

An example of the particle trajectories within the negative precipitation section of the bp-NGI is shown in Figure 2.9. The flow rate is controlled by a TPK (Copley Scientific, Nottingham, UK) attached to a vacuum pump and is set with the flow meter. The precipitation tubes are connected via BNC adapters and coaxial cables to a Keithley Instruments 6521 multi input scanner card which is connected to the electrometer for charge measurements (Keithley Instruments, Reading, UK). The system is modular in nature so that each part may be separately washed down for drug quantification via RP-HPLC. The operator is connected to earth at all times via a wrist band and the outer tubes surrounding the precipitation tubes are also connected to earth to create a Faraday shield from external electric fields and stray charges to further ensure the accuracy of the measurements.

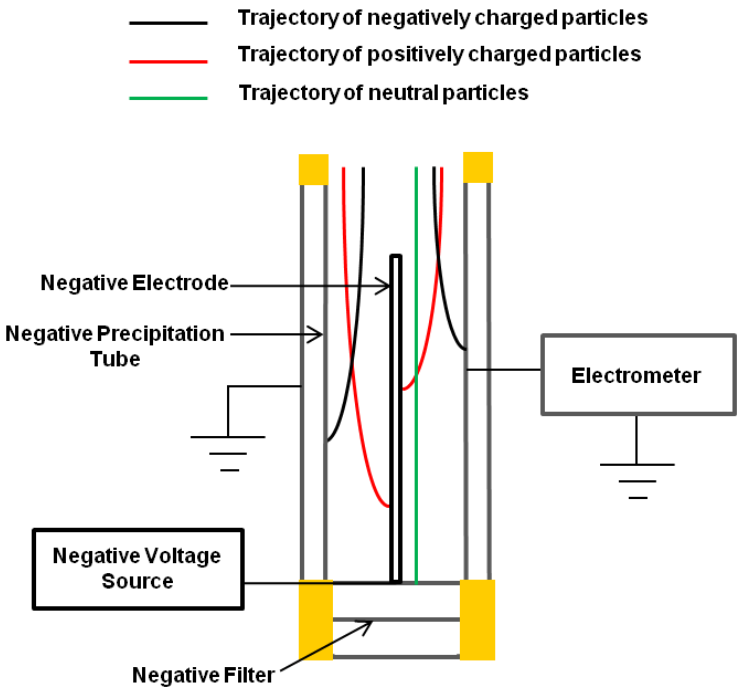

Figure 2.9 Particle trajectories within the negative precipitation section of the bp-NGI

2.5.3 Calculation of the electrical mobilities of aerosol particles

The bp-NGI is designed using the concept of the electrical mobility which is the ability of a charged particle to move within an electric field. The electrical mobility of a charged particle, Zp, may be calculated according to Equation 2.5.

$$Zp = \frac{ne}{6\pi\eta_{air} r_p} \qquad \text{Equation 2.5}$$

Where n is the number of elementary charges on the particle, e is the elementary charge, 1.602 x 10^{-19} Coulombs, η_{air} is the viscosity of air at 25°C, and r_p is the radius of the particle. The density of the particles is assumed to be 1g/cm^3. The electrostatic precipitation sections of the bp-NGI may be connected to any of stages 1-8 of the conventional NGI. Values for r_p were calculated from known particle cut off diameters for the conventional NGI. By dividing the particle cut off diameters by two in order to calculate R_p and substituting a value of 1.81 x 10^{-5} Pa.S for the viscosity of air, η_{air}, the electrical mobilities of aerosol particles with 100, 200 and 300 electrons of charge per particle were calculated.

2.5.4 Calculation of the theoretical collection efficiency of the bp-NGI

In order to maximise the collection efficiency of charged aerosol particles entering the electrostatic precipitation of the bp-NGI it was necessary to optimise the dimensions of the system by taking into account the electrical mobilities of the aerosol particles and choosing suitable dimensions for the components of the electrostatic precipitators. A plan view diagram of the cross section of one of the electrostatic precipitators is shown in Figure 2.10.

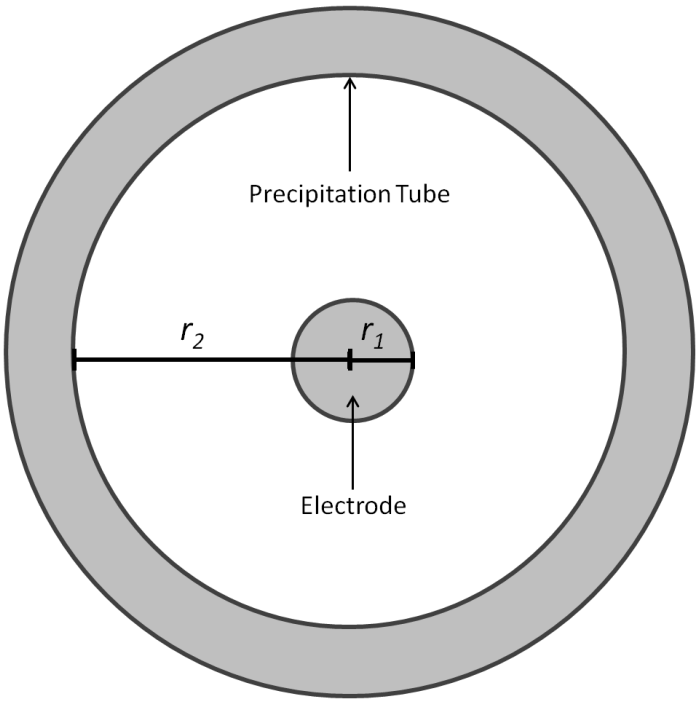

Figure 2.10 Plan view of an electrostatic precipitator

For a charged particle entering a cylindrical electrostatic precipitator under conditions of laminar flow, the theoretical collection efficiency, K_{precip} ,as given by Kulon *et al*. is given by Equation 2.6 (Kulon *et al.* 2001).

$$K_{precip}\ (\%) = \frac{2}{r_2}\sqrt{\frac{Z_p V l}{v_o\ ln(r_2/r_1)}} \times 100 \qquad \text{Equation 2.6}$$

Where r_1 is radius of the electrode, r_2 is outer tube radius, V is voltage across the electrode, l is the length of the electrode, v_0 is the speed of air past the electrode and Z_p is the electrical mobility of the particle (Kulon *et al.* 2001). By converting flow rates, Ψ,

of 15, 30 and 45 $Lmin^{-1}$ into cm^3/s, the speed of the air through the tube, v_0, is calculated using Equation 2.7.

$$v_0 = 4\Psi/\pi d^2 \qquad \text{Equation 2.7}$$

Where d is the diameter of the tube in question.

The theoretical collection efficiencies of aerosol particles entering the electrostatic precipitation system, with 100, 200 and 300 units of elementary charge per particle were calculated at flow rates of 15, 30 and 45 L/min to take into account the bifurcation of the air flow to the negative and positive precipitation sections respectively as shown in Figures 2.11 A, B and C respectively.

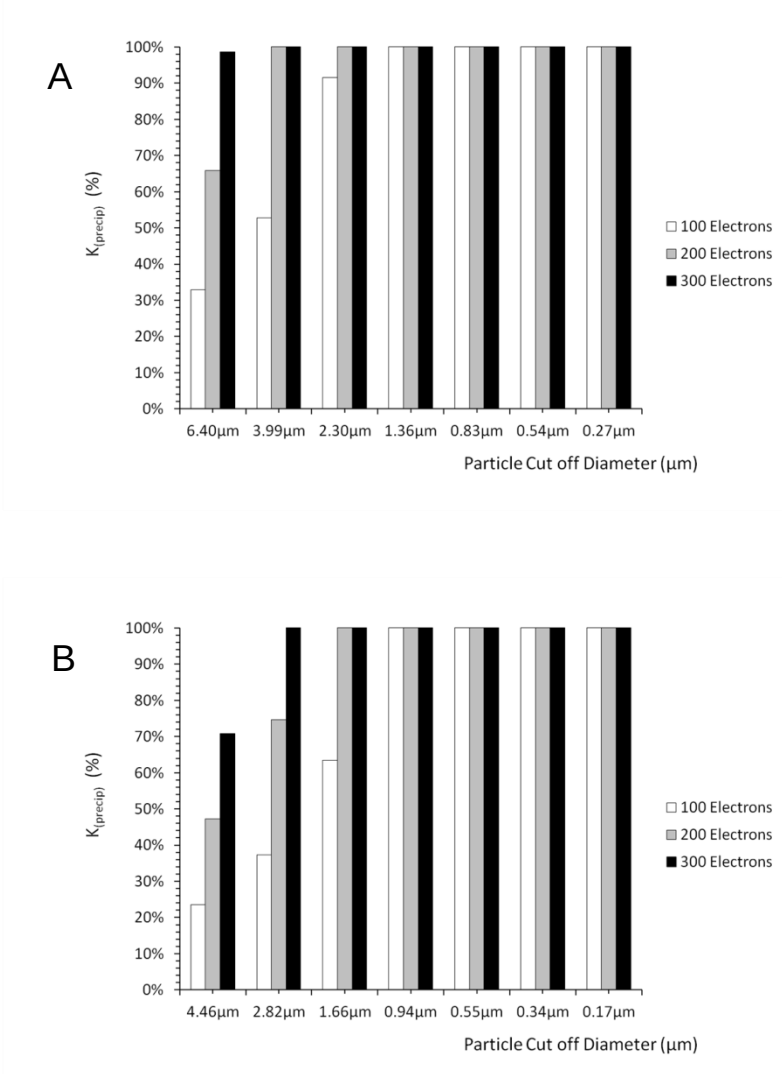

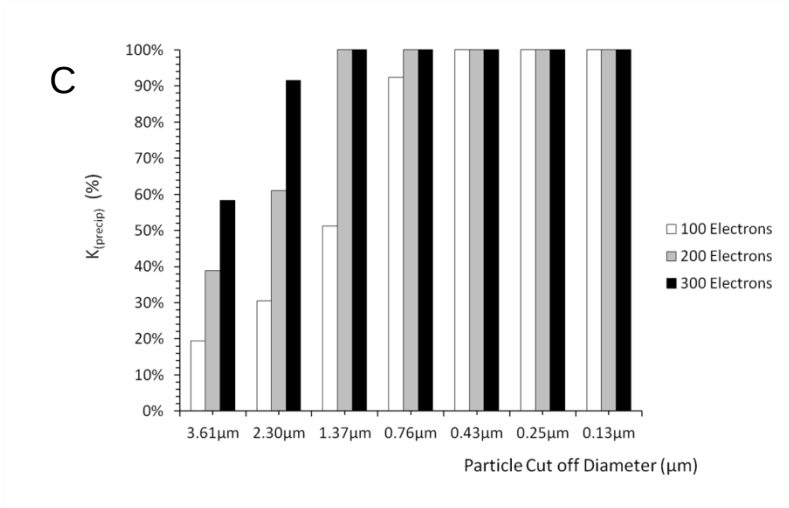

Figure 2.11 Theoretical collection efficiency of the bp-NGI at A, 15, B, 30 and C, 45 Lmin^{-1} for each NGI impaction stage for 100, 200 and 300 electrons per particle

Optimal values of V, l, r_1 and r_2 were selected to ensure maximum collection efficiency of the system was obtained, whilst at the same time ensuring the equipment was of practical dimensions for laboratory use. The length of the precipitation tubes was capped at 60 cm to allow the quantification of API particles within to be accurately determined and to prevent the bp-NGI from becoming too large in size. Under conditions of turbulent air flow, accurate deposition of charged particles within the electrostatic precipitation tubes would not be guaranteed and therefore a value for the radius of the precipitation tune, r_2, which ensured laminar flow of air at the maximum value of air flow rate through the system was selected.

2.5.5 Determination of laminar flow through the electrostatic precipitators

An indication of whether air flow will be laminar through a tube may be determined from the Reynold's number, Re, which is a dimensionless value used in fluid dynamics. For 500 < Re < 3000 the flow will be laminar (Marple *et al.* 2003b) and values outside this range will indicate transient or turbulent flow. The Reynold's number for dynamic air flow through a circular tube is given by Equation 2.8.

$$Re = \rho v d / \eta \qquad \text{Equation 2.8}$$

Where ρ is the density of air, 1.18 kg/m^3 at 25°C, v is the speed of the air through the tube, d is the diameter of the tube and η is the dynamic viscosity of air, 18.6 μPa.s = 1.86 x 10^{-5} kg/(m.s). The Reynold's numbers for the bp-NGI operating at 30, 60 and 90 Lmin^{-1} were calculated as 848, 1695 and 2543 respectively, falling within the range in which laminar flow will occur.

2.5.6 Consideration of the breakdown voltage required to create a corona discharge

One potential concern when the design of the bp-NGI was being developed was the potential of corona discharges, in the form of sparks to arc between the high voltage electrodes and the precipitation tubes. This may occur when the voltage is large enough to overcome the electrical resistance of the air between two conductive materials (Ward 1965). The breakdown voltage, V, required to form a corona discharge between the electrode and the tube was calculated using a Paschen curve for air, described by Equation 2.9.

$$V = \frac{apd}{\ln(pd) + b} \qquad \text{Equation 2.9}$$

Where a is a constant (4.36 x 10^7 V/(atm.m) for air at standard atmospheric pressure), b is also constant (12.8), p is the air pressure and d is the distance between the electrode and the precipitation tube. Using d = 0.00195, equivalent to subtracting the radius of the electrode from the radius of the precipitation tube, a value for the breakdown voltage, V, was calculated at 95.93 kV. This is in large excess of the 3 kV used for the experiments and so the equipment was deemed to be safe in this aspect.

2.5.7 CAD diagrams of the bp-NGI

Having decided on the design of the bp-NGI and finalising the preferred dimensions, a description was converted into CAD diagrams in the department of mechanical engineering at the University of Bath in order to aid in the construction. Figure 2.12 shows the complete electrostatic precipitation section of the bp-NGI drawn to scale including dimensions in mm.

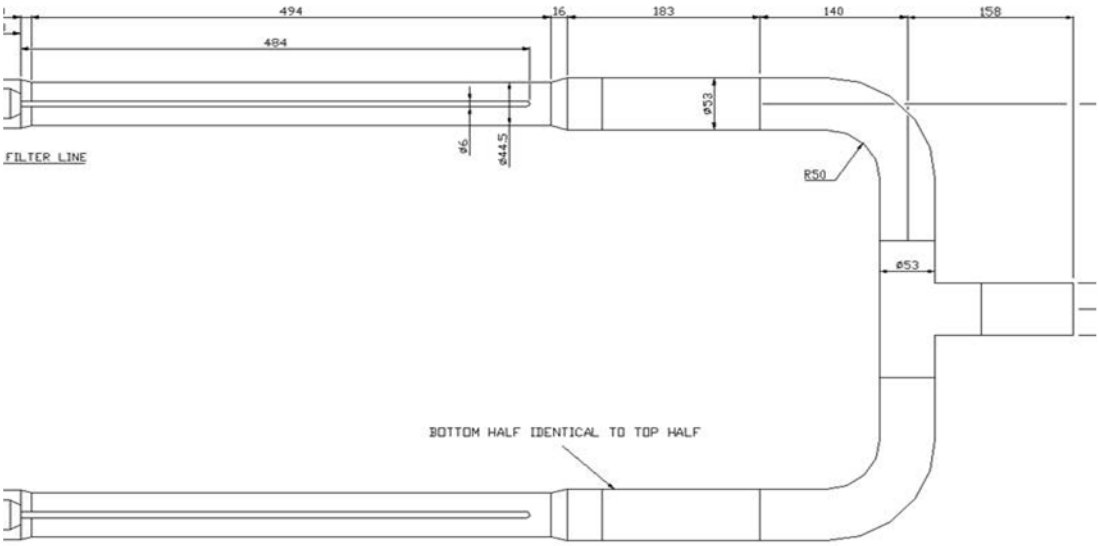

Figure 2.12 Scale diagram of the electrostatic precipitation section of the bp-NGI

A more detailed diagram of an electrostatic precipitator is shown in Figure 2.13. It includes scale representations of the inlet, electrode, electrode holder, aluminium precipitation tube, connection to the electrometer, high voltage source connection and filter.

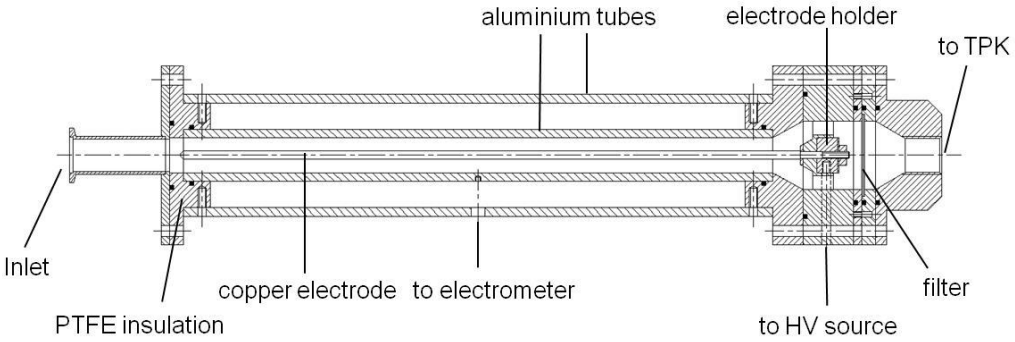

Figure 2.13 Scale diagram of an electrostatic precipitation section

As the electrostatic precipitation section of the bp-NGI was designed to attach directly to the bottom of a conventional NGI, a specially designed frame was constructed. This was designed to support the weight of the system and was required because the NGI could no longer sit directly on top of a laboratory bench due to the electrostatic precipitators beneath. The frame was designed which would provide structural rigidity and run from the top of the system, where the NGI is located, to the bottom at the exits from the electrostatic precipitators. The bottom section of the frame is shown in Figure

2.14 and shows the negative and positive electrostatic precipitation sections side by side. The diagram also shows the outlets for the air flow for each precipitator which are connected by rubber tubes (not shown) to a central manifold. This manifold was in turn connected to a TPK (Copley Scientific) and vacuum pumps, in order to control the flow rate and duration of air flow through the system. The bottom of the frame was equipped with wheels in order to allow the system to be portable.

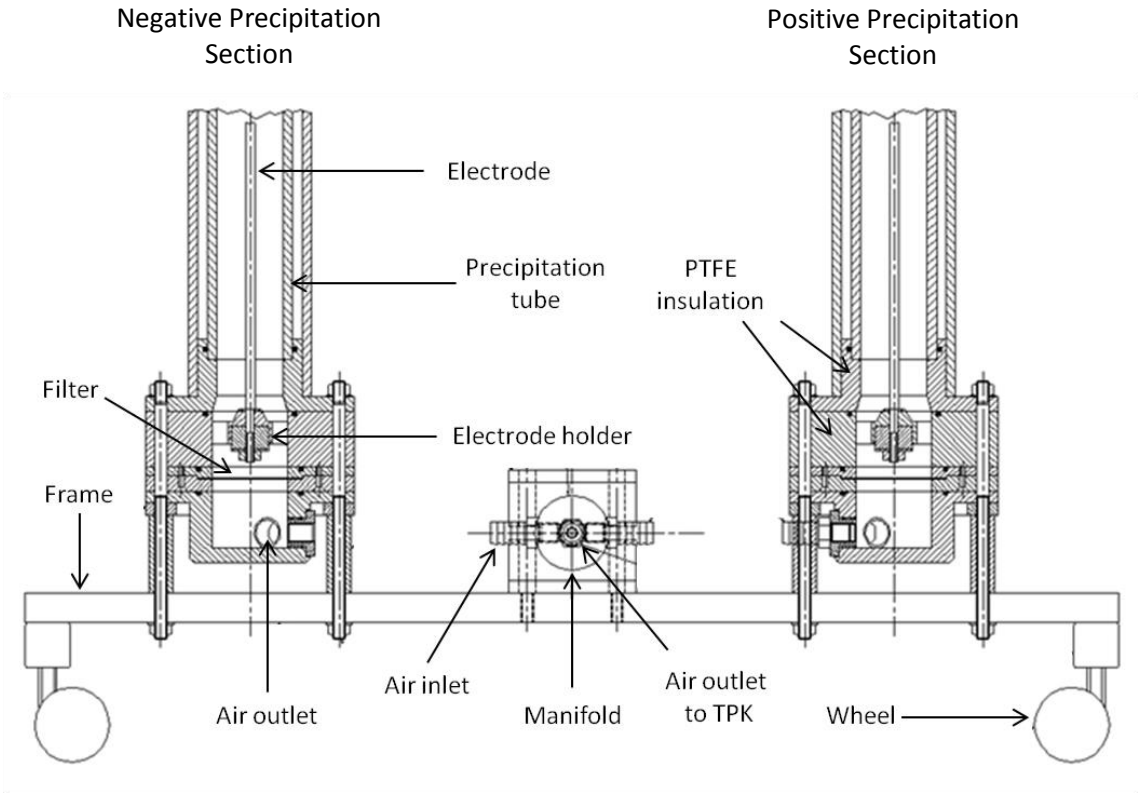

Figure 2.14 Bottom section of the bp-NGI and frame

In order to connect the electrostatic precipitation section to the bp-NGI, a specially designed NGI cup, plan view shown in Figure 2.15 A was manufactured with the inclusion of a screw thread which would allow a connector to be screwed into the bottom of the cup, once the NGI lid was closed as shown in Figure 2.15 B.

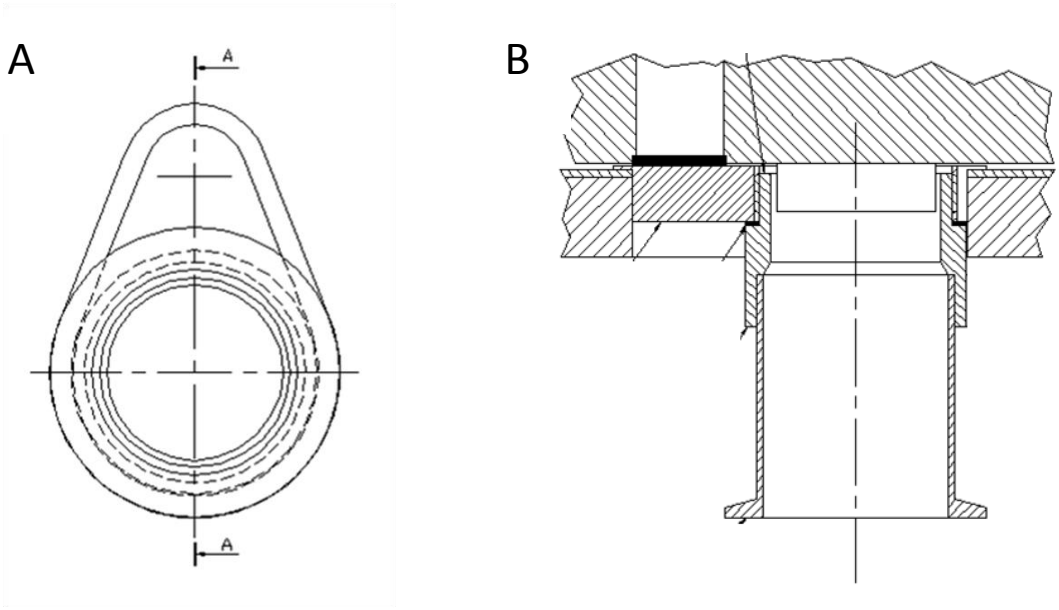

Figure 2.15 Plan view of A, modified NGI cup, and B, connection of NGI to electrostatic precipitation section

A diagram of the top section of the frame is shown in Figure 2.16 and shows a specially designed metal plate attached to the NGI via custom made screws. The NGI sits on top of the frame guided by locator pins connected to the frame, lined up with holes drilled into the metal plate.

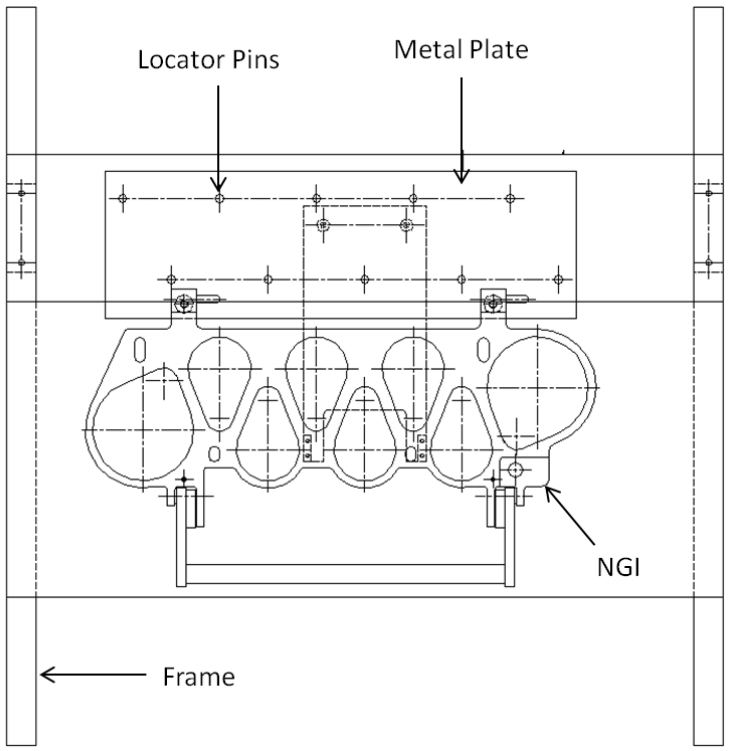

Figure 2.16 Plan view diagram of the top section of the frame and NGI

2.5.8 Charge measurement methodology

Measurements were performed using a 6517B electrometer, 6521 scanner card and KUSB-488B USB connector (Keithley Instruments Inc., Berkshire, UK) connected to a PC with Testpoint Version 6 software for data acquisition. During all measurements the operator wore a conductive wristband connected to earth to minimise external electric fields. The frame of the bp-NGI and the outer tubes of the precipitation sections were also connected to earth. To perform charge measurements the negative and positive precipitation tubes were connected to channels 1 and 2 of the scanner card respectively via coaxial cables with BNC connectors and the electrometer capacitor was discharged using the ZCHK button and then the electrometer reading was zeroed using the REL button. Static measurements of charge on the precipitation tubes were performed using charge mode, Q, when only minimal current could be recorded by the electrometer. Dynamic measurements were performed using current mode, I. A background measurement was performed for each tube by activating the TPK to pull air only through the system for the required length of time and at the required flow rate. Subsequently, five successive shots of aerosol were delivered to the bp-NGI with the current and time readings for each precipitation tube recorded in the electrometer buffer and then transferred to Microsoft Excel for data analysis. A typical plot of the current vs time profiles generated for A, the negative precipitation tube, and B, the positive precipitation tube are shown in Figure 2.17 A and 2.17 B respectively.

A

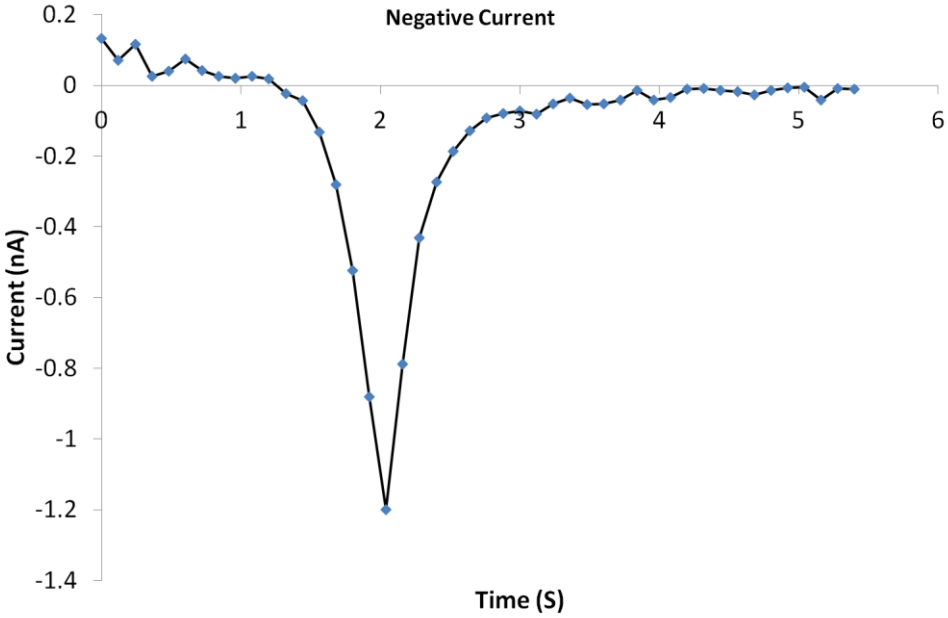

B

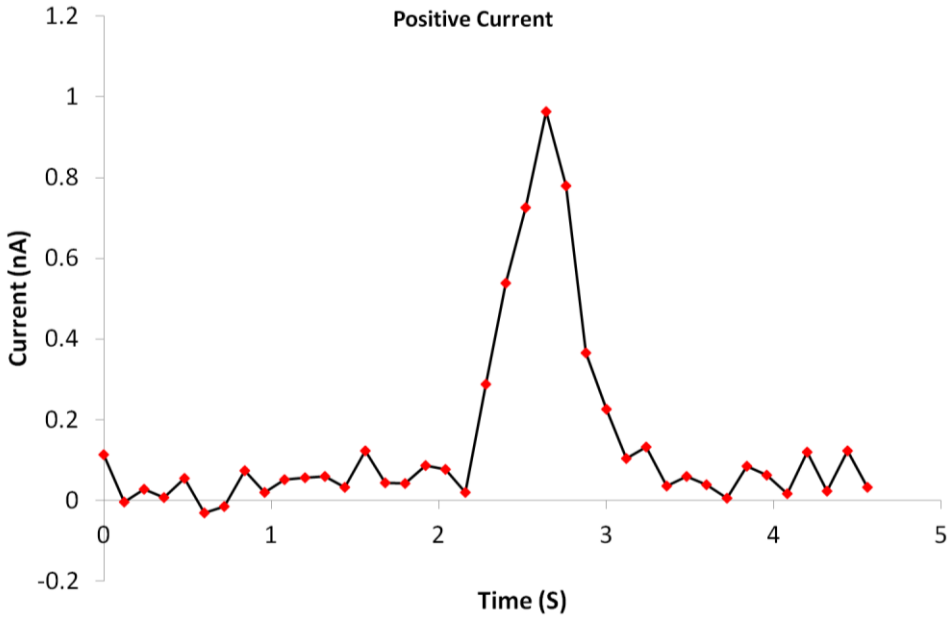

Figure 2.17 Typical current vs time plots for A, the negative precipitation tube, and B, the positive precipitation tube

Equation 2.10 shows the relationship between, current, I, charge, Q and time, t, namely that the current is equal to the rate of charge transfer over a given time.

$$I = dQ \,/\, dt \qquad \text{Equation 2.10}$$

By integrating both sides of Equation 2.10, the total charge transferred from the aerosol particles is given by Equation 2.11.

$$Q = \int_{t_i}^{t_f} I \, dt \qquad \text{Equation 2.11}$$

Where $t_{initial}$ is the time at which the current begins to rise and t_{final} is the point at which the current returns to the baseline. This value for Q is equal to the area under the curve between t_i and t_f. Therefore, the areas under the curve were calculated for each current vs time profile in order to calculate the total charge of the aerosols deposited for each dose.

2.5.9 Background measurements of the charge on the precipitation tubes

Background measurements of the charge values for each tube were recorded both with the high voltage switched off and on, in order to check that that the precipitation tubes were successfully electrically isolated from the rest of the system. At zero volts, the charge values for both tubes were shown to remain constant and at zero as a function of time indicating efficient electrical isolation of the tubes via the PTFE holders. Figure 2.18 shows the drift in the charge measurement of A, the negative precipitation tube and B, the positive precipitation tube upon applying a voltage of -3.0kV and +3.0kV to the negative and positive electrodes respectively.

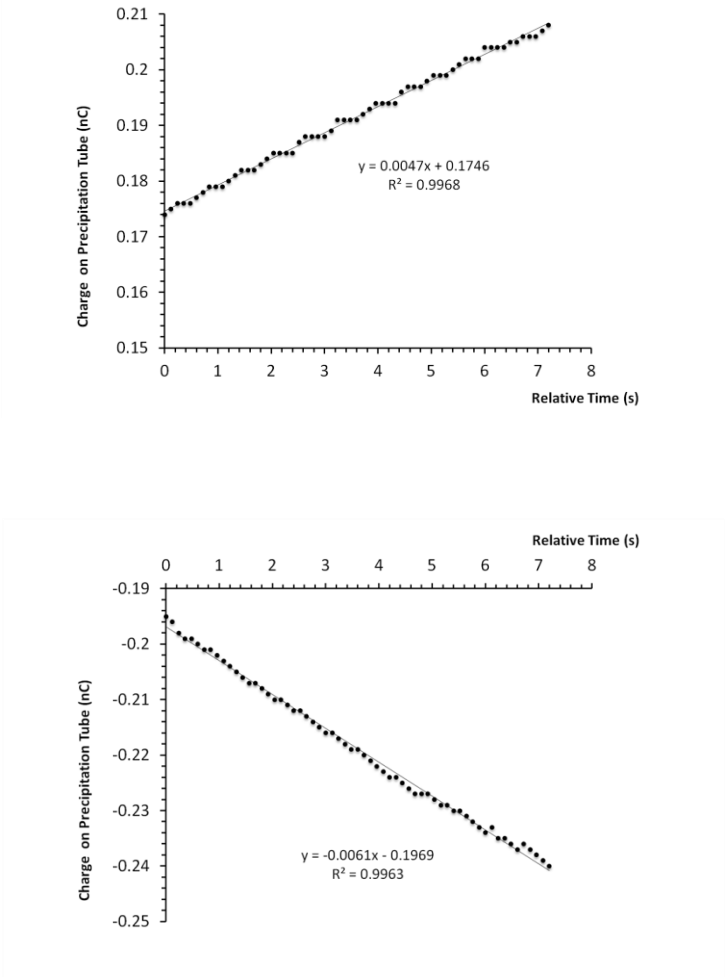

Figure 2.18 Drift in charge measurements of precipitation tubes as a function of time upon applying a voltage of -3.0kV and +3.0kV to the negative and positive electrodes respectively

The values for the rate of change of charge as a function of time were determined to be 0.0047nC/s and 0.0061 nC/s which were considered to be too small to affect the overall value of the charge measurements recorded. However, the background current created by this induced charge was subtracted from all measurements in order to normalise the data.

2.5.10 Computational Fluid Dynamic Modelling

Computational fluid dynamic (CFD) modelling is a useful tool for performing theoretical predictions of the flow of liquids and gases over surfaces and through pipes and tubes. It has many practical applications and is commonly used in areas such as meteorology (Yin *et al.* 2010), oceanography (Blazek 2001), astrophysics (Trac and Pen 2003), the oil and gas industries (Lakehal 2013), the automotive (Falcitelli *et al.* 2002), aircraft (Zhang *et al.* 2013), food industries (Scott and Richardson 1997) and ship design (Peri *et al.* 2001) .

In order for charged particles to be efficiently collected by the bp-NGI it is essential that laminar flow be maintained through the electrostatic precipitation sections. Any turbulence present would prevent particles from being subject to the principals of inertial impaction and would result in random deposition throughout the system. This would lead to innacurate determinations of the formulation performance. The theoretical Reynold's numbers (Re) for flow rates of 30, 60 and 90 L/min, equivalent to 15, 30 and 45 L/min through each precipitation section were calculated and fell between the range $300 \leq Re \leq 3000$, indicating that laminar flow through the precipitation sections should be ensured. In order to determine the validity of the calculations the design of the system was characterised using CFD to check whether laminar flow would be maintained given the dimensions of the system

A numerical model of the bp-NGI experimental apparatus was generated and solved using ANSYS ® 14.5 academic software at the Department of Civil Engineering at the University of Bath. The process included 3D CAD generation of the equipment, meshing design and refinement, selection of suitable numerics, solution of the case using the Bath University HPC (High Performance Computer) and post-processing of the final data.

2.5.10.1 Geometry

The geometry of the bp-NGI was drawn in 3D at 1:1 scale using ANSYS Workbench software via conversion of a 2D CAD diagram provided by the Department of Mechanical Engineering at the University of Bath. Some minor alterations to the exact experimental geometry were included to reduce the computational complexity of the model. This included the assumption that all pipe joints were ideal (smooth), and the route of the pipework at the outflow was simplified. Images of the completed model are shown in Figure 2.19.

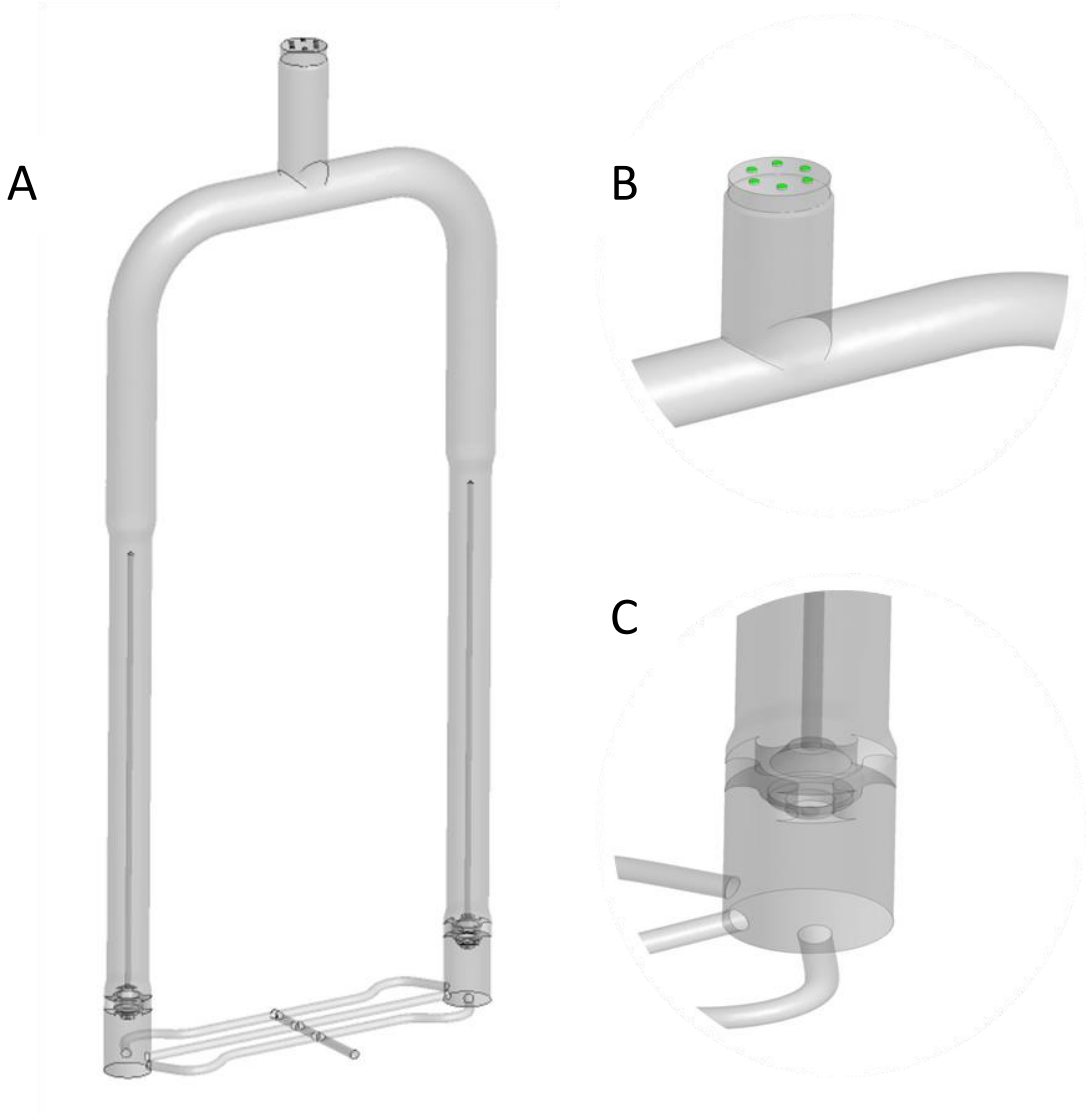

Figure 2.19 3D CAD images of bp-NGI geometry. A, the full rig; B, the connection from stage 2 of the NGI and C, the electrode holder

2.5.10.2 Meshing

Discretisation was obtained using a hybrid method on ANSYS Mesh software. All pipe inner surfaces were meshed using layered body conforming hexahedral elements, with the remaining space filled with unstructured tetrahedral elements. The cell size was tightened along the length the electrode for increased accuracy, as shown in Figure 2.20.

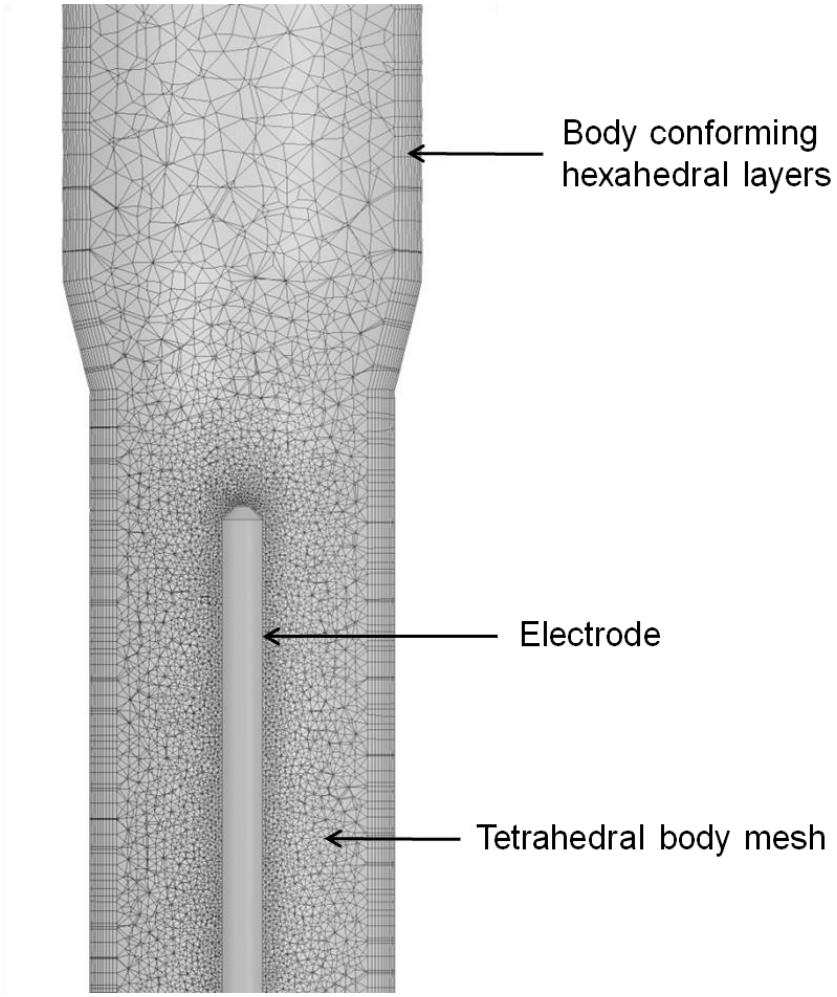

Figure 2.20 Image of a slice plane through the centre of the electrode precipitator section numerical mesh

2.5.10.3 Results

The numerical model was developed and solved using an implicit Reynolds-Averaged Navier-Stokes (RANS) method with ANSYS CFX 14.5 software. Details of the key numerical environment parameters are summarised in Table 2.3. To mimic the

experimental procedure, the transient model consisted of an initial condition of still air, followed by 2.7 seconds of suction at the outlet equal to 90 l/min, followed by a further 8 seconds with the outlet closed. The timestep control used an adaptive method, enabling the target residuals for mass and momentum to be met with high computational efficiency. The case was solved using 4 parallel central processing unit (CPU) cores taking approximately 52.4 hours. Post-processing was completed using ANSYS CFD-Post software.

Discipline	Parameter	Value
Fluid Properties	Fluid Model	Pure air at 1 atm
	Density	1.18 kg/m^3
	Dynamic Viscosity	1.831e^{-05} Pas
	Temperature	296.15 K
	Heat Transfer	Isothermal
Timestep control	Coeffcient Loops	Minimum 2, Maximum 5
Solution Control	Equation Residual Target	Maximum 1e^{-05} rms
Turbulence	Equation Model	Shear Stress Transport
Boundary Conditions	Inlet	Opening (relative pressure = 0)
	Internal Surfaces	No – slip walls
	Outlet (during suction)	0.0005925 kg/s (equiv. 30 l/min)
Mesh Properties	Total Elements	6,981,628
	Total Nodes	1,804,269

Table 2.3 Numerical solution properties for CFD analysis of the bp-NGI

Predicted airflow through the electrostatic precipitation sections at 45 L/min was visualised using a streamline representation as shown in Figure 2.21.

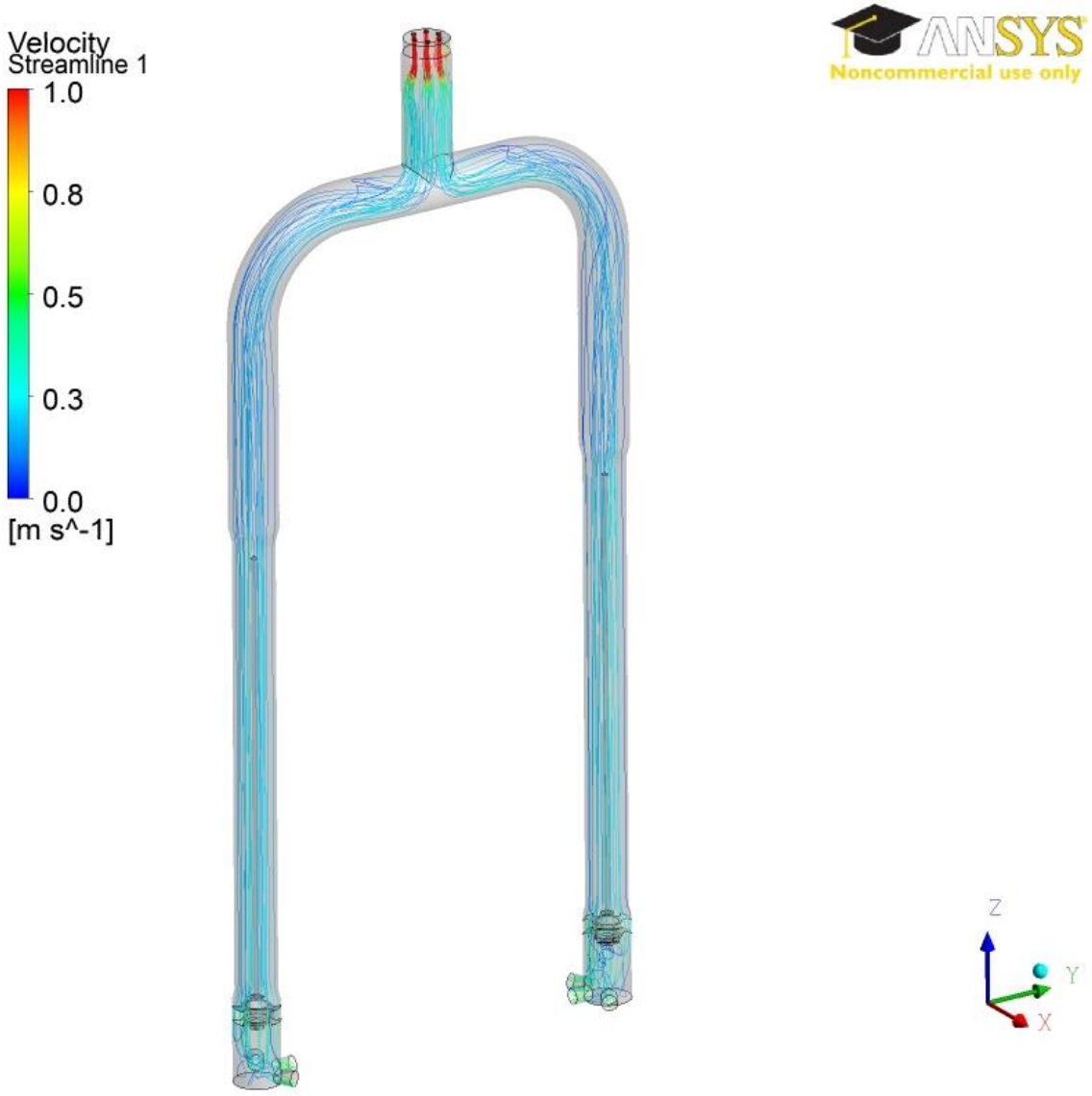

Figure 2.21 Streamline representation of air flow through the electrostatic precipitation sections of the bp-NGI at 45 L/min

Predicted airflow through the electrostatic precipitation sections at 45 L/min was visualised using a velocity contour representation as shown in Figure 2.22.

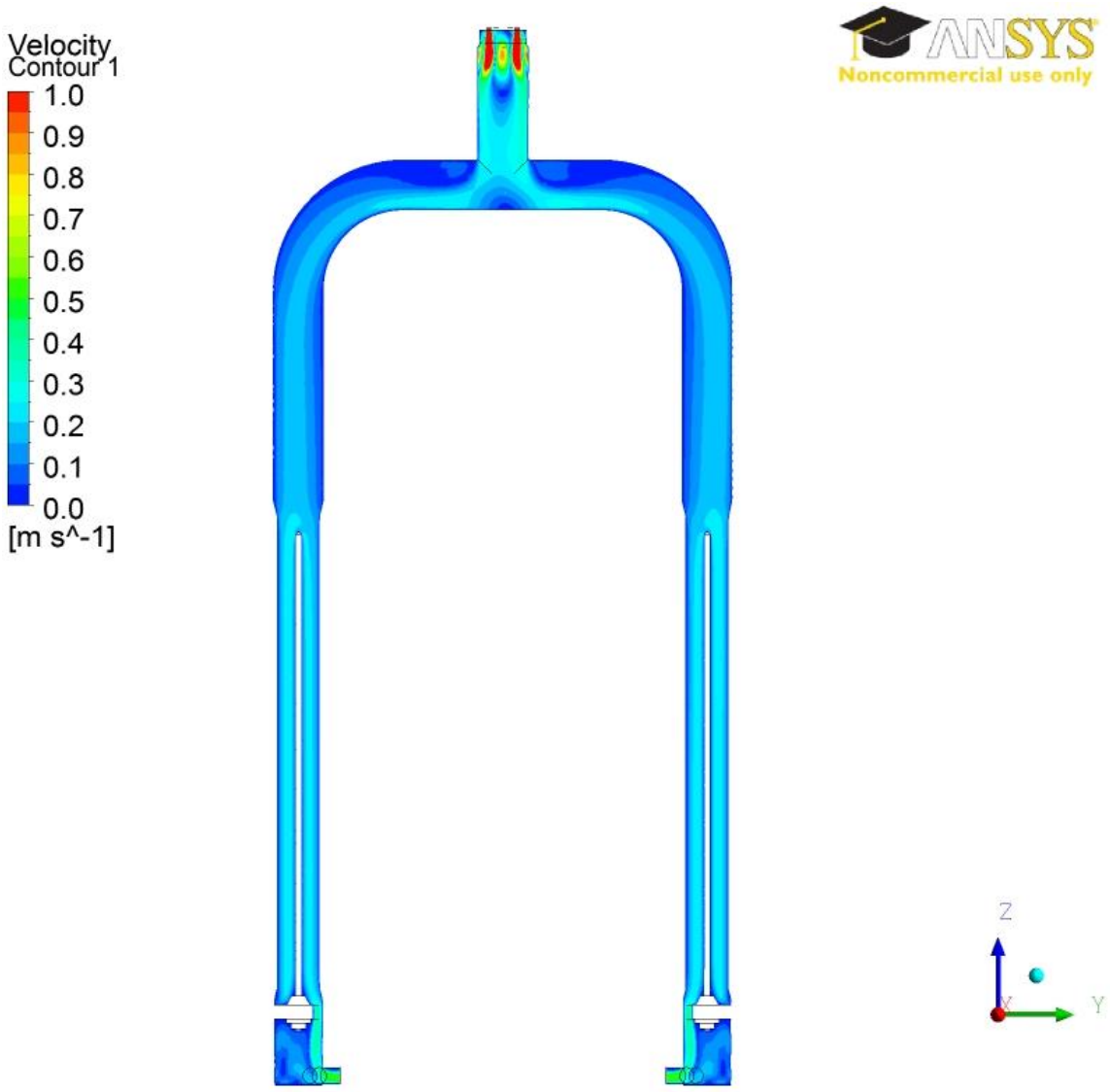

Figure 2.22 Velocity contour representation of air flow through the electrostatic precipitation sections of the bp-NGI at 45 L/min

The figures show that some turbulence is predicted at the exit of the nozzles of stage 2 where the air rapidly changes speed as the flow exits from the narrow diameter jets and into the larger diameter precipitation section. Further turbulence is also predicted at the T-piece where the airflow bifurcates into the two precipitation sections. However, by the time the airflow reaches the electrostatic precipitation sections it is predicted to be laminar, with minimal turbulence created as the air meets the tips of the two electrodes. Therefore confidence was gained that turbulence would not affect the precipitation efficiency of the system. Future CFD investigations suggested involve optimising the geometry of the T-piece to reduce any turbulence which may be created.

Chapter 3 Net Charge Measurements of Inhalation Grades of Lactose

3.1 Introduction

DPI formulations consist of an active pharmaceutical ingredient (API) mixed together with a coarse carrier particle, which is lactose monohydrate (Pitchayajittipong *et al*. 2010). The manufacture of DPI formulations consists of various processing steps such as sieving, blending, pneumatic conveying and dosing into capsules. During each processing step, lactose monohydrate particles may become statically charged via the mechanism of triboelectrification. Differences in the work function (the ability to remove an electron from the vacuum energy level) will result in electron transfer between the DPI formulation particles and the various surfaces they may encounter (Matsusaka and Masuda 2003). This may cause handling issues and influence the formulation blend structure. Simple transport of lactose by pouring will result in tribocharging of the particles, the mechanisms for which have been outlined in detail (Ireland 2010b). A study conducted by Murtomaa and Laine showed the extent of triboelectrification with lactose, glucose and mixtures of the two experienced upon passing through a glass pipe into a Faraday pail (Murtomaa and Laine 2000). Sieving is a useful process for breaking up any large agglomerates of powder, which have formed either upon storage or as a result of small quantities of moisture being present in the sample. Sieving also ensures that adequate mixing is facilitated during blending to produce a homogenous formulation (Steckel *et al*. 2006). When particles of lactose are passed through a sieve it might be hypothesised that negative charge will be transferred to the particles due to a frictional triboelectrification mechanism, with labile electrons easily removed from the surface of the metal and transferred to the sieved material. To the author's knowledge, investigations into the extent of the triboelectrification of inhalation grade lactose during sieving have not previously been reported.

Once sieving has been completed, A DPI formulation is normally blended to produce a homogenous mixture to ensure uniformity of the delivered dose of API (de Boer *et al*. 2012). It is well know that electrostatic charge will build up on the DPI formulation as a result of frictional triboelectrification resulting from lactose and API particles colliding with the internal surface of the blending vessel (Kwok and Chan 2009). Charge build up in DPI formulations during blending may produce agglomeration and flow problems resulting in handling issues (Noakes 2004) as well as material transfer from the bulk powder bed to the blending vessel walls (Lowell 1977a). Eilbeck *et al*. showed that

when lactose was tribocharged in a stainless steel vessel using an air cyclone, the particles became tribocharged and adhered to the stainless steel surface (Eilbeck *et al*. 2000). When successive runs were performed without cleaning in between, the extent of coating of the stainless steel surface increased and so the extent of charge build up on the non-adhered particles decreased. Conversely, the presence of electrostatic charge during blending may be beneficial. Staniforth and Rees used an air cyclone to purposefully induce electrostatic charge onto various sugar based pharmaceutical excipients, including lactose monohydrate, in order to produce ordered homogenous mixtures (Staniforth and Rees 1981). Similarly, Pu *et al*. performed low shear blending experiments with lactose and caffeine and showed that reducing electrostatic charge during the blending process resulted in poorer blend homogeneity. They also showed that by charging the excipient and API with a corona discharge blend homogeneity was improved (Pu *et al*. 2009). Elajnaf et. al performed a detailed study looking at the effect of blending vessel material and relative humidity on the extent of triboelectrification during low shear Turbula blending of DPI formulations containing salbutamol sulphate and ipratropium bromide (Elajnaf *et al*. 2006). Their findings showed that the type of blending vessel material used altered the charge values and that as the relative humidity increased, the extent of charge built up decreased. However, their results were achieved by pouring directly from the blending vessel into the Faraday pail post blending and this may have resulted in additional tribocharging of the sample resulting in some of the large standard deviations observed. A further study conducted by Engers et. al investigated the extent of triboelectrification of dicalcium phosphate dihydrate, microcrystalline cellulose and lactose monohydrate during low shear blending in a stainless steel vessel (Engers *et al*. 2006). The results showed very little difference in the net charge values recorded between the control experiment (pouring the material from the vessel into a Faraday pail without blending) and having blended the sample for either twenty and forty rotations. This indicated that the charge value recorded was chiefly as a result of the pouring of the sample, rather than the blending.

A further consideration is whether lactose monohydrate particles being used in the manufacture of DPI formulations carry any inherent charge prior to use. A literature search did not reveal any previous attempt to measure the net charge on unprocessed pharmaceutical grade lactose monohydrate. No doubt this is with good reason as in order to transfer the powder to the Faraday pail it has previously been very difficult to do so without either pouring it from its container or by transferring it using a spatula or similar instrument. Both methods would result firstly in disturbing particles from the powder bed and secondly tribocharging these particles by sliding them over a surface.

The aim of this study is to produce a method to record accurate, repeatable and reliable net charge measurements of pharmaceutical inhalation grades of lactose monohydrate, as received and after the critical processing steps of sieving and blending. Murtomaa *et al*. showed that particle morphology and amorphous content may have an effect on the tribocharging characteristics of particles (Murtomaa *et al*. 2002, Murtomaa *et al*. 2004) and therefore a cohesive grade of lactose monohydrate, Respitose® ML001 and a free flowing grade, Respitose® SV003 were selected for the study.

3.2 Materials and methods

3.2.1 Materials

Respitose® ML001 and Respitose® SV003 grades of lactose monohydrate obtained from DFE Pharma (Veghel, The Netherlands) were used for the study. The samples were stored in a sealed humidity cabinet with a saturated salt solution of potassium carbonate (Fisher Bioreagents, NJ, USA) at 43% relative humidity in an air conditioned room maintained at 20 ± 2ºC.

3.2.2 Methods

3.2.2.1 Particle size measurements

Particle size measurements of the lactose monohydrate samples were measured dispersed dry at a pressure of 2 bars using a Sympatec Helos laser diffraction system with an R4 lens in conjunction with a RodosT4 disperser and a Vibri feeder controlled by WINDOX software (Sympatec GmbH, Germany). Five repeat measurements were taken for each sample and the values recorded for the d_{10}, d_{50} and d_{90} were averaged as well as the percentage of particles less than 5 µm.

3.2.2.2 Scanning electron microscopy

Scanning electron microscopy (SEM) images of the lactose monohydrate samples was performed on a JEOL JSM-6480LV (JEOL, Tokyo, Japan). Samples were mounted on sticky carbon tabs and coated with an Edwards sputter coater S150B (Edwards, Israel) for 5 minutes prior to analysis. An acceleration voltage of 10 kilovolts was used for the imaging.

3.2.2.3 Characterisation of rheological properties

The rheological properties of the lactose monohydrate samples were characterised using an FT4 Powder Rheometer (Freeman Technology, Welland, UK) following the recommended operating procedures for analysing pharmaceutical powders (Freeman 2007). Samples of powder were analysed in a 20 mL split vessel. Prior to determination of the values samples measured were preconditioned using a 23.5 mm blade, which was moved down a helical path through the sample with a helix angle of 5 degrees at 60 mm/s. The two lactose monohydrate samples were exposed to increasing airflow velocities and the powder fluidisation energy (FE) with no aeration and the aeration energy (AE) at 8 m/s was recorded. The dynamic flow index (DFI) was also determined along with the conditioned bulk density (CBD) of each sample.

3.2.2.4 Net charge measurements

The net charge of the lactose monohydrate samples was determined using a custom made Faraday pail connected to a Keithley 6517B electrometer (Keithley Instruments, Cleveland, USA). A description of the principals behind the operation may be found in Chaper 2, section 2.8. Different methodologies were developed to introduce powder samples into the Faraday pail to determine the net charge of the sample prior to processing. These methodologies are described in the results and discussion section as each set of data generated influenced the development and implementation of the next method.

3.2.2.5 Sieving

A range of different sieves were employed with differing mesh sizes all manufactured from stainless steel (Endecotts Ltd., London, England). A sieve was placed directly over the top of the Faraday pail connected to the electrometer with the zero check function enabled. A small quantity of powder was poured onto the top of the sieve so that it sat on the mesh without passing through. A stainless steel scraper (grade 316) was then used to pass the powder through the mesh. Once sufficient powder had passed through the sieve, the net charge of the sieved sample was determined by reading the value from the display on the electrometer. The mass of the powder measured was then determined by using the analytical balance.

3.2.2.6 Low shear blending

Prior to all low shear blending experiments, the powder samples were passed through a 250 µm sieve in order to break up any large agglomerates. Once sieved, powder was poured directly from the sieve pan into the blender vessel and the powder was allowed to stand for 1 hour under ambient conditions to allow any charge to dissipate prior to blending. Samples were blended using a WAB type T2F Turbula blender (WAB, Nidderau-Heldenbergen, Germany) at 22 RPM for a predetermined length of time. Net charge density of the powder was determined both pre and post blending by pouring the powder directly from the vessel into the Faraday pail, as well as being measured post blending with the fourth generation powder ladle as described in the results and discussion section. For comparisons of different container materials, 500 cm^3 vessels were used made of stainless steel (grade 316), glass and polypropylene with 80 grams of Respitose® ML001 or Respitose® SV003 used for comparison. For comparisons of low shear vs high shear blending a 1000 cm^3 vessel made of stainless steel (grade 316) was used with 150 grams of Respitose® ML001 or Respitose® SV003.

3.2.2.7 High shear blending

Prior to all high shear blending experiments, the powder samples were passed through a 250 µm sieve in order to break up any large agglomerates. High sheer blending experiments were conducted using a Niro Microgral high shear blender (GEA, Maryland, USA). Once sieved, powder was directly poured from the sieve pan into the

glass vessel of the blender and the powder was allowed to stand for 1 hour under ambient conditions to allow any charge to dissipate prior to blending. The rotational speed of the impeller was set to 500 RPM and the blending time was set to the desired length using the operating software.

3.3 Results and discussion

3.3.1 Particle sizing of the two lactose monohydrate grades

The particle size distributions of the two grades of lactose monohdrate selected for the study, ML001 and SV003, are displayed in Table 3.1. The average (n=5) of the 10% undersize (d_{10}), 50% undersize (d_{50}) and 90% undersize (d_{90}) values were recorded as well as the percentage of particles with diameter less than 5 µm. The d_{10} and d_{50} values for ML001 were smaller than for SV003 and the percentage of particles less than 5 µm was greater indicating that ML001 has a greater percentage of fine particles than the SV003. The d_{90} value for ML001 was greater than for SV003 indicating that the largest particles in ML001 had a greater median diameter than those of SV003. This is the result of the manufacturing process for each grade of lactose monohydrate. ML001 is manufactured by jet milling large lactose monohydrate particles (DFE Pharma 2014a), which is a destructive process whereby a large quantity of fine particles is generated. SV003 is a sieved grade lactose monohydrate (DFE Pharma 2014b) where the lactose particles are passed through a range of different sieves and different fractions of powder are isolated with a more narrow particle diameter range than ML001.

	d_{10} (µm)	d_{50} (µm)	d_{90} (µm)	% < 5 µm
ML001	3.71 ± 0.17	48.11 ± 0.42	153.92 ± 1.89	11.16
SV003	32.86 ± 1.56	60.28 ± 0.89	91.35 ± 1.81	2.65

Table 3.1 Particle size values of ML001 and SV003 (n=5, mean ± SD)

3.3.2 Scanning electron microscopy

Scanning electron micrographs of the two grades of lactose monohydrate at 200 times magnification are displayed in Figure 3.1. The images clearly show that ML001 has a large number of fine particles present and qualitatively the particle diameter range is large. Conversely, SV003 contains much fewer fine particles of lactose monohydrate and the particle diameter range is qualitatively much narrower.

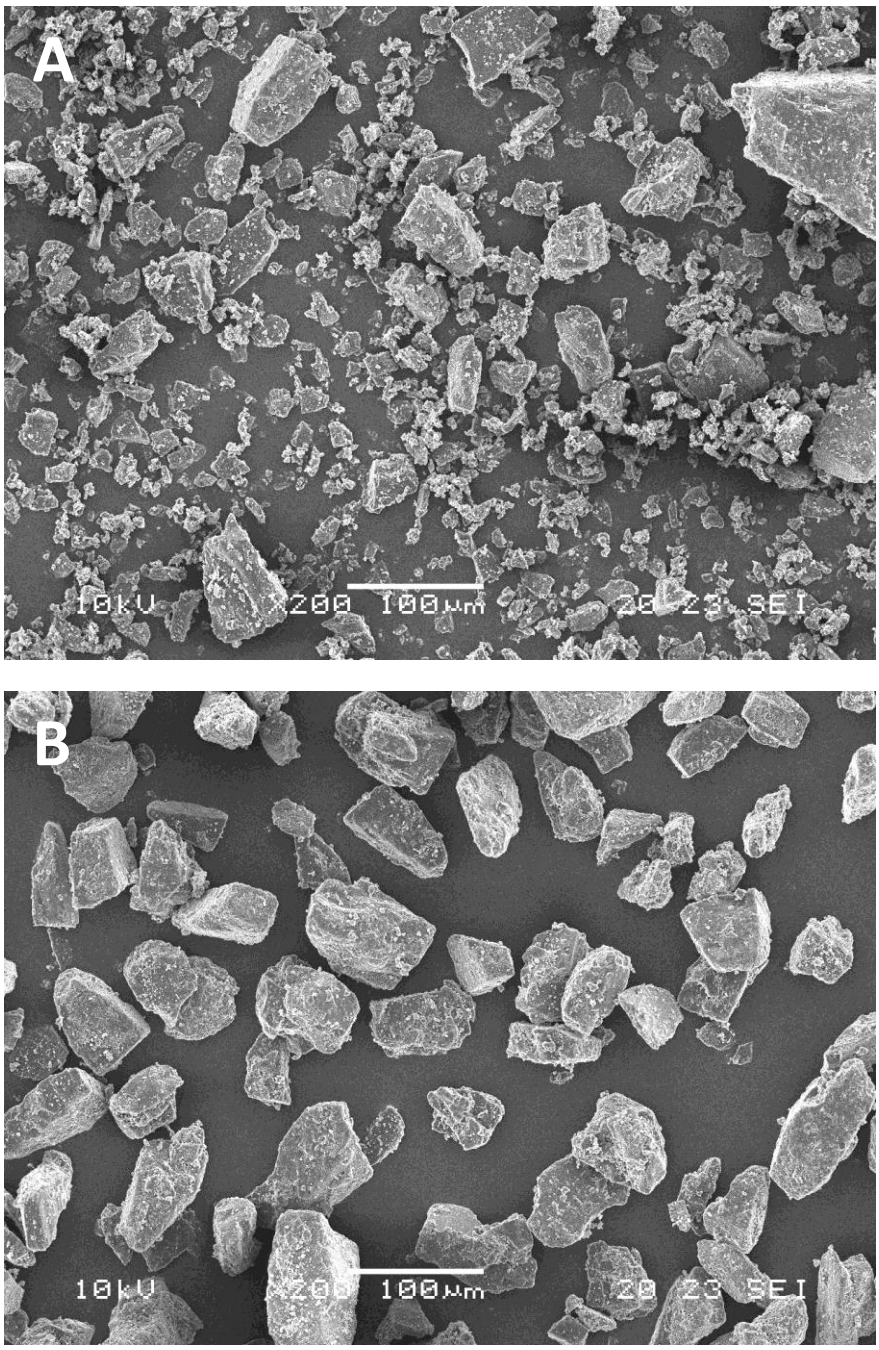

Figure 3.1 SEM Images of A, ML001 and B, SV003 grades of lactose monohydrate

3.3.3 Characterisation of rheological properties

Both grades of lactose were characterised using a FT4 Powder Rheometer (Freeman, UK) as described in Chapter 2 section 2.2.3. Identical 20 mL volumes of each grade were analysed. The values for the BFE, the conditioned bulk density (CBD), the AE at 8 m/s and the dynamic flow index (DFI) are displayed in Table 3.2. The BFE for SV003 was considerably higher than for ML001 (300.7 ± 7.5 mJ for SV003 vs 119.7 ± 12.7 mJ for ML001) indicating that the energy required to displace the SV003 particles was greater than for ML001 when the sample was not aerated. This may be understood in terms of the packing of the particles within the split vessel where owing to the increased fine particle content there is a greater amount of air within the sample for ML001 compared with SV003 and so ML001 takes less energy to displace. This is supported by the CBD data which shows that the density of the conditioned SV003 is greater than that of the ML001.

Upon aeration of the sample at 8 m/s, the AE of ML001 is greater than for SV003 (31.0 ± 3.2 mJ for ML001 vs 5.9 ± 1.1 mJ for SV003, approximately five times the difference). This is due to the fact that ML001 is a cohesive powder compared with SV003 which is relatively free flowing and is a result of ML001 having a larger particle size distribution with increased percentage of fines than SV003 where the particle size distribution is relatively narrow.

The difference in the rheological properties was why the two powders were selected for the study as one could hypothesise that a relatively free flowing, easily aeratable grade of lactose monohydrate such as SV003 might be more susceptible to triboelectrification during processes involving powder flow such as blending and filling, than a sticky, cohesive grade of lactose monohydrate such as ML001.

	BFE (mJ) ± S.D.	CBD (g/mL) ± S.D.	AE @ 8m/s ± S.D.	DFI ± S.D.
ML001	119.7 ± 12.7	0.56 ± 0.02	31.0 ± 3.2	5.5 ± 0.6
SV003	300.7 ± 7.5	0.67 ± 0.01	5.9 ± 1.1	60.9 ± 12.4

Table 3.2 Rheological properties of ML001 and SV003 (n=3, mean ± SD)

3.3.4 Sieving

Samples of ML001 and SV003 were passed through sieves of different mesh size directly into a Faraday pail and the charge/mass ratio of the samples was recorded. The results are illustrated in Table 3.3.

	Charge/Mass Ratio (nC/g) ± S.D.	
Mesh Diameter (μm)	ML001	SV003
90	-54.99 ± 2.99	-9.65 ± 1.86
125	-19.22 ± 5.32	-3.55 ± 0.15
180	-16.84 ± 2.21	-1.34 ± 0.35
212	-7.85 ± 0.44	-1.35 ± 0.14
250	-6.11 ± 0.98	-1.66 ± 0.06
355	-0.99 ± 0.52	-0.44 ± 0.02
500	-1.48 ± 0.24	-0.33 ± 0.04
850	-0.67 ± 0.12	-0.10 ± 0.02
1000	-1.20 ± 0.38	-0.11 ± 0.02

Table 3.3 Triboelectrification of ML001 and SV003 during sieving (n=3, mean ± SD)

These data show that as the mesh diameter of the sieve decreases, the extent of particle triboelectrification increases for both grades of lactose monohydrate. This is illustrated in Figure 3.2 for A, ML001, B, SV003 and C, a comparison of both grades of lactose monohydrate.

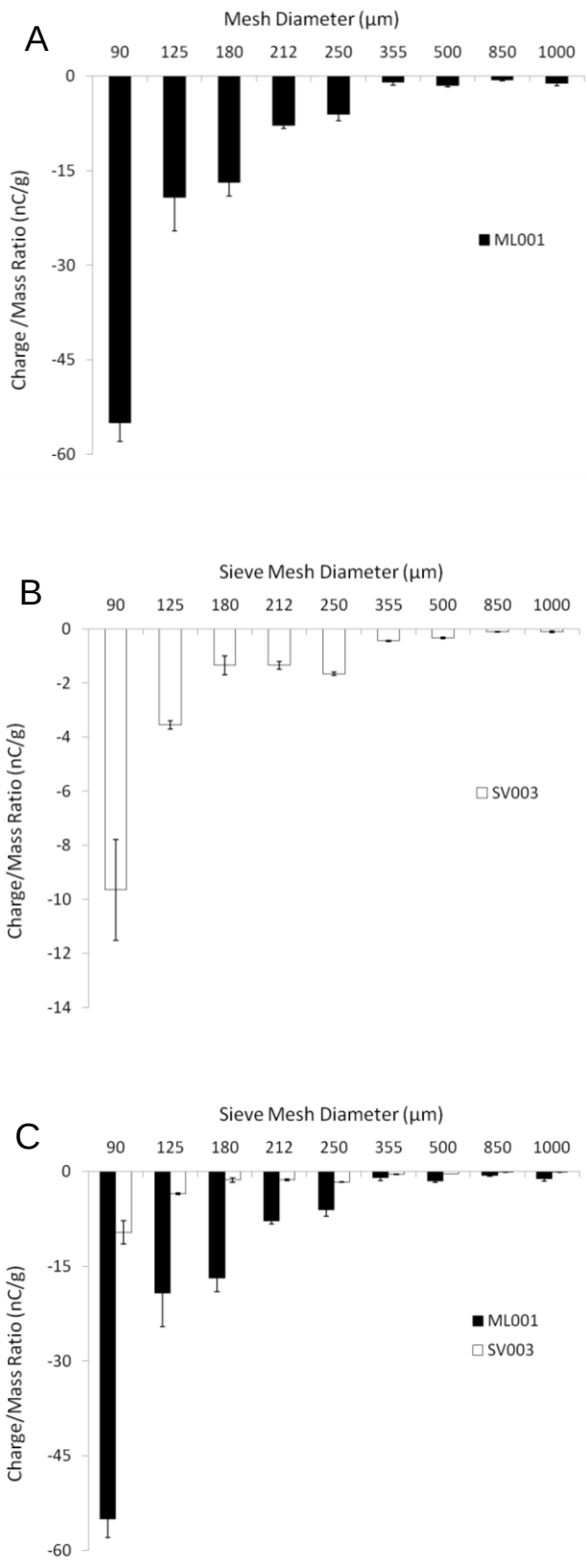

Figure 3.2 Sieving A, ML001, B, SV003 with different mesh sizes and C, a comparison

The extent of particle triboelectrification was greater for ML001 than for SV003 (e.g. average charge/mass ratio of ML001 was -54.99 ± 2.99 nC/g vs -9.65 ± 1.86 nC/g for SV003 when passed through a mesh size of 90μm). The possible reason for this may relate to the free flowing nature of SV003 which requires minimum agitation from the stainless steel scraper to be passed through the sieve due to the minimum agglomerate formation of the lactose monohydrate powder due to its low cohesive nature. Secondly, the d_{90} for ML001 is greater than for SV003 (153.92 ± 1.89 μm for ML001 vs 91.35 ± 1.81 μm for SV003). Therefore, larger particles are present in ML001 and as such, more particles will come into closer proximity with the sieve mesh resulting in a greater quantity of stainless steel – lactose contacts and thus a larger negative net charge generated on the powder. In addition, there are more fine particles in ML001, resulting in a larger surface area to mass ratio than for SV003 and therefore more particle surface area which is available to become tribocharged for ML001 than for SV003.

3.3.5 Net charge method development

Net charge measurements of powder samples are notoriously difficult to accomplish and are susceptible to a large amount of error due to a variety of factors which are sometimes difficult to control (Harper 1967). Therefore, a reliable method to measure the net charge on powder samples *in situ* seems advantageous as the majority of methods involving a Faraday pail involve displacement of the powder from its surroundings which may lead to additional triboelectrification and hence unreliable, unrepeatable measurements which are likely to be operator dependent. The easiest way to move DPI formulations into a Faraday pail is by pouring however, as the particles slide over the container surface they become tribocharged (Murtomaa *et al*. 2002) which will alter the charge on the sample before it is measured. A number of different methods were therefore developed in an attempt to measure the net charge of both ML001 and SV003 grades of lactose monohydrate, as received, without any prior processing. As the powder had not been processed it was expected that charge values recorded should be zero or close to zero. A summary of the data generated for each method is displayed in Table 3.4. Twenty measurements were taken per variable of differing masses of powder up to values of 2.50 grams. It should be noted that the operator wore a conductive wristband connected to earth to prevent unintentional charging of any equipment and the temperature and humidity was recorded during all experiments.

	Charge/Mass Ratio (nC/g) ± S.D.	
Measurement Method	ML001	SV003
Direct Pour	-0.021 ± 0.04	-9.65 ± 1.86
Modified Spatula	-0.393 ± 0.18	-3.55 ± 0.15
Modified Spatula (Earthed)	-0.500 ± 0.16	-1.34 ± 0.35
Polyethylene Scoop	0.887 ± 1.22	-1.35 ± 0.14
Polyethylene Scoop (Earthed)	0.783 ± 0.78	-1.66 ± 0.06
1st Generation Powder Ladle	-0.151 ± 0.06	-0.44 ± 0.02
1st Generation Powder Ladle (Earthed)	-0.146 ± 0.07	-0.33 ± 0.04
2nd Generation Powder Ladle	0.003 ± 0.01	0.005 ± 0.02
2nd Generation Powder Ladle (Earthed)	0.002 ± 0.01	0.001 ± 0.03
3rd Generation Powder Ladle	-0.004 ± 0.01	0.044 ± 0.03
3rd Generation Powder Ladle (Earthed)	0.003 ± 0.01	0.013 ± 0.07
4th Generation Powder Ladle	0.012 ± 0.01	0.007 ± 0.01

Table 3.4 Summary of charge/mass ratios recorded for ML001 and SV003 as received using a range of different methods (n=20 ± S.D)

The average values for the charge/mass ratio of the samples are displayed graphically in Figures 3.3 to 3.14. Single point measurements are shown as in some cases both positive and negative values for the net charge were recorded from the same sample using the same test method.

3.3.5.1 Direct pouring of lactose monohydrate

The first method employed involved pouring small quantities of lactose directly from polythene bags and into the Faraday pail as received. The data is displayed graphically in Figure 3.3.

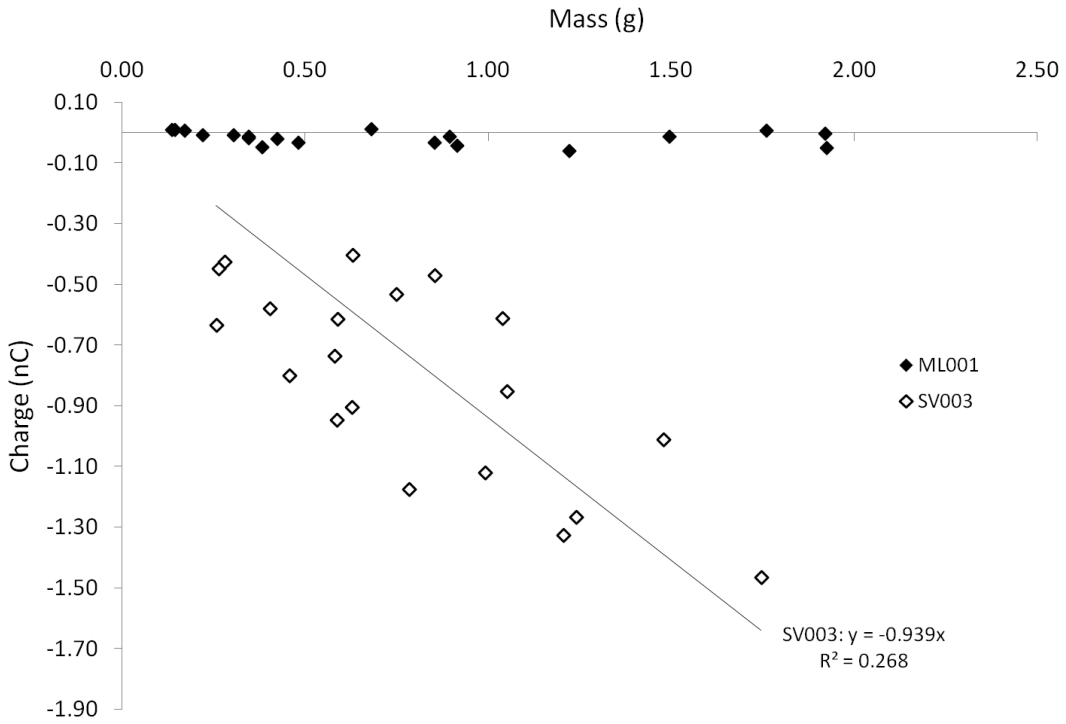

Figure 3.3 Pouring lactose samples straight from polythene bag

The results show that for ML001, the charge density values recorded were relatively low (average -0.021 ± 0.04 nC/g) and did not increase greatly with mass. In contrast for SV003, the samples recorded exhibited a net negative charge in all case and the charge density increased with increased mass, however, the linear correlation was poor (R^2 = 0.2683). It was observed that for ML001, which is a cohesive powder (Emery *et al*. 2009), once the powder approached the edge of the bag, it fractured roughly and detached from itself before falling into the Faraday pail and there was minimal sliding across the polythene surface. For SV003 which is a relatively free flowing powder (Chen *et al*. 2012) the majority of particles which fell into the Faraday pail had slid across the surface of the polythene and as such had become negatively charged. This effect was also observed by Murtomaa *et al*. who recorded the extent of triboelectrification of lactose monohydrate while flowing through a polypropylene pipe and into a Faraday pail (Murtomaa *et al*. 2002).

3.3.5.2 Modified stainless steel spatula

The next method developed involved the use of a stainless steel spatula. The leading edge of the spatula was bent upwards in an attempt to prevent powder from sliding over the metal surface. The spatula was placed into the bag of lactose monohydrate and a large heap of powder was removed. The spatula was then placed over the top of the Faraday pail and was then gently tapped so that only powder fell from the top of the heap into the well. The experiment was performed both A without and B with an earthing cable attached to the spatula and the results are displayed in Figure 3.4.

In all cases the values calculated for the net charge density were negative. For both ML001 and SV003 as the mass of powder measured increased, the net charge on the sample increased. For ML001 the correlation between charge and mass was approximately linear (R^2 values 0.802 and 0.767) for the unearthed and earthed spatula, respectively, however, for SV003 the correlation was poor (R^2 values 0.281 and 0.071). The opposite trend was observed as for pouring in that when ML001 was placed on the spatula, the spatula had to be tilted considerable before any lactose monohydrate would fall into the well and the mechanism by which involved a fracture of the bulk powder mass which then came into contact with the sides of the spatula. For SV003, particles of lactose monohydrate fell from the top of the powder heap more freely and hence less came into contact with the metal surface. The operator observed that the spatula was not a suitable method for transferring powder to the Faraday pail as powder falling into the Faraday pail over the surface of the spatula resulted in net negative charge being generated on the powder for both ML001 and SV003.

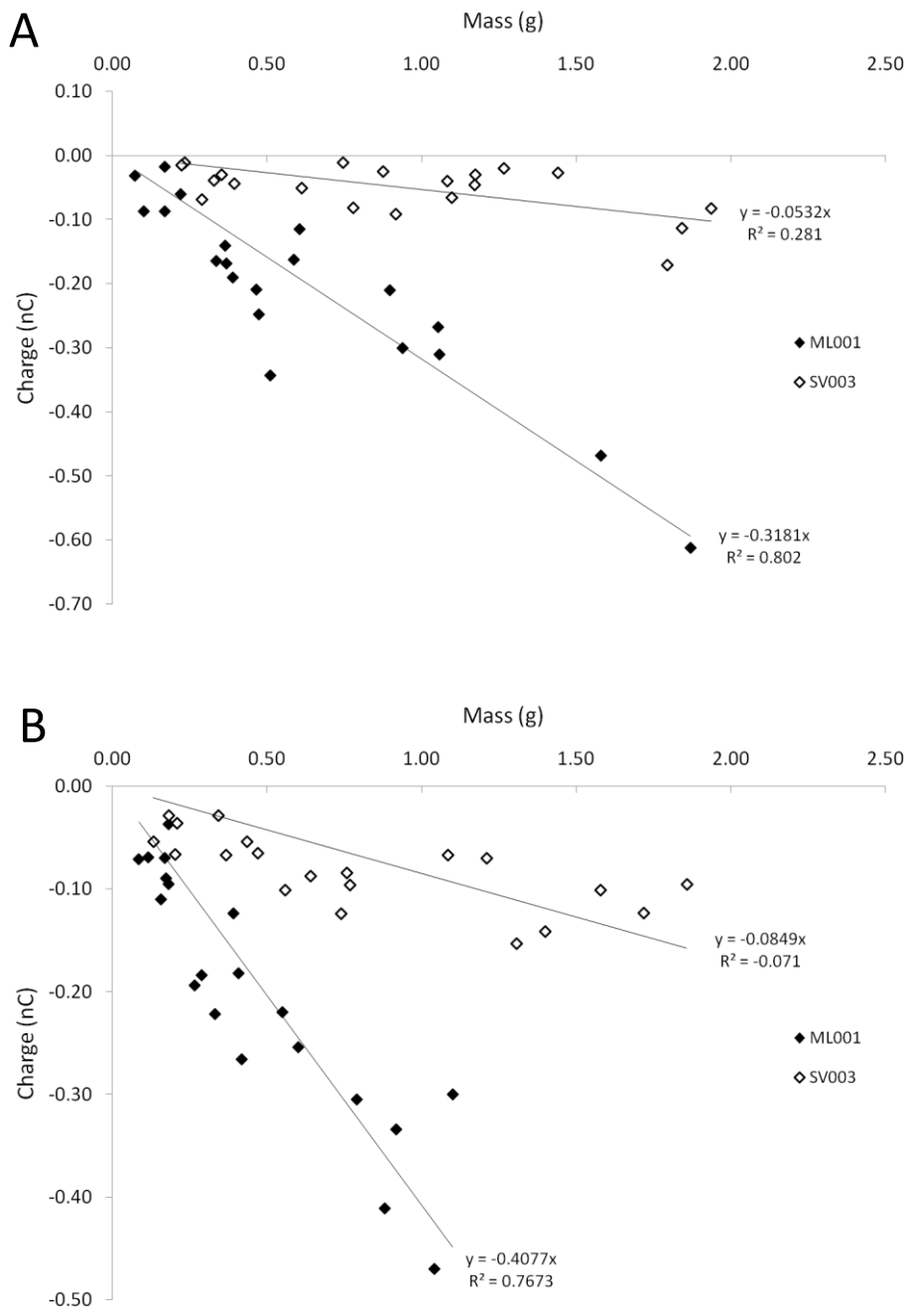

Figure 3.4 Using a modified spatula to perform net charge measurements A, without and B, with an earthing cable

3.3.5.3 Polyethylene scoop

The next method employed was to use an improvised polyethylene scoop made from a polypropylene weighing boat to see if any differences could be observed when using a polyethylene material rather than metal. The results are displayed in Figure 3.5 and

show a high level of variability and so identifying trends in the results is difficult. However, it was shown that ML001 was observed to have net positive charge and SV003 net negative charge. The high variability in the results may be partly attributed to operator error as it was difficult to pour powder into the Faraday pail in a repeatable way. Thus this method was deemed to be inappropriate for further development.

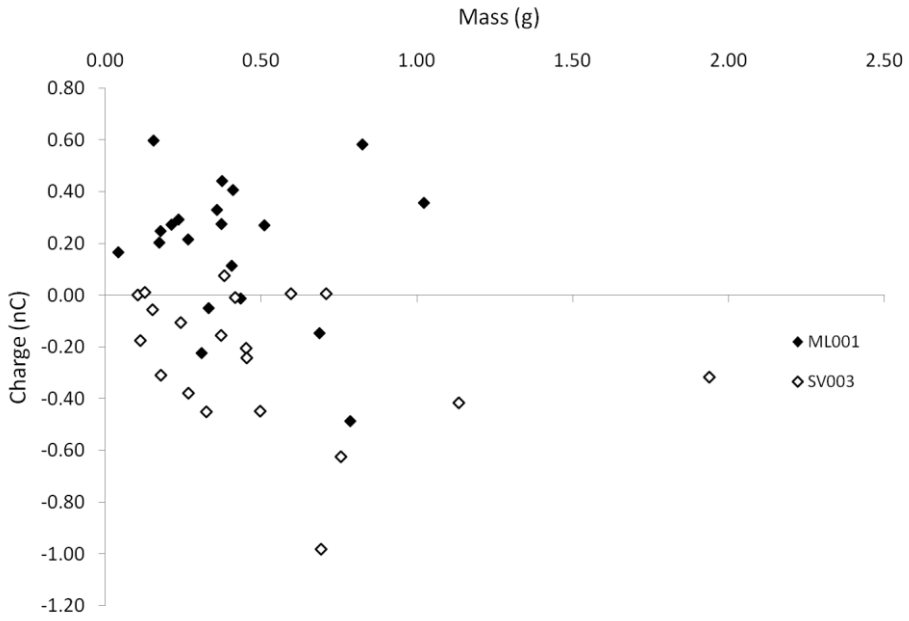

Figure 3.5 Using a polyethylene scoop to perform net charge measurements of ML001 and SV003

3.3.5.4 Development and optimisation of a powder ladle

From the first two sets of data it became apparent that any powder sliding over a surface when being transferred into the Faraday pail had the potential to be tribocharged and hence could affect the reliability of the results. As such a novel method was envisaged using a bespoke powder ladle. The criteria for the ladle was that it must be small enough to fit into the appropriate receptacle such as a polyethylene bag or blending vessel and that any powder being transferred to the Faraday pail had not been in contact with any surface of the ladle. Heaping powder onto the ladle during a scooping process and subsequently tilting the ladle over the Faraday pail, such that only particles from the top of the heap could fall into the well should result in accurate results being generated.

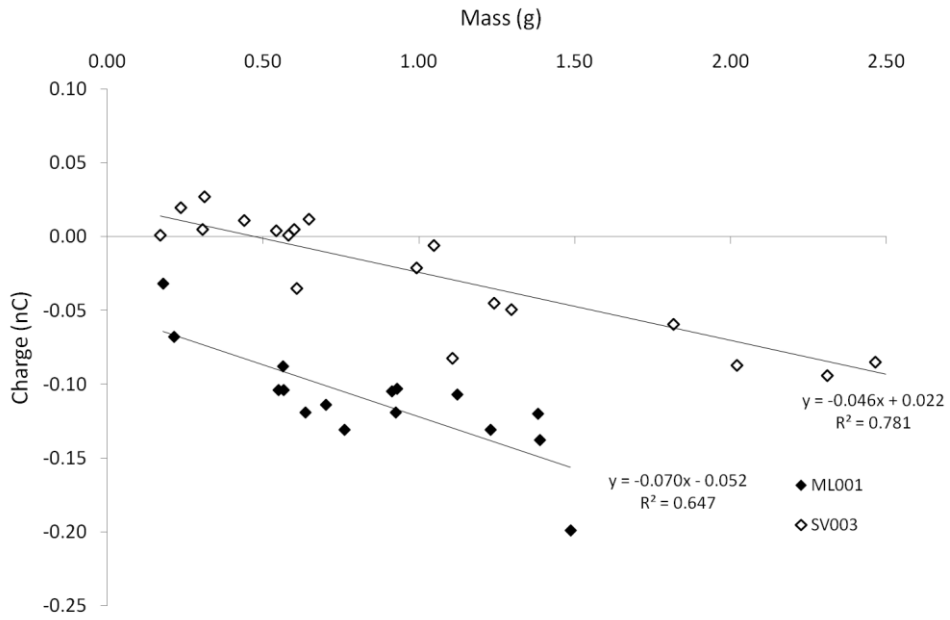

Figure 3.6 Net charge measurements using the first generation powder ladle A, without and B, with an earthing cable

For clarity, only values of the net charge recorded with SV003 for sample masses below 1.2 grams are displayed in Figure 3.6 for A, the unearthed ladle and B, the earthed ladle. It was observed that for the smaller masses of SV003, the only particles that entered the Faraday pail were those from the top of the heap of lactose monohydrate as intended. In this instance only positive values for the net charge were recorded which are circled in blue in Figure 3.7. Once larger masses were measured, particles began to slide over the metal surfaces of the ladle and the net charge recorded was negative which is circled in red in Figure 3.7.

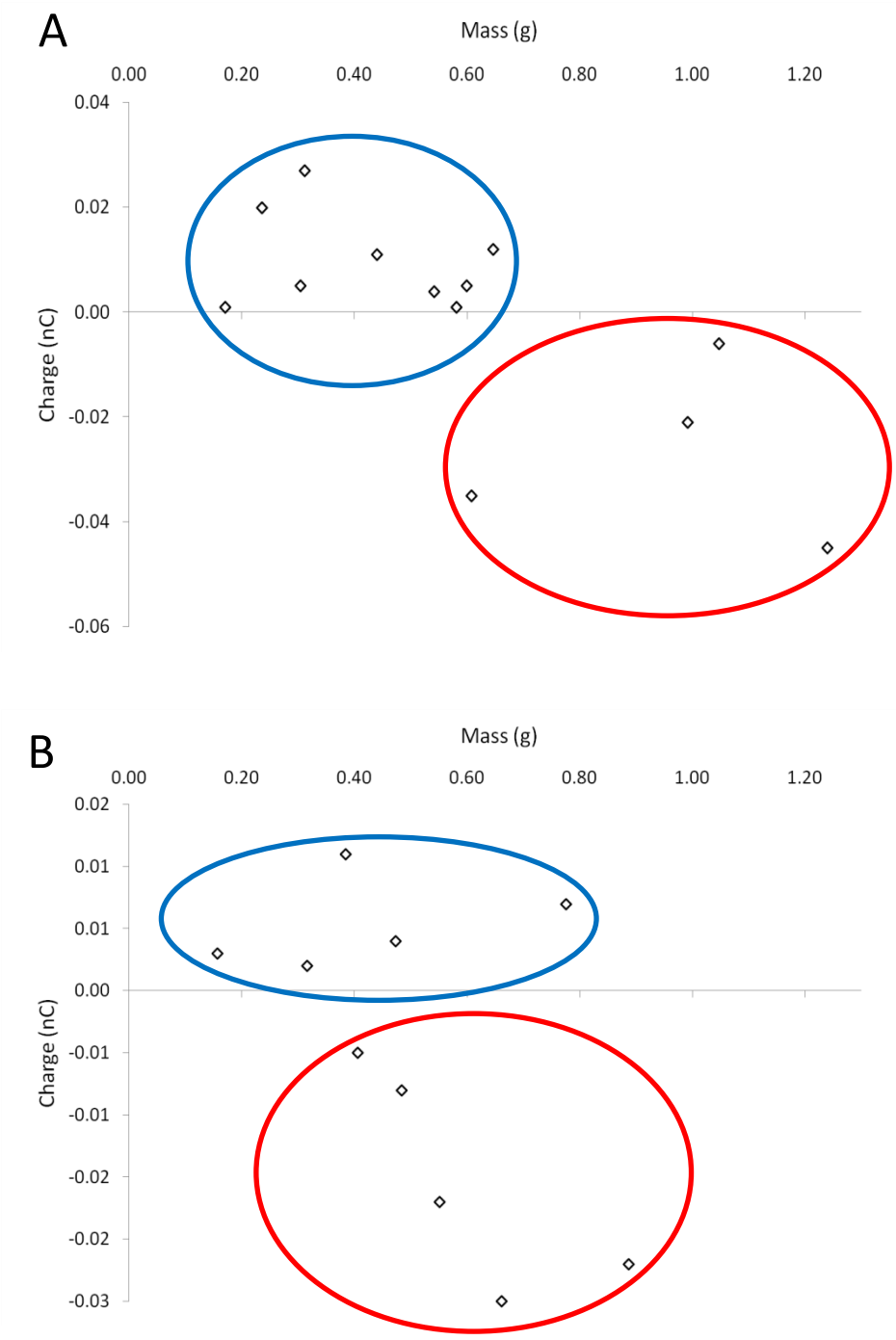

Figure 3.7 Measurements of SV003 for sample masses less than 1.2 grams with A, the unearthed and B, the earthed first generation powder ladle

To prevent any particles sliding over the metal surfaces of the ladle body, the ladle was redesigned and an image of the Second Generation Powder Ladle is displayed in Figure 3.8. Improvements included using a cylindrical handle rather than a flat one to allow powder to fall off the handle back into the measured sample rather than into the

well; narrowing the walls of the ladle body to as thin a diameter as possible (~1 mm) to prevent powder from sitting on the top edges and angling the edges of the ladle body inwards by 15 degrees to stop powder from falling out of the ladle cavity and into the Faraday pail during pouring.

Figure 3.8 Second Generation Powder Ladle

Results generated with the Second Generation Powder Ladle are displayed in Figure 3.9. A difference in the data is observed as compared with the First Generation Powder Ladle and forms of powder introduction to the Faraday pail. Rather than a propensity for the net charge recorded to become increasingly negative with increasing mass of powder, the net charge recorded appeared to be independent of the mass of the sample and was very close to zero. Additionally, in the case of both the non-earthed and earthed data, the average net charge density values calculated were positive in all cases (ML001: 0.003 ± 0.01 nC/g and 0.002 ± 0.01 nC/g, respectively; SV003 0.005 ± 0.02 nC/g and 0.001 ± 0.03 nC/g, respectively).

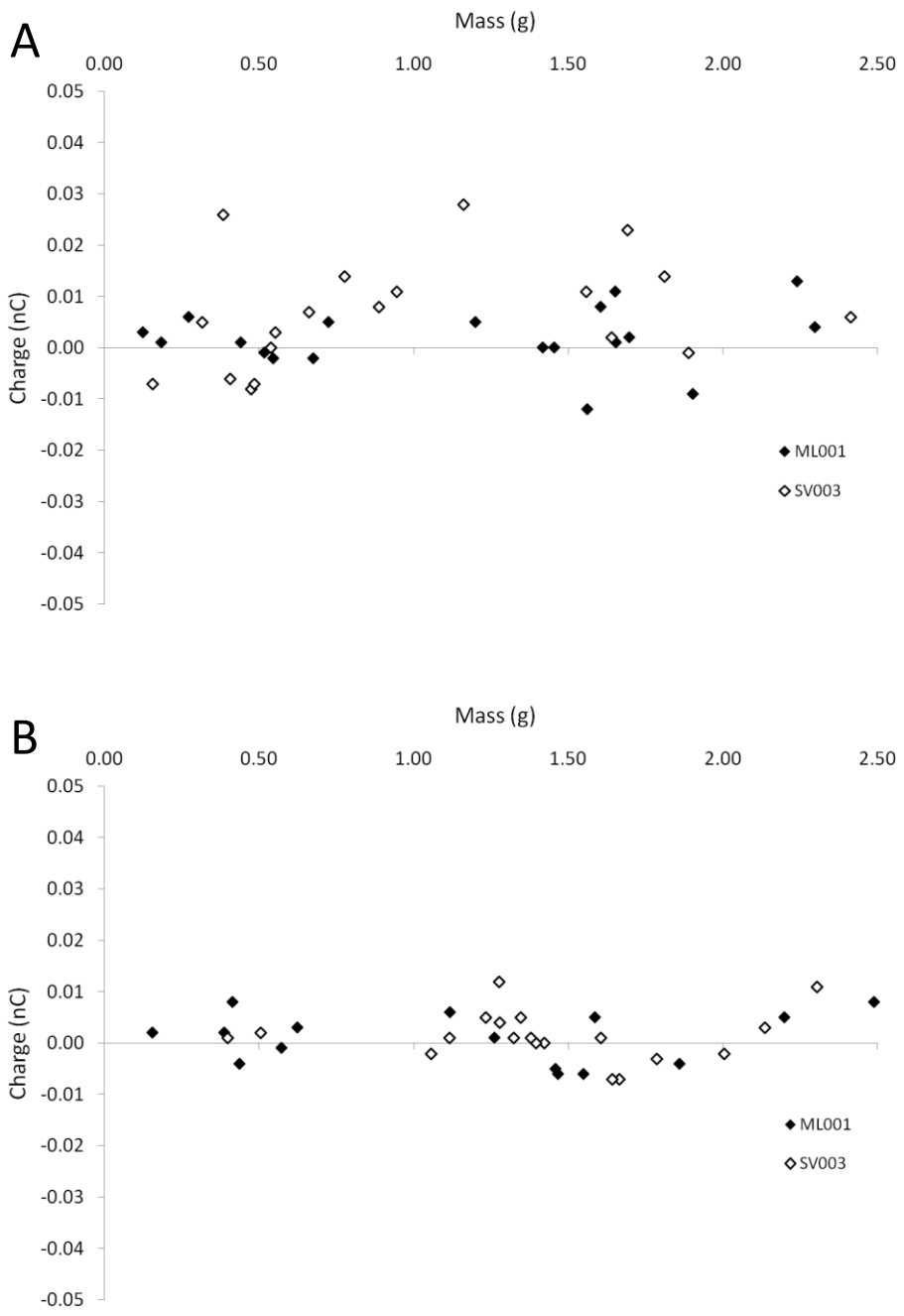

Figure 3.9 Net charge measurements using the A, unearthed and B, earthed second generation powder ladle

Despite the improvements in the design, small quantities of particles of powder were still observed to be sliding over the metal surfaces, chiefly from the handle and from the outer surfaces of the body.

The design of the ladle was further optimised as shown in Figure 3.10. Shot blasting was used to roughen the internal surfaces of the ladle to increase adherence of the

powder within the cavity. The outer surfaces of the body were highly polished to prevent powder from sticking prior to the powder transfer process. The shape of the handle was also changed from circular to triangular to further prevent powder build up on the handle.

Figure 3.10 Third Generation Powder Ladle

The results produced with the Third Generation Powder Ladle are displayed in Figure 3.11. The results, as expected, were similar with the Second Generation Powder Ladle in that the value of the charge recorded fell within a narrow range. The average values for the calculated net charge density for ML001 were similar for both the unearthed and earthed ladle and very close to zero (-0.004 ± 0.01 nC/g and 0.002 ± 0.01 nC/g, respectively). A larger average value for the net charge density for SV003 was observed for the unearthed ladle (0.044 ± 0.03 nC/g) vs the earthed ladle (0.013 ± 0.03 nC/g) and thus earthing the ladle may have contributed to increasing the accuracy of the results if the net charge density of the powder as received is assumed to be close to zero.

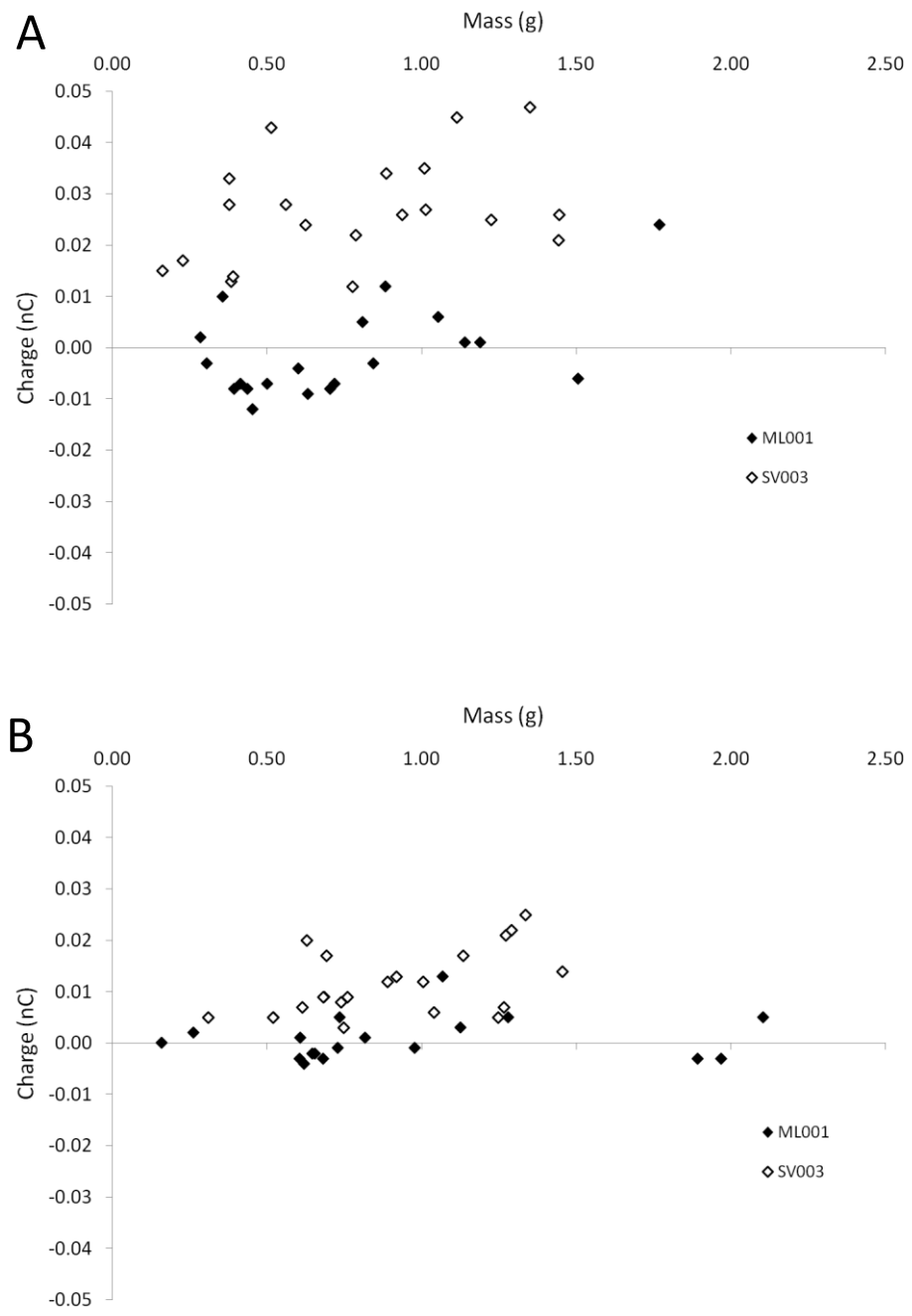

Figure 3.11 Net charge measurements using A, the unearthed and B, earthed third generation powder ladle

The Third Generation Powder Ladle led to a great reduction of variability in the net charge measurements of bulk powder samples, however, some variability was still apparent in that measurements for ML001, as received, showed both positive and negative values for the net charge density of the powder. Therefore, a Fourth Generation Powder Ladle was created by coating the Second Generation Powder Ladle with an insulative paint so as to ensure that no metal – powder contact was

made. The results are shown in Figure 3.12 and show by coating the ladle in a non-conductive material that for ML001 negative charge was prevented from being transferred from the ladle to the powder sample. This was indicated by the overall net charge measurement for the fourth generation ladle being higher than that of the third (0.012 nC/g vs 0.002 nC/g). The ladle was not earthed as attaching an earth cable to an already insulated surface would not alter the results.

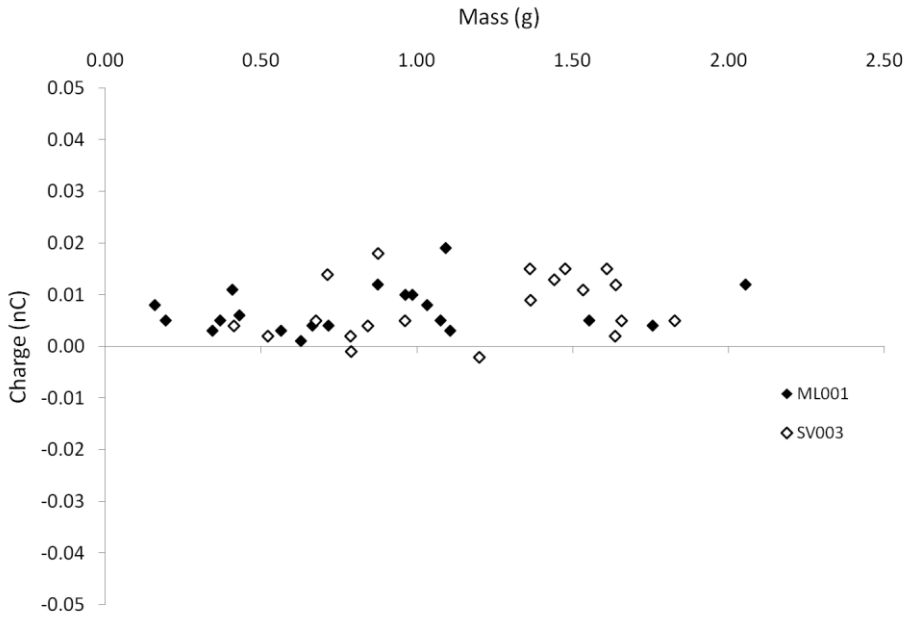

Figure 3.12 Net charge measurements using the fourth generation powder ladle

In order to show the disparity in the results generated for the First Generation and the Fourth Generation Powder Ladle, the results for both ML001 and SV003 were overlaid as shown in Figure 3.13. This figure highlights the obvious difference in measuring the net charge on a powder sample when the sample slides over a surface which frictionally tribocharges it in the case of the first generation powder ladle, or when the particles of powder fall only from the main powder body as in the case of the Third Generation Powder Ladle.

The fourth generation powder ladle method appeared to produce excellent results for the net charge measurement of the two grades of lactose monohydrate as received, preventing the sample from becoming additionally tribocharged during transfer from the bulk sample to the Faraday pail. In general, the values recorded were very small for each ladle, in the order of picoCoulombs which was to be expected as the samples had not been subjected to any charging mechanisms prior to measurement.

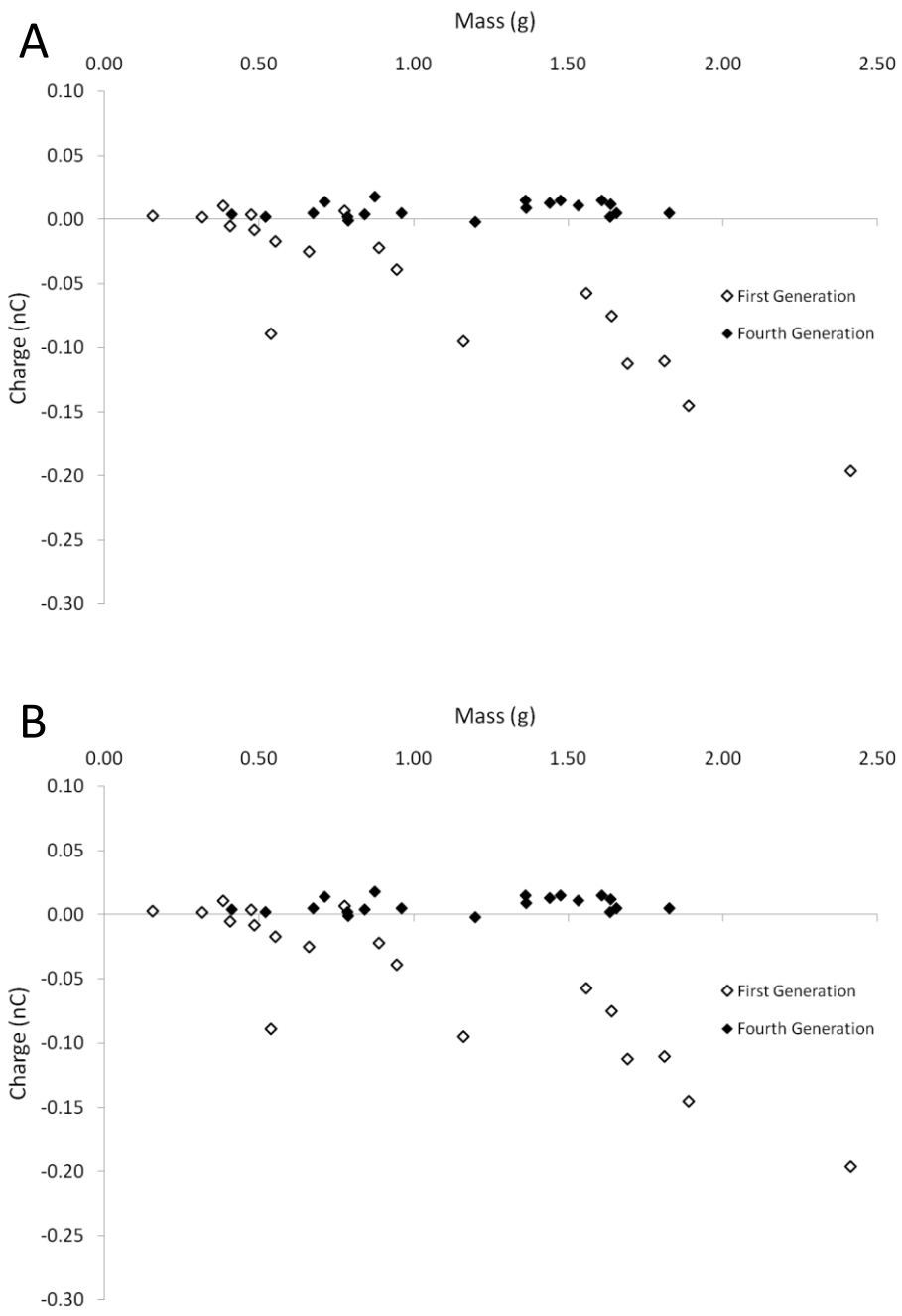

Figure 3.13 Comparison of first generation ladle (earthed) with the fourth generation ladle for A, ML001 and B, SV003

3.3.6 Low shear blending

Having developed a novel method for measuring the net charge on both ML001 and SV003 samples as received, the powder ladle method was used to measure the net charge on ML001 and SV003 post blending and the results were compared using a

traditional pouring method similar to one used previously (Adi *et al*. 2010) . Batch sizes of 80 grams were placed in 500 cm^3 vessels which were placed inside a type T2F Turbula blender. It was hypothesised that using the powder ladle post blending would be a more accurate measurement method than simply pouring as additional frictional triboelectrification of the powder samples would not occur as the powder slid against the inner wall of the mixing vessel during the pouring process. To illustrate this phenomenon, samples of lactose monohydrate were also poured directly from the various mixing vessels prior to blending. This was to illustrate that pouring tribocharges the powder samples and thus is expected to render the results of the net charge generation post blending inaccurate when using a pouring method. After transferring powder samples to the vessels, the vessels were left for one hour prior to testing to allow any charge to dissipate. The results are displayed in Table 3.5.

The results indicated that when the sample was poured out of the container prior to blending, as the powder slid over the inner surface of the vessel wall it became negatively charged via triboelectrification. The greatest extent of tribocharging occurred for the polyethylene container as this container has a greater surface roughness than either the stainless steel or glass containers.

Measurement Method	Material Container	Charge/Mass Ratio (nC/g) ± S.D.	
		ML001	SV003
Direct pour pre blending	Stainless Steel	-0.92 ± 0.16	-0.16 ± 0.02
	Polyethylene	-0.86 ± 0.26	-3.72 ± 0.29
	Glass	-0.11 ± 0.03	-0.62 ± 0.09
Direct pour post blending	Stainless Steel	-0.77 ± 0.28	-0.03 ± 0.00
	Polyethylene	-0.28 ± 0.05	0.18 ± 0.14
	Glass	0.80 ± 0.19	-0.77 ± 0.28
Powder ladle post blending	Stainless Steel	0.00 ± 0.01	0.00 ± 0.00
	Polyethylene	0.05 ± 0.01	0.01 ± 0.02
	Glass	0.00 ± 0.00	0.00 ± 0.00

Table 3.5 Net charge measurements of ML001 and SV003 pre and post blending (n=3, mean ± SD)

After blending, when samples were poured from the container directly into the Faraday pail, in all cases the total net charge either became less negative or positive compared with the samples as measured by pouring prior to blending. When the samples were measured post blending with the Foruth Generation Powder Ladle (earthed), little or no net charge was recorded for all three container materials and for both kinds of lactose monohydrate. The results of each low shear blending experiment are displayed graphically in Figure 3.14 and show charge to mass ratios of ML001 vs SV003 A, poured directly from each container without blending, B, poured from each container and C measured with the 4th generation powder ladle after blending for 20 minutes at 22 RPM.

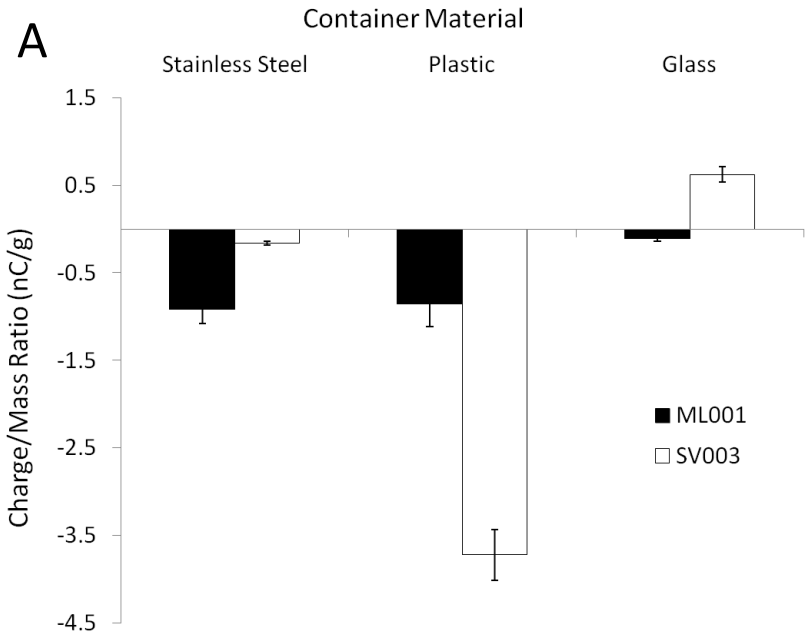

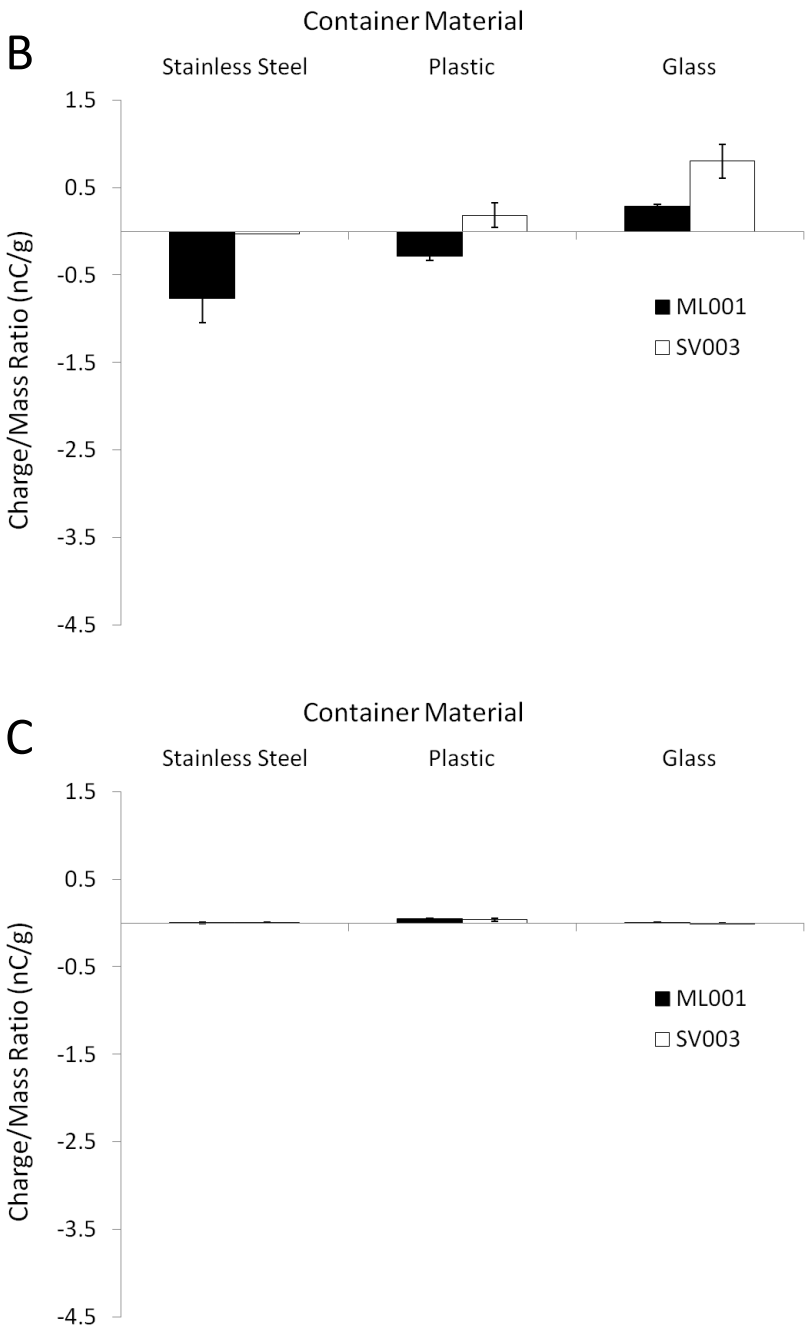

Figure 3.14 Charge to mass ratios of ML001 vs SV003 A, poured directly from each container without blending, B, poured from each container and C measured with the fourth generation powder ladle after blending for 20 minutes at 22 RPM.

These data show that by simply pouring the powder out of the container prior to blending, the powder became tribocharged. When the fourth generation powder ladle was used to measure the samples, minimal values for the net charge were recorded.

3.3.7 Low shear and high shear blending comparison – timed experiments

High shear blending is a method which can be used for manufacturing batches of DPI formulations on a large scale (Bridson *et al*. 2007). Typically, the manufacturing method is different to Turbula blending in that rather than rotating the vessel, a stainless steel impeller is lowered into the vessel and rotated in a circular direction at a much higher specified speed. A comparison was drawn between net charge generation on ML001 and SV003 post blending using the Fourth Generation Powder Ladle (earthed). 150 gram samples were blended and the net charge was recorded after each specific time point. The results are displayed in Table 3.6 and Figure 3.15 and show that in the case of low shear blending, very little charge was measured on both ML001 and SV003 post blending, regardless of the blending time.

Blending Method	Blending Time	Charge/Mass Ratio (nC/g) ± S.D.	
		ML001	SV003
Low shear (22 RPM)	1	-0.004 ± 0.002	0.001 ± 0.001
	2	-0.003 ± 0.001	-0.003 ± 0.002
	5	-0.001 ± 0.002	-0.002 ± 0.003
	10	-0.003 ± 0.001	-0.001 ± 0.001
	20	-0.006 ± 0.001	-0.002 ± 0.001
	30	-0.008 ± 0.007	-0.006 ± 0.001
High shear (500 RPM)	1	-0.002 ± 0.002	-0.002 ± 0.002
	2	0.003 ± 0.000	0.000 ± 0.000
	5	0.017 ± 0.006	0.001 ± 0.006
	10	0.006 ± 0.005	-0.001 ± 0.002
	20	0.028 ± 0.009	-0.005 ± 0.001
	30	0.047 ± 0.015	-0.003 ± 0.005

Table 3.6 Net charge measurements of ML001 and SV003 post low shear and high shear blending (n=3, mean ± SD)

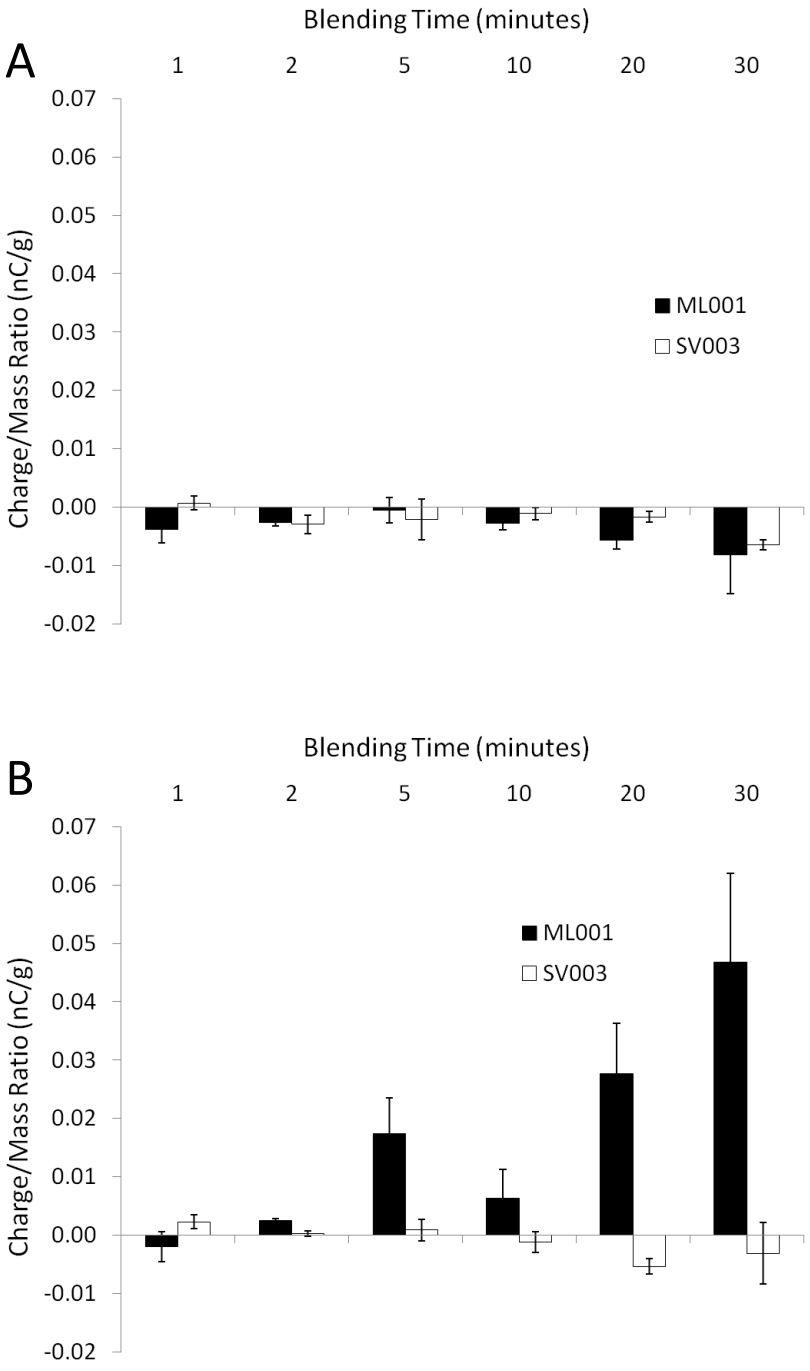

Figure 3.15 Net charge measurements of ML001 and SV003 post A, low shear and B, high shear blending.

In the case of high shear blending at 500 RPM, for SV003, the net charge measured was also very close to zero, however, for ML001 the net positive charge appeared to become slightly more positive with time up to a value of 0.047 nC ± 0.015 after 30 minutes.

After either low shear or high shear blending, minimal charge generation was detected with the powder ladle method. Elajnaf *et al*. performed static charge decay of lactose monohydrate compacts at a range of relative humidities (Elajnaf *et al*. 2007) and showed that the charge decay of lactose monohydrate was fast at the humidity range of 45 ± 5% RH used for these experiments. Sung *et al*. used a microwave-based open-reflection resonator sensor to determine the dielectric properties of microcrystalline cellulose, anhydrous lactose and α–lactose monohydrate (Sung *et al*. 2011). They showed that moisture content in lactose as well the crystal structure has an effect on the electrical permittivity which in turn will affect the ability of lactose to become statically charged. Although the resistivity of lactose monohydrate is high compared with a conductor such as stainless steel, it is lower than that of an insulator such as polytetrafluoroethylene (PTFE). This theory is supported by the fact that the net charge measurements of ML001 and SV003 were larger with an earthing cable attached to the ladle than without. As such it is possible that the charge on the lactose monohydrate generated after both low and high shear blending dissipated too quickly to be measured by the ladle.

3.4 Conclusions

Experiments have been conducted to assess various techniques of measuring the net charge on two pharmaceutical inhalation grades of lactose monohydrate with differing rheological properties. Upon sieving through different mesh sizes, ML001, which is a milled, cohesive grade of lactose monohydrate with a high percentage of fines, became more statically charged than SV003 which is a free-flowing, sieved grade of lactose monohydrate with a narrower particle size distribution. SV003 required minimal agitation to be passed through each stainless steel sieve and so the net charge build up on the lactose monohydrate particles was lower.

A number of different methodologies were employed to investigate the net charge density of ML001 and SV003 grades of lactose monohydrate as received using a Faraday pail. It was shown that simply pouring the powder from the polythene bag was enough to tribocharge the powder. In addition, any method of powder transfer to the Faraday pail which involved particles sliding over a surface was enough to tribocharge the sample and thus affects the validity of the results. A powder ladle was designed and subsequently optimised so that the only particles which fell into the Faraday pail had slid from off the top of the heap of other particles. This appeared to generate

accurate, reliable and repeatable results which are notoriously difficult to accomplish in the case of bulk powder electrostatic measurements.

The powder ladle method was then used to measure both ML001 and SV003 after blending with a type T2F lower shear Turbula blender and with a Niro Microgral high shear blender. The results showed that when samples were measured with the ladle, little to no appreciable net charge accumulation on either grade of lactose monohydrate was detected, for low shear blending, independent of container material. In the case of high shear blending a slight accumulation of positive charge was observed for ML001, however, the amount was not appreciable. It is possible that the charge on the sample dissipated during the measurement process as a result of humidity in the environment. An alternative suggestion is that the surfaces of the blending vessels became coated with charged lactose monohydrate particles during blending which may have protected additional lactose monohydrate particles from being tribocharged.

Future experiments could look at the addition of an API to lactose monohydrate to determine whether the API particles become significantly more charged than the lactose monohydrate particles during sieving and blending procedures. Additionally, performing static charge decay experiments on lactose monohydrate and API particles would determine whether the rate of charge decay is too fast for accurate measurements to be performed with the powder ladle method.

Chapter 4 The Effect of Relative Humidity on the Static Charge Decay Properties of DPI Formulations

4.1 Introduction

DPI formulations are susceptible to being electrostatically charged via the mechanism of triboelectrification (Ireland 2010a). This may occur during formulation and processing of the lactose-API blends and upon aerosolisation of the formulation within an inhaler (Bennett *et al*. 1999). The extent to which a DPI formulation will become statically charged is dependent on the type of the collisions the particles that a DPI formulation experiences during blending and filling. These may be governed by a large number of variables including the electrical and physico-chemical properties of the API, its target dose, the flow behaviour of the coarse carrier, the frequency and energy of the collisions with surfaces, the electrical properties of these surfaces and the water vapour pressure (relative humidity) of the working environment (Kwok and Chan 2008a). If the electrostatic charges generated do not dissipate quickly, problems may occur due to weighing errors, increased agglomeration, poor flow, adhesion to container surfaces, reduced API recovery, loss of content uniformity and manual handling difficulties (Karner and Anne 2011). A fundamental understanding of the role that relative humidity plays in the build up and subsequent decay rate of static charge is thus of critical importance in the development and processing of DPI formulations.

The amount of bound surface water to a particle is highly dependent on the hydrophilic/hydrophobic properties of the API, but generally increases with increasing humidity until a sorption-desorption equilibrium is reached (Lutz and Kindersberger 2009). Adsorbed water will increase the conductivity and dielectric permittivity of the surface of a particle. This, in turn, will decrease the ability of the particle to become electrostatically charge and will increase the overall rate of charge decay (Nomura *et al*. 2003). The environmental humidity may also affect the cohesive properties of micronized drugs used in inhalation therapy (Young *et al*. 2004) and of the overall performance of a dry powder inhaler (Mackin *et al*. 1997). Berard *et al*. demonstrated using atomic force microscopy that an increase in environmental RH increased the overall adhesive forces of Zanamivir/lactose blends (Berard *et al*. 2002). Guardiola *et al*. investigated the degree of static charge build up on glass beads within a fluid bed drier with the use of an electric probe. They showed that an increase in the relative humidity resulted in a decrease in the static charge build up and adhesion of the beads to internal surfaces of the drier (Guardiola *et al*. 1996). Lutz and Kindersberger showed

a linear relationship between the surface resistivity and static charge decay times on epoxy resin insulators following the application of a positive corona charge for one minute (Lutz and Kindersberger 2009). Faster rates of static charge displacement were observed as relative humidity levels increased. Elajnaf *et al*. demonstrated that over a range of RH from 0-86% an increase in RH produced a decrease in both the electrostatic charge and adhesion of salbutamol sulphate and ipratropium bromide DPI blends during low shear turbula blending (Elajnaf *et al*. 2006). Chow *et al*. performed static and dynamic charge measurements of lactose carriers and demonstrated a linear correlation between static charge build up and the humidity of the environment (Chow *et al*. 2008). Sharma *et al*. demonstrated that an increase in RH decreased the surface resistivity of acrylic polymer powders (Sharma *et al*. 2003). Grosvenor and Staniforth manufactured compacts of selected commonly used pharmaceutical excipients and demonstrated that static charge decay rates were dependent on the material's electrical resistivity, with the greater the resistivity, the longer the decay time. They also determined that by conditioning the compacts with water the resistivities were reduced, resulting in a dramatic reduction in charge decay times (Grosvenor and Staniforth 1996).

This study investigates the effect of relative humidity and API concentration on the susceptibility of a DPI formulation to become electrostatically charged and the subsequent rate of charge decay. The study also seeks to determine the effect of vessel container material on the extent of triboelectrification of a DPI formulation during low shear turbula blending and its subsequent rate of charge decay.

4.2 Materials and methods

4.2.1 Materials

Micronised fluticasone propionate was supplied by Chemagis Ltd (Bnei Brak, Israel) and micronised budesonide supplied by Farmabios (Perugia, Italy). Respitose® ML001 and Respitose® SV010 grades of lactose were obtained from DFE Pharma (Veghel, The Netherlands). Prior to use the samples were stored in a sealed humidity cabinet with a saturated salt solution of potassium carbonate (Fisher Bioreagents, NJ, USA) at 43% relative humidity in an air conditioned room maintained at 20 ± 2ºC. All solvents used were of HPLC grade (Sigma-Aldrich, St. Louis, MO, USA). Ultra pure water was

produced by reverse osmosis (MilliQ, Milliipore, Molsheim, France). Ammonium acetate was purchased from Sigma Life Sciences (St. Louis, MO, USA).

4.2.2 Methods

4.2.2.1 Dynamic vapour sorption

Dynamic vapour sorption (DVS) is a commonly used technique in the pharmaceutical industry for determining the ability of water to adsorb to the surface of an excipient or API at a definite relative humidity (Sun 2011). Moisture sorption isotherms can be used to quantify the hygroscopicity of a material over a range of relative humidity values. Measurements of the percentage change in mass are taken over a range of specified humidities, as a nitrogen carrier gas is flowed over the sample. Elajnaf *et al*. performed DVS experiments on lactose, salbutamol sulphate and ipratropium bromide and witnessed an increase in the quantity of moisture adsorbed to the sample as relative humidity increased (Elajnaf *et al*. 2007).

DVS experiments were performed with a DVS-1 instrument (Surface Measurement Systems Ltd, London, UK). 100mg of sample was weighed into a sample pan and after equilibrium with the environment has been reached; its mass was continually recorded during exposure to humidity cycles of 0-90% RH in 10% RH steps at 25°C. The rate of change of mass (dm/dt) was plotted as a function of relative humidity and an equilibrium mass change of ≤0.0005% was achieved for ten minutes before the humidity was changed to the next set point.

4.2.2.2 Manufacture of blends

Micronized budesonide and fluticasone propionate were blended with ML001 and SV010 grades of lactose to produce formulations with concentrations of 0.05%, 0.08%, 0.1%, 0.4%, 1%, 0.8% and 2% w/w, using a low shear method to produce 50g blends. Budesonide was formulated with ML001 and fluticasone with SV010. 10% of the required lactose was passed through a 250µm mesh sieve (Endicotts Ltd, UK) followed by the total required API, followed by another 10% of the required lactose to create a sandwich. This sandwich was blended for 10 minutes at 22 RPM using a type T2F Turbula Blender (WAB, Switzerland) in a sealed stainless steel vessel of capacity 250cm^3. 50% of the remaining lactose was passed through the sieve, followed by the

preblend, followed by the other 50% of the remaining lactose. The formulation was then blended at 22 RPM for an additional 20 minutes. Once blending was complete the blends were transferred to labelled polythene bags and stored in a sealed humidity cabinet with a saturated salt solution of potassium carbonate (Fisher Bioreagents, NJ, USA) at 43% relative humidity in an air conditioned room maintained at 20 ± 2ºC. Each blend was left in storage for a minimum of one week to allow any electrostatic charge present to dissipate.

4.2.2.3 Assay and content uniformity

Assay and content uniformity analysis was performed to determine the API recovery and homogeneity of each blend and was measured using reverse phase high performance liquid chromatography (RP-HPLC) using a UV detector (UV-975, Jasco Corporation, Japan) at a wavelength of 244nm for budesonide and 235 nm for fluticasone. Analysis was performed using an ODS Hypersil Column, 100x4mm (Thermo Scientific, Waltham, MA, USA) maintained at 40^0C using a column oven (Jasco CO-965) The mobile phase used contained 45% methanol, 35% acetonitrile and 20% distilled water (v/v). All solvents were HPLC grade (Fisher Chemical, Loughbrough, UK) and distilled water was produced by reverse osmosis (MilliQ, (18.2MΩ) Millipore, Molsheim, France). A run time of 5 minutes was used for each sample at a flow rate of 1.5 ml/min with an injection volume of 100µl per sample. The retention time of budesonide was 2.43 minutes and of fluticasone propionate was 1.95 minutes. 10 x 50mg samples of each blend were each dissolved in 100mL of mobile phase and the API content was calculated by comparison with an externally calibrated standard.

4.2.2.4 Charge decay measurements

A Charge Decay Time Analyser (CDTA) (JCI155 v6, Chilworth Technology Ltd. Southampton, UK) as shown in Figure 4.1 is an instrument used for determining the electrostatic charge decay rates of materials. The system applies a corona discharge to the surface of a sample which in turn creates a surface voltage as a result of the charge imparted. An electrostatic field meter, used for non-contact measurements of the electrostatic charge of an object, records the electrostatic field of the sample as a potential difference in Volts. The initial peak surface potential post corona charging (Vs)

is recorded as well as values for the time taken for the surface potential of the sample to decay to 10% and 1/e of the initial value.

Figure 4.1 Image of the JCI 155v6 Charge Decay Time Analyser (reproduced with permission from JCI Chilworth Ltd.)

8.50 ± 0.01 g samples of the blends were placed into weighing boats and stored at the required humidity for a minimum of 24h in a relative humidity cabinet (Safetech Climatezone, Hampshire, UK) in order to allow any charge present to dissipate and for the level of moisture adhered to the surface of the particles to equilibrate. Samples were added to the sample holder of the Charge Decay Time Analyser (CDTA) (JCI155 v6, Chilworth Technology Ltd. Southampton, UK) and the top of the powder bed was smoothed using an earthed metal scraper to produce a homogeneous surface. The intensity of the electric field on a charged material is at its maximum at its surface, decreasing inversely with the square of the distance from the surface (Bailey 1993). Maintaining the distance between the surface of the powder and the field meter is therefore necessary and achieved by maintaining a consistent amount of powder in the sample holder. Once the sample holder was placed within the CDTA it was further left to equilibrate for a minimum of 3 hours. The run settings for each test are shown in Table 4.1.

Run Settings	
Pretest Voltage (V)	≤ ±5
Corona Voltage (V)	8000
Corona Time (s)	0.03
Analysis Start (s)	0.07
Plate Speed	Slow
Temperature (°C)	20

Table 4.1 Run settings of the JCI Chilworth CDTA used for electrostatic charge decay measurements

The electrostatic field meter of the CDTA measures the surface potential difference of the sample in Volts. The surface potential difference is directly proportional to the charge of the material (Chubb 1996). Prior to the commencement of any experiment, the pretest voltage, that is the surface potential difference of the sample, was determined to be ≤5 V as recommended by JCI Chilworth. In reality, the surface potential of all samples prior to testing was ≤0.5 V. A plate is present within the equipment which protects the corona charger when the instrument is not in use. When the test starts, the plate slides open to expose the powder surface to the corona charger. The plate speed was set to “slow” so as not to disturb the powder bed during this process. The corona discharge voltage used for all experiments was set to -8000V. This was to simulate a powder sample becoming negatively charged when coming into contact with metallic surface, such as stainless steel which is commonly used as a material for pharmaceutical processing equipment. The maximum voltage which could be applied was selected in order provide the maximum differentiation possible between each sample in terms of its charge decay characteristics. The corona discharge was applied for 0.03 seconds for all samples and the analysis start time, that is, the time at which the field meter began taking readings, was 0.07 seconds after the corona discharge had stopped. The temperature was controlled within the relative humidity cabinet at 20°C for each experiment. In between samples the sample holder was washed with soapy water, rinsed thoroughly with methanol and allowed to dry for a minimum of one hour.

Once the corona discharge had been applied to the sample, the field meter detected and recorded the change in surface potential and plotted it as a function of time as shown in Figure 4.2

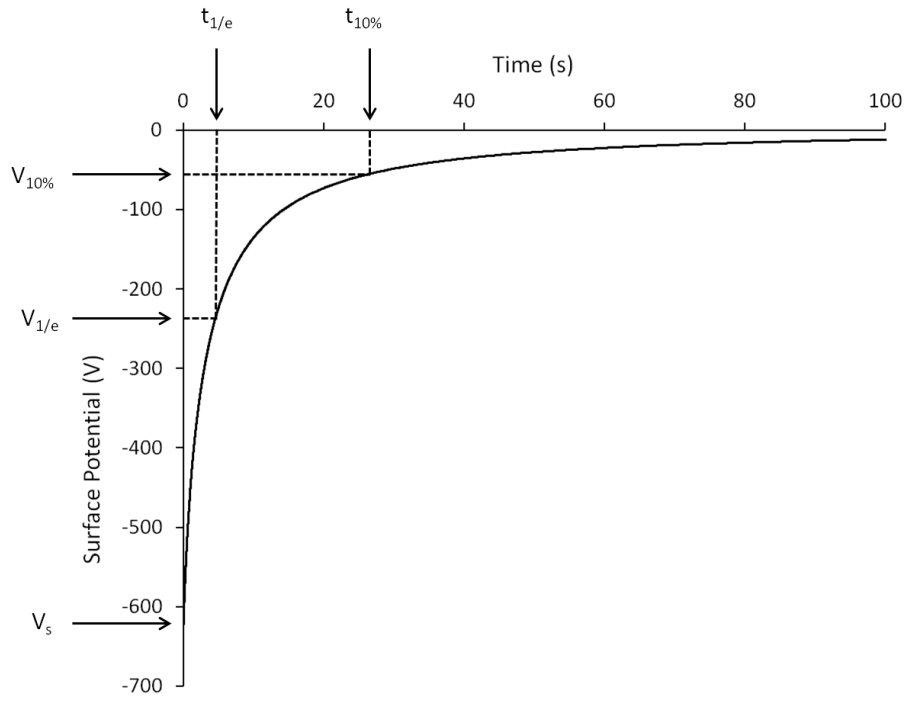

Figure 4.2 Typical surface potential verses time decay profile generated with the CDTA

The rate of charge decay is described mathematically by Equation 4.1 which shows that the charge follows an exponential relationship with time as has been experimentally determined (Chubb 1995).

$$Q = Q_0 \, e^{\frac{-1}{\tau}} \qquad \text{Equation 4.1}$$

Where Q_0 is the initial charge, Q is the charge at a set point in time after the charge decay has begun and T is the charge decay time constant of the material at that particular time.

The initial surface potential difference (Vs) was recorded as well as the time taken for the charge to dissipate to 1/e of its initial value (36.8%) and the time taken for the charge to dissipate to 10% of its initial value. Each set of blends was tested with the CDTA (n=3) at relative humidities of 35%, 55% and 75% RH. ML001 and SV010 grades of lactose as placebos were also tested for reference.

The data which was recorded by the CDTA was stored in a data buffer and results were transferred to a PC via a USB memory stick. Subsequent analysis of the data was performed using Microsoft Excel.

4.2.2.5 Blending experiments

25 gram samples of the 2% budesonide blend and 2% fluticasone blend were weighed directly into either a stainless steel or plastic vessel, approximately 250cm^3 in volume. The blend was then subjected to low shear blending using a type T2F turbula blender (WAB, Nidderau-Heldenbergen, Germany) for 20 minutes at 22 RPM within a controlled humidity cabinet at 35% RH. Once blending was complete, the sample was poured directly into the sample holder of the CDTA until a flat powder bed was achieved and the lid was closed. A charge decay time profile for the material was then plotted with no corona discharge applied to the sample. After the measurement was taken, the DPI blend was returned for further use and the blending vessel and sample holder washed with soapy water and dried with methanol. The 2% w/w API formulations were selected for the experiment as these formulations contained the highest percentage of API and therefore were predicted to undergo the greatest amount of triboelectrification.

4.3 Results and discussion

4.3.1 Dynamic vapour sorption

Dynamic vapour sorption experiments were performed on ML001, SV010, budesonide and fluticasone propionate, as shown in Figure 4.3 A-D respectively. This was undertaken to ascertain the extent of bound surface water at varying humidity, with undetectable amounts of amorphous disorder. Each material was shown to be relatively hydrophobic, with total change in mass percentages not greater than 0.3% at 90% RH for each of the samples. ML001, budesonide and fluticasone produced typical DVS adsorption isotherms, with near identical mass changes over the first and second humidity cycles.

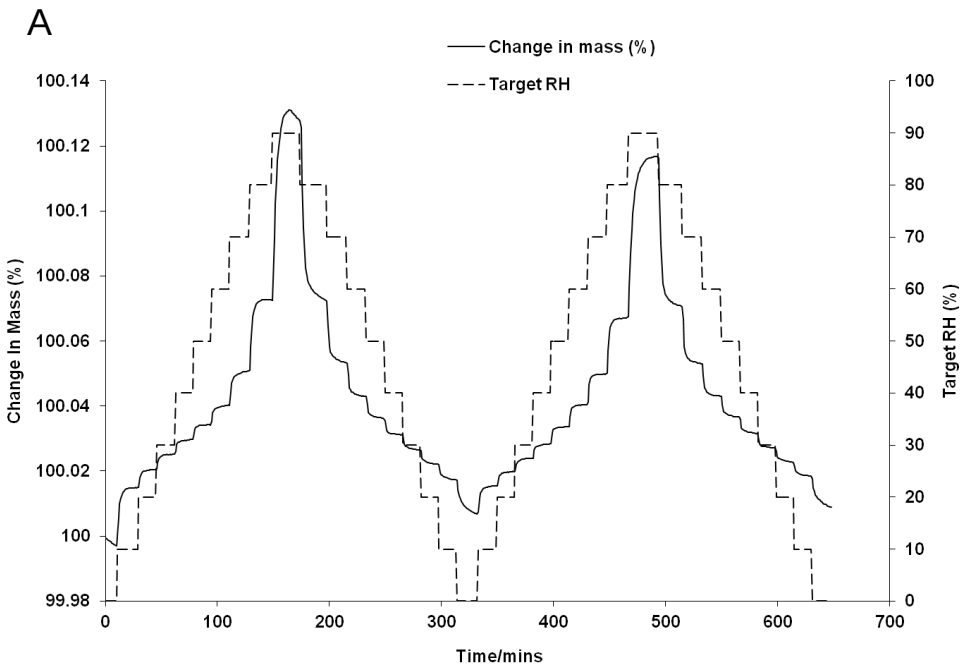

Figure 4.3 A, DVS moisture sorption plot of Respitose® ML001

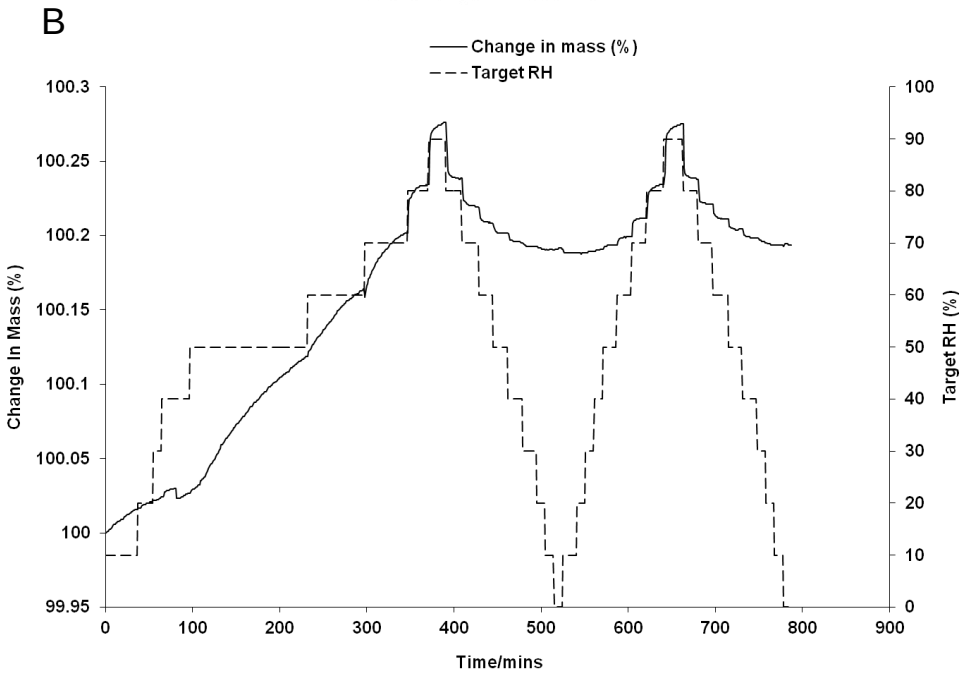

Figure 4.3 B, DVS moisture sorption plot of Respitose® SV010

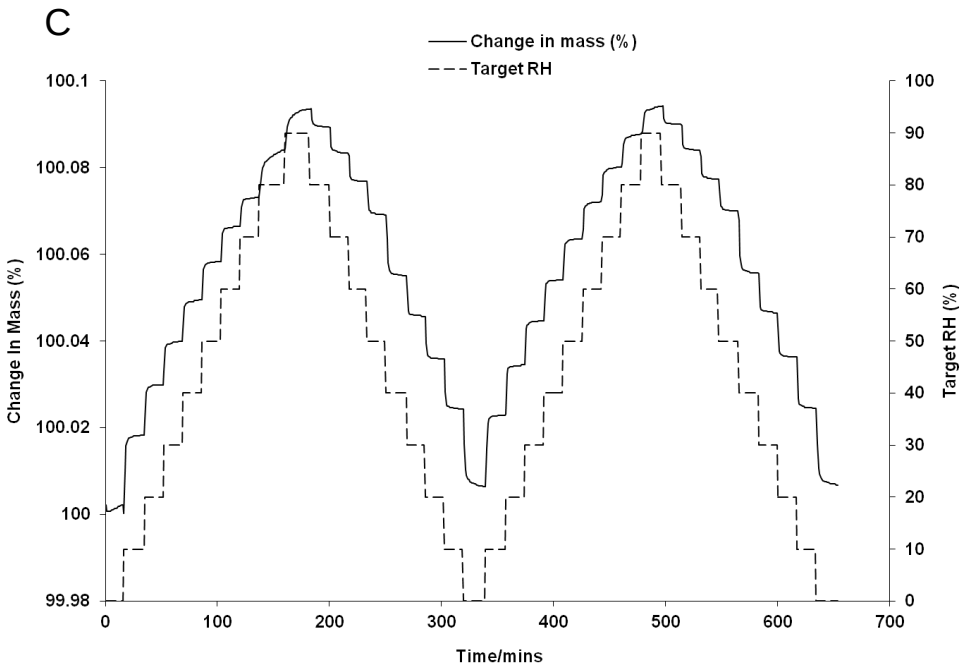

Figure 4.3 C, DVS moisture sorption plot of micronised budesonide

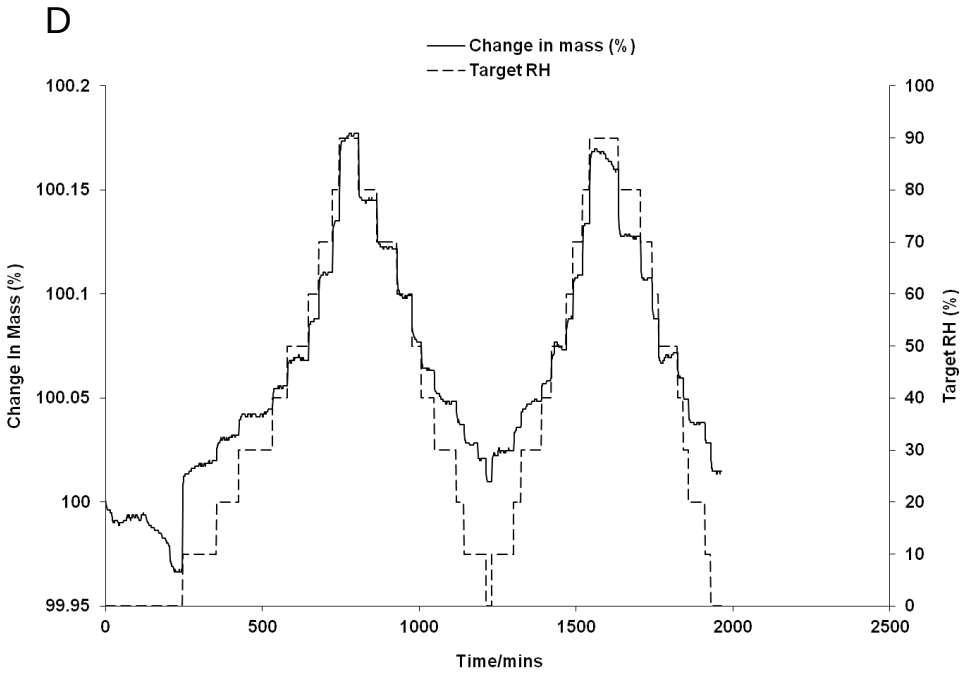

Figure 4.3 D, DVS moisture sorption plot of micronised fluticasone propionate

This indicated that increases in mass as a result of increases in relative humidity were reversible processes for each material. SV010 demonstrated a difference in behaviour between cycle 1 and cycle 2, with cycle 1 showing a greater and more variable increase in moisture as the RH increased than for cycle two. At the end of cycle 1, it was shown that an irreversible increase in moisture level of 0.2% had occurred. The reason for this is unclear, however may be due to a physical change in the lactose structure. As the SV010 blends which were used for static charge decay experiments had been equilibrated at the required humidity for a minimum of 72 hours, far greater than the length of the DVS experiment, this effect is not expected to have influenced the accuracy of the charge decay measurements. The shape of the second sorption cycle was more usual and similar in behaviour to the other samples tested.

4.3.2 Assay and content uniformity analysis

Each blend manufactured was determined to fall within the acceptable pharmacopoeia requirement for content uniformity, with an assay value of between 95-110% and relative standard deviation of ≤5%. This showed that the manufacturing process was efficient at producing homogeneously mixed DPI blends suitable for further characterisation.

4.3.3 Effect of loaded dose on the initial surface potential generated on the DPI formulations by the CDTA at varying RH

For the budesonide formulations, the initial surface potential increased as a function of API concentration for each humidity as shown in Figure 4.4 A. For API concentrations above 0.4% w/w a roughly linear correlation was observed between API concentration and initial surface potential with R^2 values of 0.900, 0.975 and 0.855 for 35%, 55% and 75% RH respectively as shown in Figure 4.4 B. At 75% RH, the only values recorded were for API concentrations of 0.4% w/w and above. Below this drug concentration, the initial surface potential was too low to be recorded by the field meter of the CDTA and result of “no peak found” was recorded.

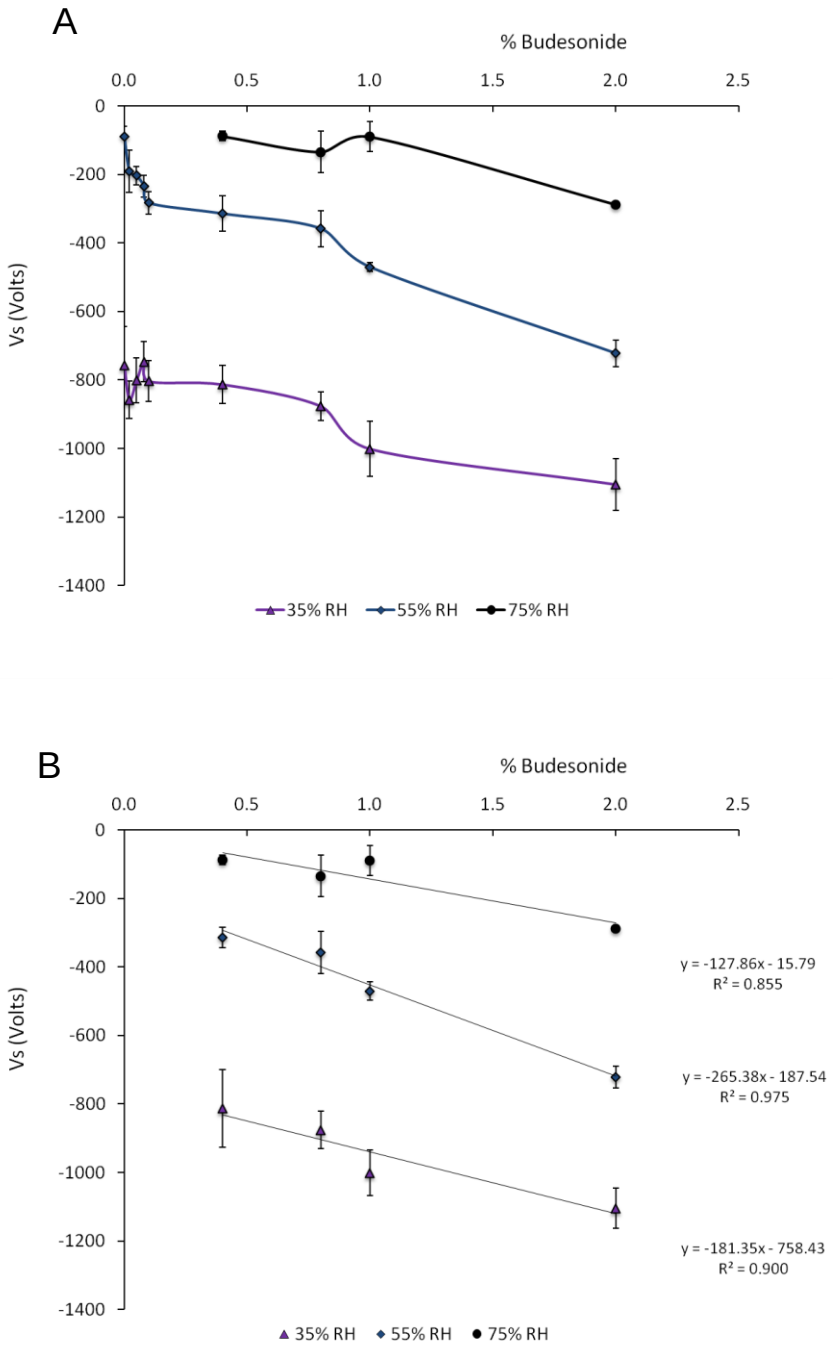

Figure 4.4 Initial surface potential plotted as a function of relative humidity for A, all budesonide concentrations and B 0.4% to 2% w/w budesonide

For the fluticasone formulations, the initial surface potential increased as a function of API concentration for each humidity as shown in Figure 4.5 A. For API concentrations above 0.4% w/w a roughly linear correlation was observed between API concentration

and initial surface potential at 35% and 55% RH with R^2 values of 0.997, 0.711 respectively. At 75% the linear correlation was poor (R^2 = 0.221) as shown in Figure 4.5 B.

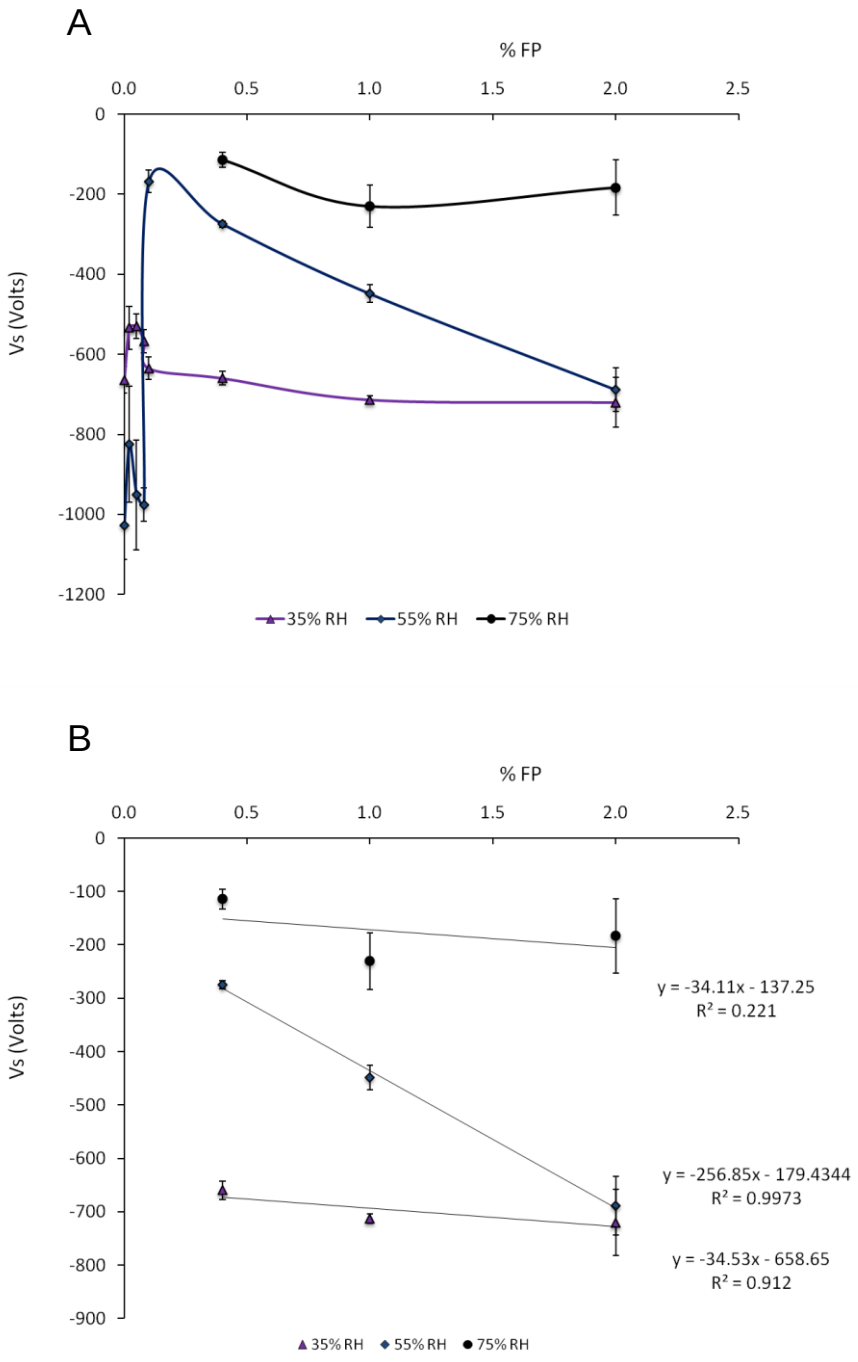

Figure 4.5 Initial surface potential plotted as a function of loaded dose for A, all fluticasone concentrations and B 0.4% to 2% w/w fluticasone

At 75% RH, the only values recorded were for API concentrations of 0.4% w/w and above. Below this concentration, the initial surface potential was too low to be recorded by the field meter of the CDTA and result of “no peak found” was recorded. The values for the initial voltage at 55% RH for fluticasone concentrations of 0%, 0.02%, 0.05% and 0.08% appear to be due to the properties of the lactose, rather than the fluticasone.

The results generated showed similar trends between the budesonide and fluticasone formulations. The lowest initial surface potentials recorded were for the lactose carriers with the values for ML001 -756.67 ± 112.65V, -89.33 ± 29.17V and 0V and for SV010 -663.83V ± 112.65V, -1027.30V ± 85.56V and 0V at 35%, 55% and 75% RH respectively (although the value for SV010 at 55%RH was determined to be an outlier). As the API concentration was increased, the initial surface potential differences increased with a linear correlation even though the mass of the sample remained constant, with the maximum values reached at an API concentration of 2%. For the 2% budesonide blends, the Time to 10% values corresponding to 35%, 55% and 75% RH were 26450.11 ± 411.95 seconds, 115.13 ± 11.95 seconds and 7.19 ± 0.24 seconds respectively and for fluticasone were 24143.28 ± 1482.08 seconds, 17546.19 ± 2270 seconds and 225.25 ± 0.59 seconds. This indicated that both budesonide and fluticasone are more electrically resistive and prone to becoming statically charged than the coarse carrier grades of lactose used to manufacture the formulations.

4.3.4 Effect of relative humidity on the initial surface potential generated on the DPI formulations by the CDTA

The initial surface potential for each budesonide concentration, plotted as a function of relative humidity is shown in Figure 4.6 A. The results indicated that as relative humidity increased the initial surface potential decreased with no values recorded for budesonide concentration below 0.4%w/w at 75% RH. For budesonide concentrations ≥ 0.4%w/w, a linear correlation was observed with R^2 values of 0.955, 0.950, 0.991 and 0.999 for concentrations of 0.4%, 0.8%, 1% and 2% budesonide, respectively, as shown in Figure 4.6 B.

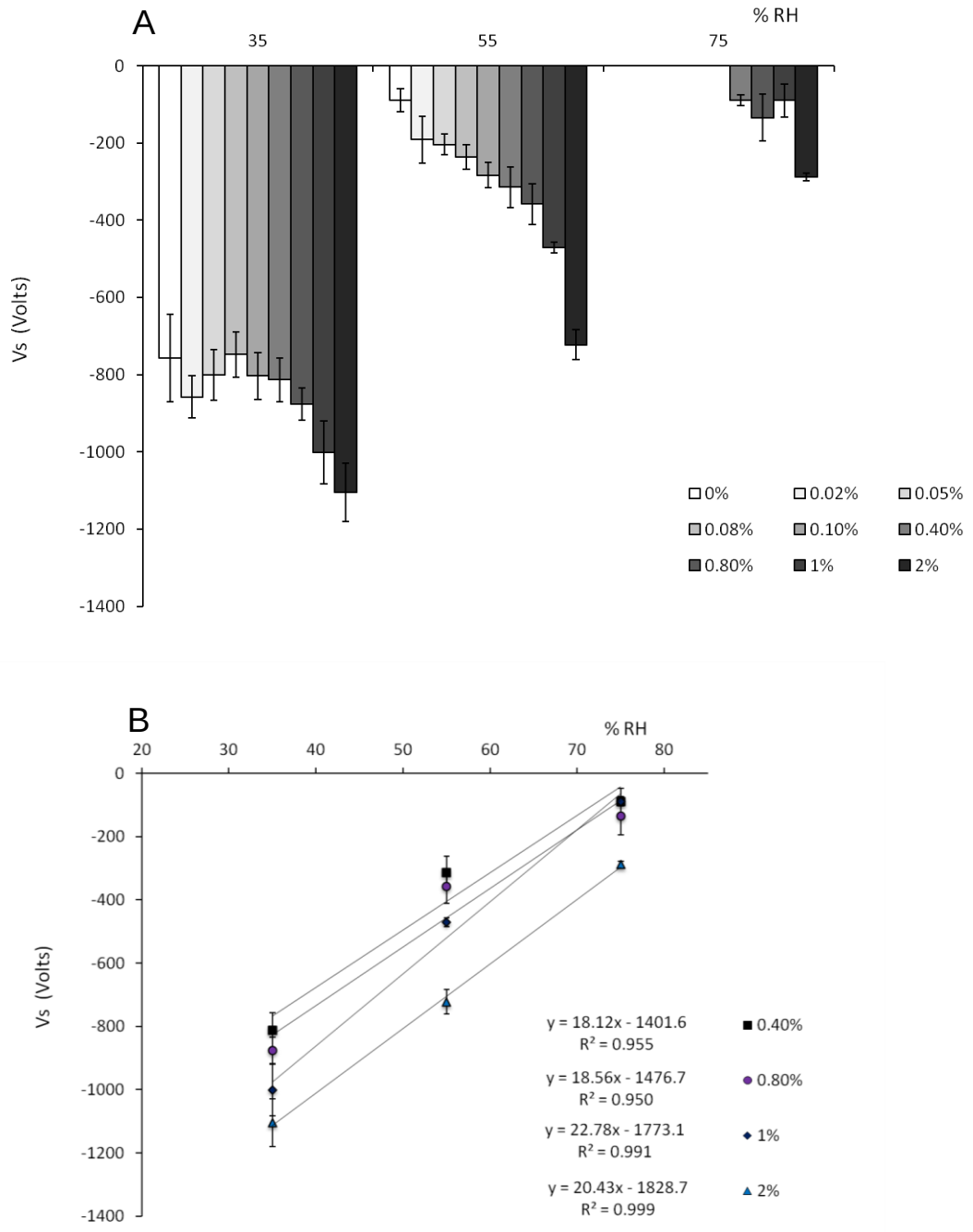

Figure 4.6 Initial surface potential plotted as a function of relative humidity for A, all budesonide concentrations and B, 0.4%-2% w/w budesonide

The initial surface potential for each fluticasone concentration, plotted as a function of relative humidity is shown in Figure 4.7 A. Excluding the values for the 0%, 0.02%, 0.05% and 0.08%w/w blends at 55% RH, the results showed that as the relative humidity increased the initial surface potential decreased with no values recorded for a fluticasone concentration of less than 0.4% at 75% RH. For fluticasone concentrations of 0.4%w/w and above, a linear correlation was observed with R^2 values of 0.947,

0.997, 0.794 for concentrations of 0.4%, 1% and 2%w/w fluticasone, respectively, as shown in Figure 4.7 B.

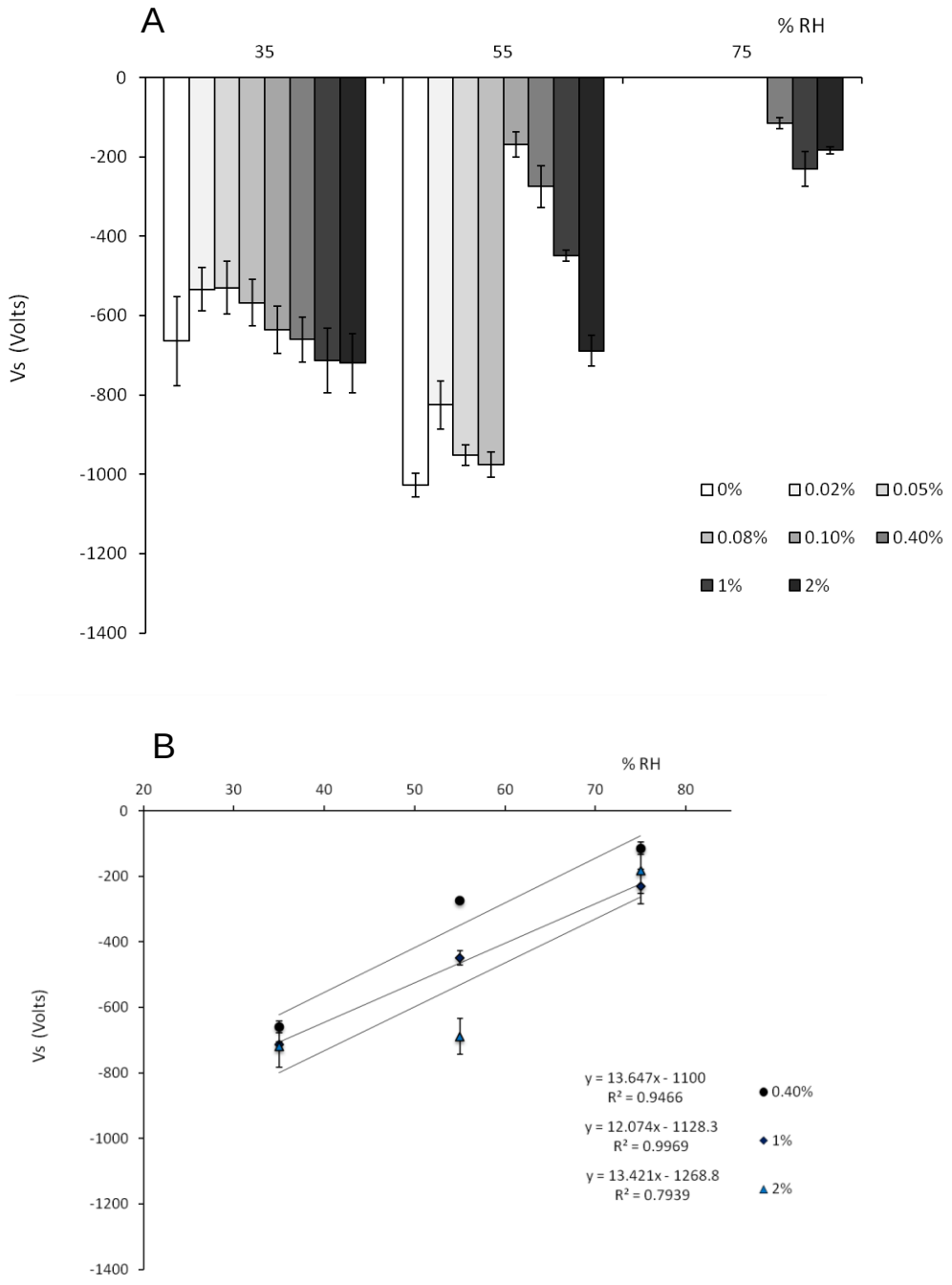

Figure 4.7 Initial surface potential plotted as a function of relative humidity for A, all fluticasone concentrations and B, 0.4%-2% w/w fluticasone

These data show that as ambient relative humidity increased, the initial surface potential differences of the budesonide and fluticasone samples decreased. For example for the 0.4%w/w budesonide blend, the initial surface potential values

corresponding to 35%, 55% and 75% RH were -813.00 ± 56.57 V, -314.27 ± 52.36 V and -88.37 ± 13.94 V, respectively, and for the 0.4% blend fluticasone the values were -659.77 ± 17.53 V, -274.50 ± 7.73 V and -113.90 ± 18.56 V respectively. For blends < 0.4% w/w the charge transferred by the corona discharge was so low that no surface potential peak could be detected by the electrostatic field meter. This highlights that the presence of adhered moisture to the particles' surfaces decreased the electrical surface resistivity, thus reducing the ability of the particles to become charged by the corona discharge of the CDTA.

4.3.5 Effect of loaded dose on the static charge decay times of the DPI formulations at varying RH

The time taken to get to 10% of the initial surface potential values (Time to 10%) increased as a function of budesonide concentration for each humidity as shown in Figure 4.8 A. For budesonide concentrations > 0.4% w/w an exponential correlation was observed with R^2 values of 0.987, 0.969 and 0.998 for 35%, 55% and 75% RH respectively as shown in Figure 4.8 B. This indicated the charge decay kinetics became dominated by the API behaviour at a critical surface coverage level of 0.4% at 75% RH and 0.1% at 35 and 55% RH.

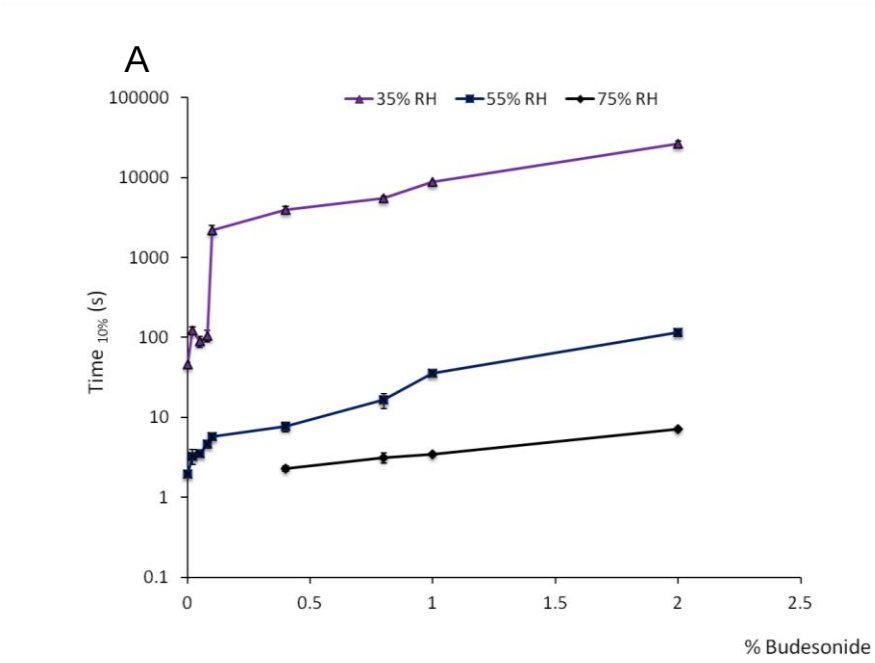

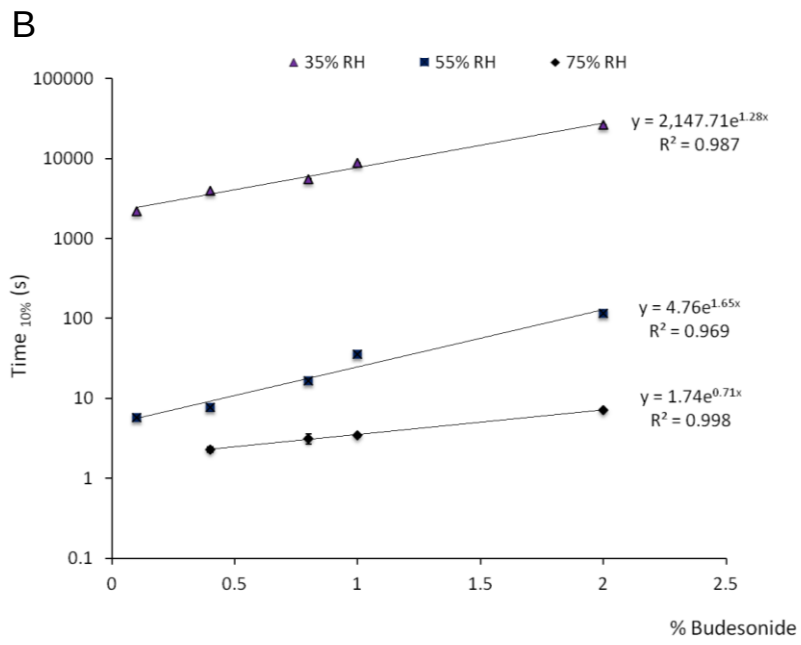

Figure 4.8 Time to 10% decay values plotted as a function of API concentration for each relative humidity for A, all budesonide concentrations and B, 0.1%-2% w/w budesonide

The time taken to reach 1/e of the initial surface potential values (Time to 1/e) increased as a function of API concentration for each humidity as shown in Figure 4.9 A. For API concentrations > 0.4% w/w an exponential correlation was observed with R^2 values of 0.756, 0.976 and 0.989 for 35%, 55% and 75% RH respectively as shown in Figure 4.9 B. This again indicated the charge decay kinetics became dominated by the API behaviour at a critical surface coverage level of 0.4% at 75% RH and 0.1% at 35 and 55% RH.

A

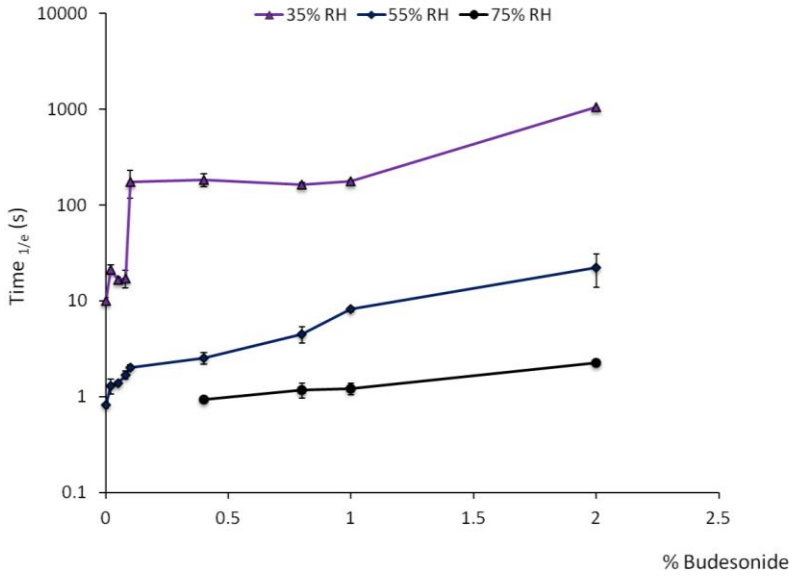

B

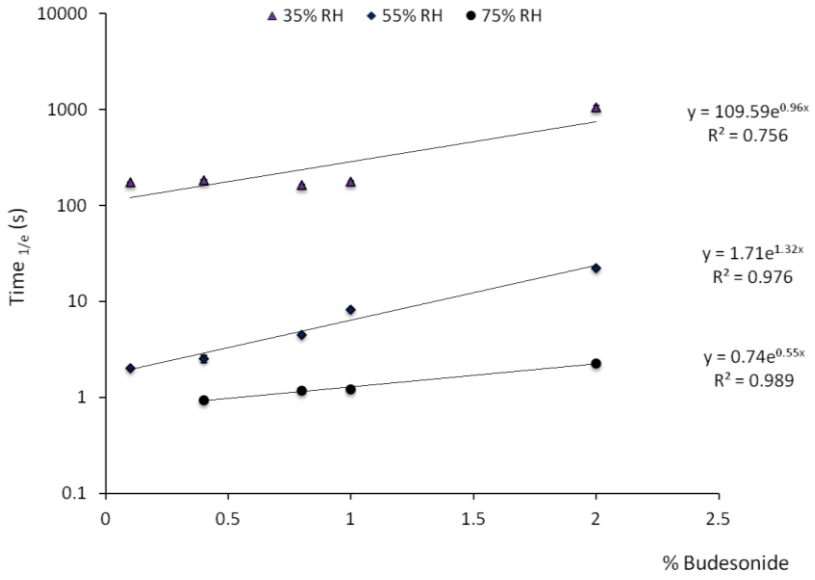

Figure 4.9 Time to 1/e decay values plotted as a function of budesonide concentration for each relative humidity for A, all budesonide concentrations and B, 0.1%-2% w/w budesonide

The Time to 10% values increased as a function of fluticasone concentration for each humidity as shown in Figure 4.10 A. For API concentrations above 0.1% w/w an

exponential correlation was observed with R^2 values of 0.997, 0.981 and 0.946 for 35%, 55% and 75% RH respectively as shown in Figure 4.10 B.

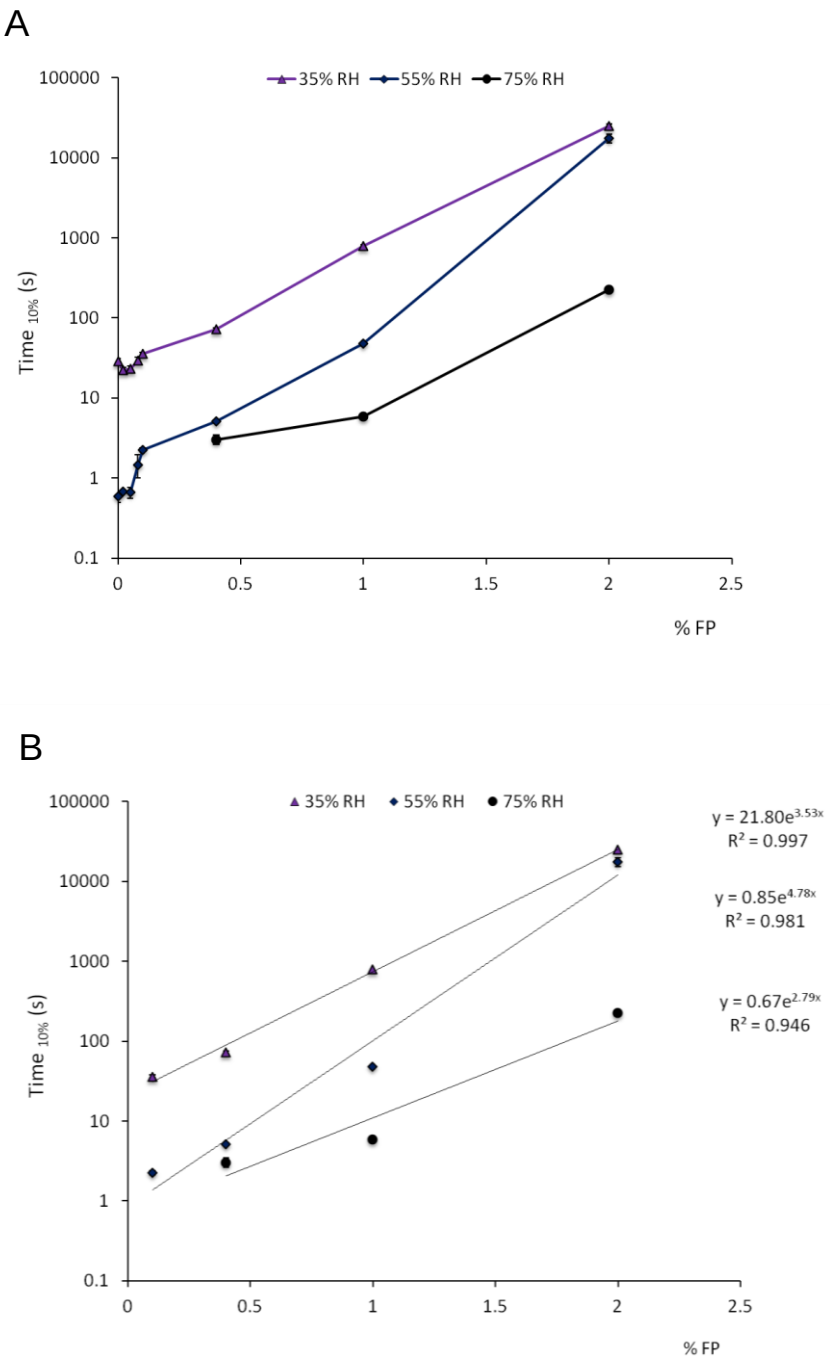

Figure 4.10 Time to 10% decay values plotted as a function of API concentration for each relative humidity for A, all fluticasone concentrations and B, 0.1%-2% w/w budesonide

The Time to 1/e values increased as a function of fluticasone concentration for each humidity as shown in Figure 4.11 A. For API concentrations above 0.1% w/w an

exponential correlation was observed with R^2 values of 0.977, 0.982 and 0.968 for 35%, 55% and 75% RH, respectively, as shown in Figure 4.11 B.

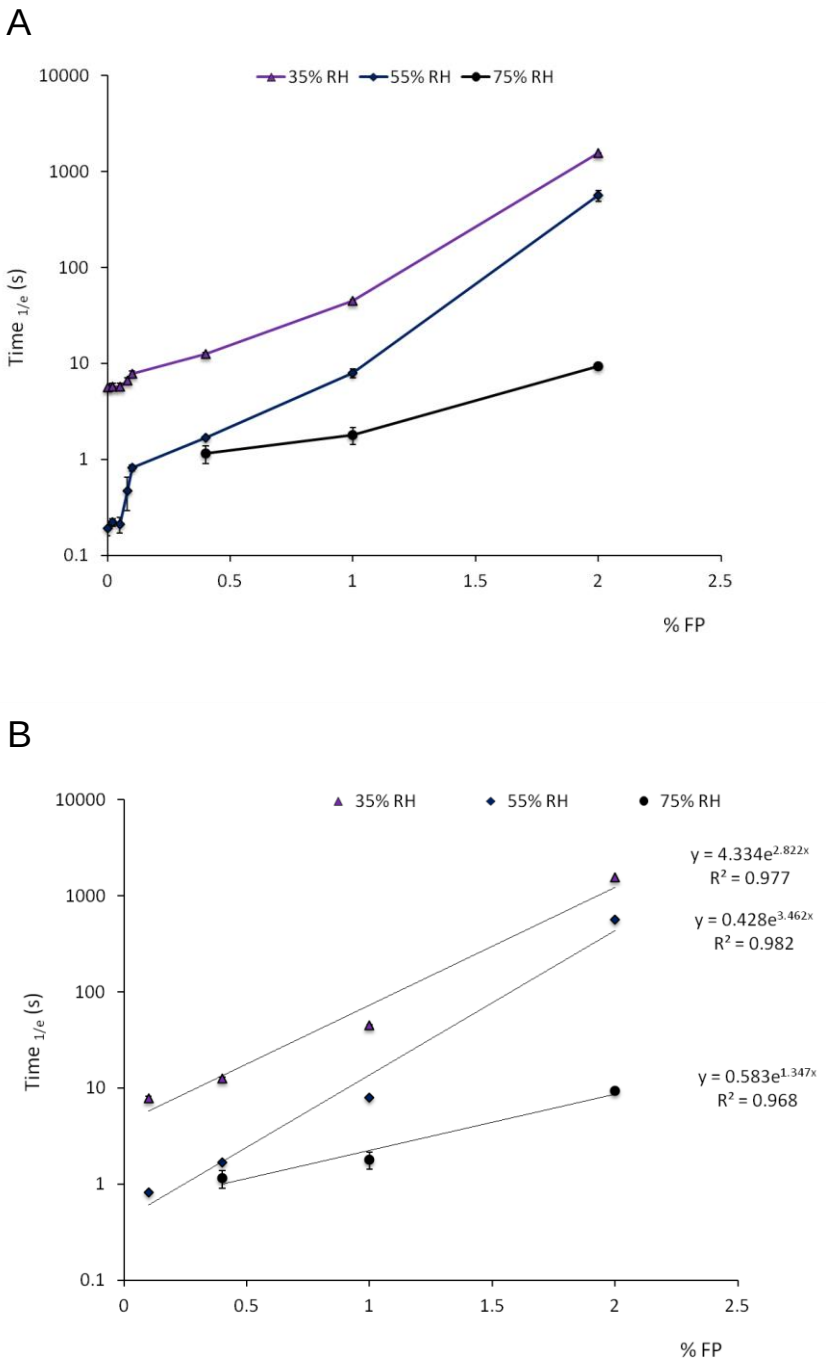

Figure 4.11 Time to 1/e decay values plotted as a function of fluticasone concentration for each relative humidity for A, all fluticasone concentrations and B, 0.1%-2% w/w fluticasone

This indicated the charge decay kinetics became dominated by the API behaviour at a critical surface coverage level of 0.4% at 75% RH and 0.1% at 35 and 55% RH as was found with the budesonide formulations.

These data also show that for both budesonide and fluticasone propionate, as the API concentration increased, the Time to 1/e and Time to 10% values also increased. Above a minimum concentration of 0.1% API an exponential relationship was determined for both sets of formulations at 35% and 55% RH. Below this minimum concentration, the bulk powder charge decay properties were dominated by the coarse carrier, with the API only having a small effect on the overall decay times. Above a concentration of 0.1% sufficient API was available such that the reading of surface potential by the field meter of the CDTA was dominated by the surface coverage and electrostatic behavior of the API particles. Although the initial surface potentials increased linearly as a function of API concentration the charge decay times increased exponentially highlighting the extent to which the API present governs the overall charge decay behavior of a DPI formulation.

4.3.6 Effect of relative humidity on the static charge decay times of the API formulations

The Time to 10% values decreased as a function of humidity for each budesonide concentration as shown in Figure 4.12 A. For API concentrations above 0.4% w/w an exponential correlation was observed with R^2 values of 0.867, 0.906, 0.948, and 0.966 for 0.4%, 0.8%, 1% and 2% w/w formulations, respectively, as shown in Figure 4.12 B.

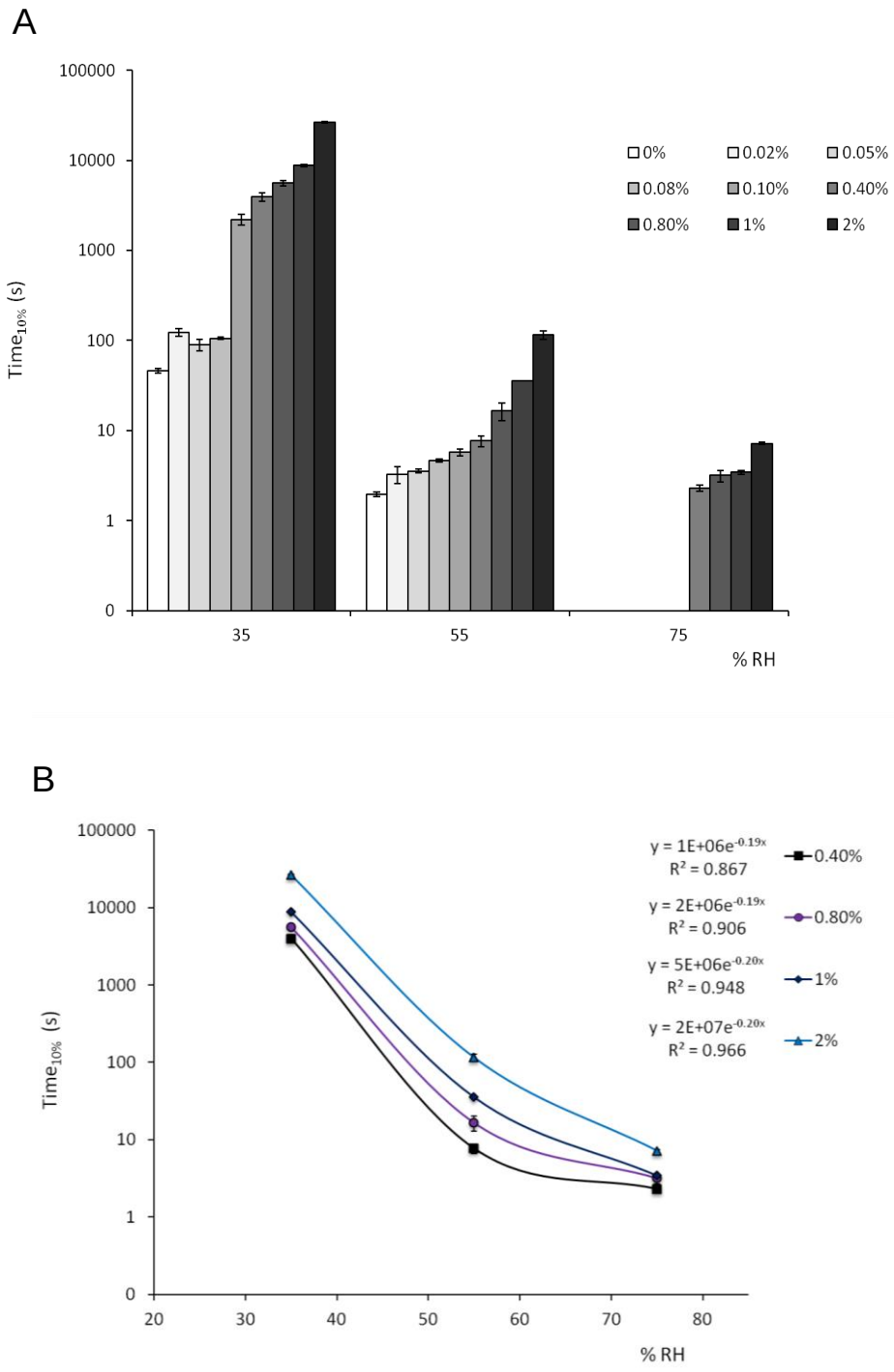

Figure 4.12 A, Time to 10% values as a function of humidity for A, all budesonide concentrations and B, 0.4%-2% w/w budesonide

At 35% RH, a change in the order of magnitude was observed in the time to 10% values between 0.08% and 1.0% budesonide concentrations. This indicated the increased susceptibility of the formulation to become statically charged as this critical surface level of API coverage. This effect was not as pronounced at 55% and 75% RH,

however, there are marked differences in the time to 10% values for the 2% budesonide formulations at all humidities.

The Time to 1/e values decreased as a function of humidity for each budesonide concentration as shown in Figure 4.13 A. For API concentrations above 0.4% w/w an exponential correlation was observed with R^2 values of 0.885, 0.935, 0.982, and 0.979 for 0.4%, 0.8%, 1% and 2% w/w formulations, respectively, as shown in Figure 4.13 B. As for the time to 10% values, an order of magnitude change was again observed between 0.08% and 1.0% budesonide concentrations.

A

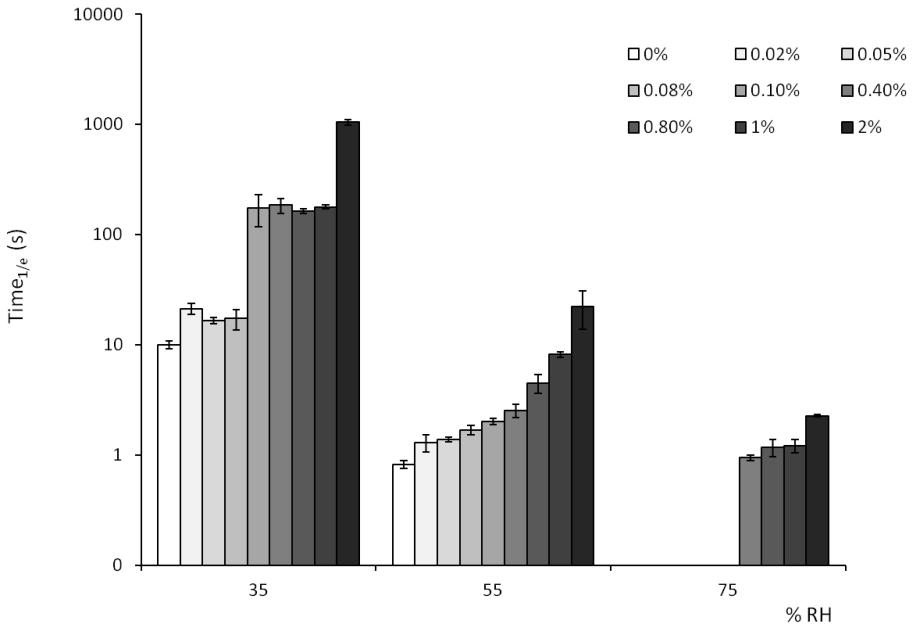

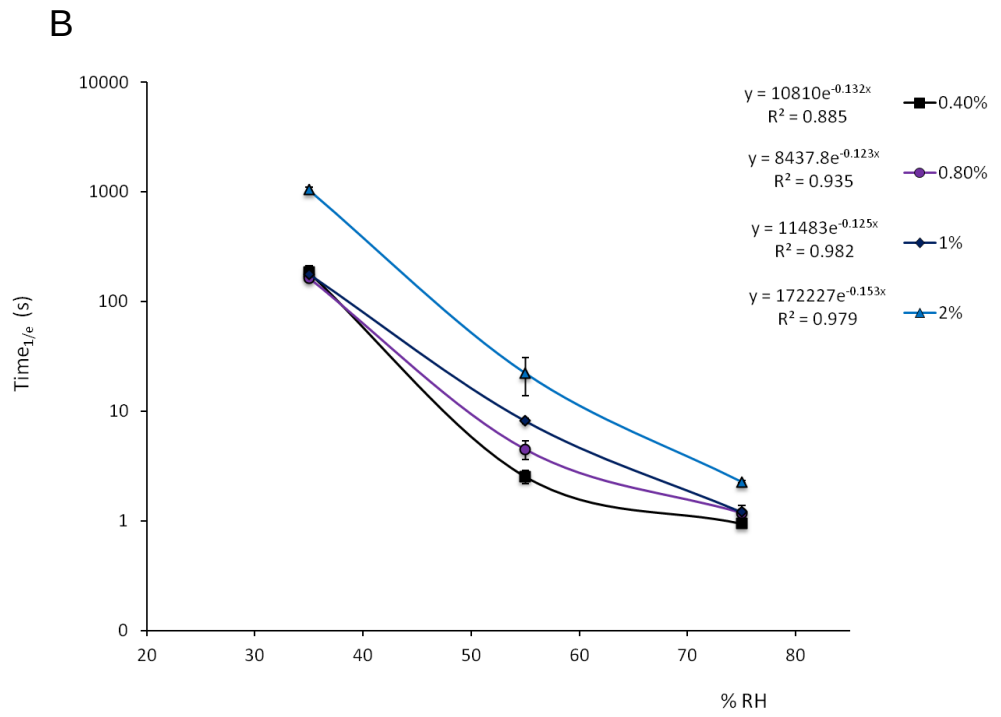

Figure 4.13 Time to 1/e decay values as a function of humidity for A, all budesonide concentrations and B, 0.4%-2% w/w budesonide

The Time to 10% values decreased as a function of humidity for each fluticasone concentration as shown in Figure 4.14 A. For concentrations above 0.4% w/w an exponential correlation was observed with R^2 values of 0.869, 0.993, and 0.807 for 0.4%, 1% and 2% w/w formulations, respectively, as shown in Figure 4.14 B.

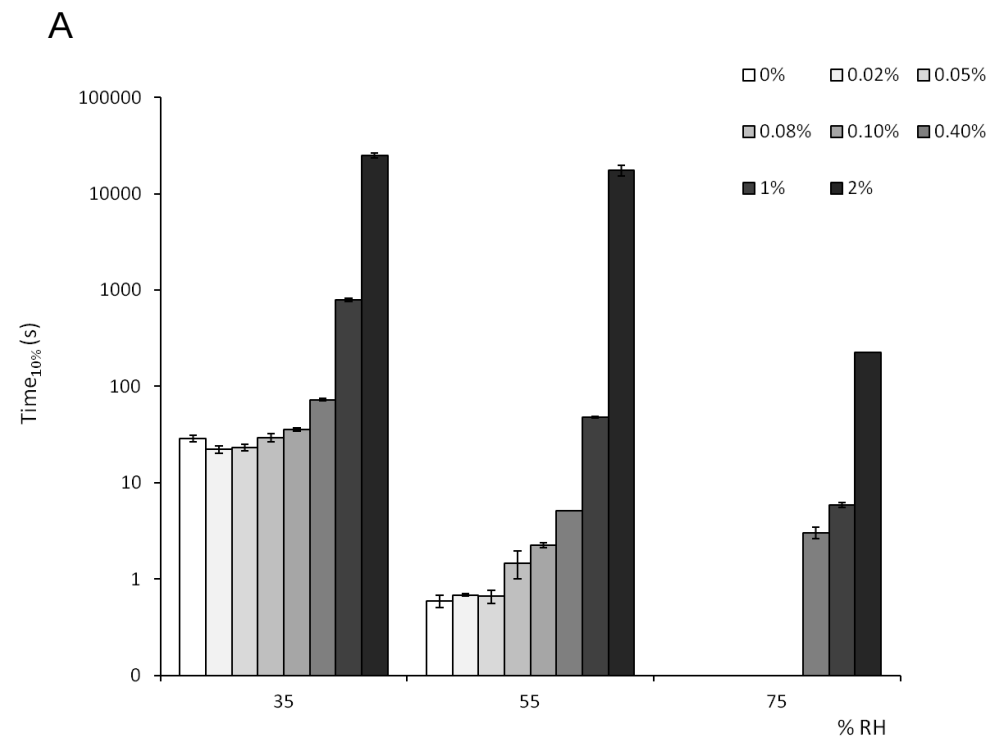

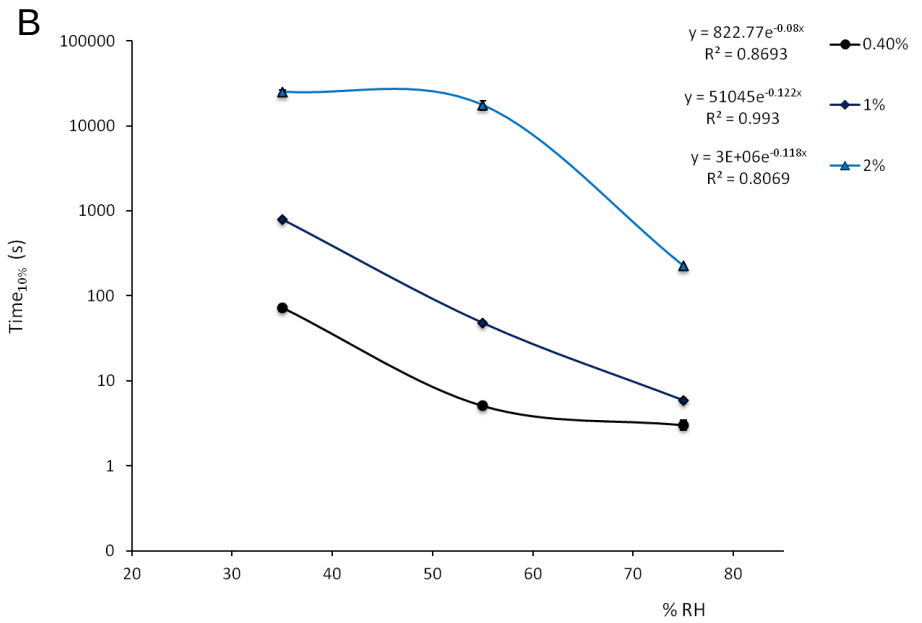

Figure 4.14 Time to 10% decay values as a function of humidity for A, all fluticasone concentrations and B, 0.4%-1% w/w fluticasone

The Time to 1/e values decreased as a function of humidity for each fluticasone concentration as shown in Figure 4.15 A. For API concentrations above 0.4% w/w an exponential correlation was observed with R^2 values of 0.864, 0.998, 0.892 for 0.4%, 1% and 2% w/w fluticasone formulations, respectively, as shown in Figure 4.15 B.

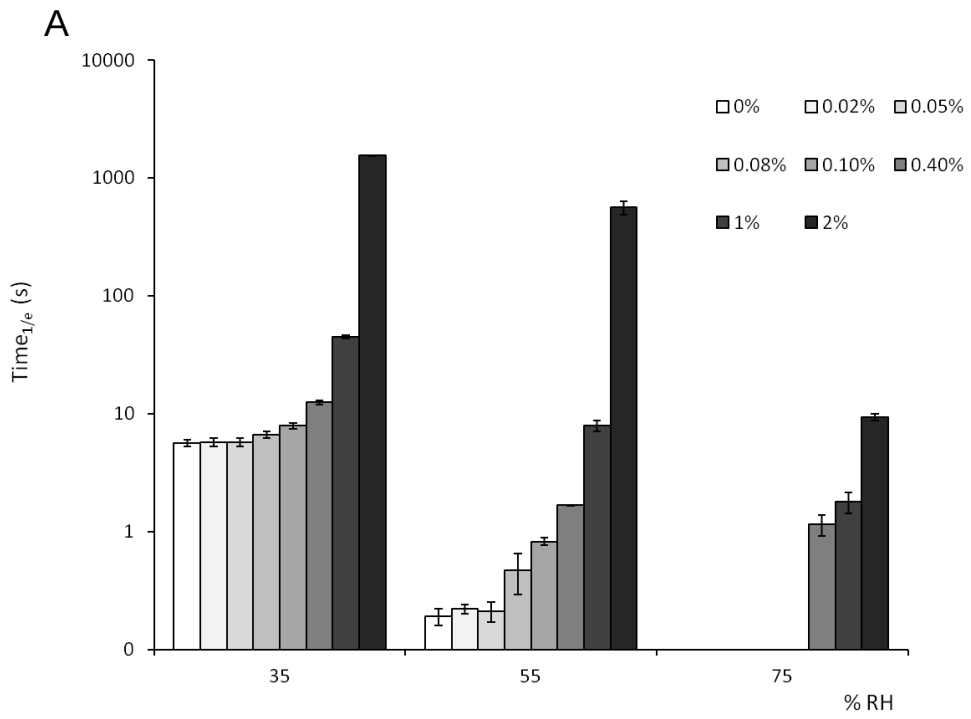

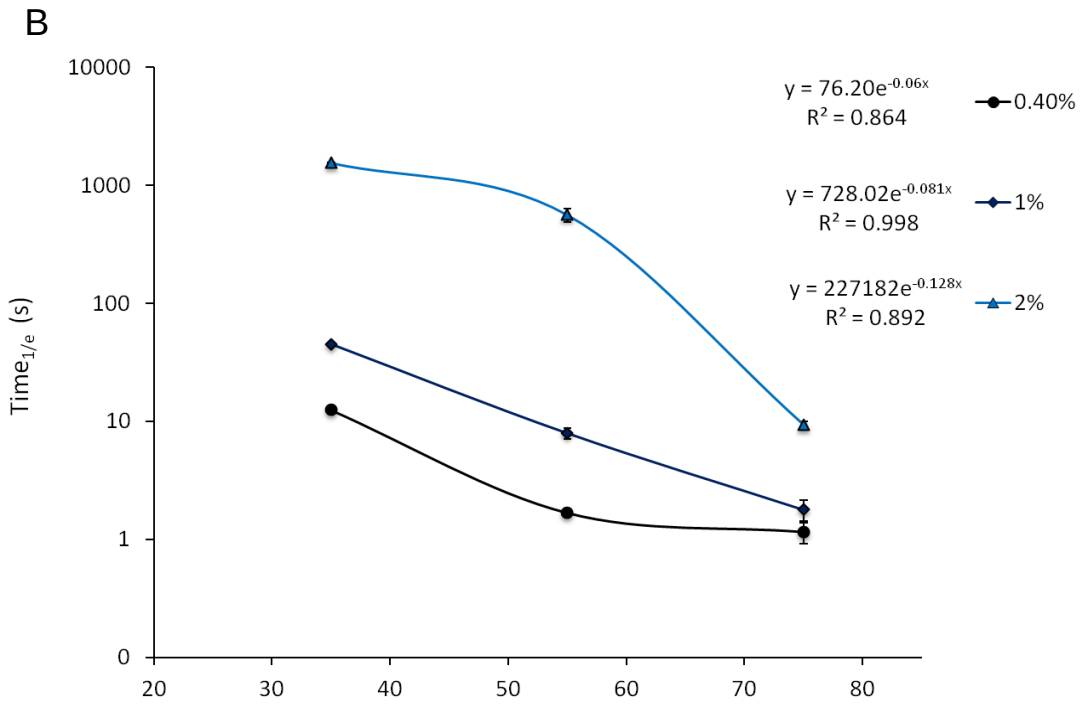

Figure 4.15 Time to 1/e decay values as a function of humidity for A, all fluticasone concentrations and B, 0.4%-1% w/w fluticasone

These data show that for both sets of formulations, as ambient relative humidity increased, the static charge decay rate of the sample following the application of the corona discharge decreased, with the slowest charge decay rates observed at 35% RH and the quickest at 75% RH. For example, for the 1% budesonide blend, the Time to 10% values corresponding to 35%, 55% and 75% RH were 8767.67 ± 211.73 seconds, 35.45 ± 0.14 seconds and 3.44 ± 0.16 seconds respectively and for fluticasone were 791.50 ± 34.02 seconds, 47.92 ± 0.92 seconds and 5.91 ± 0.36 seconds, respectively. These data highlighted an enormous difference in the decay rates between 35% and 55% RH with charge decay to 10% of the initial value taking less than a minute at 55% RH and nearly two and a half hours at 35% RH for the 1% budesonide formulation. When the API concentration was increased from 1% to 2 %w/w the Time to 1/e and Time to 10% values dramatically increased by an order of magnitude at each relative humidity tested highlighting the dominant behaviour of the API on the charging propensity and charge decay rate of the sample.

The presence of humidity in the air should in theory aid the ability of a corona discharge to transfer charge to a sample as the water molecules present will provide a

conductive path through which the discharge can travel. However, as was demonstrated from the DVS results, an increase in relative humidity will increase the total amount of water adhered to the surface of the particles. This in turn acts to increase the dielectric permittivity and conductivity of the particle surface facilitating increased mobility of the charge present. Water droplets in the air surrounding the particle will also adsorb and desorb from the particle's surface at random and during this process charge will be transferred from the particle to the water molecules in order to reduce the charge saturation on the particle and minimise the energy difference between the two species. Both of these effects will result in lower initial surface potential difference values post corona charging and more rapid charge decay rates at higher humidities. This was highlighted by the fact that for both APIs, no initial surface potential difference values were recorded for concentrations of less than 0.4% at 75% RH.

The data generated from these experiments indicates that the overall charging propensity and charge decay kinetics became dominated by the API behaviour at a critical surface coverage level of 0.1% w/w API at 35 and 55% RH for both sets of formulations. At 75% RH this value increased to 0.4% w/w API as the increased level of water adsorbed to the particles surfaces decreased the formulations electrical resistivities sufficiently to percent corona charging from occurring.

4.3.7 Blending experiments

The static charge decay times for the 2% w/w budesonide in ML001 formulation are displayed in Table 4.2 and the 2% w/w fluticasone formulation in SV010 are displayed in Table 4.3. As no corona discharge was applied, the software of the CDTA did not record an initial surface potential value, however for both the fluticasone and budesonide blends, the blending process resulted in a net negative charge build up for both the stainless steel and polypropylene containers. The values for the charge decay rates recorded data demonstrated that the blending vessel material had a marked effect on the extent of triboelectrification of the blend. The Time to 1/e values of the budesonide and fluticasone blends were 16056.8 ± 3254.1s and 1411.8 ± 203.6s for the polypropylene container and 156.6 ± 14.9s and 62.0 ± 10.1s for the stainless steel container, respectively. These data indicated that the polypropylene vessel imparted significantly more negative charge onto the sample than the stainless steel vessel. The Time to 10% value for the 2% budesonide formulation with the polypropylene container was not recorded by the CDTA as the instrument exceeded the maximum time limit for a charge decay time profile it can record, which was 24 hours.

2% w/w budesonide in ML001	Stainless Steel		Polypropylene	
	$Time_{10\%}$ (s)	$Time_{1/e}$ (s)	$Time_{10\%}$ (s)	$Time_{1/e}$ (s)
35% RH	1894.6 ± 196.2	156.6 ± 14.9	N/A	16056.8 ± 3254.1
55% RH	406.7 ± 34.5	79.8 ± 21.2	926.3 ± 87.5	387.1 ± 44.6
75% RH	N/A	N/A	28.9 ± 13.2	13.2 ± 3.0

Table 4.2 Time to 10% and Time to 1/e values for the 2% budesonide formulation post low shear turbula blending (n=3, mean ± SD)

2% w/w fluticasone in SV010	Stainless Steel		Polypropylene	
	$Time_{10\%}$ (s)	$Time_{1/e}$ (s)	$Time_{10\%}$ (s)	$Time_{1/e}$ (s)
35% RH	339.4 ± 48.6	62.0 ± 10.1	15015.2 ± 2010.2	1411.8 ± 203.6
55% RH	130.0 ± 25.2	21.5 ± 5.4	926.3 ± 87.5	148.2 ± 15.7
75% RH	N/A	N/A	40.1 ± 9.3	7.4 ± 1.9

Table 4.3 Time to 10% and Time to 1/e values for the 2% fluticasone formulation post low shear turbula blending (n=3, mean ± SD)

Humidity also affected the extent of triboelectrification; at 75% RH the surface potential difference of the sample post blending was too low for the software to detect. The trend observed was that as the humidity increased the charge decay times decreased with, for example, the Time to 1/e values for the 2% w/w fluticasone formulation being 1411.8 ± 203.6s, 148.2 ± 15.7 and 7.4 ± 1.9 s at 35%, 55% and 75% RH, respectively.

A plot of the Time to 1/e values post blending in the polypropylene vessel for each formulation as a function of humidity is displayed in Figure 4.16. These data demonstrated an exponential relationship between Time to 1/e and humidity as was observed during the previous charge decay experiments with R^2 values of 0.999 and 0.993 for the budesonide and fluticasone formulations, respectively.

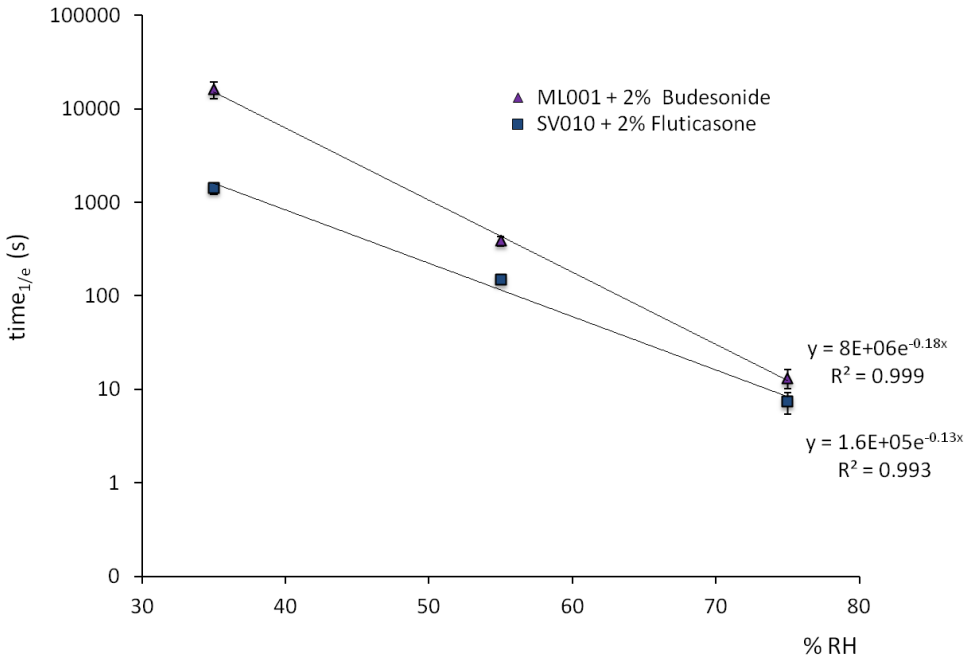

Figure 4.16 Time to 1/e values plotted as a function of RH for the 2% w/w budesonide and fluticasone formulations post low shear turbula blending at 22 RPM in a polypropylene container

It was observed that the static charge decay rates of the 2% w/w budesonide formulation were significantly greater in all cases than for the fluticasone formulations ($P<0.05$) indicating that budesonide is more susceptible to retain its surface charge than fluticasone.

4.4 Conclusions

The JCI Chilworth 155v6 Charge Decay Time Analyser is a useful tool for ranking the electrostatic charging propensity of powder blends and assessing the rate of charge decay as a function of time. If the corona discharge is kept at a constant value, the initial potential difference generated on the powder surface will give an idea of the susceptibility of a powder to pick up static charge, with the greater the initial value, the greater the expected charging propensity. In addition, the charge decay rate as quantified by the Time to 10% and Time to 1/e values will indicate how long a powder will remain statically charged for after it has undergone a tribocharging event. Lactose monohydrate has a simple carbohydrate structure, is semiconducting in nature and for

Respitose® SV010 and ML001 it was shown that the charge decay rates were very rapid after the samples had become charged by the corona discharge. As such it is believed that the greater influence in determining the extent to which a DPI formulation remains charged after triboelectrification is the API which is normally more electrically resistive in nature. The initial surface potential of the DPI formulations increased linearly as a function of API concentration, however, an exponential correlation was observed between the API concentration and charge decay rate for blends above 0.4% w/w API. This has important implications as the use of this type of measurement would provide formulators with an understanding of exactly how long they would need to leave a DPI formulation to equilibrate for after a processing step to allow any charge present to dissipate.

The effect of environmental relative humidity was investigated and it was found that humidity had a dramatic effect on the initial surface potential difference values and respective charge decay rates. For the 0.8% budesonide formulation, equivalent to a 200µg commercial dose, the charge decay rate (Time to 10%) was in the order of seconds at 75% RH, minutes at 55% RH and several hours at 35% RH. The lactose and API samples were analysed using DVS and showed only minimal increases in mass as a function of humidity. Nevertheless, as humidity increases the amount of water adhered to the particles' surfaces will also increase, decreasing the electrical resistivity which in turn decreased the initial surface potential differences and increases the charge decay rates. The environmental relative humidity will dramatically affect the extent to which a DPI formulation may become tribocharged during a processing step and also highlights that humidity control is vital when performing electrostatic measurements in order to ensure repeatable and reliable results. It was also found that the minimum level of API required to influence a DPI formulation's bulk electrostatic properties could be determined experimentally as long as humidity control was maintained.

The blending experiments performed illustrate the highly dependent nature of triboelectrification with relative humidity. Often in pharmaceutical company manufacturing environments humidity control is not employed as it is not a regulatory requirement. Therefore the extent to which triboelectrification may occur is variable and this could lead to handling and processing issues as well as variable formulation performance. The effect of container material was also shown to have a dramatic effect on the extent of triboelectrification, with the polypropylene vessel tribocharging the

blends to a much greater extent than the stainless steel vessel resulting in vast increases in the charge decay times.

Future work could look to expand on the investigations described in this chapter by using the CDTA to determine whether the effect of variables such as particle size, morphology, chemical structure, surface area and surface energy have a role in contributing to the electrostatic charge decay properties of a DPI blend. A control set of formulations should be produced such as either fluticasone propionate in ML001 or budesonide in SV010 so that a direct comparison can be made between the two sets of charge decay data generated for this experiment. In addition, as it is believed that APIs are the prime suspects in cases of static charge related processing issues, unformulated APIs could be tested under controlled humidity conditions to characterise their electrostatic properties. If a new API target is developed then measurements could be taken and compared with historical data to indicate the risk of the API being particularly susceptible to becoming tribocharged. By controlling factors such as the surface area through API particle processing, the risk of triboelectrification could be mitigated, the extent of which could be analysed using the CDTA.

Chapter 5 Measuring the bipolar charge distribution of commercial pMDI suspensions using the Bipolar Next Generation Impactor

5.1 Introduction

It is well known that upon aerosolisation of either a DPI pMDI formulation both excipient and drug particles present in the formulation are highly susceptible to becoming electrostatically charged via the mechanism of triboelectrification (Bennett *et al*. 1999, Watanabe *et al*. 2007). Pressurised metered dose inhalers (pMDIs) typically consist of a canister containing a solution or suspension of solid active pharmaceutical ingredient (API) drug particles within a pressurised propellant (for example HFA 134a) sometimes in the presence of other excipients such as surfactants. The canister is incorporated with a metering chamber and valve which allows the correct dose of API to be delivered with each actuation of the inhaler. Prior to actuation, the API particles are in contact with the walls of the metering chamber, the valve, valve seals, spring and stem (James *et al*. 2009). Upon actuation, the API particles become aerosolised and enter a highly kinetically energetic state, undergoing numerous collisions with each other and with the components of the inhaler. During these collisions electron transfer may occur to or from the API particles via the mechanism of triboelectrification causing the creation of highly charged species (Kwetkus 1998). Due to the multi-component nature of the system, the precise mechanisms remain relatively poorly understood, although it has been hypothesised that charge transfer occurs as a result of differences in the electrical properties of the materials involved. The canister and spring are metal whereas the valve, valve seals, stem are insulators. The API particles which are electrically resistive may come into contact with each surface and charge transfer may occur at each point of contact. The amount of charge transferred between the API particles and the various device components depends on the difference between the effective work functions of the two materials coming into contact, which is a measure of how much energy is required to remove an electron from the Fermi level of the material to the vacuum energy level. Charge transfer ceases when the Fermi levels of the two materials become equal, minimising the energy difference (Matsusaka *et al*. 2010).

Researchers have discussed the effects of electrostatic charge build up on aerosol particles on the efficiency of deep lung airway deposition and consequent therapeutic effect. Wilson theorised that aerosol particles with the same polarity will mutually repel and thus expand, enhancing deposition within an enclosed environment (Wilson 1947). Melandri *et al*. performed an *in vivo* study in humans which showed that increasing electrostatic charge (either positive or negative) increased the deposition of aerosol particles in deep lung (Melandri *et al*. 1983). More recently, Bailey *et al*. developed a mathematical model to describe charged particle deposition in the lung in relation to complimentary clinical studies showing that particle size, charge and breathing conditions are key to targeting specific regions of the lung for drug delivery (Bailey 1997). Further to this work, several authors have looked at the effect of electrostatic charge on spacer devices in combination with pMDIs, where interactions between electrostatic charge of the aerosol particles and the inner spacer walls has been shown to have a marked effect on the performance. For example, Kenyon *et al*. showed that in an in *vivo* study with a glucocorticosteroid pMDI, gamma scintagraphy images indicated the presence of static charge on the walls of the spacer reduced the *in vivo* deposition of the therapeutic dose (Kenyon *et al*. 1998). Glover and Chan (2004) used the electrical low pressure impactor (ELPI) to measure the net charge of both Flixotide™ and Ventolin™ pMDIs (Glover and Chan 2004a). For Flixotide™, they found that at higher particle cut off diameter, an overall net negative charge was recorded. At lower particle cut off diameter, an overall net positive charge was recorded. When plotted against the mass of deposition of the FP particles, at the lower cut off diameters, almost no FP was deposited, but a large net positive charge was recorded. This may be due to the presence of water which forms ice crystals during the actuation of the pMDI. With Kwok, they expanded their study to include Intal, Tilade and QVAR™ pMDIs together with Flixotide™ and Ventolin™ (Kwok *et al*. 2005).

Various attempts have been made to accurately quantify the charge build up on aerosol particles in proportion to their mass and surface area. The first widely available commercial method developed was the ELPI (electrical low pressure impactor) in which an Andersen cascade type impactor was modified such that the impaction plates are electrically isolated and connected to electrometers allowing for simultaneous net charge measurements and mass quantifications to be performed (Marjamaki *et al*. 2000). The idea was taken further with the development of the Electrical Next Generation Impactor (eNGI) (Hoe *et al*. 2009c) in which the impaction cups of a conventional NGI are connected to an electrometer in a similar way as the ELPI and the net charge to mass ratios of aerosol particles are determined. These two systems

also allow the mass of the aerosol particles to be quantified but both do not take into account the bipolar nature of the aerosol particles and only provide a measurement of the net of the negative and positive charges. Alternatively, by using the principals of electrostatic precipitation, systems such as those developed by O'Leary *et al*. and Kulon *et al*. (Kulon and Balachandran 2001, O'Leary *et al*. 2008) allow the bipolar charge ratios of aerosol particles to be measured. However, these systems are not ideally suitable for performing accurate quantification of the deposited aerosol particles and as such do not provide the complete picture in terms of measurement of bipolar charge to mass ratios. Ali *et al*. utilised an electrical single particle aerodynamic relaxation time (ESPART) analyser to determine electrodynamic effects of some sample DPI and pMDI formulations (Ali *et al*. 2009a). Although the system provides measurements of bipolar charge to mass ratio, only single particle measurements may be recorded and not the entire deposited aerosol dose per shot.

To further the understanding of pMDI inhalation aerosol electrostatics, the author presents a novel apparatus for performing bipolar charge measurements and quantifications of aerosol particles – the Bipolar Next Generation Impactor (bp-NGI) which has been successfully used to characterise the bipolar charge to mass distributions of Flixotide™ 250, Serevent™ 25 and Seretide™ 250 pMDIs.

The bp-NGI as described in the materials and methods section consists of a modified Next Generation Impactor which is an industry standard aerosol particle size classifier used to determine the *in vitro* performance of inhalable drug products (Marple *et al*. 2003b). An electrostatic precipitation system is connected to a preselected stage of the NGI to allow measurement of the charge to mass ratio of the aerosol particles from the selected stage and below. As opposed to conventional net charge measurement systems, which measure the sum of the positive and negative charges present (which cancel) (Saini *et al*. 2008), the system is able to accurately separate the aerosol particles according to the polarity of their charge and measure the charge and mass of these particles.

5.2 Materials and methods

5.2.1 Materials

Flixotide™ 250, Serevent™ 25, Seretide™ 250/25 Evohalers are suspension based pressurised metered dose inhaler (pMDI) formulations delivering 250µg of fluticasone propionate (FP), 25µg salmeterol xinafaote (SX) and a combination of 250µg FP and 25µg SX per actuation, respectively. These formulations contained the drug(s) suspended in HFA134a propellant and were manufactured by GlaxoSmithKline (Ware, UK). Commercial samples of the pMDIs were supplied by AAH Pharmaceuticals Ltd. (Coventry, UK). Fluticasone propionate was supplied by Chemagis Ltd (Bnei Brak, Israel) and salmeterol xinafoate supplied by Neutech Laboratories (Hyderabad, India). All solvents used were of HPLC grade (Sigma-Aldrich, St. Louis, MO, USA). Ultra pure water was produced by reverse osmosis (MilliQ, Millipore, Molsheim, France). Ammonium acetate was purchased from Sigma Life Sciences (St. Louis, MO, USA).

5.2.2 Methods

5.2.2.1 Particle size

Particle size measurements were conducted using a Helos laser diffraction unit in conjunction with Windox 5 software, both from Sympatec GmbH (Clausthal-Zellerfield, Germany). The particle size distributions of the drugs were measured using the R3 lens and the cuvette wet dispersion system. Prior to each measurement, a background reading of the dispersant, cyclohexane and 0.1% lecithin was recorded. Each pMDI was actuated into the cuvette, and more dispersant was added. The cuvette was then sonicated for five minutes in five, one minute intervals in order to produce an optical concentration of between 5 and 10%. The stir speed using the magnetic flea was set to 1500 RPM. Five repeat measurements of five seconds duration were recorded for each sample.

5.2.2.2 Experimental setup of the bp-NGI

A schematic representation of the bp-NGI for measuring bipolar charge distributions of pMDI particles is shown in Figure 5.1 incorporating two electrostatic precipitators for the collection of charged aerosols below a well-defined cut-off diameter of an NGI

stage. The precipitation section can be attached to the majority of the stages of an NGI (stage 2 through to stage 7) allowing charge to mass ratios of aerosol particles from the selected stage and all the stages below to be determined.

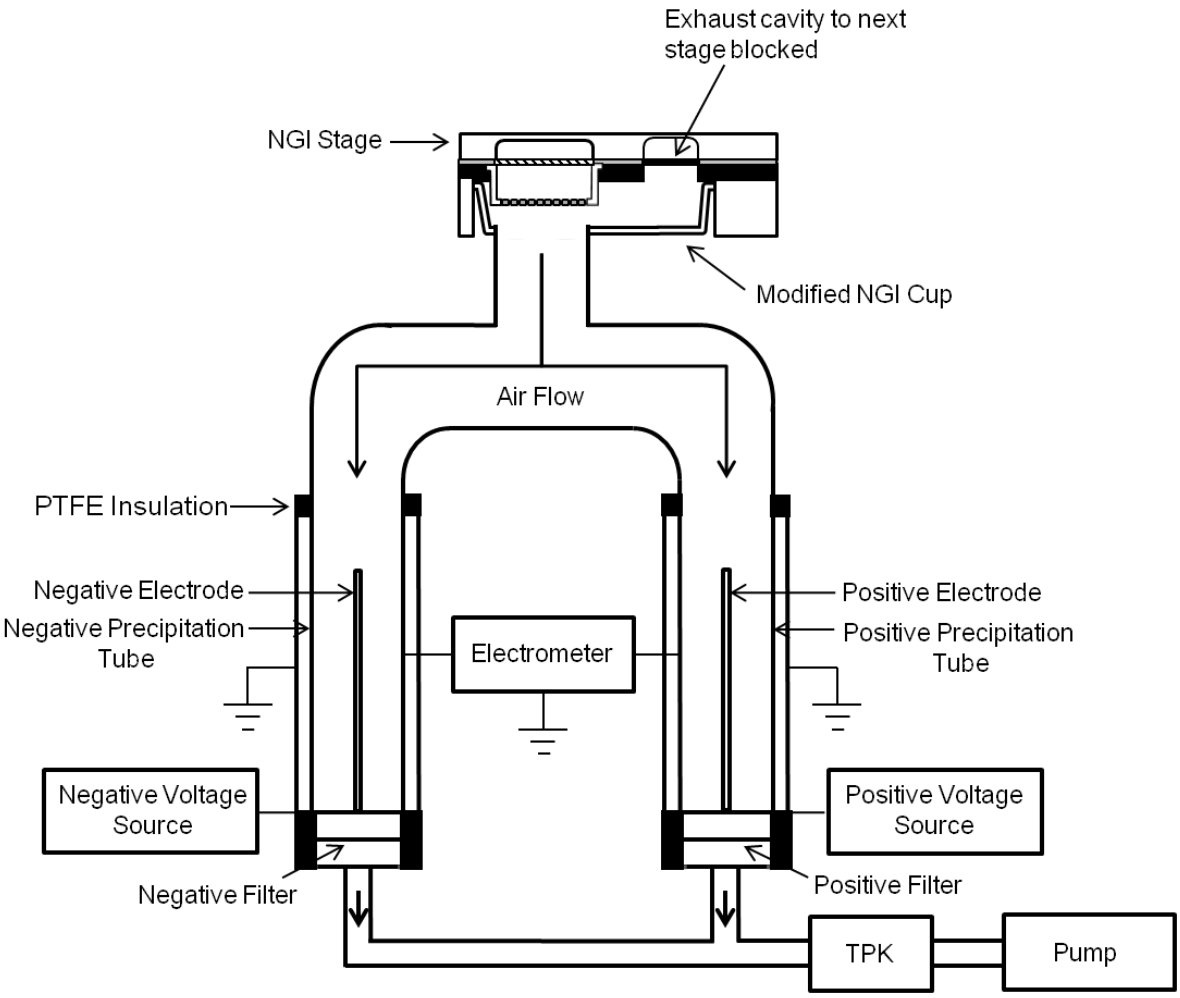

Figure 5.1 Experimental set up of bp-NGI

In this study, the electrostatic precipitators were attached to stage 2 of the NGI, with a cut-off diameter of 6.40µm at a flow rate of 30 L/min. The flow rate was controlled by a TPK (Copley Instruments, Nottingham, UK) attached to a vacuum pump which was connected to the base of the electrostatic precipitators. Below the collection cup of stage 2, the aerosol dose is bifurcated into the two precipitators with an airflow rate of 15 L/min through each section. Each section contains an earthed outer tube, to create a Faraday shield, a precipitation tube, a filter holder and a high voltage electrode, which is centrally positioned within the precipitation tube.

The bp-NGI was designed to maintain laminar flow through the precipitators. The critical dimensions of the two electrostatic precipitators were designed to maximise the collection efficiency (K_{precip}) of the electrically mobile aerosol particles by adapting a methodology used by Kulon *et al*. (Kulon *et al*. 2001). The collection efficiency was determined using Equation 4.2.

$$K_{precip}\ (\%) = \frac{2}{r_2}\sqrt{\frac{Z_p V L}{v_o \ln(r_2/r_1)}} \times 100 \qquad \text{Equation 4.2}$$

Where Z_p is the electrical mobility of the charged aerosol particle, *V* is the voltage on the central electrode, *L* is the length of the electrode, v_o is the airflow rate, r_1 is the radius of the electrode and r_2 is the radius of the precipitation tube.

The theoretical collection efficiencies of the bp-NGI at ±3.0 kV are shown in Figure 5.2 for aerosol particles exhibiting 100, 200 and 300 electrons of charge at the cut-off diameters of the NGI stages at 30 L/min. The graph shows that particles with a diameter of 6.40µm and below will be reasonably efficiently collected at ±3.0 kV, with a near maximum collection efficiency occurring when a particle gains a negative or positive charge equivalent to 200 electrons per particle.

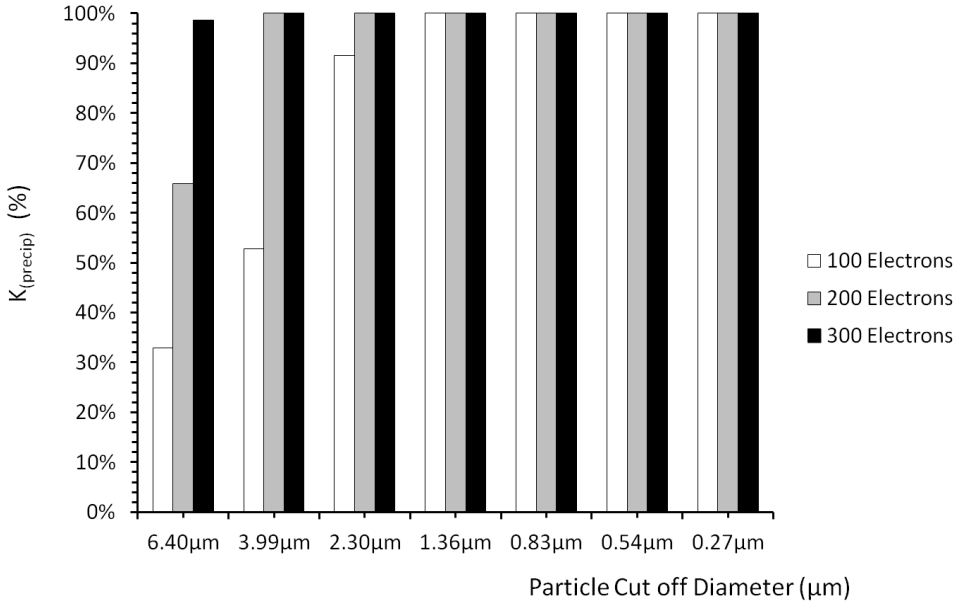

Figure 5.2 Theoretical collections efficiencies ($K_{(precip)}$ (%)) for the bp-NGI as a function of particle cut off diameter at 30 L/min.

5.2.2.3 Methodology for performing bipolar charge to mass ratio measurements of pMDI drug particles using the bp-NGI

Opposite polarity high DC voltage sources (Spellman, CZE1000R, West Sussex, UK) were applied to the electrically insulated copper electrodes, centrally located in the respective precipitators. During operation, the electric field created by the negative electrode repels the negatively charged aerosol particles onto the negative precipitation tube, while the positively charged aerosol particles are attracted onto the electrode. Conversely, negatively charged aerosol particles in the oppositely charged precipitator are deposited onto the positive electrode while the positively charge aerosols are repelled onto the positive precipitation tube. Aerosol particles with low electrical mobility, which cannot be precipitated onto either the electrodes or the precipitation tubes are collected onto 0.45µm glass fibre filters (Whatman, Fisher Scientific, UK), housed at the base of each precipitation tube. The system is modular, such that each section of the apparatus can be isolated and separately washed down for drug quantification via HPLC. The amount of drug collected on the negative precipitation tube and positive electrode indicates the quantity of drug particles that have sufficient negative electrical mobility to be precipitated within the two precipitators. The quantity of drug collected on the positive precipitation tube and negative electrode indicates the quantity of drug particles that are positively charged. The mass of drug collected from the respective filters represent the amount of aerosol dose which has insufficient positive or negative electrical mobility to be precipitated.

The precipitation tubes are connected via BNC adapters to a Keithley Instruments 6521 multi-input scanner card (Keithley Instruments, Reading, UK) connected to a Keithley 6517B electrometer for charge measurements. During each actuation of the inhaler device into the bp-NGI, the current versus time profiles during aerosol deposition onto the two precipitation tubes are recorded and subsequently integrated to measure the positive and negative charge collected per shot. The cumulative amount of positive and negative charge for a well-defined number of shots is also measured. These values are divided by the total mass of drug collected within the positive and negative precipitation tubes to determine the net charge to mass ratio of the negatively and positively charged aerosols. During the experiments, the operator is connected to earth via a wrist band and the outer tubes surrounding the electrostatic precipitators are earthed to shield the precipitation tubes from stray external fields.

A total of five shots of Flixotide™ 250, Seretide™ 250 and Serevent™ 25 were each fired through the bp-NGI. The mass of the negatively, positively and neutrally charged particles was quantified via HPLC to calculate the bipolar charge to mass distribution within the bp-NGI. The experiments were performed in triplicate for statistical robustness. The temperature range for all experiments was 20°C ± 1 and the humidity range was 40% ± 2. The flow rate through the bp-NGI was set to 30 L/min with 15 L/min being pulled through each precipitator as a result of the bifurcation. The voltage applied to the negative electrode was -3.0 kV and the positive electrode was +3.0 kV.

5.2.2.4 HPLC Analysis

Determination of the mass distribution of fluticasone propionate (FP) and salmeterol xinafoate (SX) within the bp-NGI was adapted from a previously published HPLC method (Murnane *et al*. 2006). The HPLC system consisted of a pump (Jasco PU-980, Jasco Corp., Japan) coupled to an autosampler (Jasco AS-950) and UV detector (Jasco UV-975) set at 228nm for simultaneous determination of both APIs. Separation was performed using a BDS Hypersil Column, 250x4mm (Thermo Scientific, Waltham, MA, USA) maintained at 40^0C using a column oven (Jasco CO-965). The mobile phase was a mixture of methanol–0.6% (w/v) aqueous ammonium acetate solution (75:25%, v/v), filtered through a 0.45µm nylon membrane (Whatman International Ltd., Maidstone, UK) and degassed. The retention time for salmeterol was 4.4 minutes and for fluticasone propionate was 5.4 minutes. Quantification was carried out by an external standard method and linearity was checked between 0.5 and 50 µg/mL for each individual API.

5.2.2.5 Statistical analysis

Linear regression analysis was used for the assessment of HPLC calibration. Statistical analysis between different populations was carried out using one-way analysis of variance. Comparison of the mean values was performed by Tukey's pair-wise comparison. All statistical analyses were performed using GraphPad Prism software (GraphPad Software Inc, California, USA). Error bars in graphical representations of data show ± standard deviation (S.D.) in all cases.

5.3 Results and discussion

5.3.1 Particle size

The log density distributions of the particle sizes of A, Flixotide™ 250, B, Serevent™ 25 and C, Seretide™ 250 are displayed in Figure 5.3. The average (n=5) of the 10% undersize (d_{10}), 50% undersize (d_{50}) and 90% undersize (d_{90}) values were recorded as well as the percentage of particles with diameter less than 5 µm and these data are displayed in Table 5.1.

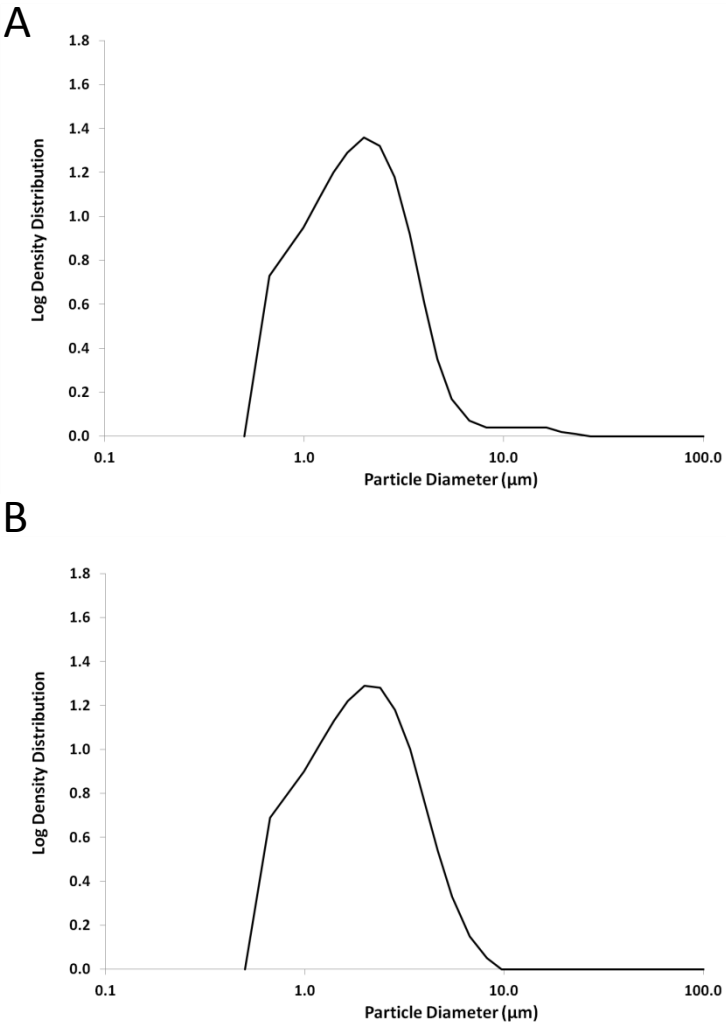

C

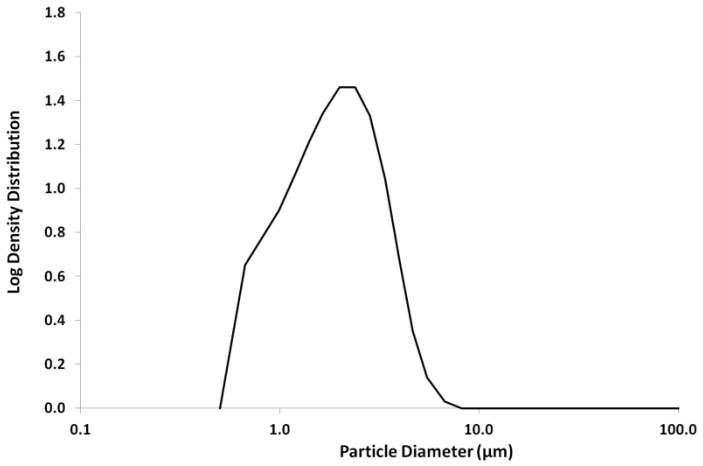

Figure 5.3 Log density distributions of the particle size of A, Flixotide™ 250, B, Serevent™ 25 and C, Seretide™ 250.

	d_{10} (µm)	d_{50} (µm)	d_{90} (µm)	% < 5 µm
Flixotide™ 250	0.72 ± 0.01	1.73 ± 0.01	3.70 ± 0.01	94.68 ± 0.09
Serevent™ 25	0.72 ± 0.00	1.79 ± 0.02	4.04 ± 0.03	93.06 ± 0.20
Seretide™ 250	0.74 ± 0.00	1.78 ± 0.02	3.55 ± 0.01	96.98 ± 0.04

Table 5.1 Average (n=5, mean ± S.D.) of the 10% undersize (d_{10}), 50% undersize (d_{50}) and 90% undersize (d_{90}) values and % < 5 µm of each pMDI

The results show that each pMDI contained micronized API particles with all three exhibiting a percentage less than 5 µm of greater than 93%. This ensures that the majority of API particles in each pMDI have the required diameter in order to reach the bronchioles in the lung which are the desired therapeutic target area. The electrostatic precipitation sections of the bp-NGI were connected to stage 2 of the NGI with a particle cut off diameter of 6.40µm. Therefore the majority of the FPF was expected to enter the electrostatic precipitation sections of the bp-NGI.

The bipolar charge nature of aerosol particles from commercial Flixotide™ 250, Serevent™ 25 and Seretide™ 250 pressurised metered dose inhalers were measured using the bp-NGI apparatus. For each inhaler, the mass deposition profile within the

electrostatic precipitators and the bipolar charge measurements of the APIs were measured at 0 V and ±3 kV. These measurements were used to calculate the charge to mass ratio of both the negatively and positively charge aerosols for each inhaler.

5.3.2 Bipolar Charge to Mass Ratio Determination of Flixotide™ 250

The mass deposition profile of FP from a commercial Flixotide™ 250 pMDI on the various sections of a bp-NGI at 0 V and ±3 kV are shown in Figures 5.4 A and B, respectively, and summarised in Table 5.2. These data are expressed in terms of the mean quantity of drug deposited on each of the precipitation tubes, electrodes and filters and the relative percentage of the total amount of drug entering each precipitation section. When no voltage is applied to the central electrodes of the bp-NGI, over 95% of the particles were recovered from the filters. The minimal deposition of FP on the electrodes and precipitation tubes at 0V suggested that a laminar flow was maintained within each section. At 0V, there was no significant difference ($p > 0.05$) in the quantities of FP entering each precipitation section of the bp-NGI (150.0 ± 10.7 µg and 149.4 ± 6.8 µg), indicating efficient bifurcation of the aerosol dose.

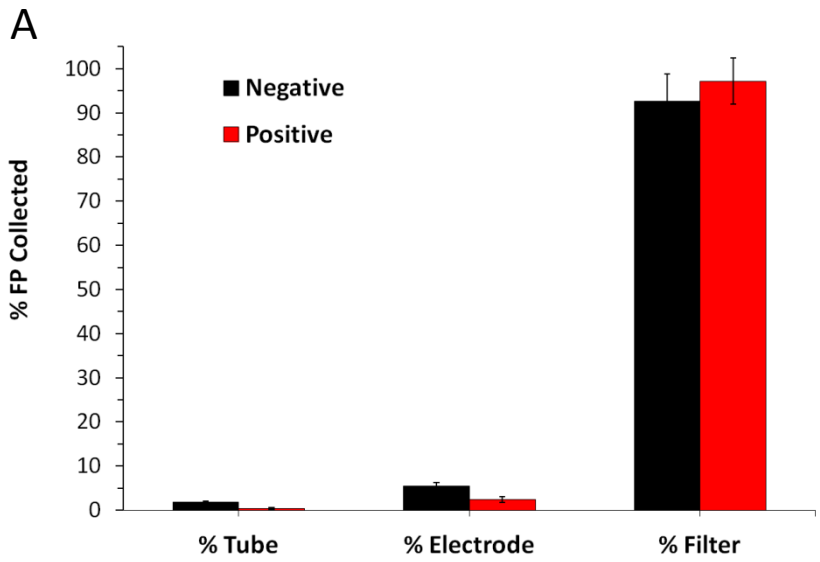

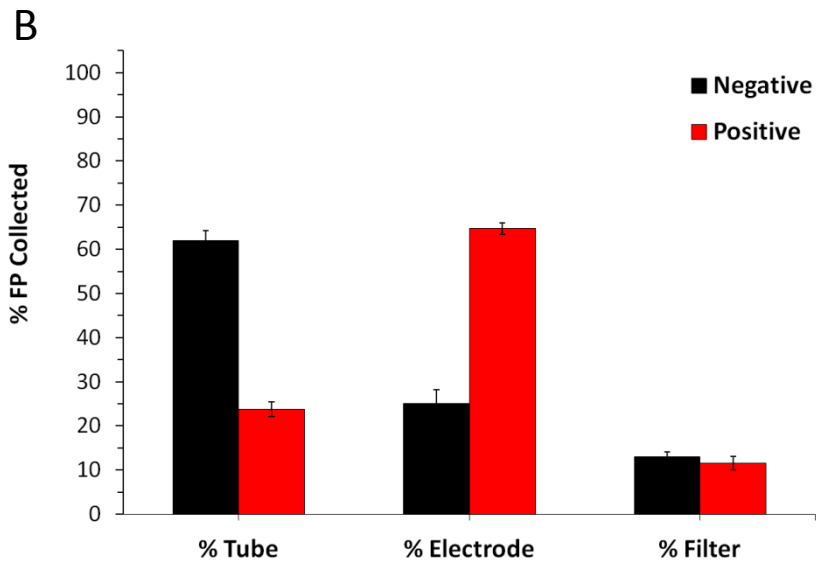

Figure 5.4 Percentage mass of FP particles deposited within the within the bp-NGI from 5 shots of Flixotide™ 250 (n=3, mean ± SD) at A, 0 Volts and B ±3000 Volts.

	0 Volts				±3000 Volts			
	Negative Section (µg ± SD)	Positive Section (µg ± SD)	Negative Section (% ± SD)	Positive Section (% ± SD)	Negative Section (µg ± SD)	Positive Section (µg ± SD)	Negative Section (% ± SD)	Positive Section (% ± SD)
Tube	2.8 ± 0.3	0.6 ± 0.3	1.9 ± 0.2	0.4 ± 0.2	95.2 ± 3.6	35.0 ± 2.5	62.0 ± 2.3	23.8 ± 1.7
Electrode	8.3 ± 1.1	3.7 ± 1.1	5.5 ± 0.8	2.4 ± 0.7	38.4 ± 4.9	95.1 ± 2.0	25.0 ± 3.2	64.7 ± 1.4
Filter	139.0 ± 9.3	145.2 ± 2.3	92.7 ± 6.2	97.2 ± 5.2	19.9 ± 1.6	17.0 ± 2.3	13.0 ± 1.2	11.6 ± 1.6
Total	150.0 ± 10.7	149.4 ± 6.8	100.0 ± 7.1	100.0 ± 6.1	153.5 ± 10.0	147.0 ± 6.8	100.0 ± 6.6	100.00 ± 4.6

Table 5.2 Mass and Percentage mass of FP particles deposited within the bp-NGI from 5 shots of Flixotide™ 250 (n=3, mean ± SD) at A, 0 Volts and B ±3000 Volts

Upon applying -3 kV and +3 kV to the central electrodes of the two precipitators, similar quantities of FP were recovered although only a relatively small percentage of the dose was collected on the filter. The percentage of aerosol particles collected on the

negative and positive filters at ± 3.0 kV was 13.0 ± 1.2% and 11.6 ± 1.6%, respectively. For the positive precipitator section (+3.0 kV), 64.7 ± 1.4% of the mass collected was recovered on the central electrode, with 23.8 ± 1.7% of the aerosols precipitating on the positive precipitation tube. For the negative precipitator section (-3.0 kV), 25.0 ± 3.2% of the mass was collected on the central electrode, with 62.0 ± 2.3% on the negative precipitation tube. The mass ratios of the negatively to positively charged particles on the positive and negative sections of the bp-NGI were an average of 2.6:1. These data suggest that FP particles undergo sufficient triboelectrification upon aerosolisation to be electrostatically precipitated and that the FP aerosols exhibit a bipolar charge distribution with the greater amount of sub 6.40 µm particles being negatively charged.

The charge measurements from the precipitation tubes of the two sections (labelled negative and positive) at 0V are shown in Figure 5.5 A and the corresponding charge measurements from the precipitated particles on the outer tube of the negatively and positively charged electrodes at ±3.0 kV are shown in Figure 5.5 B.

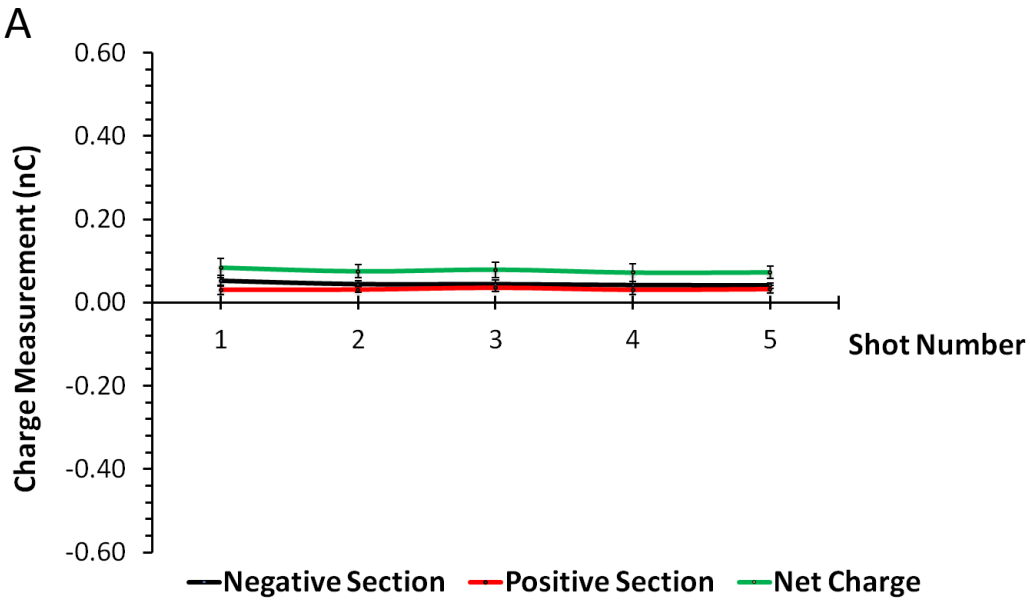

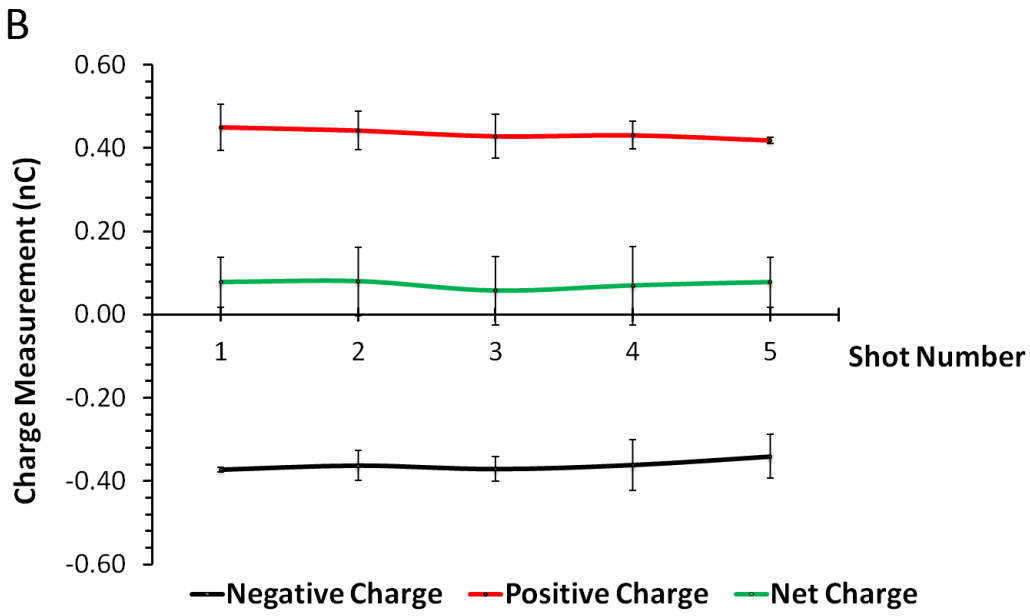

Figure 5.5 Charge measurements of FP particles deposited within the bp-NGI from 5 shots of Flixotide™ 250 (n=3, mean ± SD) at A, 0 Volts and B ±3000 Volts

Measuring in current versus time mode at 0V, each precipitation section measures the overall net charge of the small fraction of the aerosol dose that was collected on the tube surface for each actuation. Both sections exhibited a net positive charge (average +0.04 ± 0.003 nC), which is in agreement with the research findings of Peart *et al*., that showed unlike the majority of marketed pMDI products, GSK's US FP pMDI product (Flovent®) consistently produced a net positively charged aerosol cloud for the fine particle dose (Peart *et al*. 2003). Conversely, Hoe *et al*., who used an electrical Next Generation Impactor (eNGI) to measure the net charge of Flixotide™ and Seretide™ on individual stages at three different flow rates, found that the net charge to mass ratios for particles of FP and Salmeterol were slightly negative and close to zero pC/µg (Hoe 2009). Kwok *et al*. used a Faraday Well and also the ELPI to measure the net charge to mass ratios of a range of pMDIs including Flixotide [4]. For Flixotide, the overall net charge of the entire dose as measured with the Faraday well was found to be positive whereas on the ELPI stages, the FP particles were found to have net charges which were predominantly negative.

Upon applying a -3.0 kV and +3.0 kV DC voltage to the respective negative and positive electrodes, the mean charge of the negatively charged FP particles per shot

was recorded as -0.36 ± 0.01 nC, and the mean charge of the positively charged FP particles per shot was +0.43 ± 0.01 nC. The polarity of the mean net charge of the fine particle cloud per shot was electropositive and calculated to be +0.07 ± 0.01 nC. The net charge data for the aerosol dose below ≤ 6.4 µm at both 0 V and ± 3.0 kV are in good agreement with previous findings.

The bipolar charge to mass (Q/m) ratios of Flixotide™ 250 are shown in Figure 5.6. The charge to mass ratios of the negatively and positively charged particles was -18.0 ± 2.8 pC/µg and +68.8 ± 5.6 pC/µg respectively. These data indicate that although there were fewer positively charged particles, their charge per unit mass was significantly larger in magnitude than the negatively charged particles. The net charge to mass ratio is not a sum of the negative and positive charge to mass ratios as the quantity of negatively and positively charged particles is different. Instead, the net charge to mass ratio is calculated by dividing the total net charge as sum of the average negative and positive charges per shot by the total mass of the negatively and positively charged particles collected on each precipitation tube combined per shot. The overall net charge to mass ratio was much lower in magnitude (-0.9 ± 7.2 pC/µg) than the bipolar charge to mass ratios, and provides less detail of the electrostatic behaviour of the aerosol cloud emitted by the pMDI.

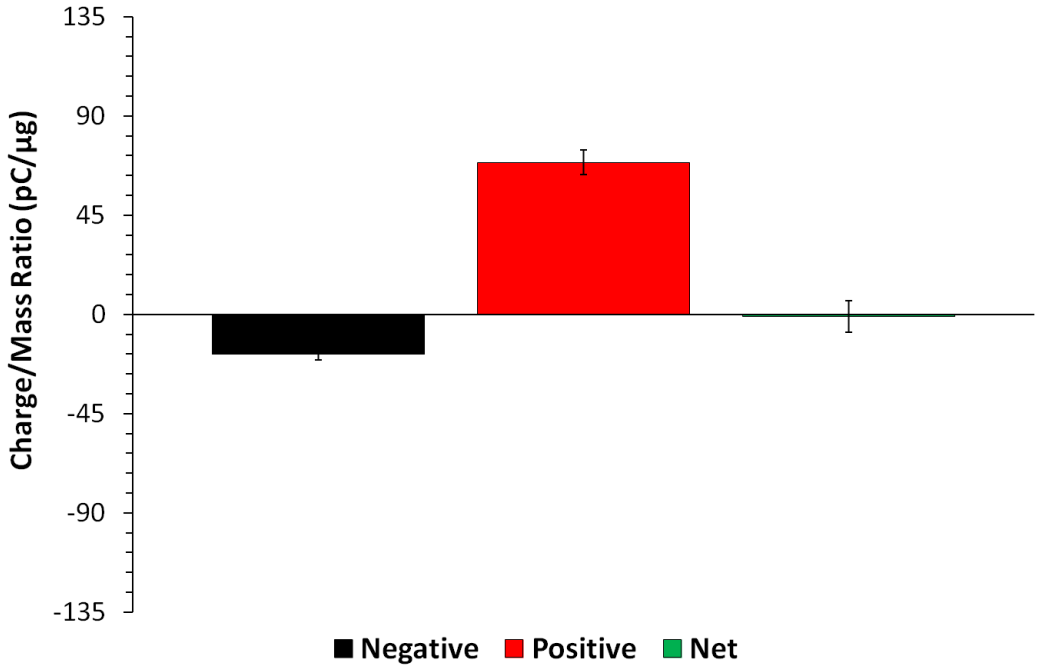

Figure 5.6 Bipolar charge to mass ratios of FP particles from 5 shots of Flixotide™ 250 (n=3, mean ± SD)

5.3.3 Bipolar Charge to Mass Ratio Determination of Serevent™ 25

The mass deposition profile of SX from a commercial Serevent™ 25 pMDI on the various sections of a bp-NGI at 0 V and ±3.0 kV are shown in Figures 5.7 A and 5.7 B, respectively and the data tabulated in Table 5.3. At 0 V, over 88% of the particles were collected on the filters, with no significant differences in the quantities entering each precipitator and that collected on respective filters ($p>0.05$).

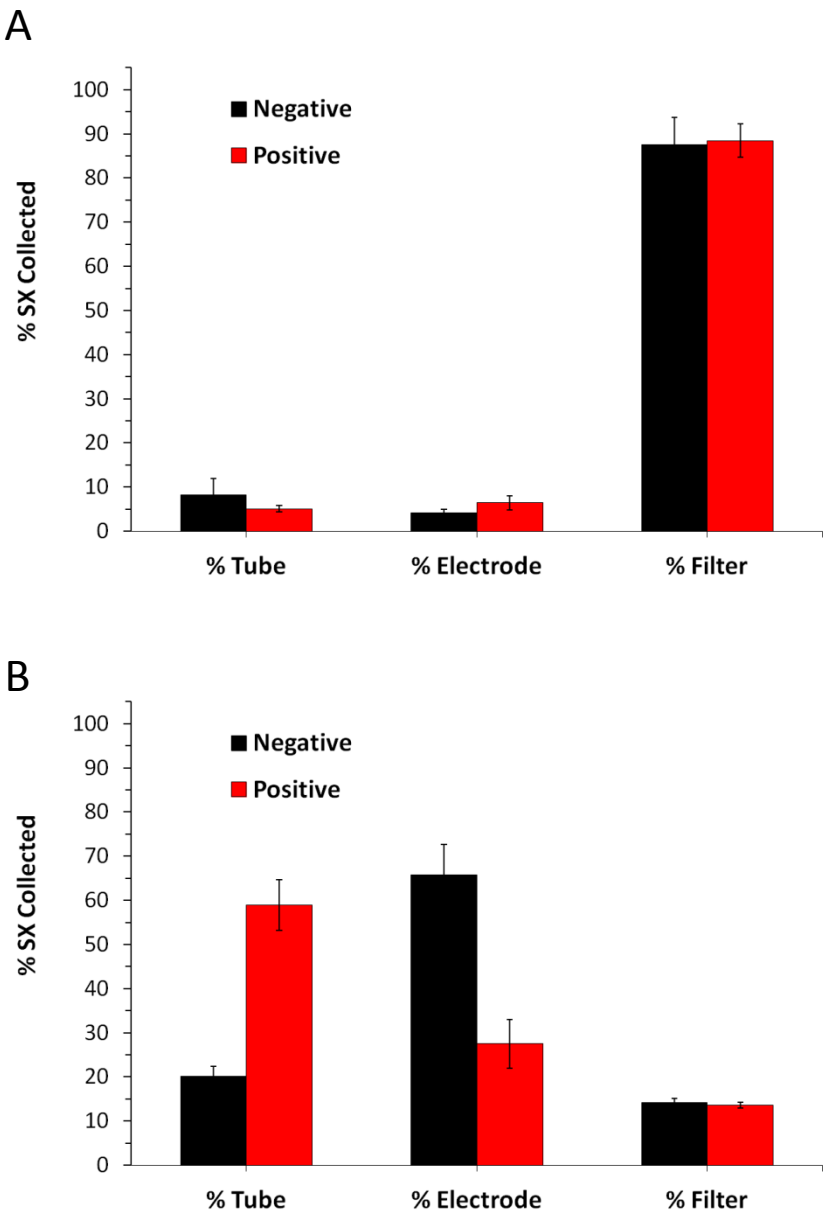

Figure 5.7 Percentage mass of SX particles deposited within the within the bp-NGI from 5 shots of Servent™ 25 (n=3, mean ± SD) at A, 0 Volts and B ±3000 Volts.

	0 Volts				±3000 Volts			
	Negative Section (µg ± SD)	Positive Section (µg ± SD)	Negative Section (% ± SD)	Positive Section (% ± SD)	Negative Section (µg ± SD)	Positive Section (µg ± SD)	Negative Section (% ± SD)	Positive Section (% ± SD)
Tube	2.0 ± 0.9	1.2 ± 0.2	8.2 ± 3.8	5.1 ± 1.4	7.8 ± 0.8	21.5 ± 1.9	20.1 ± 2.29	58.9 ± 5.7
Electrode	1.0 ± 0.2	1.6 ± 0.4	4.2 ± 0.8	6.4 ± 1.8	20.1 ± 2.4	7.1 ± 1.8	65.7 ± 6.9	27.9 ± 5.5
Filter	21.5 ± 1.4	21.5 ± 0.9	87.6 ± 6.0	88.5 ± 3.8	4.7 ± 0.3	4.4 ± 0.2	14.2 ± 1.0	13.6 ± 0.7
Total	23.8 ± 2.5	24.3 ± 1.5	100.0 ± 10.6	100.0 ± 6.1	32.6 ± 3.5	33.0 ± 3.9	100.0 ± 10.2	100.0 ± 11.9

Table 5.3 Mass and Percentage mass of SX particles deposited within the bp-NGI from 5 shots of Serevent™ 25 (n=3, mean ± SD) at A, 0 Volts and B ±3000 Volts

Applying a ±3.0 kV potential to the central electrodes significantly reduced the deposition of SX on the filters ($p > 0.05$). The percentage of low electrical mobility particles recovered from the filters dropped to below 14%. For both precipitators, there was a significantly greater recovery of positively charged SX particles than negatively charged SX particles. The mass ratio of positively charged to negatively charged particles in both precipitators was approximately 3:1. These findings are in contrast to the Flixotide™ 250 data, which showed the opposite trend.

The charge measurements from the outer precipitation tubes for the charged salmeterol particles for five consecutive shots at 0 V and ±3.0 kV is shown in Figures 5.8 A and 5.8 B, respectively. With no voltage applied, measurements indicated that the net charge of SX particles were low and slightly electropositive for both precipitators.

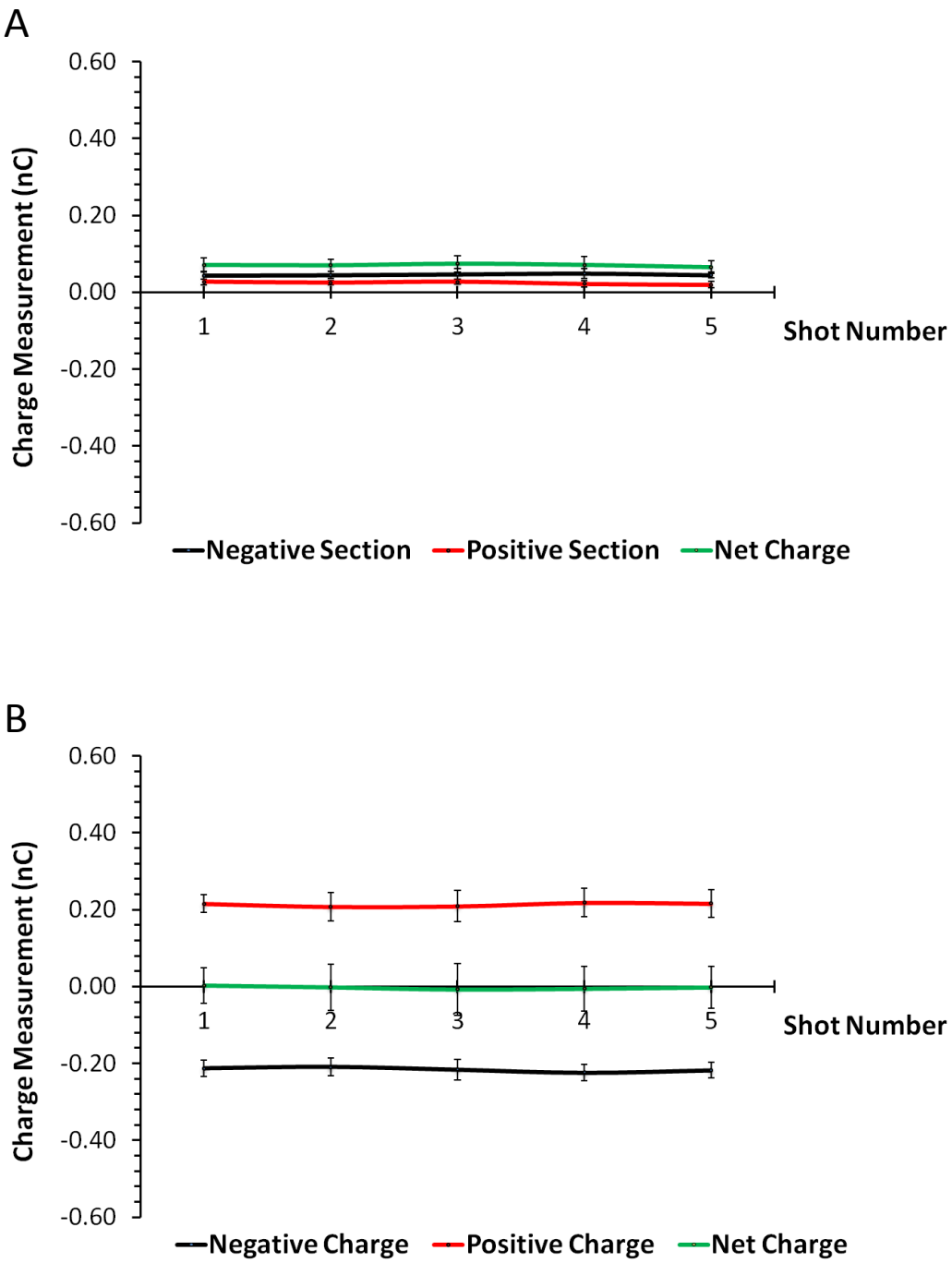

Figure 5.8 Charge measurements of SX particles deposited within the bp-NGI from 5 shots of Serevent™ 25 (n=3, mean ± SD) at A, 0 Volts and B ±3000 Volts.

Upon applying a -3.0 kV and +3.0 kV DC voltage to the respective negative and positive electrodes, there was no significant differences in the mean charge per shot of the negatively and positively charged SX particles.

The charge to mass ratios of the negatively and positively charged particles as shown in Figure 5.9 were -106.2 ± 23.4 pC/µg and +43.7 ± 3.3 pC/µg, respectively. These data indicate that while there were fewer negatively charged particles, their charge was significantly larger in magnitude than the positively charged particles which is in reverse to the trend observed for FP in Flixotide. The overall net charge to mass ratio was significantly lower in magnitude (+3.7 ± 4.5 pC/µg) than the bipolar charge to mass ratios ($P<0.05$).

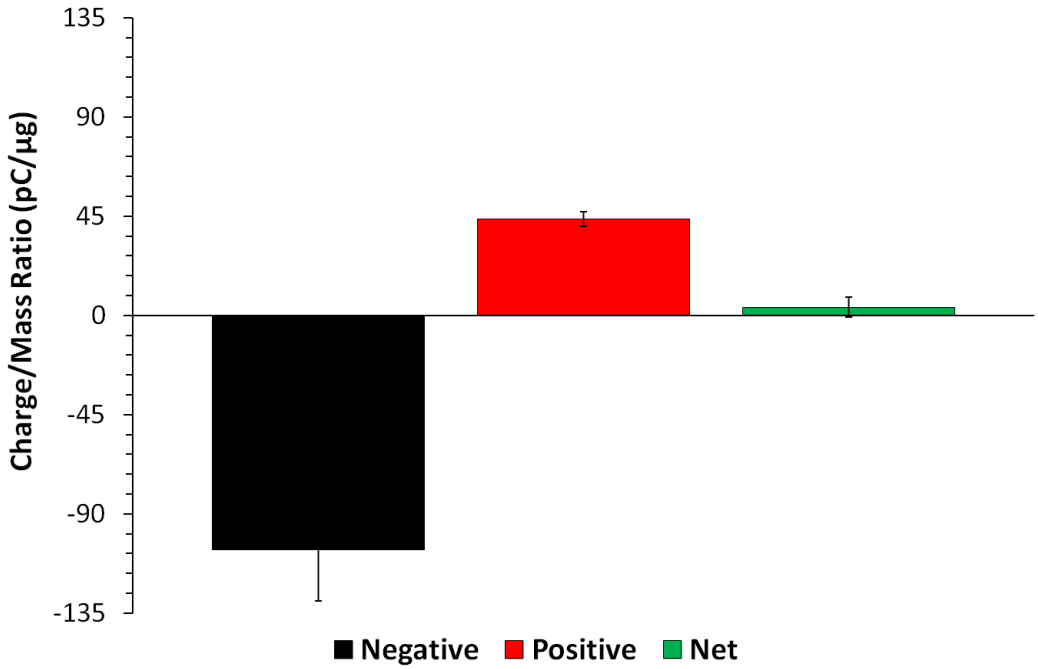

Figure 5.9 Bipolar charge to mass ratios of SX particles from 5 shots of Serevent™ 25 (n=3, mean ± SD)

5.3.4 Bipolar Charge to Mass Ratio Determination of Seretide™ 250

The mass deposition profile of FP and salmeterol from a commercial Seretide™ 250 pMDI on the various sections of a bp-NGI at 0 V and ±3 kV are shown in Figures 5.10 A-D respectively, and summarised in Tables 5.4 and 5.5.

These data show that at 0V, as shown in the other formulations, the majority of the FP and SX particles are collected on the filters, with over 85% of the recovered dose in both precipitators. Upon applying a high voltage (±3.0 kV), similar quantities of FP and

SX were recovered from each precipitation section of the bp-NGI, indicating efficient bifurcation of the fine particle cloud within the system. The mass ratio of negatively to positively charged particles of precipitated FP is 2.6:1 which is similar to that obtained for the mono Flixotide™ product.

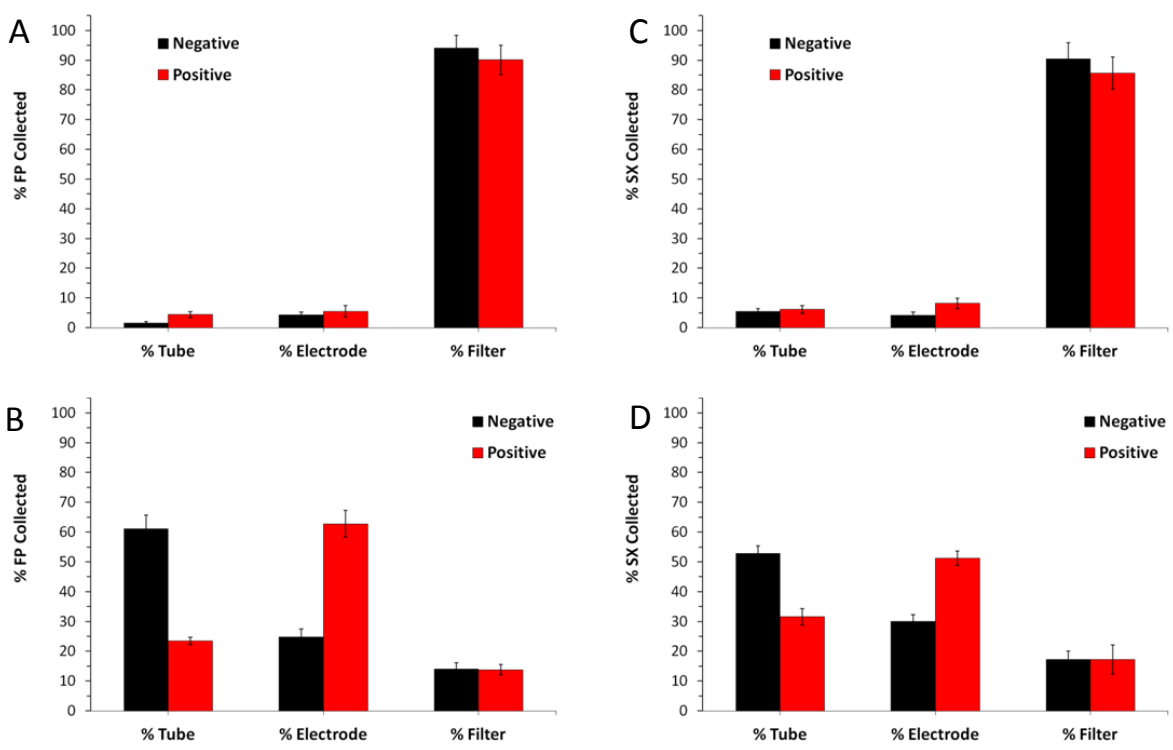

Figure 5.10 Percentage mass of FP particles deposited within the within the bp-NGI from 5 shots of Seretide™ 250 at A, 0 Volts and B ±3000 Volts and percentage mass of SX particles deposited at C, 0 Volts and D ±3000 Volts (n=3, mean ± SD).

	0 Volts				±3000 Volts			
	Negative Section (µg ± SD)	Positive Section (µg ± SD)	Negative Section (% ± SD)	Positive Section (% ± SD)	Negative Section (µg ± SD)	Positive Section (µg ± SD)	Negative Section (% ± SD)	Positive Section (% ± SD)
Tube	2.3 ± 0.7	6.9 ± 1.6	1.6 ± 0.48	4.4 ± 1.0	105.6 ± 7.8	40.7 ± 2.2	61.2 ± 4.51	23.5 ± 1.3
Electrode	6.1 ± 1.3	8.7 ± 2.9	4.3 ± 0.89	5.5 ± 1.9	42.8 ± 4.7	108.4 ± 7.8	24.8 ± 2.7	62.7 ± 4.5
Filter	133.8 ± 6.1	141.8 ± 7.7	94.1 ± 4.3	90.1 ± 4.9	24.4 ± 3.4	23.8 ± 3.1	14.1 ± 2.0	13.8 ± 1.8
Total	142.4 ± 8.0	157.4 ± 12.2	100.0 ± 5.6	100.0 ± 7.7	172.7 ± 15.8	172.9 ± 13.0	100.0 ± 9.2	100.0 ± 7.5

Table 5.4 Mass and Percentage mass of FP particles deposited within the bp-NGI from 5 shots of Seretide™ 250 (n=3, mean ± SD) at A, 0 Volts and B ±3000 Volts

	0 Volts				±3000 Volts			
	Negative Section (µg ± SD)	Positive Section (µg ± SD)	Negative Section (% ± SD)	Positive Section (% ± SD)	Negative Section (µg ± SD)	Positive Section (µg ± SD)	Negative Section (% ± SD)	Positive Section (% ± SD)
Tube	1.3 ± 0.2	1.6 ± 0.4	5.4 ± 1.0	6.1 ± 1.4	13.3 ± 0.67	9.1 ± 0.8	52.8 ± 2.7	31.6 ± 2.7
Electrode	1.0 ± 0.2	2.1 ± 0.5	4.2 ± 1.0	8.2 ± 1.8	7.6 ± 0.6	14.7 ± 0.7	30.1 ± 2.2	51.2 ± 2.4
Filter	21.2 ± 1.3	21.9 ± 1.4	90.4 ± 5.4	85.7 ± 5.4	4.3 ± 0.7	4.9 ± 1.4	17.2 ± 2.9	17.2 ± 4.9
Total	23.4 ± 1.8	25.5 ± 2.2	100.0 ± 7.5	100.0 ± 8.6	25.2 ± 2.0	28.7 ± 2.9	100.0 ± 7.8	100.0 ± 10.0

Table 5.5 Mass and Percentage mass of SX particles deposited within the bp-NGI from 5 shots of Seretide™ 250 (n=3, mean ± SD) at A, 0 Volts and B ±3000 Volts

The mass ratio of negatively to positively charged of precipitated SX particles is 1.7:1. This is opposite to the trend in the Serevent data set, which indicated the mass ratio of negatively to positively charged SX particles to be 0.6:1. These data suggest that the presence of a relatively high dose of FP compared to SX may have a significant impact on the mass deposition profile of SX within an electrostatic precipitator. The different deposition profile of SX particles may suggest that SX may form agglomerates with FP and therefore altering its response to an electric field. Agglomerate formation of FP and SX has previously been reported for Seretide pMDI formulation by (GSK) Raman spectroscopy. As was seen in Flixotide and Seretide, the FP particles show a greater propensity to become more negatively charged than positive, thus in Seretide, there is the potential to form aggregates between negatively charged FP particles and positively charged salmeterol particles via Coulombic attractive forces. The presence of FP-SX agglomerates in Seretide has recently been confirmed by Rogueda *et al*. who tested the *in vitro* performance of Seretide with an Andersen Cascade Impactor (ACI) and subsequently used Raman Spectroscopy and AFM imaging to map the distribution of FP and SX on the impaction plates (Rogueda *et al*. 2011). If, for example, an aggregate is formed with one salmeterol particle of +1 arbitrary charge unit and two FP particles with -1 arbitrary charge units or one salmeterol particle of +1 arbitrary charge units and one FP particle of -2 arbitrary charge units, the overall net charge of the aggregate will be -1 arbitrary charge units and so the whole aggregate, including the positively charge salmeterol particle will be deposited onto the negative precipitation tube. The formation of a large number of these kinds of aggregates will result in the salmeterol particles appearing to be negatively charged when it is in fact the overall negative charge of the FP-salmeterol aggregates which may cause the behaviour observed.

The charge measurements of FP and SX per shot recorded at 0V and ±3.0kV are shown in Figures 5.11 A and 5.11 B respectively. At 0V, the net charge measurement in each precipitation was low and positive. At ±3.0 kV, the average charge measured per shot for the negative and positive precipitators were 0.37 ± 0.006 nC and +0.47 ± 0.010 nC, respectively, with an average net charge per shot of +0.10 ± 0.010 nC. These results are similar to that observed for Flixotide™, with the fine particle dose being overall electropositive in nature indicating that the overall bipolar charge to mass values of Seretide™ are dominated by the FP particles which are in large excess with a dose ratio of 10:1 FP:SX.

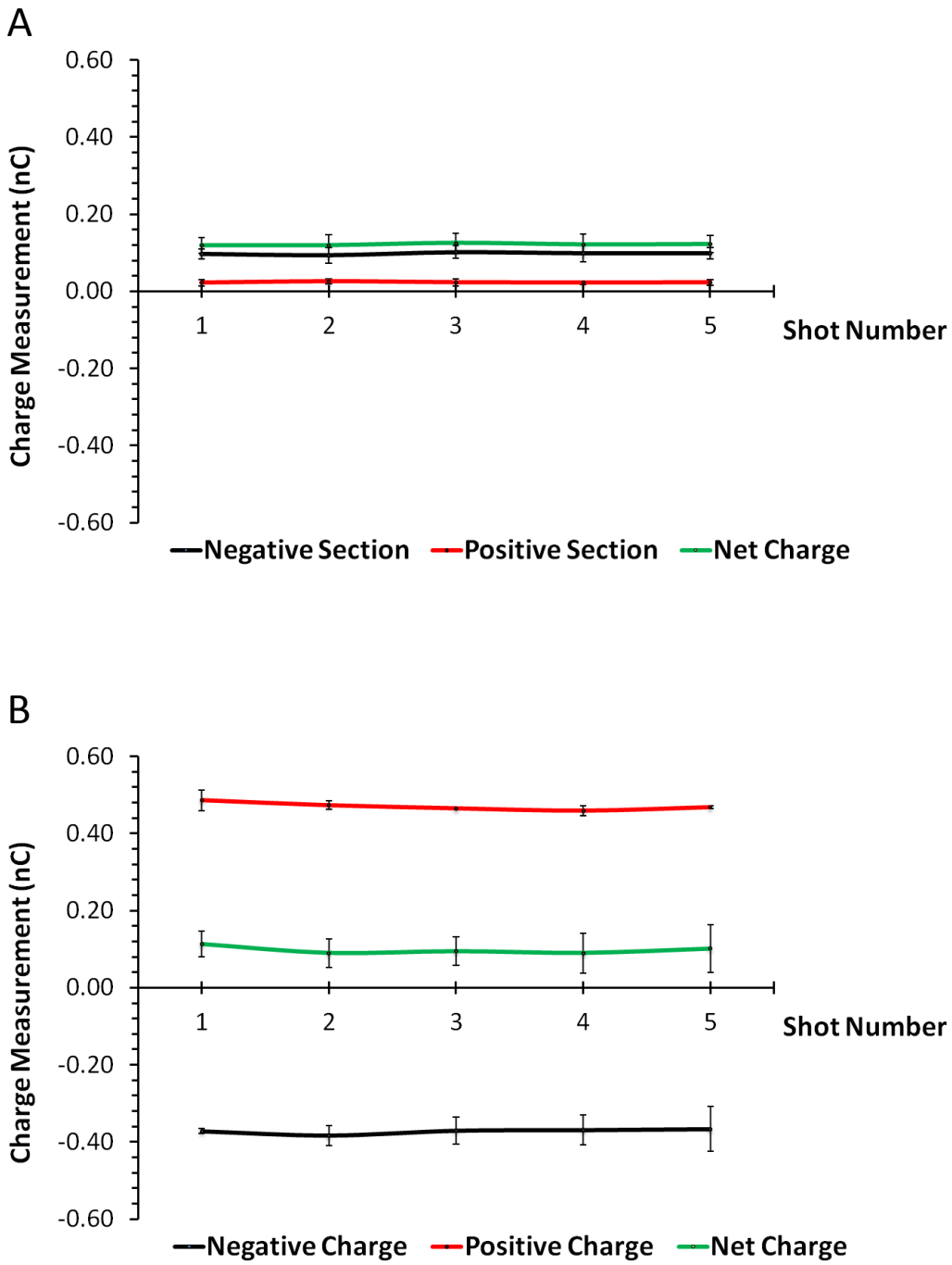

Figure 5.11 Charge measurements of FP and SX particles deposited within the bp-NGI from 5 shots of Seretide™ 250 (n=3, mean ± SD) at A, 0 Volts and B ±3000 Volts.

The bipolar charge to mass ratios of Seretide™ 250 are shown in Figure 5.12. The charge to mass ratios of the negatively and positively charged particles were -11.5 ± 0.5 pC/µg and +42.8 ± 4.6 pC/µg respectively. These data indicate that although there were more negatively charged particles, the charge per unit mass was larger for the positively charged particles. This is the same trend that was observed for FP in

Flixotide™. The overall net charge to mass ratio was again much lower in magnitude (+2.6 ± 0.4pC/µg) than the bipolar charge to mass ratios. These findings suggest that presence of salmeterol in Seretide has little effect on the electrostatic precipitation properties.

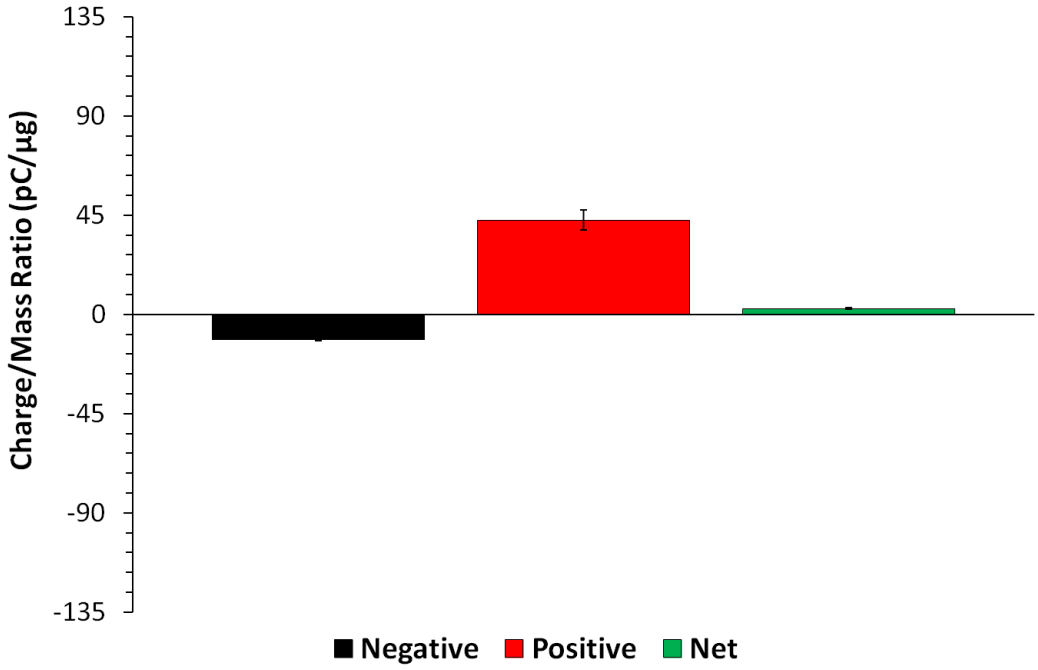

Figure 5.12 Bipolar charge to mass ratios of FP and SX particles from 5 shots of Seretide™ 250 (n=3, mean ± SD).

A summary of the percentage mass distributions recorded by the negative precipitation section of the bp-NGI of the various drug particles from each pMDI are shown in Table 5.6. For FP, the results for Flixotide 250™ and Seretide 250™ are very similar showing 62.0 ± 2.3% and 61.2 ± 4.5% for the percentage of negatively charged particles, 25.0 ± 3.2% and 24.8 ± 2.7% for the positively charged particles and 13.0 ± 1.2% and 14.1 ± 1.98% for the uncharged particles respectively. This indicates that the presence of salmeterol in Seretide has little effect on the electrostatic properties of FP within a pMDI. For salmeterol, the results for Seretide 250™ and Serevent 25™ are very different. Values of 52.8 ± 2.7% and 20.1 ± 2.3% for the percentage of negatively charged particles, 30.1 ± 2.2% and 65.7 ± 6.9% for the positively charged particles and 17.2 ± 2.9% and 14.2 ± 1.0% for the uncharged particles were recorded respectively. In the mono dose Serevent 25™, the Salmeterol particles show a propensity to become

more positively charged than negatively charged however, in Seretide 250™ the reverse trend is observed.

	Flixotide 250™ FP	Seretide 250™ FP	Seretide 250™ 250 SX	Serevent™ 25 SX
Negative Particles (% ± SD)	62.0 ± 2.3	61.2 ± 4.5	52.8 ± 2.7	20.1 ± 2.3
Positive Particles (% ± SD)	25.0 ± 3.2	24.8 ± 2.7	30.1 ± 2.2	65.7 ± 6.9
Uncharged Particles (% ± SD)	13.0 ± 12	14.1 ± 2.0	17.2 ± 2.9	14.2 ± 1.0

Table 5.6 Summary of the mass deposition of negatively, positively and uncharged particles from each pMDI (n=3, mean ± SD)

A summary of the average negative, positive and net charge per shot of drug particles from each pMDI at ±3 kV is shown in Table 5.7. These data show that the values for the charge recorded for Flixotide™ 250 and Seretide™ 250 were very similar (-0.36 ± 0.01 nC and -0.37 ± 0.01 nC for the negatively charged particles, +0.43 ± 0.01 nC and +0.47 ± 0.010 nC for the positively charged particles and 0.07 ± 0.01 nC and +0.10 ± 0.01 nC for the net charge of the particles). This shows that the addition of the small dose of salmeterol in Seretide does not overly affect the values of the charge measurements recorded, presumably as the dose of salmeterol is only 10% of that of the dose of FP. The values for the charge recorded for Serevent ™ 25 are, however, appreciable (-0.22 ± 0.01 nC for the negatively charged particles, +0.21 ± 0.01 nC for the positively charged particles and -0.003 ± 0.004 nC for the net charge of the particles). The absence of FP in Serevent™ 25 results in different charging characteristics for the salmeterol particles vs Seretide™ 250.

	Average Negative Charge Per Shot (nC ± SD)	Average Positive Charge Per Shot (nC ± SD)	Average Net Charge Per Shot (nC ± SD)
Flixotide™ 250	-0.36 ± 0.01	+0.43 ± 0.01	+0.07 ± 0.01
Seretide™ 250	-0.37 ± 0.01	+0.47 ± 0.01	+0.10 ± 0.01
Serevent™ 25	-0.22 ± 0.01	+0.21 ± 0.01	-0.003 ± 0.004

Table 5.7 Average negative, positive and net charge per shot from each pMDI. (n=3, mean ± SD)

5.4 Conclusions

This study demonstrates that more negatively charged particles were produced than positively charged from both Flixotide™ and Seretide™ in terms of mass deposited, although the charge to mass ratios of the positively charged particles were larger in magnitude than the negatively charged. In the case of Serevent, the SX particles showed a propensity to become more positively charged than negatively charged, however, the charge to mass ratios of the negatively charged particles were significantly larger in magnitude. The difference in behaviour between the SX particles in Serevent™ and Seretide™ may be attributed to the presence of FP-SX aggregates in Seretide™ which are not present in Serevent™. The results of the study illustrate that the bp-NGI is an effective tool to quantify the bipolar charge to mass ratios of respirable aerosol particles produced by the three commercially available pMDIs.

Comparisons with data generated by Kwok *et al*. with the ELPI indicated that the positive charge values recorded may have been contributed to by the presence of ice crystals exiting the inhaler as the pMDI propellant evaporated (Kwok *et al*. 2008). A control experiment is suggested to characterise a propellant only pMDI formulation; values for the propellant bipolar charge could be subtracted from the overall bipolar charge in order to determine the contribution of the API to the charge values.

Unfortunately placebo pMDI canisters of Flixotide™, Serevent™ and Seretide™ are not commercially available and could not be analysed for this study.

Further studies suggested include measuring the bipolar charge distributions of other pMDI formulations such as QVAR® and Ventolin® with the bp-NGI and comparing the bipolar charge to mass ratio values recorded with net charge to mass ratio values published in the literature. Other variables such as flow rate, dosage strength, humidity and the type and colour of the polymer used to disperse a pMDI could also be investigated as well as the addition of a spacer device. The bipolar charge of only the combined fine particle fraction from the bp-NGI from stages 2 and below of the NGI were collected, additional experiments could also be performed to connect the electrostatic precipitation system to the other stages in order to build up a more accurate picture of the relationship between aerosol particle charge and aerodynamic diameter cut off.

Chapter 6 The effect of relative humidity on the electrostatic properties of a budesonide DPI formulation

6.1 Introduction

DPI blends are manufactured using a number of steps which may induce electrostatic charge on the formulation including sieving and blending (Engers *et al*. 2006). It has been suggested that the static charge decay time of active pharmaceutical ingredients (APIs) in a DPI formulation may be long (Carter *et al*. 1998, Sharma *et al*. 2003), particularly when then initial charge generated on the particles is very large and that electrostatic charges introduced to the API particles during formulation may lead to changes in product performance (Elajnaf *et al*. 2007). The effect of storage relative humidity (RH) is also important as increased RH may result in lower initial quantities of charge building up on the DPI particles and also increase charge decay rate times (Kwok and Chan 2008b). However, if the humidity is too high, an adverse effect on performance may be observed with a drop in fine particle fraction and fine particle dose (Maggi *et al*. 1999, Voss and Finlay 2002). Young *et al*. showed a decrease in performance of a salbutamol sulphate DPI formulation at relative humidities above 60% (Young *et al*. 2007). The storage conditions may also affect the moisture content, crystallinity, polymorphism and chemical degradation of the API (Hickey and Martonen 1993). Due to these complex factors, it is expected that both the manufacturing process and the storage conditions will affect the physical and chemical stability of the formulation (Telko and Hickey 2005) and also its electrostatic properties. As processes used during formulation of a DPI blend may generate electrostatic charge on the API particles, it would be useful to measure the initial bipolar charge on the aerosol particles generated by a DPI and at subsequent time points post blending to determine if indeed charge is present on the particles and whether this charge relaxes over time.

This study is designed to determine the electrostatic properties and formulation performance of a laboratory scale, low shear, DPI blend of budesonide with Respitose® ML001, an inhalation grade lactose. Testing was performed with the bp-NGI and with the conventional NGI in order to determine both the extent of triboelectrification of the respirable dose aerosol particles and the formulation performance as a function of storage relative humidity. Measurements of the dynamic charge of the device and capsule and net charge of the capsule were also performed

using the flow through Faraday pail as used by previous researchers (Murtomaa *et al*. 2004, Chow *et al*. 2008, Karner and Urbanetz 2013) and Faraday pail respectively using experimental set up as described in Chapter 2. By recording the device, capsule and aerosol particle charge simultaneously a more complete picture of the nature of electrostatic charge build up during aerosolisation of a DPI formulation may be determined.

6.2 Materials and Methods

6.2.1 Materials

Micronised budesonide and Aerolizer® devices were supplied by Novartis Pharma AG (Basel, Switzerland). Respitose® ML001 lactose was obtained from DFE Pharma Excipients (Veghel, The Netherlands). Size 3 HPMC capsules were sourced from Qualicaps (Madrid, Spain). Samples were stored in sealed humidity cabinets with a saturated salt solution of potassium carbonate at 43% RH (Fisher Bioreagents, NJ, USA) in an air conditioned room maintained at 20 ± 2 ºC. All solvents used were of HPLC grade (Sigma-Aldrich, St. Louis, MO, USA). Ultra-pure water was produced by reverse osmosis (MilliQ, Millipore, Molsheim, France).

6.2.2 Methods

6.2.2.1 Particle size

Particle size measurements of ML001 were measured dispersed dry at a pressure of 2 bars using a Sympatec Helos laser diffraction system with an R4 lens in conjunction with a RodosT4 disperser and a Vibri feeder controlled by WINDOX software (Sympatec Gmbh, Germany). Particle size measurements of micronised budesonide were measured dispersed wet using the cuvette dispersion system with 0.1% lecithin in cyclohexane as the dispersant. A small aliquot of budesonide was suspended in the dispersant, the suspension sonicated for five minutes at one minute intervals before five repeat measurements were recorded at an optical concentration of between 5 and 10%. The values recorded for the d_{10}, d_{50} and d_{90} were averaged as well as the percentage of particles less than 5 µm.

6.2.2.2 Scanning electron microscopy

Scanning electron microscopy (SEM) images of the lactose and budesonide samples were performed on a JEOL JSM-6480LV scanning electron microscope (JEOL, Tokyo, Japan). Samples were mounted on sticky carbon tabs and coated with an Edwards sputter coater S150B (Edwards, Israel) for 5 minutes prior to analysis. An acceleration voltage of 10 kilovolts was used for the imaging.

6.2.2.3 Preparation of the budesonide DPI formulation

The budesonide DPI formulation was prepared using a small scale laboratory method to make a total batch size of 80 grams. 10% of the required lactose was passed through a 250 µm mesh sieve, followed by the budesonide, followed by another 10% of the lactose in order to break up any large agglomerates. This sandwich was then preblended in a grade 316 stainless steel vessel using a WAB type T2F turbula blender (WAB, Nidderau-Heldenbergen, Germany) at 22 RPM for 20 minutes. Half of the remaining lactose required was passed through the 250 µm mesh sieve, followed by the preblend, followed by the remaining lactose. The formulation was then blended for a further 20 minutes at 22 RPM. Size three HPMC capsules were hand filled with the formulation using a five place analytical balance to obtain a capsule fill weight of 25 ± 0.1 mg. Capsules were transferred to a sealed storage cabinet maintained at 43% RH with a saturated solution of potassium carbonate and were stored at this humidity for a minimum of 72 hours prior to testing.

6.2.2.4 In vitro aerodynamic performance determination

The *in vitro* performance of the formulation was determined using the Next Generation Impactor (NGI) (Copley Scientific, Nottingham, UK). The Aerolizer® device was used for aerosolising the formulation into the NGI equipped with a pre-separator. The flow rate of air was set to 90 L/min for 2.7 seconds as controlled by a TPK critical flow controller (also Copley Scientific). A total of five capsules were used per test. The diluent used for recovery of the API was a degassed mixture of MeOH : Acetonitrile : Water 55:35:20 (v/v/v). The limit of detection for budesonide was determined to be 0.01 µg/mL and the response was linear between concentrations of 0.01 and 50 µg/mL. The

NGI was kept within the relative humidity cabinet throughout the testing and the relative humidity was maintained at 55%.

6.2.2.5 Bipolar charge to mass ratio measurements

The bipolar charge to mass ratios of the formulation were determined using the bipolar Next Generation Impactor (bp-NGI). The Aerolizer® device was used for aerosolising the formulation into the bp-NGI equipped with a pre-separator. The flow rate of air was set to 90 L/min for 2.7 seconds as controlled by a TPK critical flow controller (Copley Scientific, Nottingham, UK). The diluents used for the recovery of lactose and the API was a mixture of ACN and deionised H_2O (75:25% v/v). A total of five capsules were used for each test and testing for each condition was performed in triplicate. The Next Generator Impactor section of the bp-NGI was retained inside the Climatezone relative humidity cabinet to ensure humidity control of the environment was maintained. The voltage applied to the negative electrode was -3000V and the positive electrode was +3000V. The flow rate of the NGI was set to 90 L/min with 45 L/min pulled through each precipitator as a result of the bifurcation. Laminar flow was maintained through the system with a Reynold's number of 1413 through each precipitator.

6.2.2.6 HPLC analysis of budesonide

Determination of the mass distribution of budesonide from the NGI and bp-NGI was determined using reverse phase high performance liquid chromatography (RP-HPLC). The HPLC system consisted of a pump (Jasco PU-980, Jasco Corp., Japan) coupled to an autosampler (Jasco AS-950). A UV detector (Jasco UV-975) set at 260 nm was used for the determination of budesonide. Separation was performed using an ODS Hypersil Column, 200x4mm (Thermo Scientific, Waltham, MA, USA) maintained at 40^0C and the retention time for budesonide was 2.0 minutes. The mobile phase was a degassed mixture of MeOH : Acetonitrile : Water 55:35:20 (v/v/v). The retention time for budesonide was 4.1 minutes. Quantification was carried out by an external standard method and linearity was checked between 0.5 and 50 µg/mL. The limit of detection for budesonide was determined to be 0.01 µg/mL and the response was linear between concentrations of 0.1 and 50 µg/mL.

6.2.2.7 HPLC analysis of lactose

Lactose does not possess a UV active chromophore and so an evaporative light scattering detector (ELS 1000, Polymer Labs, Church Stretton, Shropshire, UK) was employed. Separation was performed using an APS-2 Hypersil Column, 100x3mm (Thermo Scientific, Waltham, MA, USA) maintained at 30ºC and the retention time for lactose was 1.37 minutes. The mobile phase consisted of 75 : 25 acetonitrile to deionised water and the injection volume was 100 µl. The nebuliser temperature of the ELS detector was set to 60ºC and the evaporation temperature to 110ºC. The flow rate was 1.0 ml/min and the gas flow rate was set to 1.5. Quantification was carried out by an external standard method and linearity was checked between 0.5 and 50 µg/mL. The plot of peak area against concentration was found to follow a quadratic function as has been observed previously with similar evaporative light scattering experiments (Kaufmann *et al*. 2001).

6.2.2.8 Dynamic charge measurement of the Aerolizer® device

The change in dynamic charge of the capsule and device during aerosolisation of the formulation from a capsule was determined using the Flow Through Faraday Pail using the method described in Chapter 2. Dynamic charge measurements were performed in combination with bipolar charge measurements of the aerosol particles using the bp-NGI.

6.2.2.9 Net charge measurements of the capsules

Immediately post aerosolisation of the formulation from a capsule, the empty capsule was dropped from the device into a Faraday pail. The net charge value was then recorded.

6.2.2.10 Testing regimen

Dynamic charge measurements of the device and capsule, bipolar charge measurements of the formulation and net charge measurements of the capsules were performed using the experimental set up as shown in Figure 6.1. This experimental set up allowed for simultaneous measurements of device, capsule and aerosol particle charge, all at a controlled relative humidity. The formulation was tested at relative

humidities of 35, 55 and 75% with a working hypothesis that the higher the relative humidity, the lower the electrostatic charge generated as well as the faster the charge decay rate. Based on work by Nemeth *et al.* and Mountain *et al.* who looked at the effect of relative humidity on the electrostatic properties of polymers, it was hypothesised that for the Aerolizer® device, which is made of a plastic polymer material, acrylonitrile butadiene styrene (ABS) an increase in % RH would result in a decrease in the surface potential and charge decay rate and therefore lower dynamic charge measurements using the flow through Faraday pail (Mountain *et al*. 2001, Nemeth *et al*. 2003).

6.2.2.11 Statistical analysis

Data was subjected to statistical analysis using Minitab statistical software version 16 (Minitab Ltd., Coventry, UK). One way ANOVA analyses were performed with Tukey's post-test to determine a 95% confidence interval defined as $p < 0.05$.

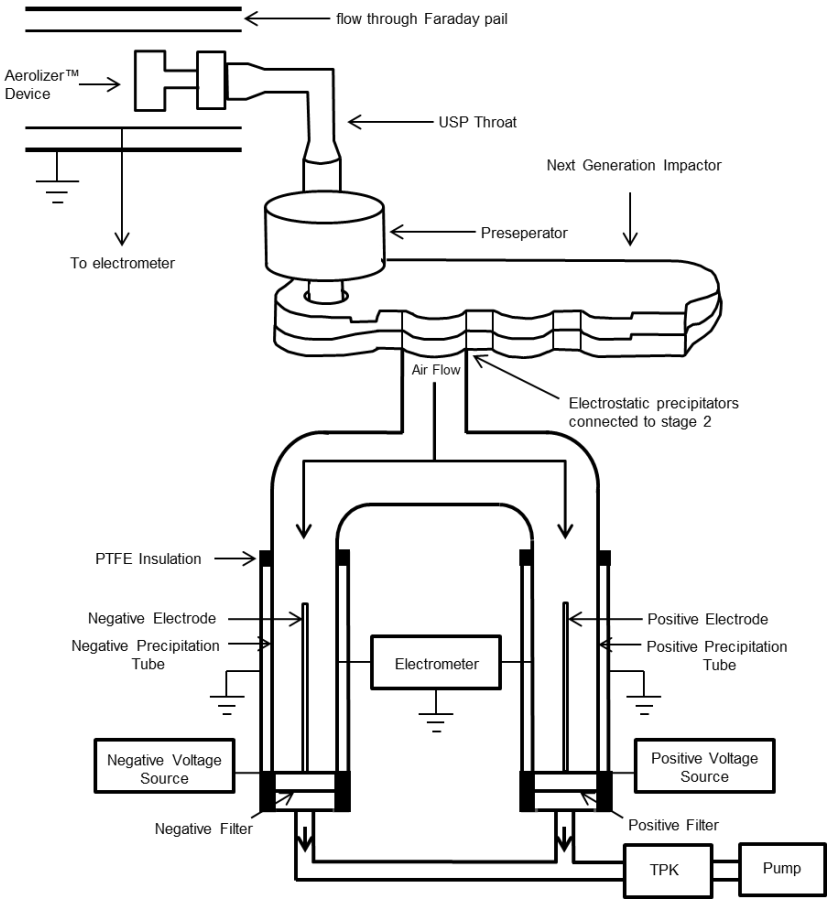

Figure 6.1 Experimental set up to perform electrostatic charge measurements of DPI formulations

6.3 Results and discussion

6.3.1 Particle size

The particle size distributions of ML001 and budesonide are displayed in Table 6.1 and the particle size distribution of budesonide is shown in Figure 6.2. The average (n=5) of the 10% undersize (d_{10}), 50% undersize (d_{50}) and 90% undersize (d_{90}) values were recorded as well as the percentage of particles with diameter less than 5 µm.

	d_{10} (µm)	d_{50} (µm)	d_{90} (µm)	% < 5 µm
Budesonide	0.9 ± 0.0	2.1 ± 0.0	4.0 ± 0.0	94.4 ± 0.1
ML001	3.7 ± 0.2	48.1 ± 0.4	153.9 ± 1.9	11.2 ± 0.3

Table 6.1 Particle size values of budesonide and ML001 (n=5, mean ± SD)

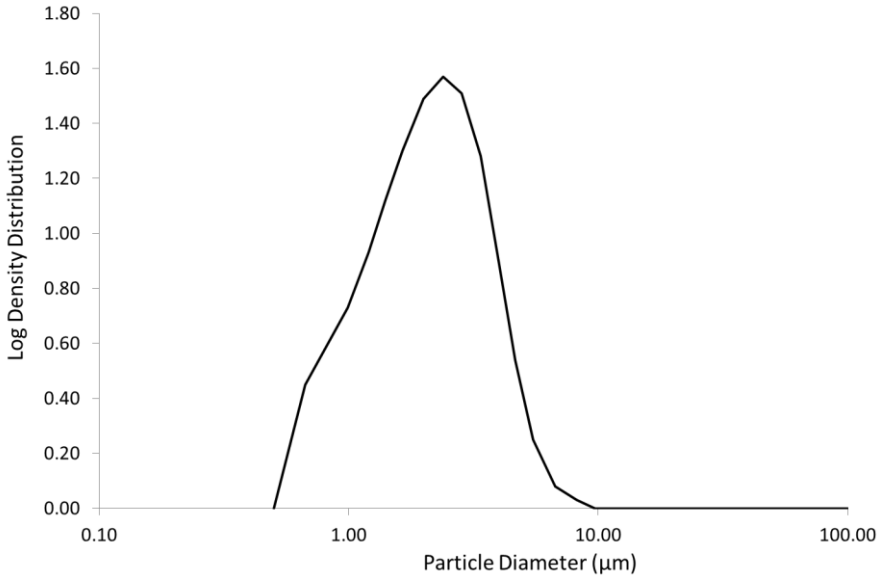

Figure 6.2 Particle size log density distribution of micronised budesonide

The results show that as ML001 is a milled carrier grade of lactose it has a much larger particle size distribution than budesonide. Budesonide was processed via micronisation and the average percentage of particles with diameter of less than 5 µm was 94.43 ±

0.07%, to ensure that upon aerosolisation and subsequent inhalation the particles are able to reach the deep lung in order to produce the desired therapeutic effect.

6.3.2 Scanning electron microscopy

Scanning electron micrographs of A, ML001 and B, budesonide are displayed in Figure 6.3. The image for ML001 at 200x magnification shows the relative large particles of the course carrier. The image for budesonide at a magnification of 15000x shows the micronised API particles with diameters less than 5 μm.

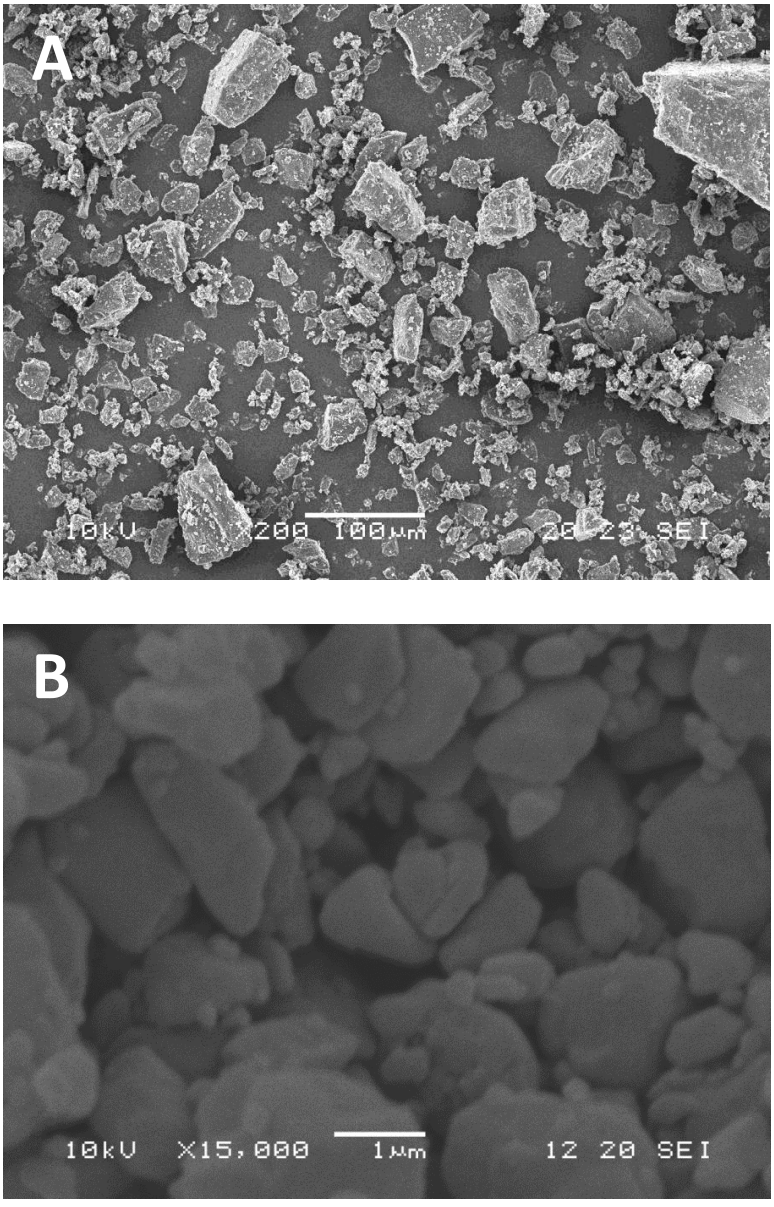

Figure 6.3 SEM Images of A, ML001 and B, Budesonide

6.3.3 Assay and content uniformity

After the blend was manufactured, 10 samples of 25mg of the formulation were dissolved in 100 mL of mobile phase. HPLC analysis was performed and the drug content was found to be 96.55 ± 1.89 % which is within the 85 - 115% USP criteria for content uniformity (USP 2011). The CV was 2.04% indicating that the blend was a homogenous mixture.

6.3.4 *In vitro* performance of the formulation at 55% RH

The *in vitro* performance of the budesonide formulation at 55% RH is shown in Figure 6.4 and Table 6.2. This is experiment was performed as a control to allow comparison with data generated with the bp-NGI. The distribution of budesonide throughout the stages of the NGI shows an *in vitro* performance distribution with a maximum deposition on stage 2 with a cut off diameter of 6.48µm at a flow rate of 90 $Lmin^{-1}$.

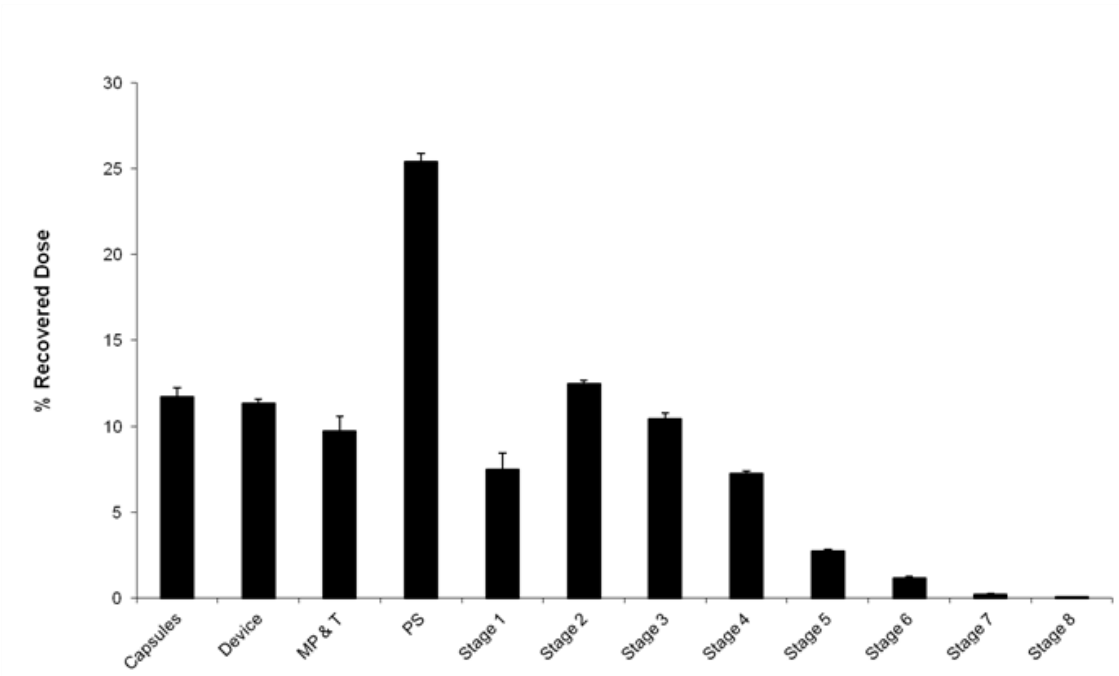

Figure 6.4 *In vitro* performance of the budesonide formulation at 55% RH (n=3, mean ± SD)

RD (µg) ± S.D.	FPF (ED) (%) ± S.D.	ISM (% of RD) ± S.D.	MMAD (µm) ± S.D.
1020.2 ± 40.1	33.4 ± 0.3	34.3 ± 0.9	3.5 ± 0.1

Table 6.2 *In vitro* performance of the budesonide formulation (n=3, mean ± SD)

These data show that the formulation performed efficiently at a relative humidity of 55%, with a fine particle fraction of the emitted dose of 33.4 ± 0.3 % and an MMAD of 3.5 ± 0.1 µm.

6.3.5 Comparison of the performance between the NGI and the bp-NGI and the effect of humidity on the formulation performance.

A potential concern highlighted during the design of the bp-NGI was whether the modifications to the system would affect the *in vitro* performance of formulations tested. Although the flow rate was maintained at the desired level, the incorporation of the bifurcator and electrostatic precipitation sections resulted in a large addition to the total interior volume, which could result in a difference in the air pressure of the system during simulated inhalation air flow. Consequently, the *in vitro* performance of the budesonide formulation was compared with the conventional NGI and the bp-NGI in order to ensure the performance of the two instruments was comparable. This was achieved by comparing the results from the capsules, device, mouthpiece and throat, preseparator and the impactor stage masses from stages 2 and below. The formulation performance results at the three different humidities tested with the bp-NGI were also compared and the results are shown in Table 6.3 and Figure 6.5.

Testing Condition	RD (µg) ± S.D.	ISM (% of RD) ± S.D.
NGI 55% RH	1020.2 ± 40.1	34.3 ± 0.9
bp-NGI 35% RH	944.5 ± 59.1	29.6 ± 3.6
bp-NGI 55% RH	1001.5 ± 60.5	31.5 ± 3.5
bp-NGI 75% RH	997.9 ± 49.4	37.2 ± 2.7

Table 6.3 Comparison of the *in vitro* performance of the budesonide formulation with the NGI and the bp-NGI (n=3, mean ± SD)

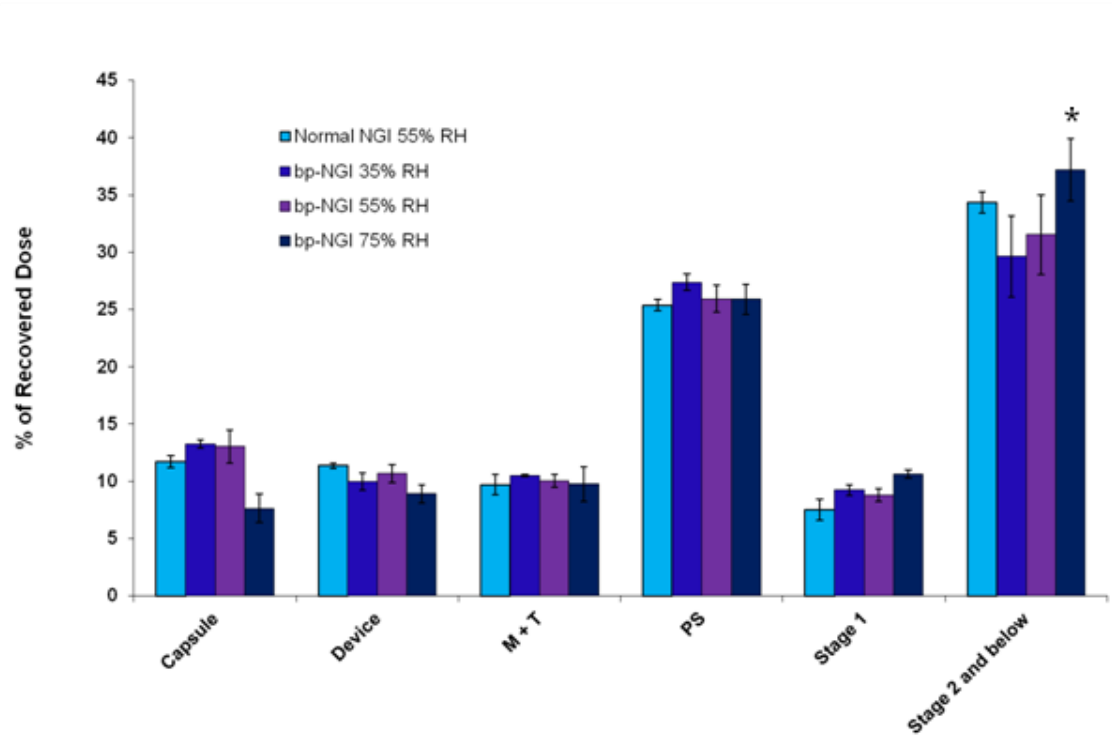

Figure 6.5 Comparison of the *in vitro* performance of the budesonide formulation with the NGI and the bp-NGI. *- significantly different from the ISM determined with the bp-NGI at 35% RH (n=3, mean ± SD)

The results were analysed using Minitab version 16 statistical analysis software for each relative humidity condition and no significant difference ($p > 0.05$) was observed between the values of ISM (equivalent to the total deposition from stage 2 and below),

for the NGI and bp-NGI, indicating that the formulation performance was comparable between the two pieces of equipment.

The effect of humidity on the formulation performance was determined with the bp-NGI at relative humidities of 35, 55 and 75% RH within the humidity cabinet. This was achieved by comparing the ISM as a percentage of the recovered dose for each humidity tested. Statistical analysis for data in Table 6.3 indicated that there was no significant difference between the values for 35% and 55% and 55% and 75% relative humidity respectively. However a statistical difference ($p < 0.05$) was observed between the values at 35% and 75% RH (29.6 ± 3.6% and 37.2 ± 2.7% respectively). This indicated that as the relative humidity increased, formulation performance increased, with increased deposition occurring on stages two and below. This is in agreement with findings by Young *et al*. (2007) who showed that the fine particle dose and fine particle fraction of the emitted dose of a salbutamol DPI formulation increased with increasing humidity in the range of 0 – 60% RH (Young *et al*. 2007).

6.3.6 Bipolar charge to mass ratios of the formulation as a function of humidity

6.3.6.1 35% RH

The mass distribution of budesonide generated within the bp-NGI at 35% RH is shown in Figure 6.6 and Table 6.4. An asymmetric mass distribution was produced which was not consistent with the symmetrical mass distributions observed with the pMDI aerosols in Chapter 5. At low values of charge, the electrical mobility of the particles is lower and as such it is harder for them to be precipitated. Under ideal conditions, the collection efficiency of the electrodes and precipitation tubes should be identical. However, when the flow is not completely uniform, the collection efficiencies of the central electrodes may be lower than that of the precipitation tubes because the electrodes have a smaller surface area. Although the computational fluid dynamic analysis performed indicated that the flow was laminar, the velocity contour diagram showed that the electrodes created some slight turbulence in the precipitation tubes, with the airflow velocity increased around the electrode and slower closer to the precipitation tube. Since an increase in velocity will result in a decrease in precipitation efficiency, this may have resulted in a reduction in collection efficiency of the electrodes and hence the asymmetric distribution of budesonide and lactose particles observed.

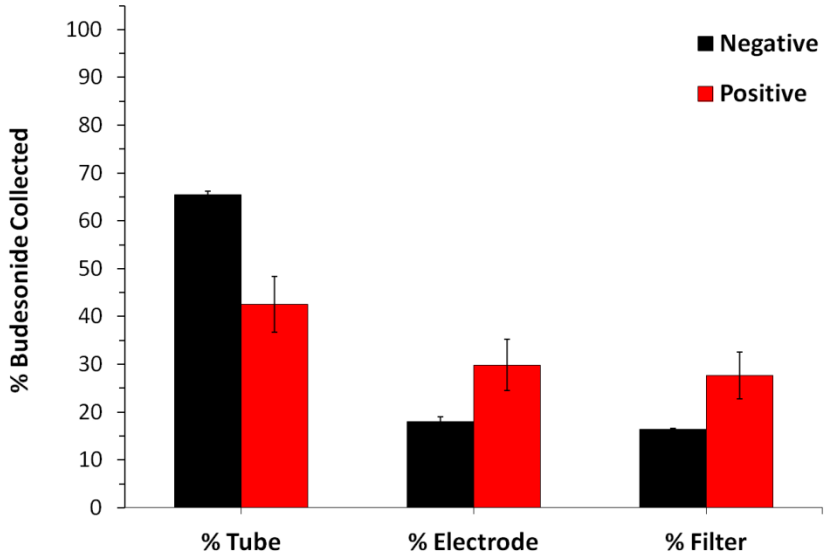

Figure 6.6 Percentages of budesonide particles deposited within the bp-NGI at 35% RH

	Precipitation Section	
	Negative	Positive
Mass Tube (µg) ± S.D.	37.0 ± 0.4	24.6 ± 3.4
Mass Electrode (µg) ± S.D.	10.2 ± 0.6	17.3 ± 3.1
Mass Filter (µg) ± S.D.	9.3 ± 0.1	16.0 ± 2.8
Total (µg) ± S.D.	56.5 ± 1.0	57.9 ± 9.3

	Precipitation Section	
	Negative	Positive
Percentage Tube (%) ± S.D.	65.5 ± 0.7	42.5 ± 5.9
Percentage Electrode (%) ± S.D.	18.1 ± 1.0	29.8 ± 5.4
Percentage Filter (%) ± S.D.	16.5 ± 0.1	27.7 ± 4.9
Total (%) ± S.D.	100.0 ± 1.8	100.0 ± 16.1

Table 6.4 Masses and percentages of budesonide particles deposited within the bp-NGI at 35% RH (n=3, mean ± SD)

The results show that budesonide exhibited a propensity to become more negatively charged than positively charged, with the ratio of negative to positive particles being 1.54 : 1 as determined from the percentage of budesonide particles deposited on the precipitation tubes. The total masses of API particles collected were 56.5 ± 1.0 and 57.9 ± 9.6 for the negative and positive precipitation sections respectively, which were very similar, highlighting an efficient bifurcation of the airflow.

The mass distribution of lactose generated within the bp-NGI at 35% RH is shown in Figure 6.7 and Table 6.5. Again an asymmetric mass distribution was produced indicating that the charge of the lactose particles entering the precipitation sections was low, resulting in reduced deposition onto the central high voltage electrodes.

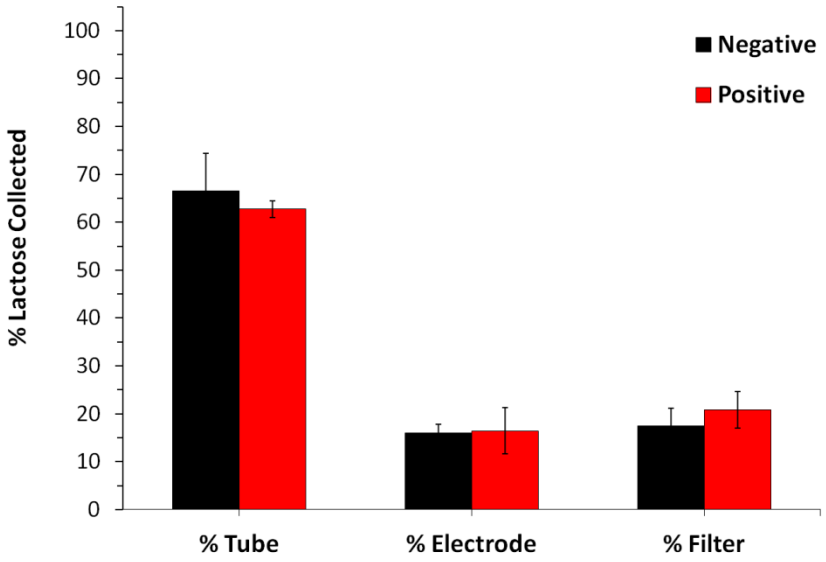

Figure 6.7 Percentages of lactose particles deposited within the bp-NGI at 35% RH

	Precipitation Section	
	Negative	Positive
Mass Tube (µg) ± S.D.	1473.4 ± 173.0	1389.9 ± 38.5
Mass Electrode (µg) ± S.D.	354.9 ± 40.3	360.9 ± 107.3
Mass Filter (µg) ± S.D.	386.4 ± 82.5	461.5 ± 85.4
Total (µg) ± S.D.	2214.7 ± 295.7	2215.3 ± 231.2

	Precipitation Section	
	Negative	Positive
Percentage Tube (%) ± S.D.	66.5 ± 7.8	62.7 ± 1.7
Percentage Electrode (%) ± S.D.	16.0 ± 1.8	16.4 ± 4.8
Percentage Filter (%) ± S.D.	17.5 ± 3.7	20.8 ± 3.9
Total (%) ± S.D.	100.0 ± 13.4	100.0 ± 10.4

Table 6.5 Masses and percentages of lactose particles deposited within the bp-NGI at 35% RH (n=3, mean ± SD)

The results show that for lactose, the ratio of negatively charged : positively charged particles was 1 : 0.9 as determined from the mass of particles deposited on the precipitation tubes. The masses of lactose particles collected were 2214.7 ± 295.7 and

2215.3 ± 231.2 for the negative and positive precipitation sections respectively, which were much larger than the quantities of API particles collected. This demonstrated that ML001 has a significant quantity of fine particles generated from the milling process used to manufacture it (Steckel *et al*. 2006).

The charge measurements of the < 6.48 µm particles from each shot of the formulation which entered the precipitation sections at 35% RH are shown Figure 6.8. The negative charge values were fairly consistent with an average value of -0.31 ± 0.10 nC. The positive charge values were lower in magnitude with an average value of +0.21 ± 0.13 nC. This resulted in the net charge measurements (as calculated from the sum of the negative and positive values) being overall negative in nature with an average value of -0.09 ± 0.26 nC.

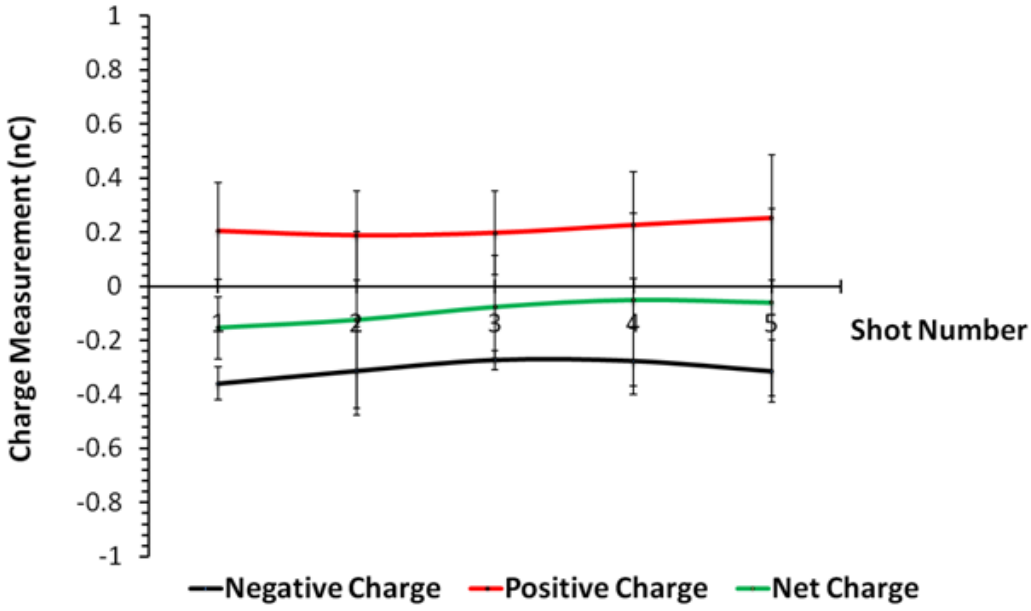

Figure 6.8 Charge measurements of five successive shots of the budesonide formulation at 35% RH

The bipolar charge measurements of the < 6.48 µm budesonide and lactose particles at 35% RH are shown in Figure 6.9. The results show that the average charge to mass ratio of the positively charged particles (+0.77 ± 0.20 pC/µg) was lower in magnitude than the negatively charged particles (-1.03 ± 0.31 pC/µg). The overall net charge to mass ratio of the particles was -0.16 ± 0.45 pC/µg highlighting the greater charge contribution from the negatively charged particles to this value.

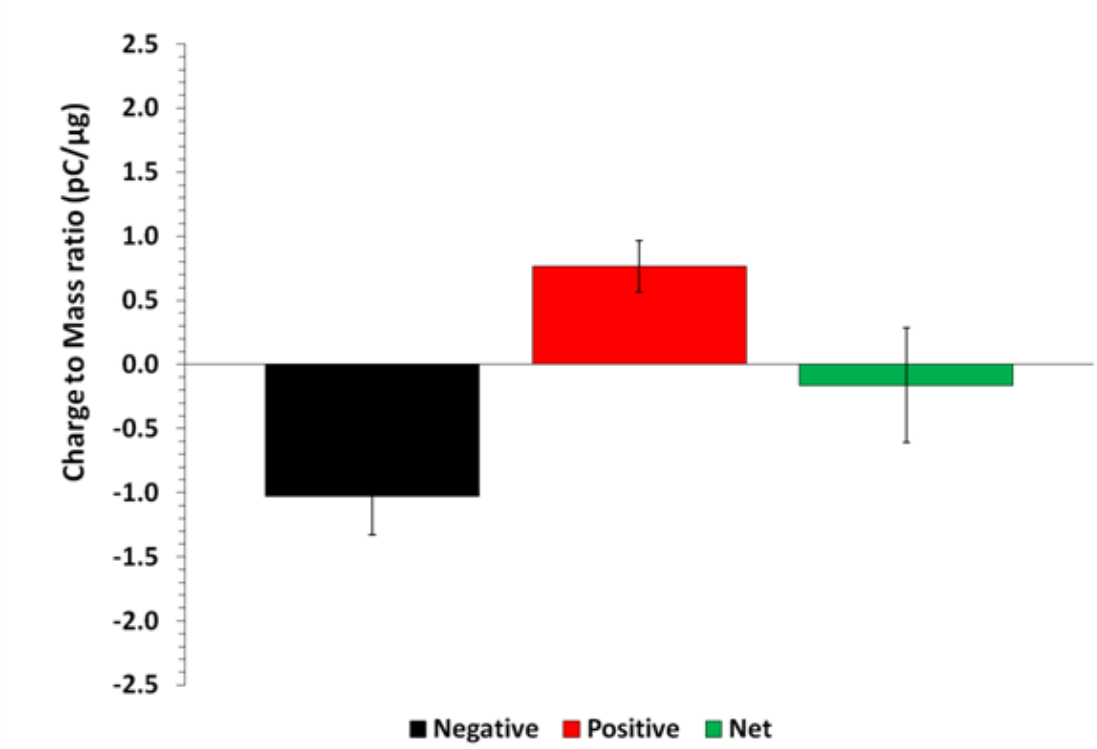

Figure 6.9 Bipolar charge to mass ratios of the budesonide and lactose particles collected within the bp-NGI at 35% RH

6.3.6.2 55% RH

The mass distribution of budesonide generated within the bp-NGI at 55% RH is shown in Figure 6.10 and Table 6.6. The mass distribution within the precipitation sections was similar to 35% RH, with the budesonide particles showing a greater propensity to become negatively charged than positively charged with the ratio of positive : negative particles being 1.10 : 1, as determined from the percentages collected on the precipitation tubes of the electrostatic precipitation sections. The total masses of API particles collected were 63.9 ± 5.2 and 69.4 ± 4.5 for the negative and positive precipitation sections respectively, again demonstrating efficient bifurcation of the airflow and an increase in the total amount of budesonide which entered the precipitation sections as compared with 35% RH.

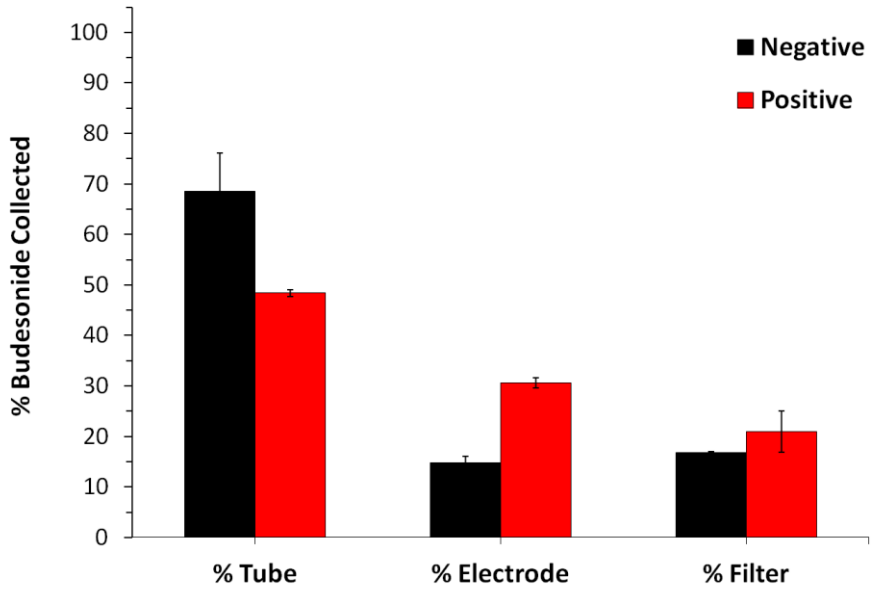

Figure 6.10 Percentages of budesonide particles deposited within the bp-NGI at 55% RH storage

	Precipitation Section	
	Negative	Positive
Mass Tube (µg) ± S.D.	48.2 ± 5.3	33.2 ± 0.4
Mass Electrode (µg) ± S.D.	10.4 ± 0.9	21.0 ± 0.7
Mass Filter (µg) ± S.D.	11.8 ± 0.2	14.4 ± 2.8
Total (µg) ± S.D.	70.3 ± 6.5	68.6 ± 3.9

	Precipitation Section	
	Negative	Positive
Percentage Tube (%) ± S.D.	68.5 ± 7.6	48.4 ± 0.6
Percentage Electrode (%) ± S.D.	14.8 ± 1.3	30.6 ± 1.0
Percentage Filter (%) ± S.D.	16.8 ± 0.3	21.0 ± 4.1
Total (%) ± S.D.	100.0 ± 9.2	100.0 ± 5.7

Table 6.6 Masses and percentages of budesonide particles deposited within the bp-NGI at 55% RH (n=3, mean ± SD)

The mass distribution of lactose generated within the bp-NGI at 55% RH is shown in Figure 6.11 and Table 6.7. The distribution was similar to 35% RH with less lactose collected on the electrodes than the precipitation tubes. The lactose particles showed a slight propensity to become negatively charged rather than positively charged with a ratio of 1.1 : 1 negative : positive particles recorded from the precipitation tubes. The mass of lactose collected in each precipitation section was again high with 1945.6 ±

70.4 µg and 1869.6 ± 88.9 µg collected in the negative and positive sections respectively.

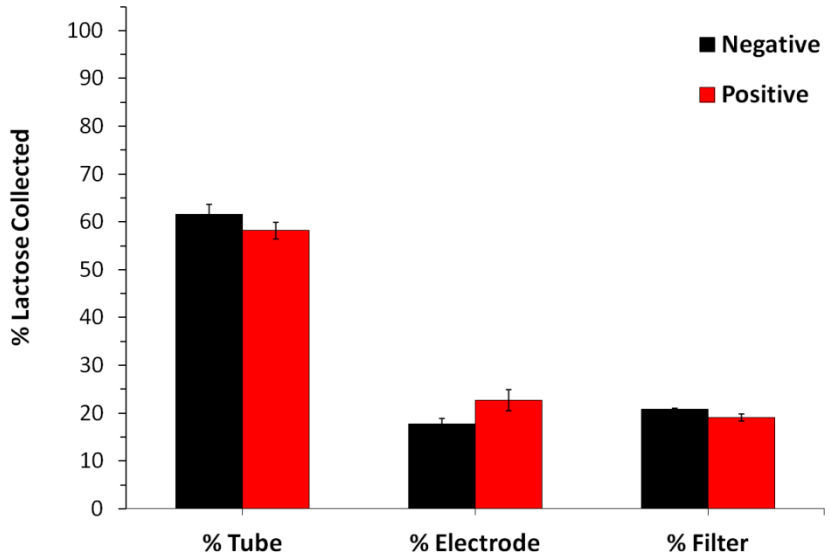

Figure 6.11 Percentages of lactose particles deposited within the bp-NGI at 55% RH

	Precipitation Section	
	Negative	Positive
Mass Tube (µg) ± S.D.	1197.3 ± 41.1	1087.7 ± 33.1
Mass Electrode (µg) ± S.D.	344.4 ± 24.1	424.8 ± 41.9
Mass Filter (µg) ± S.D.	403.9 ± 5.2	357.1 ± 13.9
Total (µg) ± S.D.	1945.6 ± 70.4	1869.6 ± 88.9

	Precipitation Section	
	Negative	Positive
Percentage Tube (%) ± S.D.	61.5 ± 2.1	58.2 ± 1.8
Percentage Electrode (%) ± S.D.	17.7 ± 1.2	22.7 ± 2.2
Percentage Filter (%) ± S.D.	20.8 ± 0.3	19.1 ± 0.7
Total (%) ± S.D.	100.0 ± 3.6	100.0 ± 4.8

Table 6.7 Masses and percentages of lactose particles deposited within the bp-NGI at 55% RH (n=3, mean ± SD)

The charge measurements of the < 6.48 µm particles from each shot of the formulation which entered the precipitation sections at 55% RH are shown Figure 6.12. The average negative and positive charge values were slightly lower than those at 35% RH with averages values of -0.27 ± 0.03 nC and +0.24 ± 0.06 nC respectively. The overall net charge also decreased in magnitude with a calculated average of -0.01 ± 0.05 nC recorded.

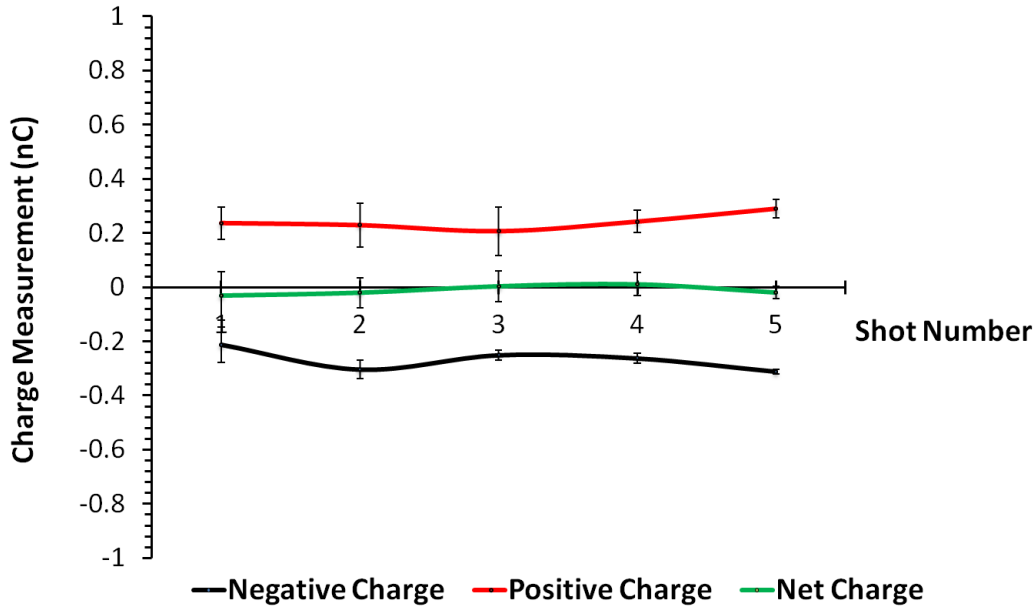

Figure 6.12 Charge measurements of five successive shots of the budesonide formulation at 55% RH

The bipolar charge measurements of the < 6.48 µm budesonide and lactose particles at 55% RH are shown in Figure 6.13. The results show a reduction in the average charge to mass ratio of the positively charged particles from +3.18 ± 0.25 pC/µg to +2.08 ± 0.25 pC/µg which was a direct consequence of the lower positive charge value recorded at this condition. The charge to mass ratio of the negatively charged particles also showed a slight reduction in magnitude from -1.54 ± 0.29 pC/µg to -1.22 ± 0.44 pC/µg although this was not significantly different. The lower positive charge values also resulted in a reduction in the overall net charge to mass ratio of the particles which decreased from +1.12 ± 0.01 pC/µg to +0.72 ± 0.07 pC/µg.

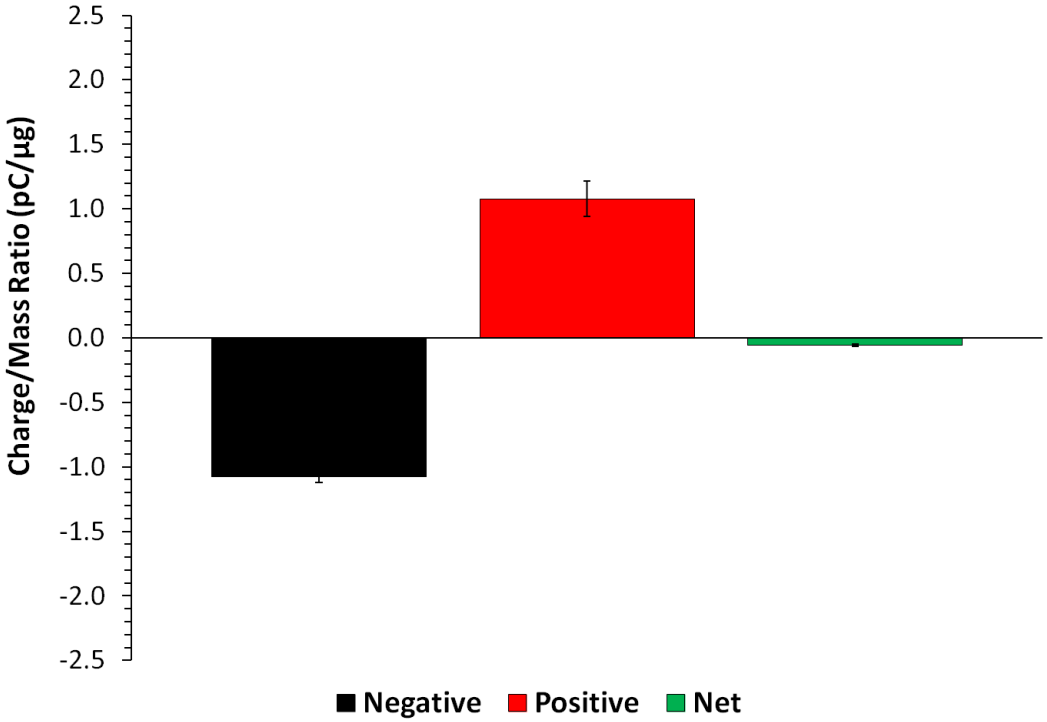

Figure 6.13 Bipolar charge to mass ratios of the budesonide and lactose particles collected within the bp-NGI at 55% RH

6.3.6.3 75% RH

The mass distribution of budesonide generated within the bp-NGI at 75% RH is shown in Figure 6.14 and Table 6.8. The mass distribution within the precipitation sections was similar to 35% RH and 55% RH, with the budesonide particles showing a greater propensity to become negatively charged than positively charged with the ratio of positive : negative particles being 1.25 : 1. The total masses of API particles collected were 71.4 ± 5.3 and 83.7 ± 5.6 for the negative and positive precipitation sections respectively, again demonstrating efficient bifurcation of the airflow and showing an increase in the total amount of API entering the precipitation sections compared with 35% and 55% RH.

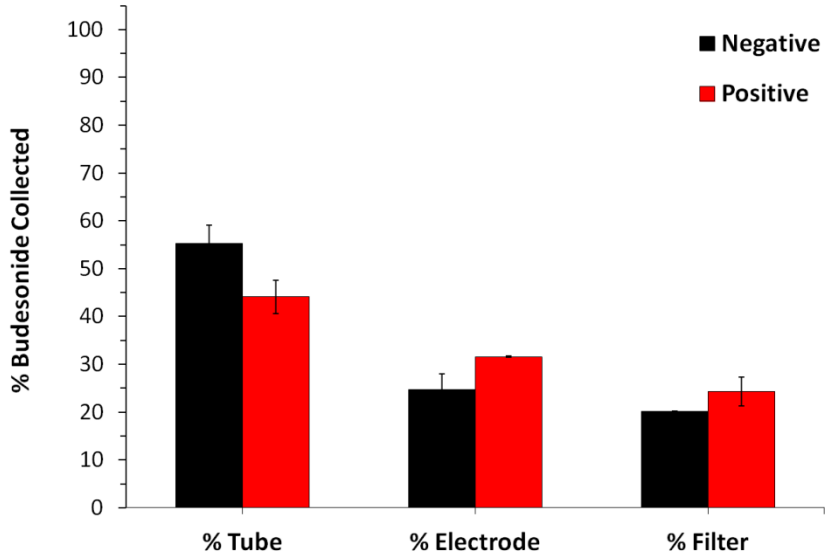

Figure 6.14 Percentages of budesonide particles deposited within the bp-NGI at 75% RH

	Precipitation Section	
	Negative	Positive
Mass Tube (µg) ± S.D.	39.4 ± 2.8	36.9 ± 2.9
Mass Electrode (µg) ± S.D.	17.6 ± 2.4	26.4 ± 0.1
Mass Filter (µg) ± S.D.	14.4 ± 0.1	20.3 ± 2.5
Total (µg) ± S.D.	71.4 ± 5.3	83.7 ± 5.6

	Precipitation Section	
	Negative	Positive
Percentage Tube (%) ± S.D.	55.2 ± 3.9	44.1 ± 3.5
Percentage Electrode (%) ± S.D.	24.7 ± 3.4	31.6 ± 0.2
Percentage Filter (%) ± S.D.	20.1 ± 0.2	24.3 ± 3.0
Total (%) ± S.D.	100.0 ± 7.4	100.0 ± 6.7

Table 6.8 Masses and percentages of budesonide particles deposited within the bp-NGI at 75% RH (n=3, mean ± SD)

The mass distribution of lactose generated within the bp-NGI at 75% RH is shown in Figure 6.15 and Table 6.9. The distribution was similar to 35% and 55% RH with less lactose collected on the electrodes than the precipitation tubes. The bipolar charge distribution of the lactose also showed a slight propensity for more negatively charged particles to be formed with a ratio of 1.05 : 1 negative : positive particles recorded from the precipitation tubes. The mass of lactose collected in each precipitation section was

again high with 2219.3 ± 114.2 µg and 2344.9 ± 47.8 µg collected in the negative and positive sections respectively.

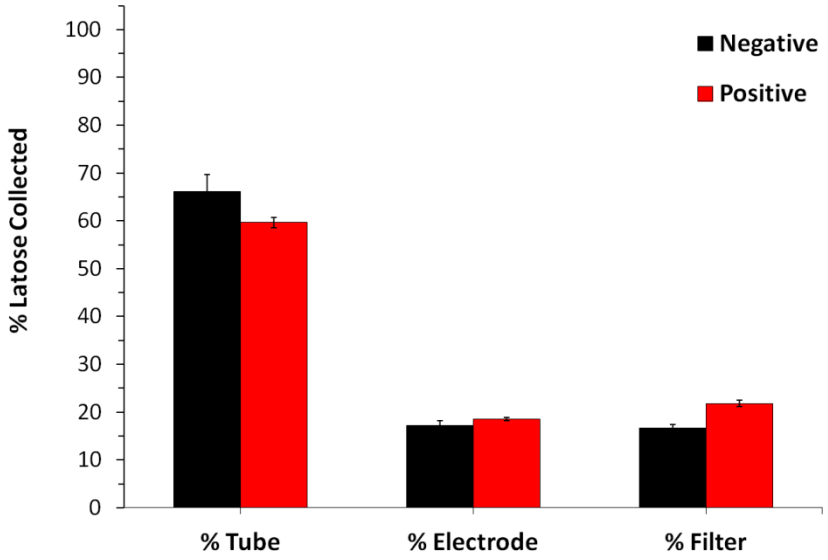

Figure 6.15 Percentages of lactose particles deposited within the bp-NGI at 75% RH

	Precipitation Section	
	Negative	Positive
Mass Tube (µg) ± S.D.	1467.3 ± 77.9	1399.0 ± 25.6
Mass Electrode (µg) ± S.D.	383.07 ± 19.7	434.8 ± 7.1
Mass Filter (µg) ± S.D.	368.9 ± 16.5	511.2 ± 15.2
Total (µg) ± S.D.	2219.3 ± 114.2	2344.9 ± 47.8

	Precipitation Section	
	Negative	Positive
Percentage Tube (%) ± S.D.	66.1 ± 3.5	59.7 ± 1.0
Percentage Electrode (%) ± S.D.	17.3 ± 0.9	18.5 ± 0.3
Percentage Filter (%) ± S.D.	16.6 ± 0.7	21.8 ± 0.7
Total (%) ± S.D.	100.0 ± 5.2	100.0 ± 2.0

Table 6.9 Masses and percentages of lactose particles deposited within the bp-NGI at 75% RH (n=3, mean ± SD)

The charge measurements of the < 6.48 µm particles from each shot of the formulation which entered the precipitation sections at 75% RH are shown Figure 6.16. The negative and positive charge values were both lower than at 35% and 55% RH with average values of -0.15 ± 0.04 nC. and +0.16 ± 0.07 nC respectively. The average

overall net charge per shot was +0.04 ± 0.11 nC which was positive in nature rather than negative as was seen at 35% and 55% RH.

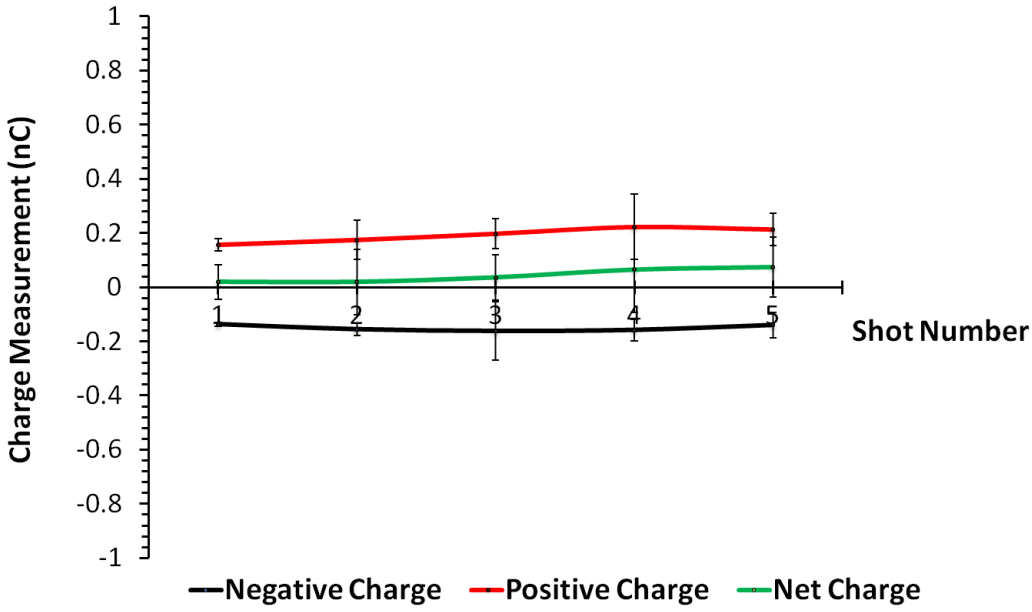

Figure 6.16 Charge measurements of five successive shots of the budesonide formulation at 75% RH

The bipolar charge measurements of the < 6.48 µm budesonide and lactose particles at 75% RH are shown in Figure 6.17. The results showed the average charge to mass ratio of the negatively charged and positively charged particles was of -0.50 ± 0.16 pC/µg and +0.64 ± 0.42 pC/µg, respectively. These values were significantly lower than the values at 35% and 55% RH. There was also a switch in the overall net charge to mass ratio of the particles to positive rather than negative as seen for 35% and 55% RH with a calculated value of +0.06 ± 0.09 pC/µg.

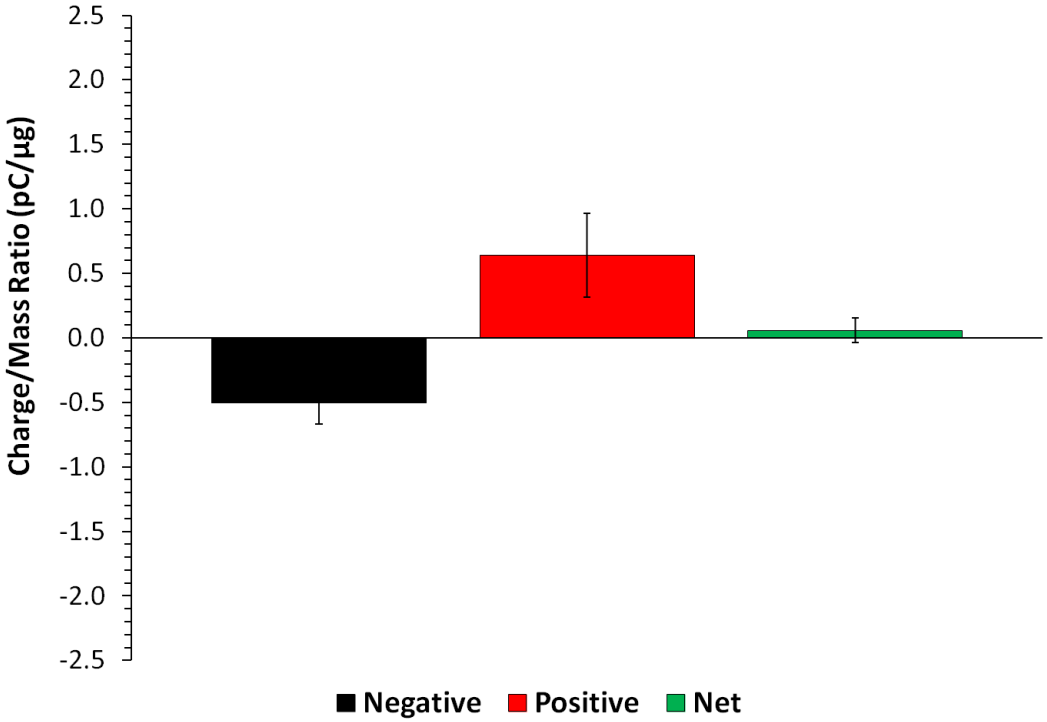

Figure 6.17 Bipolar charge to mass ratios of the budesonide and lactose particles collected within the bp-NGI at 75% RH

6.3.7 Comparison of charge and charge to mass ratios recorded at each humidity

A plot of average negative, positive and net charge per shot for each humidity tested is shown in Figure 6.18 and a plot of the corresponding charge to mass ratios is shown in Figure 6.19. The results show that the bipolar charge values recorded decreased in magnitude as a function of relative humidity. The average negative charge per shot decreased from -0.31 ± 0.10 nC at 35% RH to -0.15 ± 0.04 nC at 75% RH and the average positive charge per shot decreased from +0.21 ± 0.05 nC at 35% RH to +0.16 ± 0.07 nC at 75% RH. This was as a result of the increase in humidity, resulting in a decrease on the initial triboelectric charge generation on the particles within the inhaler, and a faster rate of charge decay of the particles as they travelled through the bp-NGI before being collected onto the precipitation tubes. Interestingly, the overall net charge started off being negative at 35% RH at +0.16 ± 0.07 nC and became positive at 75% RH at +0.16 ± 0.07 nC. The bipolar charge to mass ratios were more variable, but the values at 75% RH were lower than at 35% RH ($p < 0.05$) with the negative value falling from -1.03 ± 0.31 pC/µg to -0.50 ± 0.16 pC/µg and the positive value falling from +0.77 ± 0.20 pC/µg to +0.64 ± 0.32 pC/µg.

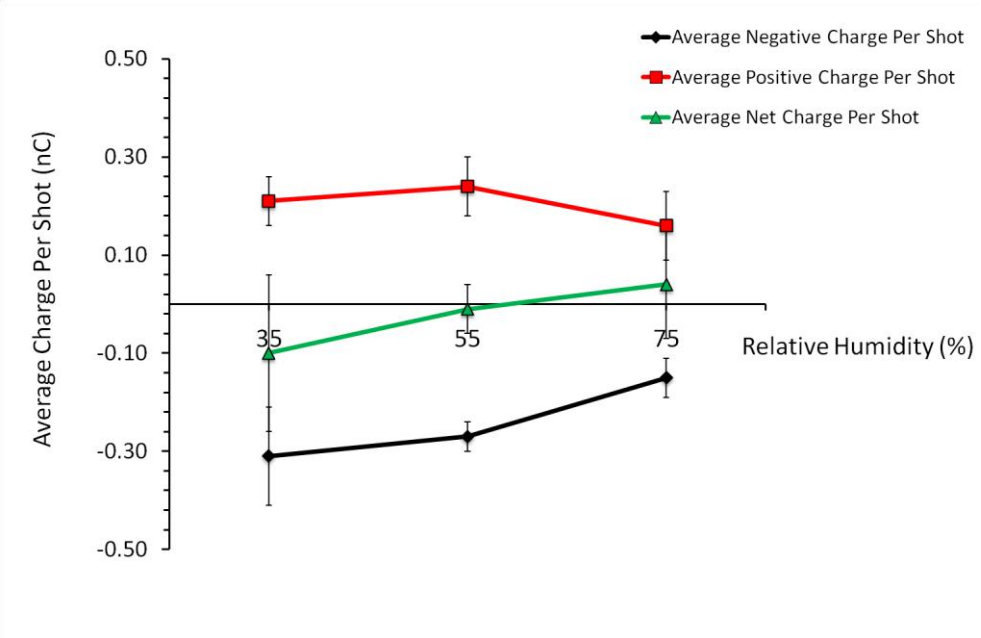

Figure 6.18 Average negative, positive and net charge per shot vs relative humidity

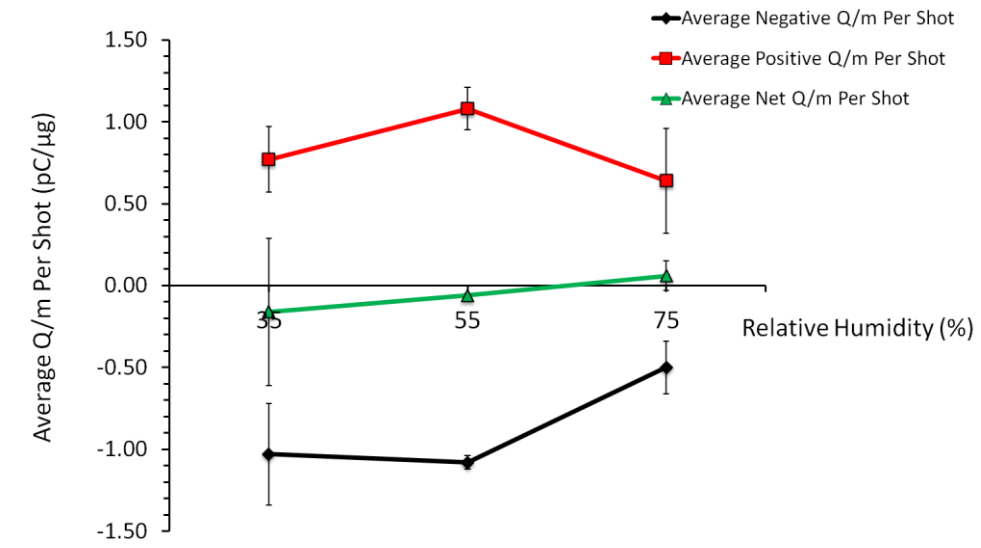

Figure 6.19 Average negative, positive and net charge to mass ratio vs relative humidity

As was seen with the charge values the net charge to mass ratio also switched from a negative value at 35% RH, -0.16 ± 0.45 pC/µg to a positive value at 75% RH, +0.06 ± 0.09 pC/µg. The switch from the negative values for net charge and charge to mass ratio at 35% RH to positive values at 75% RH may have been due to the lactose, which exhibited a slight propensity to become negatively charged, experiencing a faster charge decay rate than the API and hence increasing the overall positive charge of the

system. The magnitude of the bipolar charge to mass ratios recorded were overall less than 2 pC/µg which were significantly lower than the charge values recorded for the pMDIs previously tested (range 20-90 pC/µg). This shows that overall the frictional charging of the API and lactose particles was very low and based on the performance results recorded, triboelectrification of the budesonide formulation DPI particles may not have significantly affected the inhaler *in vitro* performance.

6.3.8 Dynamic Charge Measurements of the Aerolizer® Device

The dynamic charge measurements of the Aerolizer device together with the formulation and capsule upon aerosolisation of a shot are plotted against relative humidity for each shot successive shot in Figure 6.20 and are plotted against shot number for each humidity in Figure 6.21.

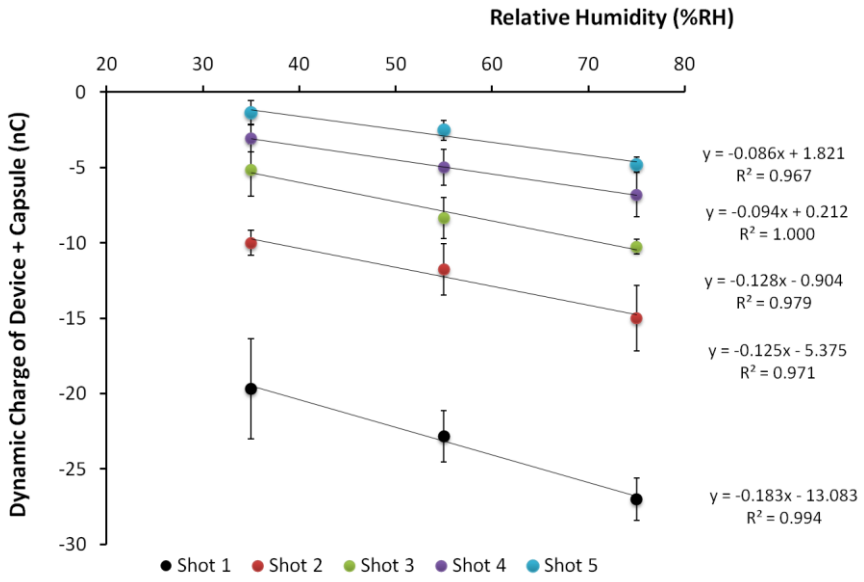

Figure 6.20 Dynamic charge of the Aerolizer® device plotted against relative humidity for each successive shot

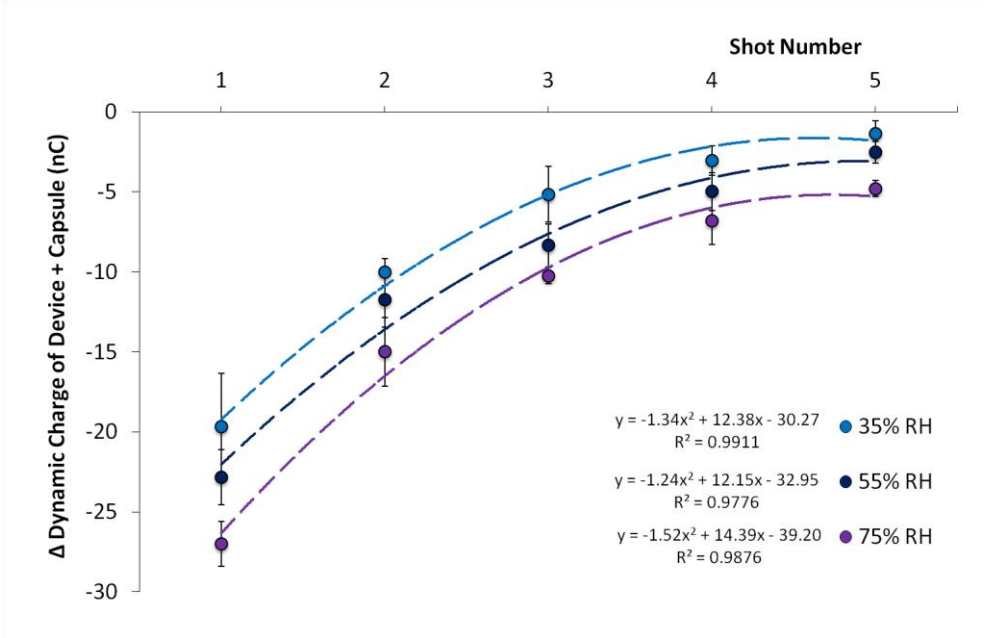

Figure 6.21 Dynamic charge of the Aerolizer® device plotted against shot number for each relative humidity

The results in Figure 6.20 show that a linear relationship was recorded for each successive shot number when plotted against relative humidity. This may be due to increased water adhesion to the particle surfaces resulting in a greater magnitude of net charge recorded. However, by the time the aerosol particles had entered the precipitation sections of the bp-NGI, the charge had mostly dissipated. The results in Figure 6.21 show the dynamic net charge recorded when plotted against shot number, with the dynamic charge becoming more negative as a function of each successive shot. This indicates that the charge build up on the device was increasing as each shot was fired but by a progressively smaller amount each time. This may be due to the device becoming saturated with charge as each shot was fired and the relationship was maintained as during the course of the experiment as the charge was only dissipating very slowly. The $Ax^2 + Bx + C$ relationship observed indicates that the charge build up on the device may be a function of its internal surface area.

6.3.9 Net charge measurements of the capsules

The net charge measurements of the capsules as plotted against shot number for each humidity are shown in Figure 6.22. The results show that the capsule charge increase was positive in nature and the average values were independent of shot number which

was in agreement with the charge measurements recorded with the bp-NGI. The standard deviations were quite large which may be due to variability in the way the capsule was tapped out of the device and into the Faraday pail.

The average net charge per capsule for each of set of five capsules is plotted against relative humidity in Figure 6.23 and shows a linear relationship between net capsule charge post aerosolisation (R^2=0.998) within the device and humidity which is in agreement with the dynamic charge measurements plotted in Figure 6.20. As relative humidity increased, the net capsule charge decreased which may be due to the increased humidity dissipating the charge, or that the device itself was becoming less negatively charged as humidity decreased.

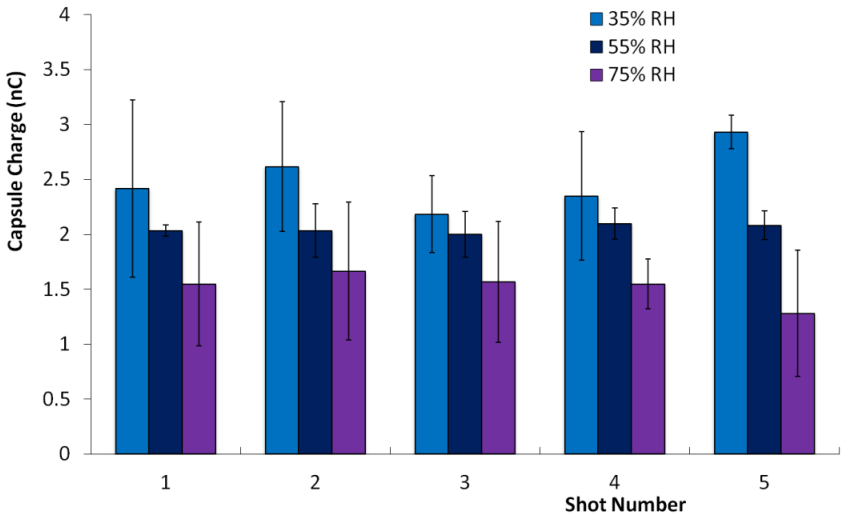

Figure 6.22 Average net capsule charge plotted against shot number for each relative humidity tested

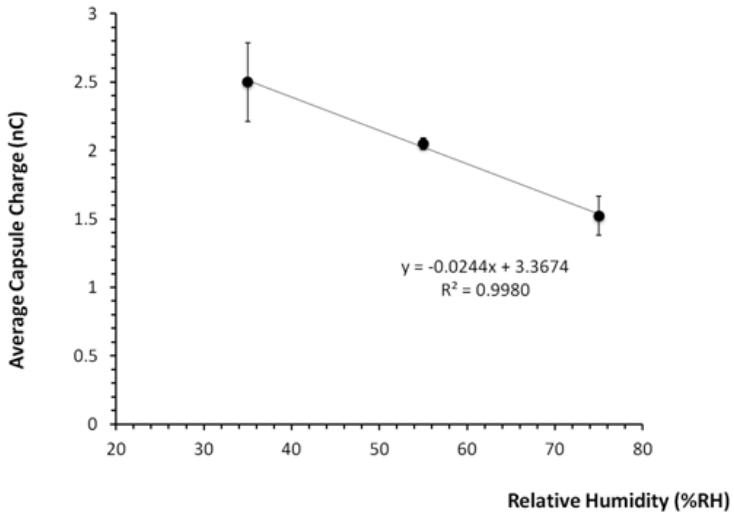

Figure 6.23 Average net capsule charge plotted against relative humidity

6.4 Conclusions

This study describes a novel, comprehensive methodology for performing electrostatic characterisation of the respirable particles emitted from a DPI device as well as the build-up of static charge on the capsules and device as a function of shot number

The effect of relative humidity on the electrostatic properties of a budesonide DPI formulation, including the bipolar charge to mass ratios of the respirable dose, the dynamic charge of the Aerolizer® device and the net charge of the capsules, as well as the *in vitro* performance was determined. The bipolar charge to mass ratios of the aerosol particles were much lower than previously seen with pMDI formulations and the presence of charge did not appear to significantly affect the *in vitro* performance. However, a linear correlation was observed between the bipolar charge measurements recorded of the aerosol particles and the relative humidity, with an increase in RH resulting in a decrease in the aerosol particle charge. This may have an effect on the *in vivo* performance as the presence of electrostatic charge on aerosol particles is expected to increase the amount deposited into the lung.

The amount of net negative charge on the Aerolizer® device increased as a function of relative humidity, suggesting that the presence of adhered moisture to the particles' surfaces may have increased the frictional contact with the internal surfaces of the device. Conversely an increase in relative humidity decreased the overall amount of bipolar charge recorded on the aerosol particles, which could be due to an increased charge decay rate while the particles were travelling from the inhaler to the electrostatic precipitation sections of the bp-NGI. Faraday pail measurements showed that HPMC capsules became net positively charged and that the quantity of charge decreased linearly as a function of humidity, but was independent of the shot number.

Further suggested work would be to investigate the effect of a range of other variables such as flow rate, type of device and aerosolisation mechanism, capsule material, type of API and coarse carrier grade of lactose on the dynamic device charge, the capsule charge and the bipolar charge to mass ratios of the therapeutic aerosol particles. The electrostatic precipitation sections could also be connected to the other stages of the NGI in order to produce a measurement of the bipolar charge distribution for each particle diameter cut off.

Chapter 7 General conclusions and future work

7.1 Summary

Electrostatic charge is a commonly occurring phenomena which is experienced by all solid materials, particularly in the case of free flowing particulate systems which possess large surface are to mass ratios. In order to treat respiratory illnesses, therapeutic drug particles must be delivered to the lung and the most efficient way of achieving this is through inhaled therapies. The nature of the human respiratory tract requires that airborne particles must be in the region of 5μm or less in diameter to ensure that deposition will occur in the bronchi and bronchioles and not impact in the mouth, throat and upper airways. This poses a challenge for pharmaceutical scientists as the production and delivery of such particles requires a high level of process understanding. Inhaled API particles are normally electrically resistive in nature which results in a high probability that they will become triboelectrically charged during micronisation to the required size, formulation with excipients and packaged for use with inhalation devices. The presence of charge on bulk powders may lead to problems including weighing errors, agglomeration, adhesion to surfaces and poor flow. In addition during the processes of de-aglommeration and fluidisation, the particles will undergo numerous collisions with themselves and with the internal surfaces of the inhaler resulting in further triboelectrification. This may affect the formulation performance and subsequent *in vivo* deposition. A further consideration is that traditional net charge measurements with instruments such as the Faraday pail do not take into account the bipolar nature of the charge present, only recording a sum of the combined negative and positive charges.

7.2 General Conclusions

Experiments were conducted to assess various techniques of measuring the net charge on two pharmaceutical inhalation grades of lactose with differing rheological properties. During sieving, ML001, a cohesive grade of lactose was shown to experience greater triboelectrification than SV003 which is free flowing. This showed that the process of breaking up lactose agglomerates in ML001 resulted in greater contact time and frictional forces with the metallic sieve which in turn lead to a greater amount of net negative charge being transferred to the particles.

The net charge of unprocessed lactose samples was recorded with a Faraday pail using a variety of different methods to transfer and dispense the material. It was shown that free flowing SV003 was more prone to frictional triboelectrification than ML001 during transport and that using a metallic instrument imparted negative charge to the sample. The development of a bespoke powder ladle prevented triboelectrification during dispensing, allowing for the intrinsic net charge of both grades of lactose to be recorded.

Post low shear and high shear turbula blending, at 50% RH, very little net charge was recorded when the powder ladle was used to transfer the lactose samples to the Faraday pail. This implies that at the environmental conditions of the experiment the charge decay rate was too fast to allow meaningful measurements from being performed.

Static charge decay measurements of DPI blends were performed using a Charge Decay Time Analyser which artificially charged the sample with a corona discharge and then measured the subsequent rate of charge decay. Results showed that the charging propensity of a DPI blend followed a linear correlation with API concentration, but charge decay rates followed an exponential correlation above a critical API concentration of 0.4% w/w. The charge decay rates for the placebos were extremely fast and it may thus be concluded that for commercial DPI formulations, where the API loading may reach values of up to 2% w/w, the electrostatic behaviour will be dominated by the API.

The effect of humidity on charge decay kinetics of DPI blends was also investigated. DVS experiments indicated that at increased environmental RH, the quantity of water adsorbed to the particles' surface increased. This lead to a decrease in the electrical resistivity and a concomitant reduction in the charging propensity and the charge decay rates. Charge decay rates followed an exponential decrease with increased humidity and with higher concentration API blends, charge decay times were hours at 35% RH, minutes at 55% and seconds at 75% RH. Humidity control of the environment should thus be controlled during to ensure repeatability and reliability of the steps required to formulate and process DPI blends.

The bipolar Next Generation Impactor (bp-NGI) was designed, constructed and assessed as a tool for measuring the bipolar charge to mass ratios of aerosol particles exiting inhaler devices. Assessment of commercially available pMDIs of Flixotide™, Serevent™ and the combination product Seretide™ suggested that fluticasone propionate showed a propensity to become more negatively charged than positively

charged whereas the reverse was shown for salmeterol xinafoate in Serevent. In the combination product the bipolar charge to mass ratio distribution of salmeterol xinafoate switched, with more particles exhibiting negative charge which has been suggested to have been caused by the formation of salmeterol-fluticasone aggregates. Data was in agreement with literature findings, however, when fluticasone pMDIs were tested with the ELPI, positive charge was found to be recorded at the lower stages of the impactor despite the fact that little API was present. This may possibly be due to positively charged propellant or ice crystals which are not possible to quantify accurately due to rapid evaporation.

The bipolar Next Generation Impactor was subsequently used to assess the bipolar charge to mass ratios of a budesonide DPI formulation at a range of controlled humidities. Fine particle budesonide showed a slight preference to become negatively charged over positively charged whereas for ML001 the distribution was 50:50. Much lower values for the bipolar charge to mass measurements were recorded than for the pMDI suspensions with a result that a decreased quantity of material was precipitated onto the central electrodes. A linear correlation was observed between an increase in the relative humidity of the environment and a decrease in the overall amount of bipolar charge present on the fine particle fraction. Although the *in vitro* deposition was not significantly affected this may have implications for the *in vivo* performance, where the presence of charge on aerosol particles has been shown to increase the overall deposition in the lung.

Dynamic charge measurements of the Aerolizer® device were performed and it was shown that as successive shots were fired through the inhaler, the device became increasingly net negatively charged. However, the amount of charge imparted to the device decreased with each successive shot, indicating that a saturation limit was being approached. An increase in humidity of the environment caused an increase in the total amount of negative charged transferred from the formulation to the device, possibly as a result of increased frictional triboelectrifaction as a result of increased bound water. The HPMC capsules used in the study became net positively charged during the aerosolisation process, the magnitude by which was independent of the shot number fired. A linear correlation was observed between a reduction in the capsule charge with relative humidity, possibly due to an increased charge decay rate of the capsule, or an electrostatic interaction with the device which increased in overall net negative charge under the same conditions.

7.3 Future work

Novel methodologies were developed for performing both static and dynamic charge measurements of DPI and pMDI formulations, however, investigations performed during the course of this project were only able to investigate a limited number of variables. The powder ladle developed in Chapter 3 could be used to assess the static charge build up DPI formulations during low shear and high shear blending to determine the effect of variables such as API type and concentration, coarse carrier grade of lactose, blend physico-chemical properties and environmental RH. It could also be employed as a tool for sampling DPI formulations at various points during large scale manufacturing processes to monitor electrostatic charge levels and the information used to determine the length of hold times.

The Charge Decay Time Analyser could be introduced as a science of scale tool for performing routine electrostatic characterisation of all powder pharmaceutical excipients and APIs. Values for the initial surface potential and charge decay times could be compared with physico-properties such as surface area, morphology, surface energy, water content, crystallinity, polymorphism and surface chemistry to determine the influence of each variable on the susceptibility of the material to become tribocharged. The effects of varying the magnitude, polarity and application time of the corona discharge to the material could also be investigated.

The bipolar Next Generation impactor could be employed by pharmaceutical scientists, as a tool to characterise the bipolar charge distributions of aerosol particles emitted from DPIs and pMDIs during formulation development. Data generated could be compared with clinical data to determine whether aerosol particle charge is a contributing factor to the variability observed in pharmacokinetic and pharmacodynamic data. Only one set of electrostatic precipitators was constructed for the study, however, a refined design is suggested to add further precipitators to a Next Generation Impactor in order to determine the bipolar charge present on aerosol particles collected at each cut off diameter simultaneously. Construction of a system to quantify the bipolar charge distribution present on API and coarse carrier particles deposited in the throat and preseparator sections of the Next Generation Impactor is also suggested.

References

Abbas, A., S. Shahid, A. Sabah, S. Tanwir, S. W. Ahmed, M. Kashif, A. H. Jatoi, S. Adnan, and S. A. Rizvi. 2014. An insight to chronic obstructive pulmonary disorder COPD and its pharmacotherapy. Br. Biomed. Bull. 2:66-84.

Adachi, K., S. Yamana, and T. Nakamura. 2005. Development system by toner transportation using traveling wave electric field. Is&T's Nip21: International Conference on Digital Printing Technologies, Final Program and Proceedings:597-601.

Adi, H., P. C. L. Kwok, J. Crapper, P. M. Young, D. Traini, and H.-K. Chan. 2010. Does electrostatic charge affect powder aerosolisation? Journal of Pharmaceutical Sciences 99:2455-2461.

Ahlvik, P., L. Ntziachristos, J. Keskinen, and A. Virtanen. 1998. Real time measurements of diesel particle size distribution with an electrical low pressure impactor. Soc. Automot. Eng., [Spec. Publ.] SP SP-1335:215-234.

Alagusundaram, M., N. Deepthi, S. Ramkanth, S. Angalaparameswari, T. S. Mohamed Saleem, K. Gnanaprakash, V. S. Thiruvengadarajan, and C. Madhusudhana Chetty. 2010. Dry Powder Inhalers - An Overview. Int. J. Res. Pharm. Sci 1:34-42.

Ali, M., M. K. Mazumder, and T. B. Martonen. 2009a. Measurements of Electrodynamic Effects on the Deposition of MDI and DPI Aerosols in a Replica Cast of Human Oral-Pharyngeal-Laryngeal Airways. Journal of Aerosol Medicine and Pulmonary Drug Delivery 22:35-44.

Ali, M., M. K. Mazumder, and T. B. Martonen. 2009b. Measurements of electrodynamic effects on the deposition of MDI and DPI aerosols in a replica cast of human oral-pharyngeal-laryngeal airways. J Aerosol Med Pulm Drug Deliv 22:35-44.

Andersen, A. A. 1958. New sampler for the collection, sizing, and enumeration of viable airborne particles. J Bacteriol 76:471-484.

Anderson, J. H. 1996. The effect of additives on the tribocharging of electrophotographic toners. Journal of Electrostatics 37:197-209.

Anderson, P. J. 2005. History of aerosol therapy: liquid nebulization to MDIs to DPIs. Respir Care 50:1139-1150.

Bailey, A. G. 1993. Charging of solids and powders. J. Electrost. 30:167-180.

Bailey, A. G. 1997. The inhalation and deposition of charged particles within the human lung. Journal of Electrostatics 42:25-32.

Bailey, A. G., A. H. Hashish, and T. J. Williams. 1998. Drug delivery by inhalation of charged particles. J. Electrost. 44:3-10.

Barnes, P. J., S. D. Shapiro, and R. A. Pauwels. 2003. Chronic obstructive pulmonary disease: molecular and cellular mechanisms. Eur. Respir. J. 22:672-688.

Beasley, R., J. Crane, C. K. Lai, and N. Pearce. 2000. Prevalence and etiology of asthma. J Allergy Clin Immunol 105:466-472.

Begat, P., D. A. V. Morton, J. N. Staniforth, and R. Price. 2004. The Cohesive-Adhesive Balances in Dry Powder Inhaler Formulations I: Direct Quantification by Atomic Force Microscopy. Pharm. Res. 21:1591-1597.

Beilmann, B., P. Langguth, H. Häusler, and P. Grass. 2006. High-performance liquid chromatography of lactose with evaporative light scattering detection, applied to determine fine particle dose of carrier in dry powder inhalation products. Journal of Chromatography A 1107:204-207.

Bennett, F. S., P. A. Carter, G. Rowley, and Y. Dandiker. 1999. Modification of electrostatic charge on inhaled carrier lactose particles by addition of fine particles. Drug Development and Industrial Pharmacy 25:99-103.

Berard, V., E. Lesniewska, C. Andres, D. Pertuy, C. Laroche, and Y. Pourcelot. 2002. Dry powder inhaler: influence of humidity on topology and adhesion studied by AFM. Int. J. Pharm. 232:213-224.

Blazek, J. 2001. Computational fluid dynamics: principles and applications. Elsevier.

Bridson, R. H., P. T. Robbins, Y. Chen, D. Westerman, C. R. Gillham, T. C. Roche, and J. P. K. Seville. 2007. The effects of high shear blending on α-lactose monohydrate. International Journal of Pharmaceutics 339:84-90.

Brookman, L. J., L. J. Knowles, M. Barbier, B. Elharrar, R. Fuhr, and S. Pascoe. 2007. Efficacy and safety of single therapeutic and supratherapeutic doses of indacaterol versus salmeterol and salbutamol in patients with asthma. Curr. Med. Res. Opin. 23:3113-3122.

BSI. 1991. Code of practice for control of undesirable static electricity, British Standards Institute. BS5958.

Byron, P. R., J. Peart, and J. N. Staniforth. 1997. Aerosol electrostatics I: properties of fine powders before and after aerosolization by dry powder inhalers. Pharm. Res. 14:698-705.

Carter, P. A., G. Rowley, E. J. Fletcher, and V. Stylianopoulos. 1998. Measurement of electrostatic charge decay in pharmaceutical powders and polymer materials used in dry powder inhaler devices. Drug Development and Industrial Pharmacy 24:1083-1088.

Carvalho, T. C., J. I. Peters, and R. O. Williams. 2011. Influence of particle size on regional lung deposition - what evidence is there? Internation Journal of Pharmaceutics 406:1-10.

Castle, G. S. P. and L. B. Schein. 1995. General model of sphere sphere insulator contact electrification. Journal of Electrostatics 36:165-173.

Chan, T. L. and C. P. Yu. 1982. Charge effects on particle deposition in the human tracheobronchial tree. Annals of occupational hygiene 26:65.

Chen, X., K. Seyfang, and H. Steckel. 2012. Development of a micro dosing system for fine powder using a vibrating capillary. Part 1: The investigation of factors influencing on the dosing performance. International Journal of Pharmaceutics 433:34-41.

Chen, Y. P., Y. M. Chen, and M. Tang. 2002. Micronization of pharmaceutical compounds using the supercritical antisolvent process. Kona 20:178-187.

Chow, K. T., K. Zhu, R. B. H. Tan, and P. W. S. Heng. 2008. Investigation of Electrostatic Behavior of a Lactose Carrier for Dry Powder Inhalers. Pharmaceutical Research 25:2822-2834.

Chubb, J. N. 1995. Dependence of charge decay characteristics on charging parameters. Inst. Phys. Conf. Ser. 143:103-108.

Chubb, J. N. 1996. Corona charging of practical materials for charge decay measurements. J. Electrost. 37:53-65.

Chung, K. F. and I. M. Adcock. 2004. Combination therapy of long-acting β2-adrenoceptor agonists and corticosteroids for asthma. Treat. Respir. Med. 3:279-289.

Coelho, R., L. Levy, and D. Sarrail. 1989. Charge decay measurements and injections in insulators. Applied Physics 22:1406-1409.

Cotler, P., G. Castle, and L. Schein. 1995. General model of sphere–sphere insulator contact electrification. Journal of Electrostatics 36:165-173.

Crampton, M., R. Kinnersley, and J. Ayres. 2004. Sub-micrometer particle production by pressurized metered dose inhalers. J Aerosol Med 17:33-42.

Cullum, V. A., J. B. Farmer, D. Jack, and G. P. Levy. 1969. Salbutamol: a new, selective β-adrenoceptive receptor stimulant. British Journal of Pharmacology 35:141-151.

Dahl, R., K. F. Chung, R. Buhl, H. Magnussen, V. Nonikov, D. Jack, P. Bleasdale, R. Owen, M. Higgins, and B. Kramer. 2010. Efficacy of a new once-daily long-acting inhaled beta2-agonist indacaterol versus twice-daily formoterol in COPD. Thorax 65:473-479.

Davies, D. K. 1969. Charge generation on dielectric surfaces. Brit. J. Appl. Phys. 2:1533-1537.

de Boer, A. H., H. K. Chan, and R. Price. 2012. A critical view on lactose-based drug formulation and device studies for dry powder inhalation: Which are relevant and what interactions to expect? Adv. Drug Delivery Rev. 64:257-274.

Demir, G. and S. Saryal. 2003. Nebuliser therapy. Tuberk Toraks 51:325-332.

DFEPharma. 2014a. http://www.dfepharma.com/en/excipients/inhalation-lactose/respitose-ml001.aspx.

DFEPharma. 2014b. http://www.dfepharma.com/en/excipients/inhalation-lactose/respitose-sv003.aspx.

Disse, B. 2001. Antimuscarinic treatment for lung diseases. From research to clinical practice. Life Sci. 68:2557-2564.

Dunbar, C. A. 1998. Atomization mechanisms of the pressurized metered dose inhaler. Part. Sci. Technol. 15:253-271.

Eilbeck, J., G. Rowley, P. A. Carter, and E. J. Fletcher. 2000. Effect of contamination of pharmaceutical equipment on powder triboelectrification. International Journal of Pharmaceutics 195:7-11.

Elajnaf, A., P. Carter, and G. Rowley. 2006. Electrostatic characterisation of inhaled powders: Effect of contact surface and relative humidity. European Journal of Pharmaceutical Sciences 29:375-384.

Elajnaf, A., P. Carter, and G. Rowley. 2007. The effect of relative humidity on electrostatic charge decay of drugs and excipient used in dry powder inhaler formulation. Drug Development and Industrial Pharmacy 33:967-974.

EMEA. 2006. Ref.: EMEA/CHMP/QWP/49313/2005 Corr. Guideline on the Pharmaceutical Quality of Inhalation and Nasal Products.

Emery, E., J. Oliver, T. Pugsley, J. Sharma, and J. Zhou. 2009. Flowability of moist pharmaceutical powders. Powder Technol. 189:409-415.

Engers, D. A., M. N. Fricke, R. P. Storey, A. W. Newman, and K. R. Morris. 2006. Triboelectrification of pharmaceutically relevant powders during low-shear tumble blending. Journal of Electrostatics 64:826-835.

Erni, F. 1990. Use of high-performance liquid chromatography in the pharmaceutical industry. J. Chromatogr. 507:141-149.

Everard, M. L., A. R. Clark, and A. D. Milner. 1992. Drug delivery from jet nebulisers. Arch Dis Child 67:586-591.

Falcitelli, M., L. Tognotti, and S. Pasini. 2002. An algorithm for extracting chemical reactor network models from CFD simulation of industrial combustion systems. Combust. Sci. Technol. 174:27-42.

Faraday, M. 1844. On Static Electrical Inductive Action. Philsophical Journal 22:200-204.

Fraser, D. A. 1966. The deposition of unipolar charged particles in the lungs of animals. Arch Environ Health 13:152-157.

Freeman, R. 2007. Measuring the flow properties of consolidated, conditioned and aerated powders — A comparative study using a powder rheometer and a rotational shear cell. Powder Technology 174:25-33.

Gady, B., R. Reifenbereger, D. Rimai, and L. Demejo. 1996. Identification of electrostatic and van der Waals interaction forces between a micrometer size sphere and a flat substrate. Phys. Rev. B. 53:8065-8070.

Gañán-Calvo, A. M., J. Dávila, and A. Barrero. 1997. Current and droplet size in the electrospraying of liquids. Scaling laws. Journal of aerosol science 28:249-275.

Gern, J. E., R. F. Lemanske, Jr., and W. W. Busse. 1999. Early life origins of asthma. J. Clin. Invest. 104:837-843.

Glover, W. and H.-K. Chan. 2004a. Electrostatic charge characterization of pharmaceutical aerosols using electrical low-pressure impaction (ELPI). Journal of aerosol science 35:755-764.

Glover, W. and H.-K. Chan. 2004b. Electrostatic charge characterization of pharmaceutical aerosols using electrical low-pressure impaction (ELPI). J. Aerosol Sci. 35:755-764.

Gomez, A. 2002. The electrospray and its application to targeted drug inhalation. Respir Care 47:1419-1431; discussion 1431-1413.

Gonda, I. 2004. Pharmaceutical inhalation aerosol technology. Marcel Dekker Inc, New York.

Grant, H., B. Hughes, W. Vogel, and A. Moilliet. 1968. The spectrum of temperature fluctuations in turbulent flow. Journal of Fluid Mechanics 34:423-442.

Griesenbach, U., D. M. Geddes, and E. W. F. W. Alton. 2004. Gene therapy for cystic fibrosis: an example for lung gene therapy. Gene Ther 11 Suppl 1:S43-50.

Griffith, B., S. Pendyala, L. Hecker, P. J. Lee, V. Natarajan, and V. J. Thannickal. 2009. NOX enzymes and pulmonary disease. Antioxid Redox Signal 11:2505-2516.

Gross, B. 1950. Static Charges on Dielectrics. British Journal of Applied Physics 1:259.

Grossman, J. 1994. The Evolution of Inhaler Technology. Journal of Asthma 31:55-64.

Grosvenor, M. P. and J. N. Staniforth. 1996. The Influence of Water on Electrostatic Charge Retention and Dissipation in Pharmaceutical Compacts for Powder Coating. Pharmaceutical research 13:1725-1729.

Guardiola, J., V. Rojo, and R. Guadalupe. 1996. Influence of particle size, fluidization velocity and relative humidity on fluidized bed electrostatics. Journal of Electrostatics 37:1-20.

Harper, W. R. 1967. Contact and Frictional Electrification. Oxford: Clarendon.
Hasleton, P. S. 1972. The internal surface area of the adult human lung. J Anat 112:391-400.

Hewitt, D., T. Zhang, and Y.-H. Kao. 2008. Quantitation of polysorbate 20 in protein solutions using mixed-mode chromatography and evaporative light scattering detection. Journal of Chromatography A 1215:156-160.

Hickey, A. J. and T. B. Martonen. 1993. Behavior of hygroscopic pharmaceutical aerosols and the influence of hydrophobic additives. Pharm. Res. 10:1-7.

Hoe, S. 2009. The Influence of Flow Rate on the Aerosol Deposition Profile and ElectrostaticCharge of Single and Combination Metered Dose Inhalers. Pharmaceutical research 26:2639.

Hoe, S., D. Traini, H.-K. Chan, and P. Young. 2009a. The influence of flow rate on the aerosol deposition profile and electrostatic charge of single and combination metered dose inhalers. Pharmaceutical research 26:2639-2646.

Hoe, S., D. Traini, H.-K. Chan, and P. M. Young. 2009b. Measuring charge and mass distributions in dry powder inhalers using the electrical Next Generation Impactor (eNGI). Eur J Pharm Sci 38:88-94.

Hoe, S., P. Young, H.-K. Chan, and D. Traini. 2009c. Introduction of the electrical next generation impactor (eNGI) and investigation of its capabilities for the study of pressurized metered dose inhalers. Pharmaceutical research 26:431-437.

Hoshino, Y., K. Li, D. J. Karunanayake, and T. Hasegawa. 2010. Review of toner-based priniting technologies and fundamentals of toner charging mechanism. Journal of Imaging Science and Technology 54:1-5.

Ireland, P. M. 2010a. Triboelectrification of particulate flows on surfaces: Part I - Experiments. Powder Technology 198:189-198.

Ireland, P. M. 2010b. Triboelectrification of particulate flows on surfaces: Part II - Mechanisms and models. Powder Technology 198:199-210.

James, J., M. Davies, R. Toon, P. Jinks, and C. J. Roberts. 2009. Particulate drug interactions with polymeric and elastomeric valve components in suspension formulations for metered dose inhalers. International Journal of Pharmaceutics 366:124-132.

Jaworek, A., A. Krupa, and T. Czech. 2006. Modern electrostatic devices and methods for exhaust gas cleaning: A brief review. J. Electrost. 65:133-155.

Jonassen, N. 2002. Decay of Charge. Pages 41-50 Electrostatics.

Karner, S. and U. N. Anne. 2011. The impact of electrostatic charge in pharmaceutical powders with specific focus on inhalation-powders. J. Aerosol Sci. 42:428-445.

Karner, S. and N. A. Urbanetz. 2013. Triboelectric characteristics of mannitol based formulations for the application in dry powder inhalers. Powder Technol. 235:349-358.

Kaufmann, A., B. Ryser, and B. Suter. 2001. HPLC with evaporative light scattering detection for the determination of polar compounds in used frying oils. Eur. Food Res. Technol. 213:372-376.

Kenyon, C. J., L. Thorsson, L. Borgstrom, and S. P. Newman. 1998. The effects of static charge in spacer devices on glucocorticosteroid aerosol deposition in asthmatic patients. European Respiratory Journal 11:606-610.

Keskinen, J., K. Pietarinen, and M. Lehtimaki. 1992. Electrical low pressure impactor. J. Aerosol Sci. 23:353-360.

Kiao, I., L. T. Choi, J. Tu, S. Ding, and F. Thien. 2010. Micron particle deposition in a tracheobronchial airway model under different breathing conditions. Medical Engineering and Physics 32:1198-1212.

Kimura, K., M. Tabata, and K. Konishi. 2009. Peripheral airway treatment based on drug characteristics. Inhaled corticosteroids. Arerugi, Men'eki 17:36-44.

Knoch, M. and M. Keller. 2005. The customised electronic nebuliser: a new category of liquid aerosol drug delivery systems. Expert Opin. Drug Delivery 2:377-390.

Knowles, M. R. and R. C. Boucher. 2002. Mucus clearance as a primary innate defense mechanism for mammalian airways. J Clin Invest 109:571-577.

Knox, A. J., L. Pang, and Y. M. Zhu. 2000. Targeting remodeling in respiratory inflammation. Curr. Opin. Invest. Drugs 1:428-434.

Kok, J. F. and D. J. Lacks. 2009. Electrification of granular systems of identical insulators. Physical Review E 79:051304.

Kulon, J. and W. Balachandran. 2001. The measurement of bipolar charge on aerosols. Journal of Electrostatics 51-52:552-557.

Kulon, J., S. Hrabar, W. Machowski, and W. Balachandran. 2001. A Bipolar Charge Measurement System for Aerosol Characterization. IEEE Transactions on Industry Applications 37:472-479.

Kulvanich, P. and P. J. Stewart. 1987. An evaluation of the air stream Faraday cage in the electrostatic charge measurement of interactive drug systems. Int. J. Pharm. 36:243-252.

Kwetkus, B. A. 1998. Particle Triboelectrification and its Use in the Electrostatic Separation Process. Particulate Science and Technology 16:55-68.

Kwok, P., W. Glover, and H. K. Chan. 2005. Electrostatic Charge Characteristics of Aerosols Produced from Metered Dose Inhalers. Journal of Pharmaceutical Sciences 94:2789-2799.

Kwok, P., T. Noakes, and H.-K. Chan. 2008. Effect of moisture on the electrostatic charge properties of metered dose inhaler aerosols. Journal of aerosol science 39:211-226.

Kwok, P. C. L. and H.-K. Chan. 2008a. Effect of relative humidity on the electrostatic charge properties of dry powder inhaler aerosols. Pharm Res 25:277-288.

Kwok, P. C. L. and H.-K. Chan. 2008b. Effect of Relative Humidity on the Electrostatic Charge Properties of Dry Powder Inhaler Aerosols. Pharm. Res. 25:277-288.

Kwok, P. C. L. and H. K. Chan. 2009. Electrostatics of pharmaceutical inhalation aerosols. Journal of Pharmacy and Pharmacology 61:1587-1599.

Lakehal, D. 2013. Advanced simulation of transient multiphase flow & flow assurance in the oil & gas industry. Can. J. Chem. Eng. 91:1201-1214.

Lass, J. S., A. Sant, and M. Knoch. 2006. New advances in aerosolised drug delivery: vibrating membrane nebuliser technology. Expert Opin. Drug Delivery 3:693-702.

Latchford, G., A. Duff, J. Quinn, S. Conway, and M. Conner. 2009. Adherence to nebulised antibiotics in cystic fibrosis. Patient Educ Couns 75:141-144.

Lee, L. H. 1994. Dual mechanism for metal-polymer contact electrification. Journal of Electrostatics 32:1-29.

Lowell, J. 1977a. The role of material transfer in contact electrification. J. Phys. D 10:L233-L235.

Lowell, J. 1977b. The role of material transfer in contact electrification. Journal of Physics D: Applied Physics 10:L233.

Lowell, J. and A. C. Rose-Innes. 1980. Contact electrification. Adv. Phys. 29:947-1023.

Lowell, J. and W. S. Truscott. 1986a. Triboelectrification of identical insulators. I. An experimental investigation. Journal of Physics D: Applied Physics 19:1273.

Lowell, J. and W. S. Truscott. 1986b. Triboelectrification of identical insulators. II. Theory and further experiments. Journal of Physics D: Applied Physics 19:1281.

Lutz, B. and J. Kindersberger. 2009. Influence of relative humidity on surface charge decay on epoxy resin insulators. Proceedings of the 9th international conference on properties and applications of dielectric materials:883-886.

Mackin, L., G. Rowley, and E. Fletcher. 1997. An investigation of carrier particle type, electrostatic charge, and relative humidity on in vitro drug deposition from dry powder inhalers. Pharmaceutical Sciences 3:583-586.

Maggi, L., R. Bruni, and U. Conte. 1999. Influence of the moisture on the performance of a new dry powder inhaler. Int. J. Pharm. 177:83-91.

Manjunath, K. 2011. Effect of physical properties of particulates on dust explosions and fires. AIChE Spring Meeting & 7th Global Congress on Process Safety, Conference Proceedings, Chicago, IL, United States.

Marjamaki, M., J. K. Keskinen, D.-R. Chen, and D. Pui. 2000. Performance evaluation of the electrical low-pressure impactor (ELPI). Journal of aerosol science 31:249.

Marple, V. A., B. A. Olson, K. Santhanakrishnan, J. P. Mitchell, S. C. Murray, and B. L. Hudson-Curtis. 2003a. Next generation pharmaceutical impactor (a new impactor for pharmaceutical inhaler testing). Part II: Archival calibration. J Aerosol Med 16:301-324.

Marple, V. A., D. L. Roberts, F. J. Romay, N. C. Miller, K. G. Truman, M. Van Oort, B. Olsson, M. J. Holroyd, J. P. Mitchell, and D. Hochrainer. 2003b. Next generation pharmaceutical impactor (a new impactor for pharmaceutical inhaler testing). Part I: Design. Journal of aerosol medicine 16:283–299.

Matera, M. G., G. Curradi, and M. Cazzola. 2008. Long-acting β2 agonists in asthma and allergic rhinitis. Expert Opin. Pharmacother. 9:1531-1539.

Matsusaka, S., H. Maruyama, T. Matsuyama, and M. Ghadiri. 2010. Triboelectric charging of powders: A review. Chemical Engineering Science 65:5781-5807.

Matsusaka, S. and H. Masuda. 2003. Electrostatics of particles. Adv. Powder Technol. 14:143-166.

Mayya, Y. S. and B. K. Sapra. 2002. Image forces on a collection of charged particles near conducting surfaces. Journal of aerosol science 33:817-828.

Mazumder, M. K., R. E. Ware, and W. G. Hood. 1983. Simultaneous measurements of aerodynamic diameter and electrostatic charge on a single-particle basis. Pages 327-341 *in* Meas. Suspended Part. . Wiley.

Melandri, C., G. Tarroni, V. Prodi, T. De Zaicomo, M. Formignani, and C. Lombardi. 1983. Deposition of charged particles in the human airways. Journal of aerosol science 14:657.

Mie, G. 1908. Contributions to the Optics of Turbid Media, Especially Colloidal Metal Solutions. Ann. Phys. (Weinheim, Ger.) 25:377-445.

Miller-Larsson, A. and O. Selroos. 2006. Advances in asthma and COPD treatment: combination therapy with inhaled corticosteroids and long-acting β2-agonists. Curr. Pharm. Des. 12:3261-3279.

Millikan, R. A. 1911. The Isolation of an Ion, a Precision Measurement of its Charge, and the Correction of Stokes' Law. Science (Washington, DC, U. S.) 32:436-448.

Mitchell, J., M. Copley, Y. Sizer, T. Russell, and D. Solomon. 2012. Adapting the Abbreviated Impactor Measurement (AIM) concept to make appropriate inhaler aerosol measurements to compare with clinical data: a scoping study with the "Alberta" idealized throat (AIT) inlet. J Aerosol Med Pulm Drug Deliv 25:188-197.

Mitchell, R. I. and J. M. Pilcher. 1959. Cascade impactor for measuring aerosol particle sizes. Ind. Eng. Chem. 51:1039-1042.

Mizes, H. A., E. M. Conwell, and D. P. Salamida. 1990. Direct observation of ion transfer in contact charging between a metal and a polymer. Applied Physics Letters 56:1597-1599.

Mohammed, H., D. Roberts, M. Copley, M. Hammond, S. Nichols, and J. Mitchell. 2012. Effect of sampling volume on dry powder inhaler (DPI)-emitted aerosol aerodynamic particle size distributions (APSDs) measured by the Next-Generation Pharmaceutical Impactor (NGI) and the Andersen eight-stage cascade impactor (ACI). Aaps Pharmscitech 13:875-882.

Mountain, J. R., M. K. Mazumder, R. A. Sims, D. L. Wankum, T. Chasser, and P. H. Pettit. 2001. Triboelectric charging of polymer powders in fluidization and transport processes. IEEE Transactions on Industry Applications 37:778-784.

Murnane, D., G. P. Martin, and C. Marriott. 2006. Validation of a reverse-phase high performance liquid chromatographic method for concurrent assay of a weak base (salmeterol xinafoate) and a pharmacologically active steroid (fluticasone propionate). Journal of Pharmaceutical and Biomedical Analysis 40:1149–1154.

Murtomaa, M., P. Harjunen, V. Mellin, V. P. Lehto, and E. Laine. 2002. Effect of amorphicity on the triboelectrification of lactose powder. Journal of Electrostatics 56:103-110.

Murtomaa, M. and E. Laine. 2000. Electrostatic measurements on lactose-glucose mixtures. J. Electrost. 48:155-162.

Murtomaa, M., V. Mellin, P. Harjunen, T. Lankinen, E. Laine, and V. P. Lehto. 2004. Effect of particle morphology on the triboelectrification in dry powder inhalers. International Journal of Pharmaceutics 282:107-114.

Nemeth, E., V. Albrecht, G. Schubert, and F. Simon. 2003. Polymer tribo-electric charging: dependence on thermodynamic surface properties and relative humidity. J. Electrost. 58:3-16.

Newhouse, M. T., P. H. Hirst, S. P. Duddu, Y. H. Walter, T. E. Tarara, A. R. Clark, and W. J. G. 2003. Inhalation of a dry powder tobramycin pulmosphere formulation in health volounteers. Chest 124:360-366.

Newman, S. P. 2004. Dry powder inhalers for optimal drug delivery. Expert Opinion on Biological Therapy 4:23-33.

Newton, R. 1982. Scattering theory of waves and particles. Springer-Verlag New York, Inc.

Noakes, T. 2002. Medical aerosol propellants. J. Fluorine Chem. 118:35-45.

Noakes, T. 2004. Electrostatics: the next isssue for inhaled medications? Drug delivery technology 4:64.

Noakes, T. J., I. D. Pavey, D. Bray, and R. C. Rowe. 1990. Apparatus for producing a spray of droplets of a liquid. Imperial Chemical Industries Plc, UK .

Nomura, T., T. Satoh, and H. Masuda. 2003. The environment humidity effect on the tribo-charge of powder. Powder Technology 135-136:43-49.

O'Leary, M., W. Balachandran, P. Rogueda, and F. Chambers. 2008. The bipolar nature of charge resident on supposedly unipolar aerosols. Journal of Physics: Conference Series 142:012022.

Overbeek, J. T. G. and M. J. Sparnaay. 1954. Coagulation and flocculation. General introduction. I. Classical coagulation. London-van der Waals' attraction between macroscopic objects. Discuss. Faraday Soc. 18:12-24.

Patton, J. S., S. C. Fishburn, and J. G. Weers. 2004. The lungs as a portal of entry for systemic drug delivery. Proceedings of the American Thorasic Society 1:338-344.

Peart, J., P. Kulphaisal, and J. C. Orban. 2003. Relevance of Electrostatics in Respiratory Drug Delivery. Business Briefing: Pharmagenerics:1-4.

Peart, J., J. N. Staniforth, P. R. Byron, and B. J. Meakin. 1996. Electrostatic charge interactions in pharmaceutical dry powder aerosols. Pages 85-93. Interpharm Press.

Perera, R. W. H. and W. J. Lough. 2011. Assessment of chiral stationary phases for suitability for combined enantiomeric impurity/related substances assays. J. Chromatogr. A 1218:8655-8663.

Peri, D., J. bloggs, C. smith, and F. bumble. 2001. Design Optimization of Ship Hulls via CFD Techniques. Journal of Ship Research 45:140-149.

PhEur. 2008. European Pharmacopoeia 6.0, 2.9.18.

Pingali, K. C., T. Shinbrot, S. V. Hammond, and F. J. Muzzio. 2009. An observed correlation between flow and electrical properties of pharmaceutical blends. Powder Technology 192:157-165.

Pitchayajittipong, C., R. Price, J. Shur, J. S. Kaerger, and S. Edge. 2010. Characterisation and functionality of inhalation anhydrous lactose. Int. J. Pharm. 390:134-141.

Placke, M. E. and W. C. Zimlich, Jr. 2002. Developing an advanced pulmonary delivery technology: leveraging engineering challenges into clinical opportunities. Drug Delivery Technol. 2:40, 42-46.

Price, R., P. M. Young, S. Edge, and J. N. Staniforth. 2002. The influence of relative humidity on particulate interactions in carrier-based dry powder inhaler formulations. Int. J. Pharm. 246:47-59.

Prime, D., P. J. Atkins, A. Slater, and B. Sumby. 1997. Review of dry powder inhalers. Advanced Drug Delivery Reviews 26:51-58.

Prokopovich, P., editor. 2013. Inhaler Devices, Fundamentals, Design and Drug Delivery.

Pu, Y., M. Mazumder, and C. Cooney. 2009. Effects of Electrostatic Charging on Pharmaceutical Powder Blending Homogeneity. Journal of Pharmaceutical Sciences 98:2412-2421.

Rabe, K. F., S. Hurd, A. Anzueto, P. J. Barnes, S. A. Buist, P. Calverley, Y. Fukuchi, C. Jenkins, R. Rodriguez-Roisin, W. C. van, and J. Zielinski. 2007. Global strategy for the diagnosis, management, and prevention of chronic obstructive pulmonary disease: GOLD executive summary. Am J Respir Crit Care Med 176:532-555.

Revel, J., C. Gatumel, J. Dodds, and J. Taillet. 2003. Generation of static electricity during fluidisation of polyethylene and its elimination by air ionisation. Powder Technology 135-136:192-200.

Robins, E. S., A. C. Rose-Innes, and J. Lowell. 1975. Are adsorbed ions involved in the contact charging between metals and insulators. Conference Series - Institute of Physics 27.

Rogueda, P. G. A., R. Price, T. Smith, P. M. Young, and D. Traini. 2011. Particle synergy and aerosol performance in non-aqueous liquid of two combinations metered dose inhalation formulations: An AFM and Raman investigation. Journal of Colloid and Interface Science 361:649-655.

Rowley, G. 2001. Quantifying electrostatic interactions in pharmaceutical solid systems. International Journal of Pharmaceutics 227:47-55.

Rowley, G. and L. A. Mackin. 2003. The effect of moisture sorption on electrostatic charging of selected pharmaceutical excipient powders. Powder Technology 135:50-58.

Rubin, B. K. and J. B. Fink. 2005. Optimizing aerosol delivery by pressurized metered-dose inhalers. Respir Care 50:1191-1200.

Saini, D., A. S. Biris, P. K. Srirama, and M. K. Mazumder. 2007. Particle size and charge distribution analysis of pharmaceutical aerosols generated by inhalers. Pharmaceutical Development and Technology 12:35-41.

Saini, D., S. Trigwell, P. K. Srirama, R. A. Sims, R. Sharma, A. S. Biris, and M. K. Mazumder. 2008. Portable Free-Fall Electrostatic Separator for Beneficiation of Charged Particulate Materials. Part. Sci. Technol. 26:349-360.

Sbirlea-Apiou, G., G. Caillibotte, Y. Yang, I. Katz, and T. B. Martonen. 2007. Deposition mechanics of pharmaceutical particles in human airways. Lung Biology in Health and Disease 221:1-30.

Schein, L. 2008. 50 years of toner adhesion control in electrophotography. 日本画像学会誌 47:425.

Schlacht, E. C. 1941. Apparatus for the manufacture of abrasive products such as sandpaper. Behr-Manning Corp. .

Schmitt, C. and M. Lebienvenu. 2003. Electrostatic painting of conductive composite materials. J. Mater. Process. Thechnol 134:303-309.

Schwarz, H., A. Thornton, W. Conklin, and H. Stanley. 2001. Fraunhofer and/or Mie theory? LaborPraxis 25:90, 92, 94.

Scott, G. and P. Richardson. 1997. The application of computational fluid dynamics in the food industry. Trends in Food Science & Technology 8:119-124.

Sharma, R., S. Trigwell, A. S. Biris, R. A. Sims, and M. K. Mazumder. 2003. Effect of ambient relative humidity and surface modification on the charge decay properties of polymer powders in powder coating. IEEE Trans. Ind. Appl. 39:87-95.

Sharmene Ali, F., M. Adnan Ali, R. Ayesha Ali, and I. I. Inculet. 1998. Minority charge separation in falling particles with bipolar charge. Journal of Electrostatics 45:139-155.

Sheean, J. L. 1930. The beginnings of electrochemical activities. Journal of Chemical Education 7:33.

Shekunov, B., P. Chattopadhyay, H. Tong, and A. Chow. 2007. Particle Size Analysis in Pharmaceutics: Principles, Methods and Applications. Pharm. Res. 24:203-227.

Shekunov, B. Y., J. C. Feeley, A. H. L. Chow, H. H. Y. Tong, and P. York. 2002. Physical properties of supercritically-processed and micronized powders for respiratory drug delivery. Kona 20:178-187.

Shur, J., H. Harris, M. D. Jones, J. S. Kaerger, and R. Price. 2008. The Role of Fines in the Modification of the Fluidization and Dispersion Mechanism Within Dry Powder Inhaler Formulations. Pharmaceutical Research 25:1631-1640.

Shur, J., S. Lee, W. Adams, R. Lionberger, J. Tibbatts, and R. Price. 2012. Effect of Device Design on the In Vitro Performance and Comparability for Capsule-Based Dry Powder Inhalers. AAPS J. 14:667-676.

Sidebotham, H. J. and W. R. Roche. 2003. Asthma deaths; persistent and preventable mortality. Histopathology 43:105-117.

Soltani, M. R. and G. Ahmadi. 1999. Charged particle trajectory statistics and deposition in a turbulent channel flow. Aerosol Science and Technology 31:170-186.
Staniforth, J. N. and J. E. Rees. 1981. Powder mixing by triboelectrification. Powder Technol. 30:255-256.

Stankovich, J. J., F. Gritti, P. G. Stevenson, P. Vajda, L. A. Beaver, and G. Guiochon. 2014. Volume based vs. time based chromatograms: Reproducibility of data for gradient separations under high and low pressure conditions. J. Chromatogr. A:Ahead of Print.

Steckel, H., P. Markefka, W. H. te, and R. Kammelar. 2006. Effect of milling and sieving on functionality of dry powder inhalation products. Int. J. Pharm. 309:51-59.

Stevens, N., S. Tedeschi, K. Powers, B. Moudgil, and H. El-Shall. 2009. Controlling unconfined yield strength in a humid environment through surface modification of powders. Powder Technol. 191:170-175.

Sun, J. 2011. The use of dynamic vapor sorption method in the determination of water sorption limit and setting specification for drug substance. Am. Pharm. Rev. 14:76, 78-80.

Sung, P. F., Y. L. Hsieh, K. Angonese, D. Dunn, R. J. King, R. Machbitz, A. Christianson, W. J. Chappell, L. S. Taylor, and M. T. Harris. 2011. Complex dielectric properties of microcrystalline cellulose, anhydrous lactose, and alpha-lactose monohydrate powders using a microwave-based open-reflection resonator sensor. J Pharm Sci 100:2920-2934.

Supuk, E., C. Seiler, and M. Ghadiri. 2009. Analysis of a simple test device for tribo-electric charging of bulk powders. Part. Part. Syst. Charact. 26:7-16.

Telko, M. J. and A. J. Hickey. 2005. Dry powder inhaler formulation. Respiratory Care 50:1209-1227.

Trac, H. and U. Pen. 2003. A Primer on Eulerian Computational Fluid Dynamics for Astrophysics. Publications of the Astronomical Society of the Pacific 115:303-332.

Tselishchev, Y. G. and V. A. Val'tsifer. 2003. Influence of the Type of Contact between Particles Joined by a Liquid Bridge on the Capillary Cohesive Forces. Colloid J. 65:385-389.

Unger, K., R. Skudas, and M. Schulte. 2008. Particle packed columns and monolithic columns in high-performance liquid chromatography-comparison and critical appraisal. J. Chromatogr. A 1184:393-415.

USP. 2011. United States Pharmacopoeia. <905>.

Visser, J. 1989. Van der Waals and other cohesive forces affecting powder fluidization. Powder Technology 58:1-10.

Voss, A. and W. H. Finlay. 2002. De-agglomeration of dry powder pharmaceutical aerosols. Int. J. Pharm. 248:39-50.

Ward, A. L. 1965. Calculations of Electrical Breakdown in Air at Near-Atmospheric Pressure. Physical Review 138:A1357-A1362.

Watanabe, H., M. Ghadiri, T. Matsuyama, Y. L. Ding, K. G. Pitt, H. Maruyama, S. Matsusaka, and H. Masuda. 2007. Triboelectrification of pharmaceutical powders by particle impact. International Journal of Pharmaceutics 334:149-155.

Wei, Y. and M.-Y. Ding. 2000. Analysis of carbohydrates in drinks by high-performance liquid chromatography with a dynamically modified amino column and evaporative light scattering detection. Journal of Chromatography A 904:113-117.

Wells, O. 1974. Scanning Electron Microscopy. New York ; London : McGraw-Hill:37.

WHO. 2011. World Health Organisation. http://www.who.int/features/factfiles/asthma/en/.

Williams, M. W. 2011. Triboelectric charging of insulators - evidence for electrons versus ions. IEEE Transactions on Industry Applications 47:1093-1099.

Wilson, I. 1947. The deposition of charged particles in tubes, with reference to the retention of therapeutic aerosols in the human lung. Journal of colloid science 2:271.

Wong, J., P. C. L. Kwok, T. Noakes, A. Fathi, F. Dehghani, and H.-K. Chan. 2014. Effect of Crystallinity on Electrostatic Charging in Dry Powder Inhaler Formulations. Pharm. Res. 31:1656-1664.

Xu, R. 1997. Improvements in particle size analysis using light scattering. Pages 27-56. Medpharm Scientific Publishers.

Xu, R. 2002. Light Scattering. Pages 56-110 *in* B. Scarlett, editor. Particle Characterization: Light Scattering Methods.

Yin, X., J. Zhang, and F. Zhang. 2010. CFD simulations of influences of meteorologic conditions on the dispersion of benzene. Jisuanji Yu Yingyong Huaxue 27:1099-1102.

Yli-Ojanpera, J., A. Ukkonen, A. Jarvinen, S. Layzell, V. Niemela, and J. Keskinen. 2014. Bipolar Charge Analyzer (BOLAR): A new aerosol instrument for bipolar charge measurements. J. Aerosol Sci. 77:16-30.

Young, P. M., R. Price, M. J. Tobyn, M. Buttrum, and F. Dey. 2004. The influence of relative humidity on the cohesion properties of micronized drugs used in inhalation therapy. J. Pharm. Sci. 93:753-761.

Young, P. M., A. Sung, D. Traini, P. Kwok, H. Chiou, and H. K. Chan. 2007. Influence of humidity on the electrostatic charge and aerosol performance of dry powder inhaler carrier based systems. Pharmaceutical Research 24:963-970.

Yu, C. P. and J. P. Hu. 1983. Diffusional deposition of ultrafine particles in the human lung. Aerosols Min. Ind. Work Environ. 1:139-149.

Zeng, X. M., G. P. Martin, and C. Marriott. 2001. Particulate interactions in dry powder formulations for inhalation. Taylor and Francis.

Zhang, L., B. Ashgarian, and S. Anjilvel. 1996. Inertial and interceptional deposition of fibers in a bifurcating airway. Journal of aerosol medicine 9:419-430.

Zhang, T., P. Li, Y. Zhao, and S. Wang. 2013. Various air distribution modes on commercial airplanes-Part 2: Computational fluid dynamics modeling and validation. HVAC&R Res. 19:457-470.

Zhang, Y., T. Chia, and W. Finlay. 2006. Experimental Measurement and Numerical Study of Particle Deposition in Highly Idealized Mouth-Throat Models. Aerosol Sci. Technol. 40:361-372.

Zhou, H., M. Gotzinger, and W. Peukert. 2003. The influence of particle charge and roughness on particle-substrate adhesion. Powder Technol. 135-136:82-91.

Zhu, K. W., W. K. Ng, S. C. Shen, R. B. H. Tan, and P. W. S. Heng. 2008. Design of a device for simultaneous particle size and electrostatic charge measurement of inhalation drugs. Pharmaceutical Research 25:2488-2496.